Evolution des mécanismes de formation des asymétries habénulaires chez les gnathostomes : la petite roussette, Scyliorhinus canicula, comme référence

Maxence Lanoizelet

Université Fédérale
Toulouse Midi-Pyrénées

THÈSE

En vue de l'obtention du

DOCTORAT DE L'UNIVERSITÉ DE TOULOUSE

Délivré par l'Université Toulouse 3 - Paul Sabatier

Présentée et soutenue par

Maxence LANOIZELET

Le 17 septembre 2021

Evolution des mécanismes de formation des asymétries habénulaires chez les gnathostomes : la petite roussette, Scyliorhinus canicula, comme référence

---

Ecole doctorale : **BSB - Biologie, Santé, Biotechnologies**

Spécialité : **BIOLOGIE DU DEVELOPPEMENT**

Unité de recherche :
CBD - Centre de Biologie du Développement

Thèse dirigée par
Patrick BLADER et Sylvie MAZAN

Jury

Mme Marion COOLEN, Rapporteure
M. Abderrahman KHILA, Rapporteur
M. Philippe VERNIER, Examinateur
M. Patrick BLADER, Directeur de thèse
Mme Sylvie MAZAN, Co-directrice de thèse

Remerciements

Je tout d'abord à remercier mes rapporteurs et jurys de thèse pour avoir acceptés d'évaluer mon travail.

Je souhaiterais remercier Sylvie MAZAN, qui m'a encadré et accueilli dans son équipe pour y effectuer mon doctorat. J'ai appris énormément sur le plan scientifique, ainsi que la rigueur nécessaire pour mener de tels travaux de recherche. Elle m'a également enseigné ce que c'était que d'avoir un regard critique et une méthodologie de travail. Pour sa bienveillance, je tenais une nouvelle fois à la remercier. Je remercie tout le reste de l'équipe pour m'avoir aidé et soutenu tout au long de ma thèse, en particulier, Ronan LAGADEC, ingénieur de recherche, qui m'a encadré sur le plan expérimental. Je remercie Hélène MAYEUR pour avoir réalisé l'ensemble des analyses bio-informatiques de ma thèse. Je remercie également Léo MICHEL, étudiant en thèse dans l'équipe, pour l'entre-aide et le soutien dont il a fait preuve à mon égard.

Je tenais à remercier la structure du laboratoire ARAGO de l'observatoire océanologique de Banyuls sur mer. Un grand merci pour l'accueil chaleureux de l'ensemble de ses équipes et d'avoir mis à ma disposition les outils nécessaires à la réalisation de mon projet de recherche.

Je voudrais aussi remercier Patrick BLADER, pour m'avoir également accueilli dans son équipe. Même si la situation n'a pas permis que je vienne travailler à Toulouse, je voulais le remercier pour avoir participer à mon encadrement et pour les nombreux conseils qu'il a pu me donner qui m'ont beaucoup aidé tout au long de ma thèse. Je remercie également tout le reste de l'équipe pour leurs accueils chaleureux à chaque déplacement que j'ai pu faire à Toulouse.

Des remerciements particuliers s'imposent aux personnes qui m'ont soutenues au quotidien, sans qui je ne serais pas allé au bout de ce long travail. Merci Doudou, ami de toujours et de tout temps, les bancs de la fac nous paraissent bien loin mais notre amitié n'a jamais été aussi forte qu'aujourd'hui. Merci, ma Loutre, d'avoir été aussi présente pendant ces 4 longues années, pourtant si courtes à tes côtés. Merci Lydvina, nos soirées « pizza labo dodo » me manqueront à n'en pas douter. Merci Fanny, d'éprouver la même passion enflammée que moi pour le Seigneur des Anneaux et White Fire, 2 films que tout le monde devrait avoir vu. Merci Agnès et Seb, pour m'avoir rassuré dans les moments où je doutais le plus de moi-même et de mes choix. Il est enfin venu le temps de remercier l'ensemble des agents du Z.O.B. pour son soutien morale et logistique en temps de confinement, nous avons su faire face à cette crise ensemble. Ainsi je remercie les prestigieux agents Chattière, Immotep, Condor, Kum, Link et Tim pour leur dévouement sans faille à la cause. Je tenais plus largement à remercier l'organisation du G.E.R.B et évidemment la F.O.U.F.E. sans qui rien de tout cela n'aurais été réalisable !

Résumé en Français

Les habénulas sont des structures épithalamiques bilatérales, retrouvées chez tous les vertébrés. Une de leurs particularités est qu'elles présentent des asymétries marquées entre la droite et la gauche chez un grand nombre d'espèces, ce qui en fait un modèle de référence pour l'étude des asymétries du système nerveux central des vertébrés. Jusqu'ici, la nature des asymétries habénulaires et les mécanismes responsables de leur formation ont été étudiés principalement chez le poisson-zèbre. Mon projet de thèse a visé à caractériser ces asymétries ainsi que leurs mécanismes de formation chez un chondrichtyen, la petite roussette *Scyliorhinus canicula*, puis à utiliser ces données comme référence pour préciser leur évolution chez les gnathostomes. La stratégie expérimentale a reposé sur trois approches complémentaires, (1) une caractérisation moléculaire des habénulas de roussette au cours de leur développement par étude de gènes candidats, (2) une analyse transcriptomique des asymétries, complétée par des études d'expression in situ, et (3) des analyses expérimentales des mécanismes impliqués dans leur formation. J'ai ensuite utilisé ces données pour une étude comparée, à la fois expérimentale et bibliographique, des asymétries habénulaires chez un spectre large de gnathostomes, comprenant les modèles génétiques traditionnels, souris et poisson-zèbre, mais également des espèces non conventionnelles choisies pour leur position phylogénétique, le xénope, *X. tropicalis*, deux actinoptérygiens, *Erpetoichthys calabaricus* et *Lepisosteus oculatus*, et un holocéphale *Callorhinchus milii.* Ce travail met en évidence des asymétries neurogénétiques très marquées dans les habénulas embryonnaires de roussette, ainsi qu'une organisation en sous-domaines fortement asymétrique de l'organe différencié. L'analyse des mécanismes impliqués met en évidence une régulation temporelle asymétrique de la neurogenèse et des choix de différenciation neuronale, impliquant les voies Nodal et Wnt canonique. La comparaison de ces données à l'échelle des gnathostomes permet de préciser le mode d'évolution des asymétries habénulaires, et suggère des pertes indépendantes chez les actinoptérygiens et les sarcoptérygiens. Ces diversifications pourraient être liées à une implication conservée de la voie Wnt dans l'élaboration des identités neuronales dans l'épithalamus et des variations de la régulation de cette activité dans le temps et l'espace.

Résumé en Anglais

Habenulae are bilateral epithalamic structures found in all vertebrates. One of their specificities is that they exhibit marked asymmetries along the left/right axis in many species, which makes them a reference model for the study of asymmetries in the vertebrate central nervous system. So far, the nature of habenular asymmetries and the mechanisms responsible for their formation have been primarily investigated in the zebrafish. My thesis project aimed at a characterisation of these asymmetries and their formation mechanisms in a chondrichthyan, the catshark *Scyliorhinus canicula*, and the exploitation of these data as a reference to gain insight into their mode of evolution in gnathostomes. The experimental strategy relied on three complementary approaches, (1) a molecular description of developing catshark habenulae by a candidate gene analysis, (2) a transcriptomic characterisation of asymmetries, complemented by in situ expression studies, and (3) experimental analyses of the mechanisms involved in their formation. I then used these data for a comparative study, both experimental and bibliographic, of habenular asymmetries in a broad range of gnathostomes, including traditional genetic models, such as the mouse, and zebrafish, as well as unconventional species chosen for their phylogenetic position, the xenopus, *Xenopus tropicalis*, two actinopterygians, *Erpetoichthys calabaricus* and *Lepisosteus oculatus*, and a holocephalan, *Callorhinchus milii*. This work highlights the presence of marked neurogenetic asymmetries in the catshark embryonic habenulae, as well as a highly asymmetrical subdomain organisation of the differentiated organ. Analysis of underlying mechanisms reveals an asymmetric temporal regulation of neurogenesis and of neuronal differentiation choices, involving Nodal and canonical Wnt pathways. Comparisons across gnathostomes provide new insights into the mode of evolution of habenular asymmetries, suggesting independent losses in actinopterygians and sarcopterygians. These diversifications could be related to a conserved involvement of Wnt pathway in the elaboration of neuronal identities in the epithalamus, and to variations in the regulation of this activity in time and space.

Table des matières

INTRODUCTION

I. Les habénulas chez les vertébrés

I-1. Description neuroanatomique

I-1-a. Aspects généraux

L'épithalamus est localisé dans la partie la plus dorsale du diencéphale. Il est constitué de l'organe pinéal, d'un organe parapinéal, retrouvé uniquement chez certaines espèces, et d'une structure bilatérale avec des composants droit et gauche bien individualisés, les habénulas (Hb). Morphologiquement, ces dernières sont localisées à la base de l'organe pinéal et sont reliées par la commissure habénulaire (Figure 1).

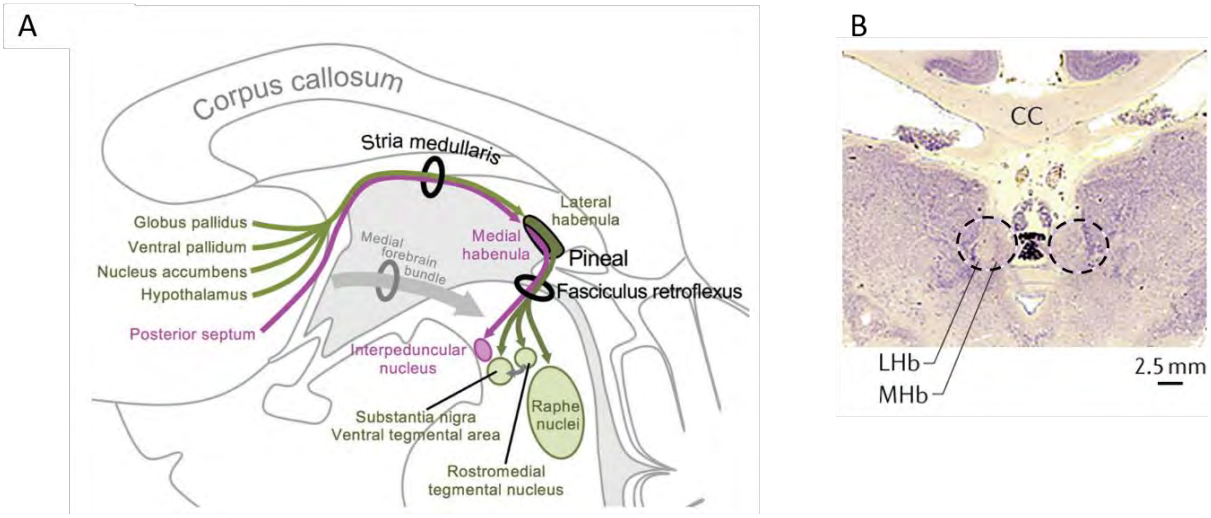

Figure 1 : Localisation et morphologie des habénulas chez l'homme. (A) Schémas des habénulas et de leurs projections en vue sagittale chez l'homme. (B) Section coronale du cerveau humain avec un agrandissement sur les noyaux habénulaires (entourés par des tirets noirs). *CC : corpus callosum, LHb : habénula latérale ; MHb : habénula médiane.* (Aizawa & Zhu, 2019; Hu, Cui, & Yang, 2020).

On les retrouve chez tous les vertébrés (Concha & Wilson, 2001). Sur la base d'analyses morphologiques et histologiques, elles ont été identifiées depuis plus de 20 ans comme des structures constituant un relai dans des circuits reliant notamment les noyaux de la base du télencéphale au mésencéphale (Sutherland, 1982). Ces circuits comprennent deux faisceaux majeurs. Le premier, la *stria medullaris* (SM), est localisé antérieurement à l'organe et contient des afférences neuronales provenant des noyaux entopédonculaires, des noyaux suprachiasmatiques, de l'aire pré-optique latérale, ou encore du cortex préfrontal. Le second, le *fasciculus retroflexus* (FR) marque la limite postérieure des habénulas et projette majoritairement sur les noyaux interpédonculaires et le noyau médian du raphé (Figure 1). Les habénulas ont été associées depuis de nombreuses années à des processus émotionnels et cognitifs complexes, incluant des réponses aux aversifs tels que la douleur (Nagao, Kamo, Akiguchi, & Kimura, 1993), le stress (Murray, Murphy, Ross, & Haun, 1994), et leur apprentissage (Zagami, Ferraro, Montalbano, Sardo, & La Grutta, 1995). De façon remarquable, elles présentent des asymétries plus ou moins marquées entre la gauche et la droite chez un grand nombre de vertébrés. Cette particularité en a fait un système de référence pour l'étude des asymétries du système nerveux chez les vertébrés.

I-1-b. Organisation en sous-domaines et connectivité chez les rongeurs

L'organisation en sous-domaines des habénulas a été étudiée en détail chez les rongeurs, et notamment la souris et le rat. Ces études, initialement fondées sur des approches morphologiques et immunohistochimiques, ont été récemment étendues à des approches moléculaires et transcriptomiques. Une subdivision en deux grands sous-domaines, l'un médian et l'autre latéral (Hbm et Hbl) a ainsi été proposée sur une base histologique chez la souris comme chez le rat, les Hbm présentant une densité cellulaire plus importante que les Hbl (Aizawa, Kobayashi, Tanaka, Fukai, & Okamoto, 2012; Herkenham & Nauta, 1979, 1977; Wagner, Stroh, & Veh, 2014) (Figure 2). Leur existence a par la suite été confirmée par hybridation *in situ*, avec la mise en évidence de gènes sélectivement exprimés dans chaque sous-domaine, tels que *Tac2*, pour l'Hbm, et *Pcdh10, Sox1* pour l'Hbl (Amo et al., 2010; Kan et al., 2007; Meberg & Routtenberg, 1991; Wagner et al., 2014) (Figure 2).

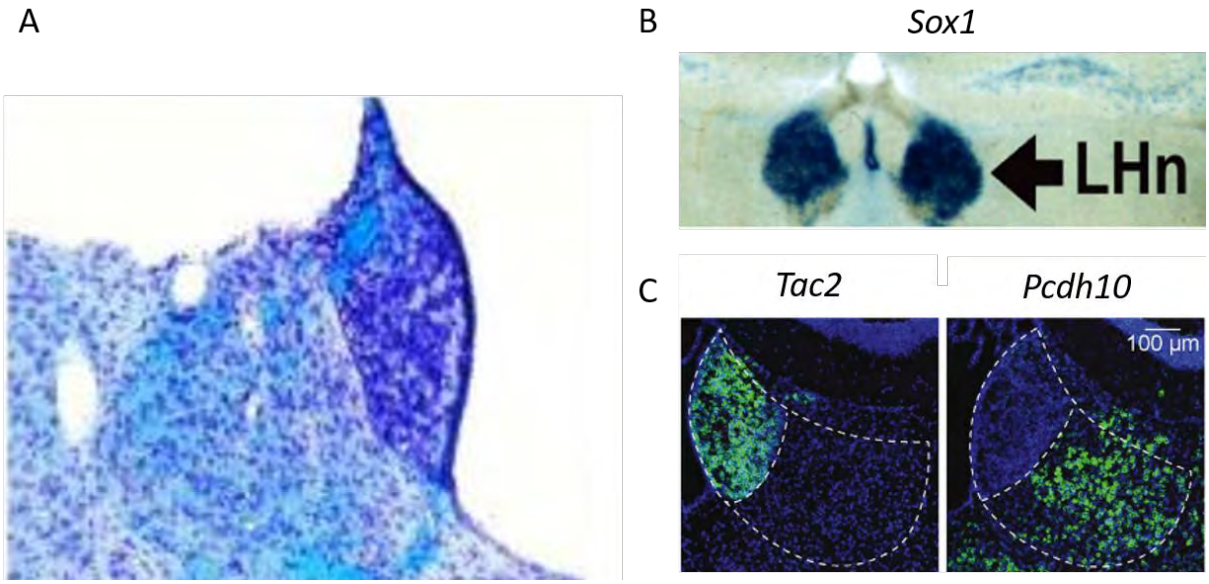

Figure 2 : Organisation en sous-domaines médians et latéraux des habénulas chez les rongeurs. (A) Section transverse de l'habénula droite de souris après coloration au bleu de Luxol (coloration de Klûver-Barrera). (B) Profil d'expression d'un rapporteur LacZ inséré par recombinaison homologue dans le locus de *MmSox1* exprimé dans les Hbl de souris sur une section transverse des habénulas. *LHn : noyaux habénulaires latéraux.* (C) Profil d'expression de *MmTac2* et de *MmPcdh10* respectivement dans les Hbm et Hbl de souris sur une section transverse des habénulas. (Kan et al., 2007; Wagner et al., 2014)

Ces deux grands sous-domaines contiennent des populations neuronales complexes, comme l'ont révélé des analyses plus récentes, combinant l'étude de l'atlas moléculaire Allen et des études transcriptomiques (Wagner, French, & Veh, 2016) (Figure 3). Enfin, très récemment, deux études par séquençage ARN « cellule unique » (ScRNA-seq) ont permis d'étendre la liste des gènes ayant une expression dans les deux grands sous-domaines Hbm et Hbl, avec l'identification de 170 gènes exprimés au sein du premier et 289 gènes exprimés au sein du second (Hashikawa et al., 2020a; Wallace et al., 2020). Les données obtenues confirment également l'hétérogénéité des populations neuronales qui les constituent. Après cartographie des clusters de cellules par hybridation *in situ*, des sous-domaines semblables à ceux identifiés dans les études morphologiques et transcriptomiques précédentes de Wagner et al., 2016 ont été identifiés : entre 5 et 6 territoires distincts pour les Hbm

et entre 4 et 6 territoires distincts pour les Hbl (Hashikawa et al., 2020a; Wallace et al., 2020) (Figure 3).

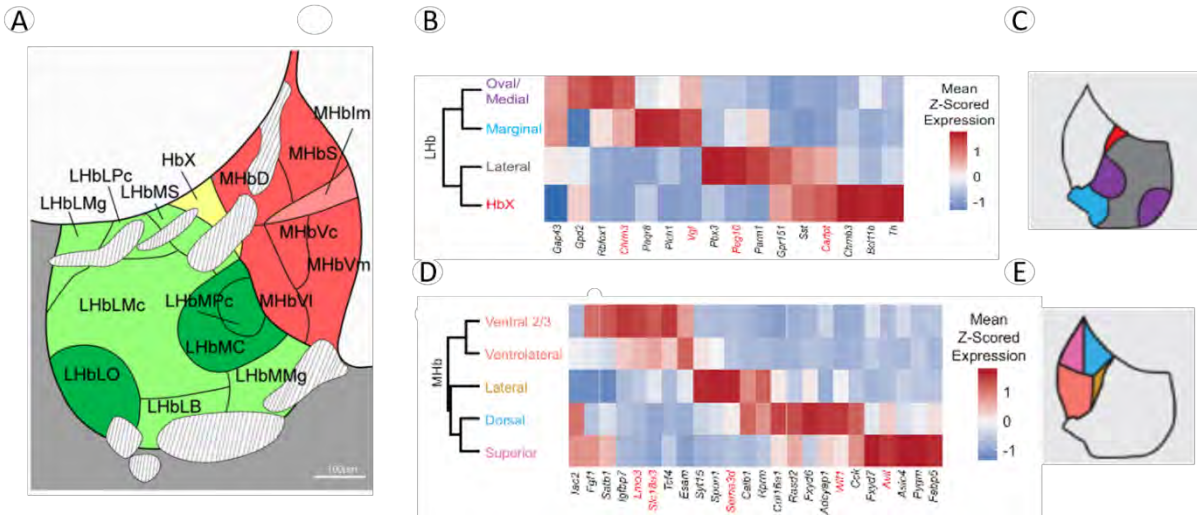

Figure 3 : Subdivisions des habénulas chez la souris d'après des analyses morphologiques, transcriptomiques et par séquençage ScRNA-seq. (A) Schémas des subdivisions des habénulas latérale et médiane gauche (respectivement en vert et rouge) (en différentes nuances de vert) et de l'Hbm (en différentes nuances de rouge) d'après (Wagner et al., 2016). Ces subdivisions ont été inférées d'analyses histologiques, immunohistochimiques et par hybridation *in situ* à l'aide de sondes sélectionnées après études de microarrays. *LHbMPc : sous-noyaux parvocallulaires de la division médial de l'Hbl; LHbMC : sous-noyaux centraux de la division médial de l'Hbl; LHbLO : sous-noyaux ovales de la division latérale de l'Hbl; LHbLMg : sous-noyaux marginaux de la division latérale de l'Hbl; LHbLPc : sous-noyaux parvocellulaires de la division latérale de l'Hbl; LHbLMc : sous-noyaux magnocellulaires de la division latérale de l'Hbl; LHbLB : sous-noyaux basaux de la division latéral de l'Hbl; LHbMS : sous-noyaux supérieurs de la division médiale de l'Hbl; LHbMMg : sous-noyaux marginaux de la division médial de l'Hbl; MHbIm : sous-noyaux intermédiaires de l'Hbm. MHbD : sous-noyaux dorsaux de l'Hbm; MHbS : sous-noyaux supérieurs de l'Hbm; MHbVl : sous-noyaux de l'Hbm ventrale latérale; MHbVc : sous-noyaux médians de l'Hbm ventrale centrale; MhbVm : sous-noyaux médians de l'Hbm ventrale médiane.* (B) Heatmap de l'expression relative (score moyen z-) des gènes enrichis dans chaque cluster des Hbl. (C) Schémas des subdivisions de l'Hbl inférées d'une analyse par séquençage de cellules uniques. (D) Heatmap de l'expression relative (score moyen z-) des gènes enrichis dans chaque cluster des Hbm (E). Schémas des subdivisions de l'Hbm à la suite de l'analyse par séquençage de cellule unique. (Wallace et al., 2020).

Les Hbm et Hbl diffèrent également par les neurotransmetteurs qu'elles expriment et leurs patrons de connectivité, bien documentées. Les Hbl sont composées essentiellement de neurones glutamatergiques exprimant VGlut2, Elles possèdent des afférences provenant du pallidum ventral, du système limbique antérieur, dont l'hypothalamus, des noyaux entopédonculaires, du pallidum dorsal, de l'aire tegmentale ventrale (VTA) et projettent sur de nombreux sites dont les noyaux tegmentaux rostromédiaux (RMTg), le VTA et au niveau du mésencéphale, sur le raphé dorsal. Les Hbm contiennent des neurones glutamatergiques mais aussi cholinergiques. Elles reçoivent des afférences provenant du septum. Au niveau du mésencéphale, elles projettent notamment sur les noyaux interpédonculaires (IPN) (Beretta, Dross, Guiterrez-Triana, Ryu, & Carl, 2012; Hashikawa et al., 2020b; Herkenham & Nauta, 1979, 1977; Hu et al., 2020; Kim, 2009; Lima et al., 2017; Roman et al., 2020) (Figure 4).

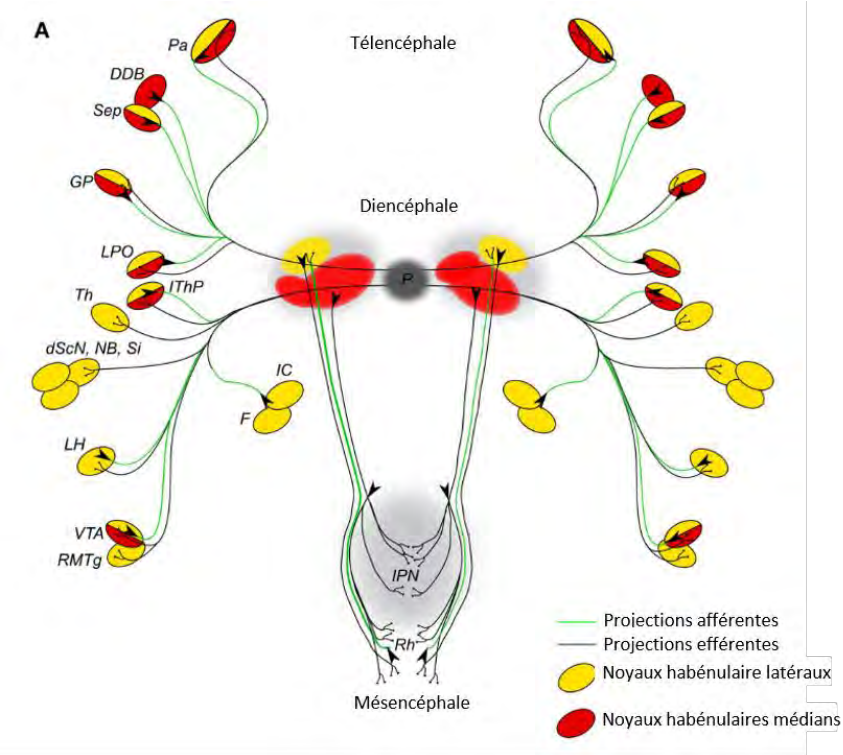

Figure 4 : Patrons de connectivité des sous-domaines habénulaires chez la souris. Schémas des afférences et efférences principales des Hbm et Hbl et des structures cérébrales sur lesquelles elles projettent. *DDB : Noyaux de la bande diagonale ; dScN : noyaux superchiasmatiques dorsaux ; F : Fornix; GP : globus pallidus; IC : capsule interne; IPN : noyaux interpédonculaires; IThP : pédoncule thalamique inférieure; LH : aire hypothalamique latérale; LPO : aire préoptique latérale; NB : noyaux de la base; P : pinéal ; Pa : Pallium; Rh : Raphé; RMTg : noyaux tegmental rostro-médian; Sep : septum; Si : substancia innominate; Th : noyaux thalamiques; VTA : aire tegmental ventral de Tsai.* (Beretta et al., 2012)

I-1-c. Organisation en sous-domaines et connectivité chez les téléostéens

L'organisation en sous-domaines des habénulas a également été décrite chez les téléostéens, en particulier chez l'organisme modèle de référence du groupe, le poisson-zèbre. Chez ce dernier, les habénulas présentent une subdivision principale en deux sous-domaines, l'un dorsal (Hbd) et l'autre ventral (Hbv). L'Hbv présente une densité de neurones plus importante que l'Hbd (Figure 5).

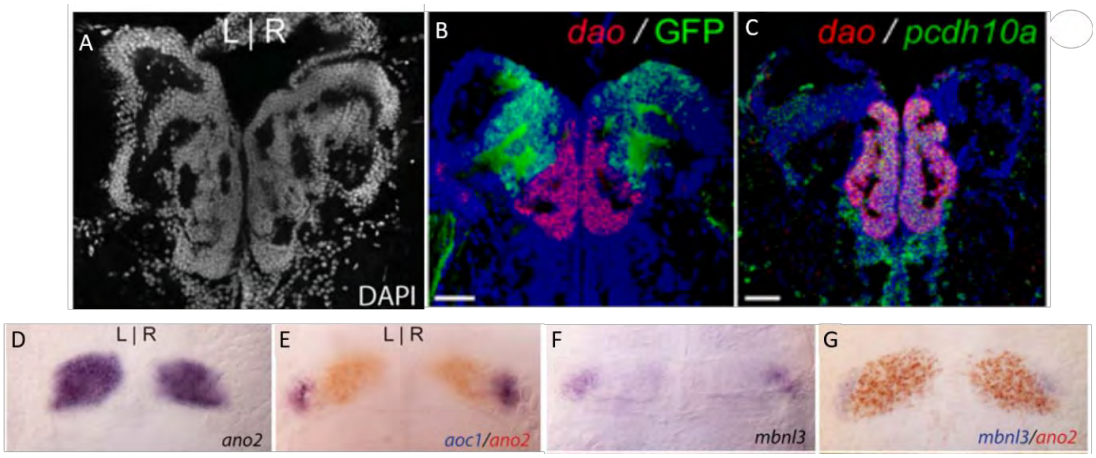

Figure 5 : Organisation en sous-domaines des habénulas chez le poisson-zèbre. (A) Noyaux cellulaires des Hb après coloration au DAPI sur une section optique coronale des habénulas de poisson-zèbre adulte. (B-C) Profils d'expression de *DrDao* (rouge) avec l'expression du transgène *DrPou4f1* Tg(*Pou4f1-hsp70:GFP)* (B, vert) ou avec le profil d'expression de *DrPcdh10a* (C,vert) sur une section optique coronale des habénulas de poisson-zèbre adulte. (D-G) Expressions de marqueurs des Hb dorsales (*DrAno2* [D, bleu ; E et G, rouge]) et ventrales (*DrAoc1* |E, bleu] et de *DrMbln3* [F et G, bleu]) chez des larves de 4 jours. (Amo et al., 2010; deCarvalho et al., 2014; Signore et al., 2009)

Plusieurs marqueurs de chaque sous-domaine ont été identifiés, tels que *kiss1, aoc1 (ex dao), pcdh10a*, *mbln3* pour les Hbv (Amo et al., 2010; deCarvalho et al., 2014; Kitahashi, Ogawa, & Parhar, 2009; Servili et al., 2011) et *ano2, cadps2, cxcr4b* pour les Hbd (deCarvalho et al., 2014; Gamse, Thisse, Thisse, & Halpern, 2003; Roussigne, Bianco, Wilson, & Blader, 2009). Les Hbd sont elles-mêmes subdivisées en sous-domaines. *kctd12.2* (ex *ron*) a un profil d'expression médian dans l'Hbd, complémentaire à celui de *kct12.1* (ex *lov*) et *kctd8* (ex *dex*) exprimés dans la partie la plus latérale de l'Hbd. Une étude par séquençage ScRNA-seq a mis en évidence une organisation complexe, comprenant 18 clusters de cellules, caractérisés chacun par des signatures d'expression génique. La réalisation d'ISH sur une sélection de gènes signatures de ces 18 clusters, a permis de préciser leur organisation spatiale chez l'adulte. 4 clusters sont localisés dans les Hbv contre 14 dans les Hbd .(Figure 6) (Pandey, Shekhar, Regev, & Schier, 2018).

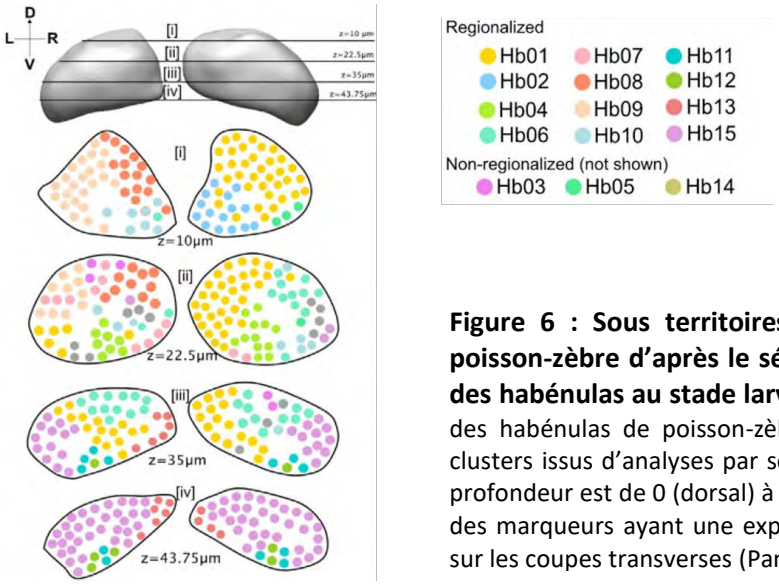

Figure 6 : Sous territoires habénulaires proposés chez le poisson-zèbre d'après le séquençage ARN sur cellule unique des habénulas au stade larvaire. Schémas de coupes transverses des habénulas de poisson-zèbre au stade larvaire regroupant les clusters issus d'analyses par séquençage ARN sur cellule unique. La profondeur est de 0 (dorsal) à 75µm (ventral). Seuls les clusters avec des marqueurs ayant une expression régionalisée sont représentés sur les coupes transverses (Pandey et al., 2018).

Les projections majeures impliquant les habénulas ont également été analysées chez le poisson-zèbre à l'aide de traçages neuronaux. En accord avec les différences observées de répertoires transcriptomiques, les projections issues des sous-domaines Hbd et Hbv sont différentes : les Hbv projettent majoritairement sur le noyau médian du raphé alors que les Hbd projettent sur les noyaux interpédonculaires (Amo et al., 2010; Tomizawa, Katayama, & Nakayasu, 2001) (Figure 7).

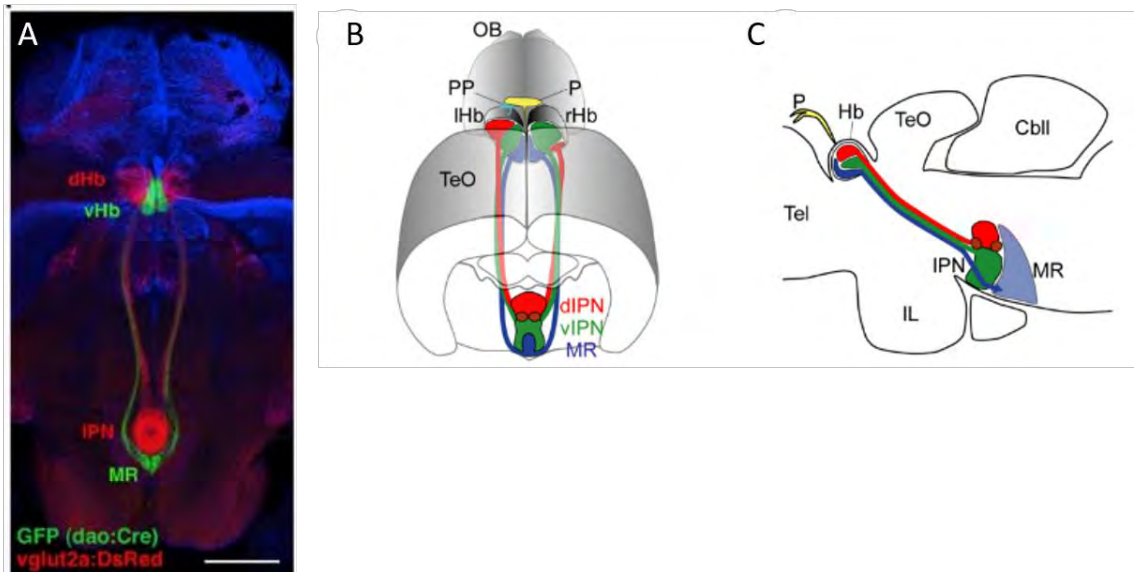

Figure 7 : Principales projections issues des habénulas dorsales et ventrales chez le poisson-zèbre. (A) Expression des transgènes *Tg*(*dao:cre-mCherry*) (rouge) et *Tg(vglut2a:lox-P-DsRed-loxP-GFP)* (vert) sur une section oblique du cerveau de poisson-zèbre. (B,C) Schéma d'une vue oblique dorsale (B) et sagittale (C) des projections axonales des Hbv vers les noyaux médians du raphé (MR; bleu) et des Hbd vers les noyaux interpédonculaires (IPN ; rouge et vert) dans le cerveau du poisson zèbre adulte. *CbII : cerebellum; dIPN : noyau interpédonculaire dorsal; dHb : habénula dorsale; Hb : habénula; lHb : habénula gauche; IL : lobe inférieur de l'hypothalamus; IPN : noyaux interpédonculaires; MR : noyau médian du raphé; P : pinéale; PP : parapinéale; OB : bulbes olfactifs; rHb : habénula droite; Tel : télencéphale; TeO : tectum optique; vIPN: noyau interpédonculaire ventral; vHb : habénula ventrale.* (Amo et al., 2010, 2014)

I-1-d. Aspects évolutifs

Les comparaisons des organisations en sous-domaines des habénulas ont été effectuées entre un nombre relativement restreint d'espèces, et cela sur deux types d'arguments, la conservation des répertoires moléculaires et celle des patrons de projections. En ce qui concerne les comparaisons fondées sur des expressions géniques, elles n'ont concerné à ce jour que les comparaisons entre souris et poisson-zèbre, ces deux espèces étant les seules chez lesquelles des caractérisations détaillées existent. Ces études ont conduit à proposer une homologie entre les habénulas médianes (respectivement latérales) de souris avec les habénulas dorsales (respectivement ventrales) de poisson-zèbre. Cette hypothèse a été fondée sur un nombre relativement faible de marqueurs d'expressions, dont celle de *Pcdh10 (pcdh10a* chez le poisson-zèbre) qui s'exprime dans les Hbl de souris et dans les Hbv du poisson-zèbre, et celle de *Tac2* (*tac2* chez le poisson-zèbre), qui s'exprime dans les Hbm de souris et dans les Hbd du poisson-zèbre (Aizawa et al., 2005; Amo et al., 2010; Gamse et al., 2005b). L'intégration de données scRNA-Seq entre souris et poisson-zèbre a conduit à la même conclusion, malgré le nombre restreint de marqueurs signatures partagés, voire son absence dans le cas des habénulas ventrales (poisson-zèbre) et latérales (souris) (Hashikawa et al., 2020a) (Figure 8).

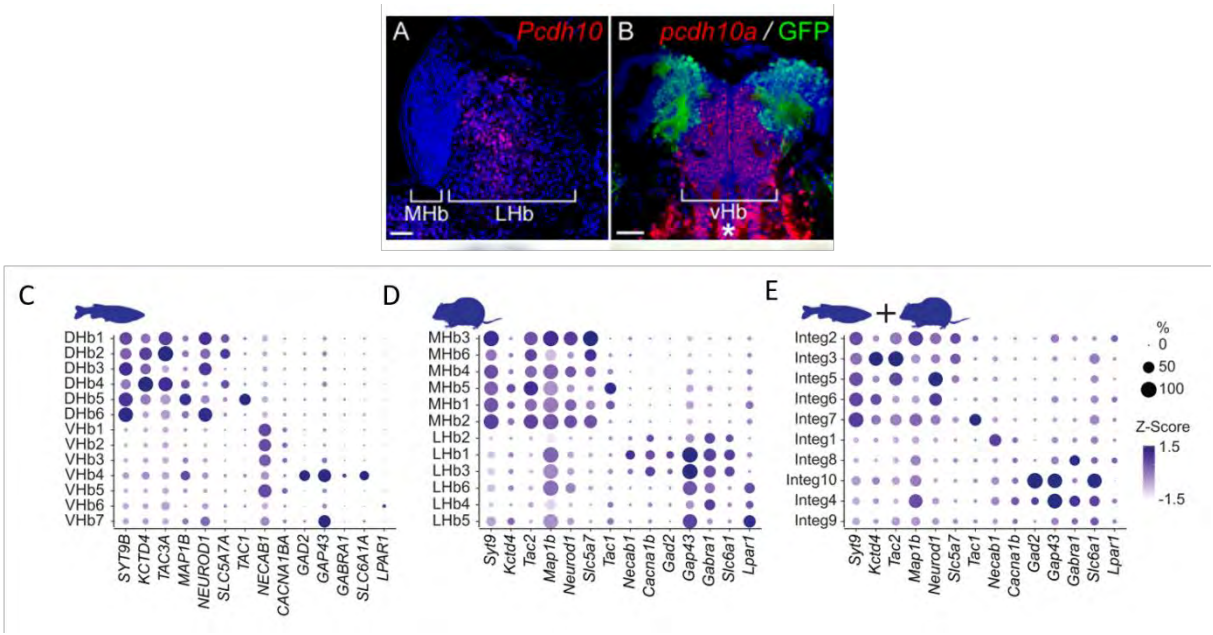

Figure 8 : Bases moléculaires des homologies proposées entre les Hbv-Hbl et les Hbd-Hbm respectivement du poisson-zèbre et des mammifères. (A) Profil d'expression de *RnPcdh10* (rouge) dans l'Hbl sur une section coronale de l'HbD de rat. (B) Profils d'expressions de *DrPcdh10a* dans les Hbv d'une section coronale d'Hb de poisson-zèbre adulte transgénique Tg(*Pou4f1-hsp70:GFP*) (vert). (C-E) Graphiques en points montrant les niveaux d'expression (couleur) et la proportion du nombre de cellules (taille des points) des marqueurs des clusters identifiés par séquençage ARN sur cellule unique des habénulas de poissons zèbres (C), de souris (D) et intégrés (E). *LHb : Habénula latérale ; MHb : Habénula médiane ; vHb : Habénula ventrale.* (Amo et al., 2010; Hashikawa et al., 2020b)

Les arguments de projections, décrits ci-avant, soutiennent cette distinction, puisque les habénulas médianes de souris et dorsales de poisson-zèbre présentent dans les deux cas une projection majeure sur les noyaux interpédonculaires, et que les habénulas latérales et ventrales de ces deux espèces projettent toutes deux vers les noyaux du raphé. Des projections issues de sous-territoires bilatéraux bien définis des habénulas vers les IPNs ont également été décrites chez un lézard, *Uta stansburiana*, un amphibien, *Bombina orientalis*, et chez la lamproie, *Lampetra fluviatilis*, suggérant une conservation de cette partition chez l'ensemble des vertébrés. De plus, les afférences des habénulas rostro-dorsales et rostro-ventrales des habénulas de lamproie provenant de l'hypothalamus latéral et du pallidum dorsal sont aussi similaire à celles des Hbl des mammifères (Stephenson-Jones, Floros, Robertson, & Grillner, 2012) (Figure 9).

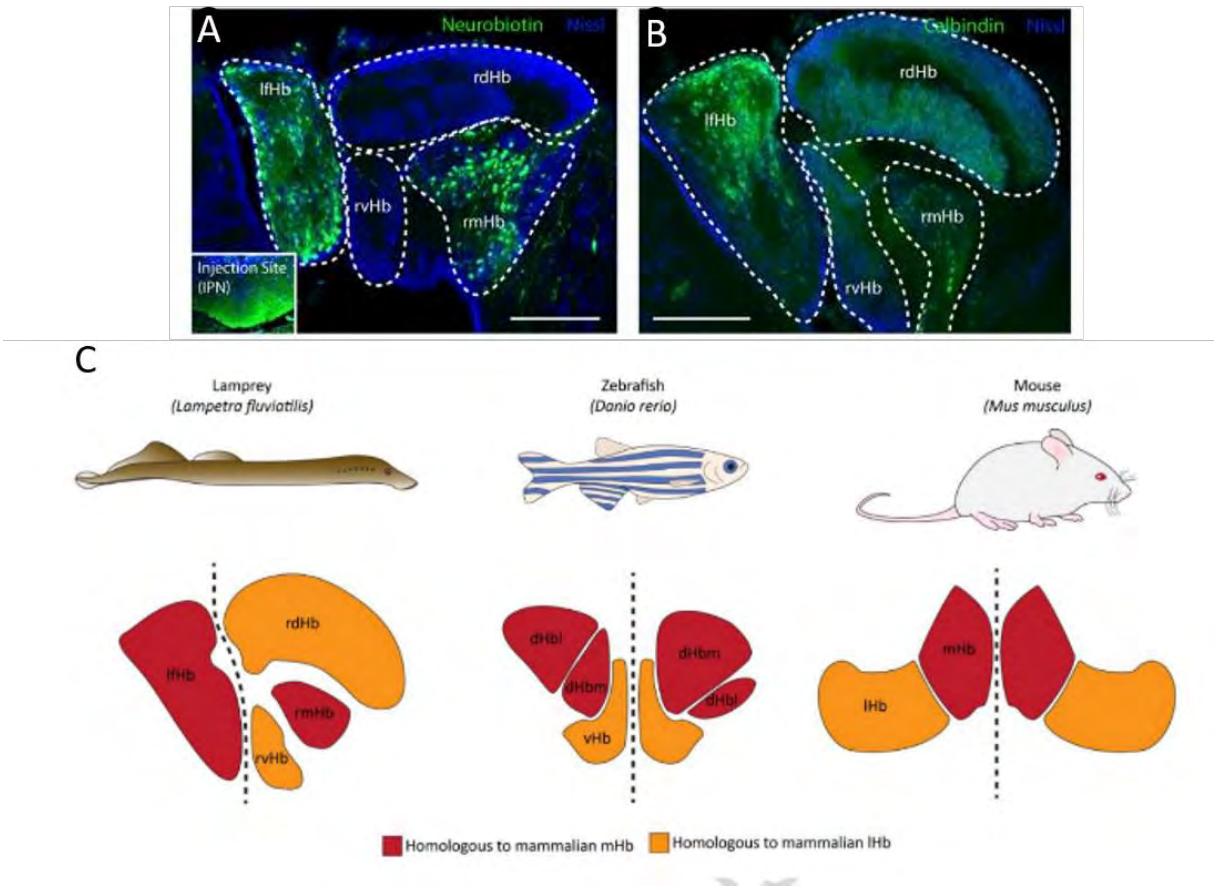

Figure 9 : Homologies proposées entre subdivisions habénulaires de lamproie, poisson-zèbre et souris. (A, B) (A) Traçage neuronal rétrograde à l'aide de neurobiotine injectée dans les noyaux interpédonculaires (C:Encadré ; vert) et (B) immunohistochimie avec un anticorps dirigé contre la calbindine sur des coupes transverses d'épithalamus de lamproie, *L. fluviatilis.* . Barre d'échelle : 200µm. (C) Schéma des sous-domaines habénulaires homologues aux Hbm (rouge) et aux Hbl (jaune) des mammifères chez la lamproie, le poisson-zèbre et la souris en vue transverse basé sur leurs homologies de projections vers les IPNs. *dHbl : Habénula latérale dorsale; dHbm : Habénula dorsale médiane; lfHb : Habénula gauche; lHb : Habénula latérale; mHb : Habénula médiane; rdHb: Habénula rostro-dorsale; rmHb: Habénula rostro-médiane; rvHb : Habénula rostro-ventrale* (Schmidt & Pasterkamp, 2017; Stephenson-Jones et al., 2012).

I-2. Rôles des habénulas

I-2-a. Rôles des Hbm et Hbl chez les rongeurs

La fonction des habénulas est longtemps restée imprécise, du fait de la limitation des techniques permettant l'analyse fonctionnelle des régions cérébrales. Des analyses par ablation ou traçages neuronaux ont néanmoins permis des premières hypothèses sur le rôle de ces structures dans la modulation du comportement, notamment lié à l'anxiété, via l'ablation du FR chez les rongeurs (Murphy, DiCamillo, Haun, & Murray, 1996). Ces études ont montré que les différentes subdivisions des habénulas sont associées à des rôles distincts. Aujourd'hui les approches optogénétiques couplées à des tests comportementaux fournissent des outils puissants permettant de préciser les fonctions de chacune de ces subdivisions. L'Hbl intervient dans les circuits dopaminergiques, impliqués dans les réponses aux aversifs et aux récompenses (Jhou, Fields, Baxter, & Saper, 2009; Lecourtier & Kelly, 2007;

Proulx, Hikosaka, & Malinow, 2014; A. M. Stamatakis et al., 2016). Ces circuits impliquent les projections du *globus pallidus* (ou pallidum dorsal) (Gph) sur les Hbl, qui elles-mêmes projettent sur l'aire tegmentale ventrale (VTA) via les noyaux de l'aire tegmentale rostro-médiale (RMTg) (Baker et al., 2016; Jhou et al., 2009) (Figure 10).

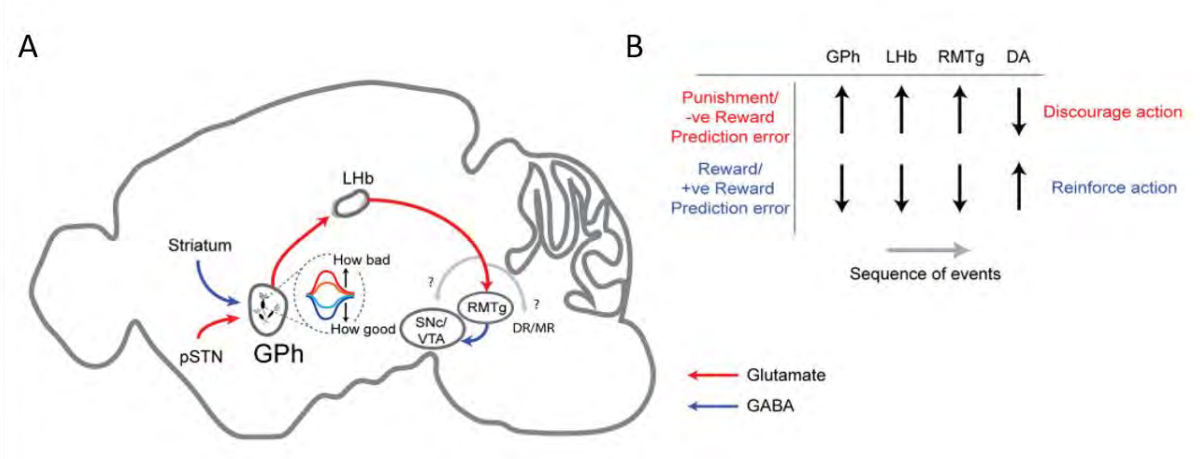

Figure 10 : Fonctionnement du circuit de l'évaluation de récompense des projections du *globus pallidus* vers le mésencéphale. (A) Schémas en vue sagittale du système dopaminergique diencéphalique de souris sous le contrôle de l'activité des neurones du Gph et du circuit neuronal en aval passant par les Hbl. (B) Séquence d'évènement proposé par laquelle l'activité des neurones du Gph peut influencer le taux d'activation des autres structures du circuit (Baker et al., 2016).

C'est chez les primates que ce phénomène a été observé pour la première fois, à la suite de leur exposition à un signal de punition inattendue (aversif) à la place d'une récompense attendue (Matsumoto & Hikosaka, 2007). L'activation optogénétique des régions cérébrales avec lesquelles les Hbl sont connectées, induisent des comportements aversifs similaires chez les rongeurs (Alice M Stamatakis & Stuber, 2012; G.-W. Zhang et al., 2018) (Figure 11).

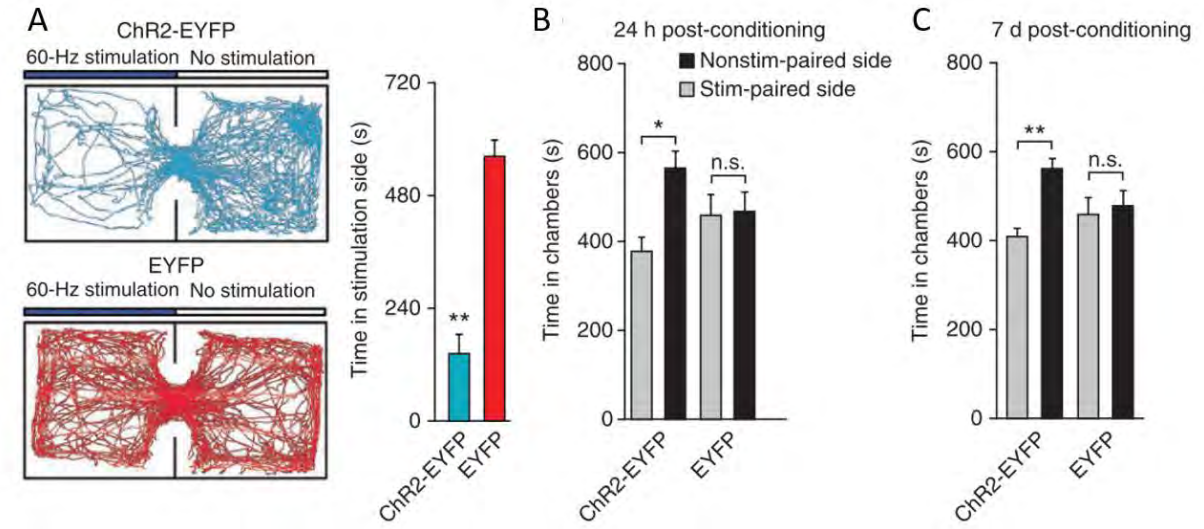

Figure 11 : L'activation des afférences du RMtg provenant des Hbl induit un comportement d'aversion passif et conditionné. (A) A gauche, tracés de la trajectoire en temps réel d'une souris exprimant ChR2-EYFP (neurones de l'Hbl activables par stimulation lumineuse, bleu) et d'une souris exprimant EYFP (contrôle, rouge) lors d'une session de 20 minutes entre une chambre sans stimulation et une chambre avec stimulation lumineuse de 60Hz. A droite, histogramme du temps passé dans la chambre de stimulation

lumineuse des souris exprimant ChR2-EYFP et EYFP. (B-C) Histogrammes du temps passés dans les chambres avec et sans stimulation des souris exprimant ChR2-EYFP et EYFP 24 heures après conditionnement (B) et 7 jours après conditionnement (C). (Alice M Stamatakis & Stuber, 2012).

Les Hbl sont aussi impliquées dans le comportement de dépression. L'application de stress chroniques légers imprédictibles (« Chronic Mild Stress » ou CMS) ou de traitements pharmacologiques néonataux à l'aide d'un anti-dépresseur, la clomipramine (CLI), conduisent à un comportement dépressif identifiable à l'aide du test de nage forcée (« Forced Swimming Test » ou FST). L'ablation électrolytique des Hbl résulte en une insensibilité des rats à ces traitements dépressifs. (Yang, Hu, Xia, Zhang, & Zhao, 2008). D'autres études ont également montré l'implication des Hbl dans les processus liés à la mémoire de travail (Mathis et al., 2017) et la mémoire spatiale (Lecourtier, Neijt, & Kelly, 2004), le sommeil et le rythme circadien (Beilin Zhang, Gao, Li, Yang, & Zhao, 2016) et dans le traitement des signaux nociceptifs (Mészáros, Gajewska, & Tarchalska-Kryńska, 1985).

L'Hbm est quant à elle associée aux comportements de peur et d'anxiété. Des traçages neuronaux ont montré que l'Hbm projette sur le septum triangulaire (TS) et sur les noyaux de la commissure antérieure (BAC), via différentes sous-populations de neurones. Ainsi deux voies de transductions du signal ont été mises en évidence : l'une composée du TS-Hbmv-NIPc (noyau interpédonculaire caudal) et l'autre composée des BAC-Hbmd-NIPp (noyaux interpédonculaires postérieurs) (Figure 12).

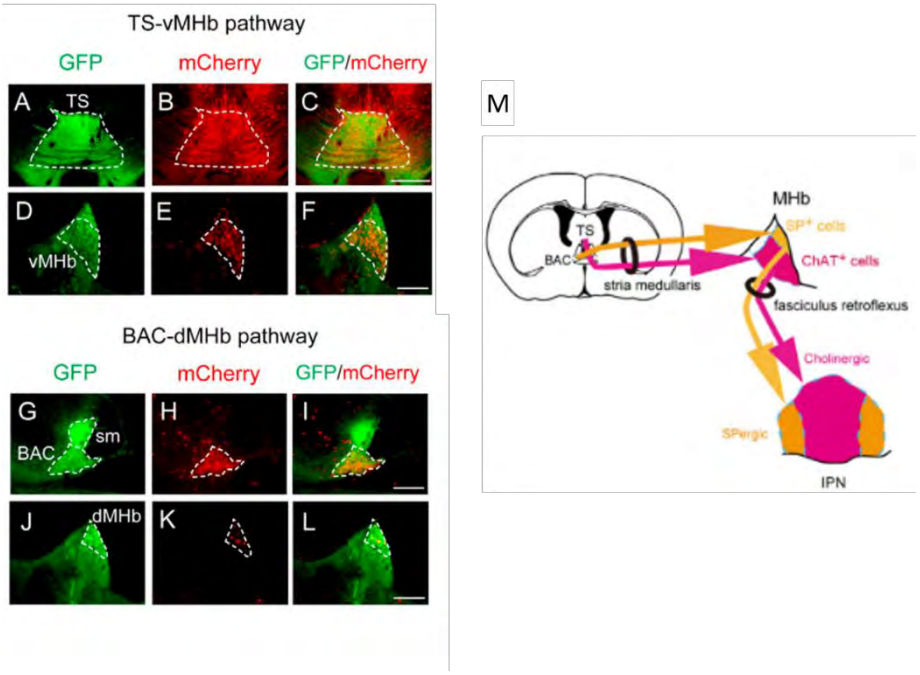

Figure 12 : Traçages antérogrades des neurones du TS et de la BAC sur les neurones de l'Hbm. Injection du traceur antérograde (AAV-CAG-mCherry) (rouge) dans les neurones du TS (A-C) et de la BAC (G-I) séparément marqués dans les neurones GFP^+ de l'Hbm ventrale (D-F) ou dans l'Hbm dorsale (J-L) respectivement. Barre d'échelle 500µm en (A-C) et 200µm en (D-L). (M) Schémas des projections des neurones du TS et de la BAC sur les IPN via les Hbm. (Yamaguchi, Danjo, Pastan, Hikida, & Nakanishi, 2013).

L'utilisation d'immunotoxine sur des cellules cibles permet de supprimer spécifiquement les projections allant du TS ou des BAC vers les Hbm. La suppression de la voie passant par le TS induit une diminution du comportement d'anxiété alors que la suppression de la voie passant par le BAC amplifie la réponse à la peur et son apprentissage. (Yamaguchi et al., 2013). (Figure 13).

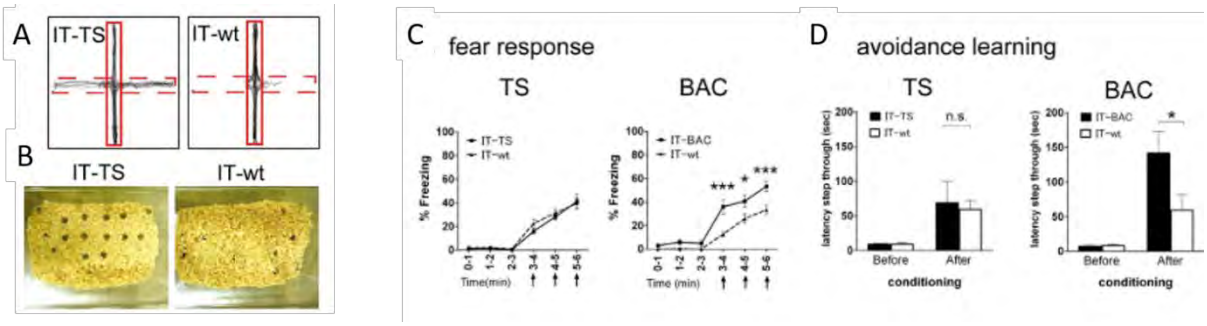

Figure 13 : Dissociation fonctionnelle des voies de signalisations BAC-Hbl et TS-Hbl dans le comportement d'anxiété et la réponse à la peur et son apprentissage. (A-B) Exemple de trajectoires dans un test de labyrinthe en croix surélevé (A) et de test d'enfouissement défensif (B) de souris avec ablation du TS (IT-TS) ou sauvage (IT-wt). (C) Pourcentage de « freezing » déterminé à la suite d'une période d'1 minute après un choc électrique d'une durée de 3, 4 et 5 min (flèches). Les marques et les barres représentent la moyenne ±, SEM, respectivement ; souris avec ablation du TS (n=9), avec ablation de la BAC (n=9), et sauvage injecté à l'IT (n=8). Des ANOVA bidirectionnelles ont été réalisées entre les durées et les génotypes, suivi par un test de Bonferonni ; *p<0.05, ***p<0.001. (D) Apprentissage des aversifs testés par l'utilisation de test d'évitement inhibiteur chez des souris avec ablation du TS (n=9), avec ablation de la BAC (n=7), et sauvage injecté à l'IT (n=9 ou 10). Les colonnes et les barres représentent la moyenne ±, SEM, respectivement. Des ANOVA bidirectionnelles ont été réalisées entre les souris transgéniques injectées à l'IT et les souris sauvages, suivi par un test de Bonferonni : *p<0.05n non significatif. (Yamaguchi et al., 2013).

Les Hbm sont aussi impliquées dans des processus d'addiction. La présence de récepteurs nicotiniques α2 et α5 dans les Hbm ainsi que la réduction du comportement de manque à la nicotine de souris mutantes pour ces récepteurs montrent que les Hbm jouent un rôle dans l'addiction à la nicotine (Salas, Sturm, Boulter, & De Biasi, 2009).

I-2-b. Rôles des Hbv et Hbd chez les téléostéens

Les fonctions des habénulas chez le poisson-zèbre ont fait l'œuvre de nombreuses études lors de ces 20 dernières années, visant à évaluer la similitude du rôle des habénulas entre téléostéens et rongeurs. Chez le poisson-zèbre, l'Hbv est associée au processus d'apprentissage de stimulus lié à des aversifs. En effet, une lignée transgénique de poisson-zèbre ayant une neurotransmission de l'Hbv localement inhibée, présente un apprentissage du comportement d'aversion moindre que les poissons contrôles (Figure 14).

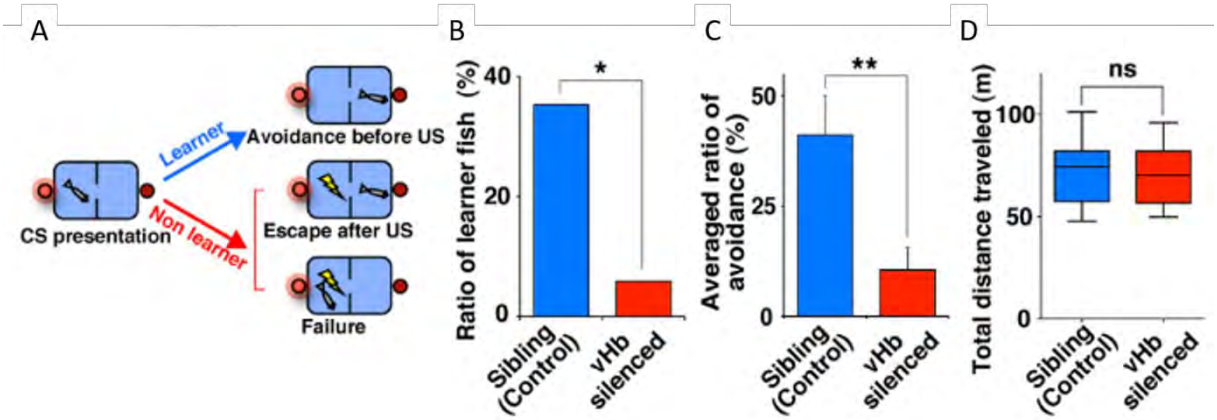

Figure 14 : L'inhibition de la neurotransmission de la voie Hbv – MR diminue l'apprentissage actif des aversifs. (A) Schémas du test d'aversion actif. Le poisson doit franchir une haie pour éviter le US (stimulus aversif non conditionné) lors de la présentation du CS (stimulus conditionné). Dans le comportement d'évitement, le poisson nage vers le compartiment opposé pendant la période de présentation du CS. Dans le comportement de " fuite ", le poisson franchi la haie pendant la période de présentation du US. Dans le comportement " échec ", le poisson ne franchi pas la haie pendant la période de présentation du CS et du US qui suit. (B) Ratio de poissons atteignant le critère de réussite, 80% d'évitement dans dix essais séquentiels dans la tâche d'évitement actif (contrôle, n = 17 ; vHb-silencieux, n = 17 ; p = 0.0339, test c2). (C) Taux moyen de réponses d'évitement réussies au cours de la première session de la tâche d'évitement actif (contrôle, n = 17 ; vHb-silence, n = 17 ; test de Mann-Whitney). (D) Activité locomotrice pendant la période d'adaptation (contrôle, n = 13 ; vHb-silence, n = 12 ; p = 0,9350 ; test de Mann-Whitney).(Amo et al., 2014).

De plus, ce processus est sous le contrôle du système sérotoninergique, car une diminution de l'apprentissage aversif est aussi observée chez des poissons ayant subi une injection locale d'un traitement pharmacologique dégradant les terminaisons des axones sérotoninergiques (Amo et al., 2014). Des tests comportementaux de ces animaux en milieu aversif induisent un état dépressif, tel qu'observé chez les rongeurs. L'imagerie calcique des habénulas des poissons passant à l'état dépressif, à la suite de l'exposition à ce test, montre une activation spécifique des neurones de l'Hbv (Figure 15).

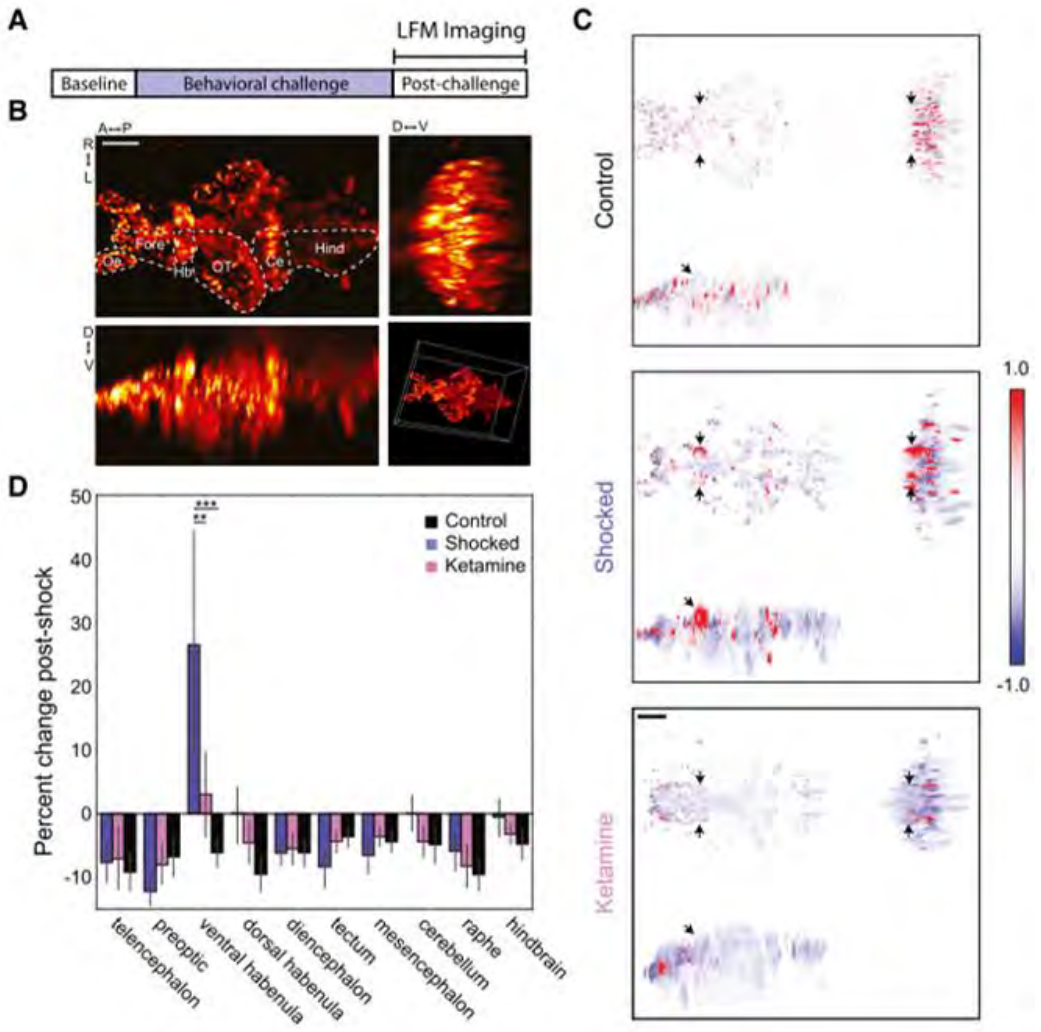

Figure 15 : Hyperactivité spécifique des neurones de l'Hbv à la suite du test comportemental induisant un état d'évitement passif ou de dépression. (A) Le LFM (microscopie à champ lumineux) a été utilisé pour mesurer les signaux Ca2+ du GCaMP6s pendant une période de 45 minutes après le BC (test comportemental). (B) Projections orthogonales d'intensité maximale d'un volume de LFM (barre d'échelle, 50 mm). Hb, habenula ; OT, tectum optique ; Fore, cerveau antérieur ; Oe, épithélium olfactif ; Ce, cervelet ; Hind, cerveau postérieur. (C) Projections orthogonales min-max des volumes montrant le changement de fluorescence au cours de la période post-BC chez un poisson représentatif du groupe témoin (en haut), du groupe choqué (au milieu) et du groupe kétamine (en bas). Le rouge et le bleu indiquent une augmentation et une diminution de la fluorescence, respectivement (unités arbitraires ; les flèches noires montrent l'emplacement de l'Hbv ; barre d'échelle, 50 mm). (D) Changement de la fluorescence moyenne au cours de la période post-BC. Les poissons choqués ont montré une augmentation de l'activité de l'Hbv (bleu, n = 6) par rapport aux poissons témoins (noir, n = 4 ; p = 0,0002, ANOVA à deux voies à mesures répétées avec comparaison post hoc Tukey HSD). Cet effet est réduit chez les poissons choqués préalablement traités à la kétamine (rose, n = 8 ; p = 0,0014). (Andalman et al., 2019).

L'activation optogénétique de ces mêmes neurones, induit un état dépressif alors que leurs inhibition prévient et empêche le passage à l'état dépressif (Andalman et al., 2019).

Les Hbd sont quant à elles associées au comportement de peur et d'anxiété, comme les Hbm de rongeurs. Des expériences utilisant des lignées de poisson-zèbres ayant des Hbd « silencieuses » (inactives), montrent que ces poissons mettent plus de temps pour passer d'un état d'immobilité à un état d'agitation à la suite de la présence d'un danger (Agetsuma et al., 2010; Okamoto & Aizawa, 2013) (Figure 16).

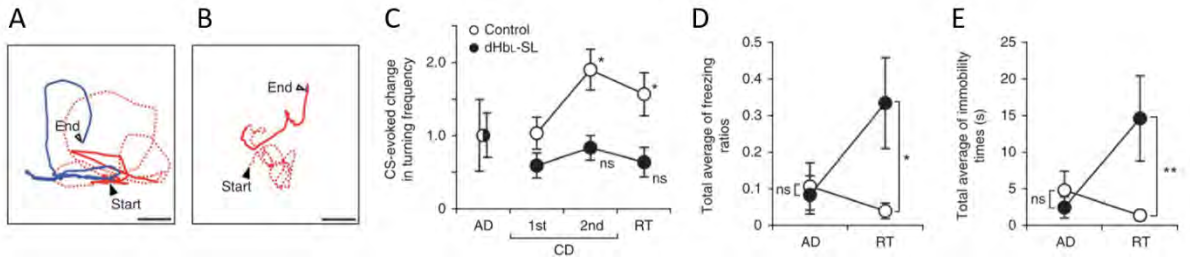

Figure 16 : Les poisons aux Hbd "silencieuses" montrent une phase immobile plus importante au lieu d'un comportement de fuite face à un stimulus conditionné. Les poissons privés d'Hbdl ont montré des phases de « freezing » accrues au stimulus conditionné au lieu de comportements de fuite. (A, B) Exemples de trajectoires du poisson témoin (A) et du poisson à l'Hbdl inactive(B) pendant les sessions de récupération, avant (20 s, lignes pointillées rouges), pendant (8,5 s, lignes pleines rouges) et après (20 s, lignes bleues) l'exposition au stimulus conditionné (CS). (C) Changement de la fréquence de rotation pendant la présentation du CS. Les valeurs sont normalisées par rapport aux moyennes des sessions d'adaptation. Les moyennes ± s.e.m. sont représentées. *P < 0,05, test du rang signé de Wilcoxon (comparaison avec la première session de conditionnement). (d,e) Moyenne totale des rapports des « freezing » (D) et de leur durée (E) pendant 50 s après le décalage du stimulus conditionné. Les moyennes ± s.e.m. sont représentées. ANOVA à deux voies à mesures répétées, état de l'habénula (contrôle, réduit au silence) × conditionnement (avant le conditionnement, après le conditionnement) (d, F = 4,66, P = 0,04 ; e, F = 6,04, P = 0,02). **P < 0,01 et *P < 0,05, post-tests de Bonferroni (contrôle contre dHbl réduit au silence). (Agetsuma et al., 2010).Les Hbd sont aussi requises pour

Les Hbd sont aussi impliquées dans l'adaptation du comportement à de nouvelles conditions environnementales. L'ablation des Hbd résultent en une meilleure vitesse de mémorisation de l'environnement et ce pendant une durée plus longue que chez des poissons sauvages, mais induit un temps beaucoup plus long de ré-apprentissage (ré-association) de nouvelles règles lors des tests comportementaux (Palumbo, Serneels, Pelgrims, & Yaksi, 2020).

Les Hb chez le poisson-zèbre jouent enfin un rôle dans les conflits sociaux. Des études comportementales proposent que les Hbv sont nécessaires au maintien du comportement de perdant (Chou et al., 2016) alors que l'inactivation de différentes sous-régions de l'Hbd, inhibées par transgénèse, modifie de façon différente le comportement lors des conflits sociaux (Chou et al., 2016) (Figure 17).

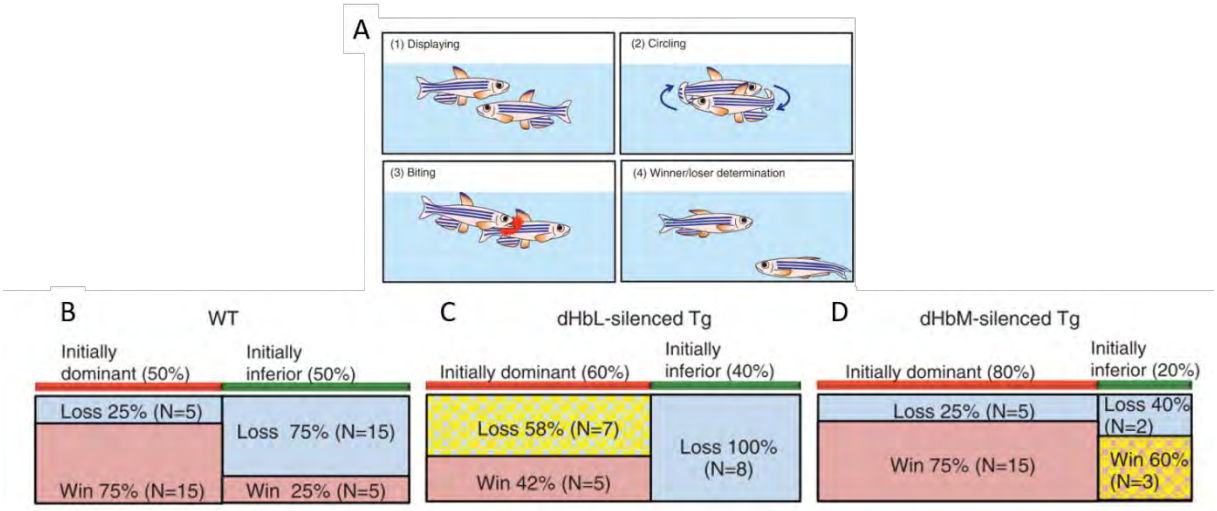

Figure 17 : L'inactivation spécifique des Hbdl et Hbdm perturbent de manière différentes le comportement de conflits sociaux chez le poisson-zèbre. (A) Schémas du test comportementale lié aux conflits sociaux chez le poisson zèbre. (B-D) Résultat du combat et du taux de dominance initial des poissons sauvages (B), aux Hbdl « silencieuses » (C) et aux Hbdm « silencieuses » (D) lorsqu'ils se battent contre d'autres poissons sauvages. (Chou et al., 2016).

I-3. Les asymétries habénulaires : le poisson-zèbre comme référence

Une particularité des habénulas est qu'elles présentent des asymétries chez de très nombreux vertébrés(Concha & Wilson, 2001). Ces asymétries ont été observées il y a plus de 30 ans chez certains téléostéens, comme l'anguille, *Anguilla anguilla* (Braitenberg & Kemali, 1970) ou le saumon argenté, *Oncorhynchus kisutch* (Ekström & Ebbesson, 1988). Elles ont été détectées par la suite chez le poisson-zèbre et c'est sur cette espèce que ce sont concentrées les caractérisations morphologiques et moléculaires, ainsi que l'étude des mécanismes contrôlant leur formation (Concha, Burdine, Russell, Schier, & Wilson, 2000a).

I-3-a. Asymétries morphologiques et moléculaires

Les asymétries détectées dans les habénulas de poisson-zèbre sont restreintes à leur sous-domaine dorsal, Hbd. Elles concernent la taille, l'organisation cellulaire, l'organisation en sous-domaines et les projections efférentes. L'asymétrie la plus évidente entre les habénulas droite et gauche de poisson-zèbre concerne la taille, avec une habénula dorsale gauche de taille plus importante que la droite. L'organisation cellulaire diffère également entre la gauche et la droite : comme l'ont montré des analyses par immunohistochimie avec un anticorps dirigé contre la tubuline acétylée, la densité du neuropile est plus importante dans l'habénula gauche que dans l'habénula droite (Concha et al., 2000a) (Figure 18).

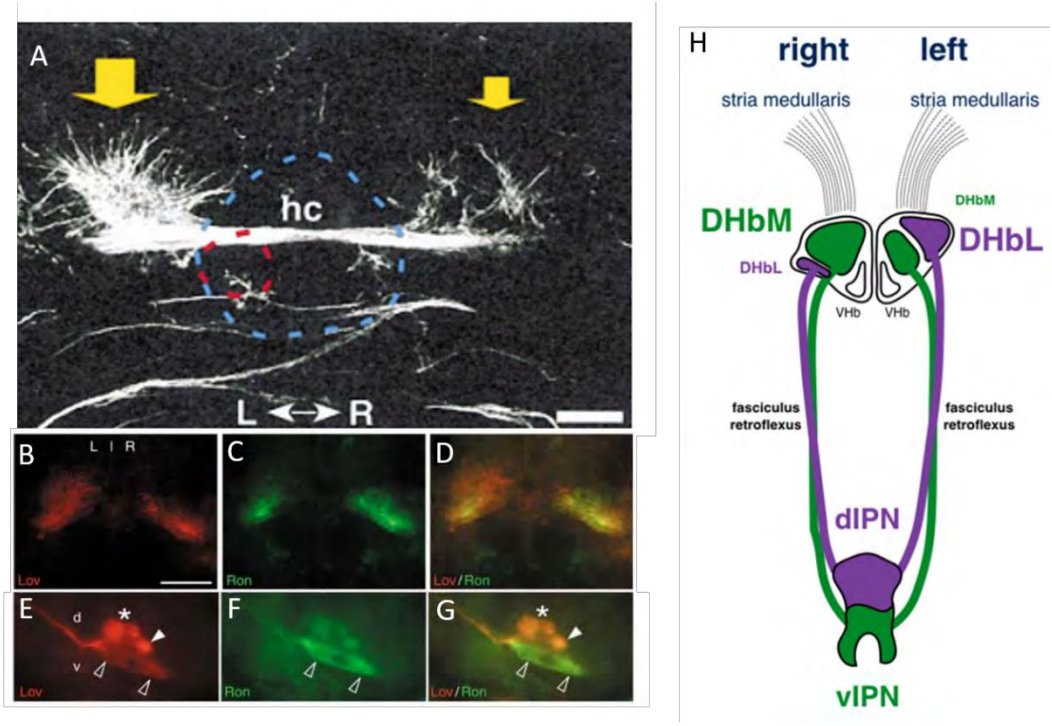

Figure 18 : Asymétries de la morphologie et des projections des habénulas du poisson-zèbre. (A) Vue dorsale des projections habénulaires à la suite d'un immunomarquage contre l'α tubuline acétylée, chez une larve de poisson zèbre (Concha et al., 2000a). (B-D) Imagerie confocale de l'immunodétection de kctd12.1(ex*lov*) (B, rouge) et kctd12.2 (*exron*) (C, vert) et de leur colocalisation dans les Hb (D). (E-G) Les axones kctd12.1+ innervent la région antéro-dorsale (astérisque) et antéro-ventrale (têtes de flèches pleines) des noyaux interpédonculaires (IPN) dorsaux et ventraux (têtes de flèches creuses). Les axones kctd12.2+ innervent l'IPN ventrale (Gamse et al., 2005b). (H) Vue schématique des asymétries habénulaires et de leurs connectivités asymétriques aux IPN dorsaux et ventraux chez le poisson-zèbre adulte (Ichijo, Nakamura, Kawaguchi, & Takeuchi, 2017).

Les asymétries moléculaires des habénulas chez le poisson-zèbre sont observables dès le stade 48hpf. Parmi les gènes présentant des expressions asymétriques, ceux de la famille *kctd*, présentent des expressions bilatérales, mais avec des territoires de proportions relatives différentes entre l'Hbd droite et l'Hbd gauche. *kctd12.2 (ex ron)* et *kctd8 (ex dex)* ont un profil d'expression plus étendu dans la partie latérale de l'habénula dorsale droite contrairement à *kctd12.1* (*ex lov*) qui a un profil d'expression plus étendu dans la région latérale de l'habénula dorsale gauche , complémentaire à celui de *kctd8*. Ces territoires ont conduit à la définition de deux sous-domaines de l'Hbd. *kctd12.1* est ainsi un marqueur de l'habénula dorsale latérale (Hbdl) chez le poisson-zèbre, plus étendue à gauche. Quant à l'autre sous-domaine de l'Hbd, l'habénula dorsale médiane (Hbdm), elle a été caractérisée par l'expression de *kctd8* ainsi que *pou4f1* (ex *brn3a)*, plus étendue à droite. Cette asymétrie, sur laquelle se sont concentrées les étude mécanistiques (Cf II.2), repose donc sur une différence de proportion relative entre la gauche et la droite de la taille de deux subdivisions dorsales (Gamse, 2003; Gamse et al., 2005a; Hidenori Aizawa et al., 2005) (Figure 19).

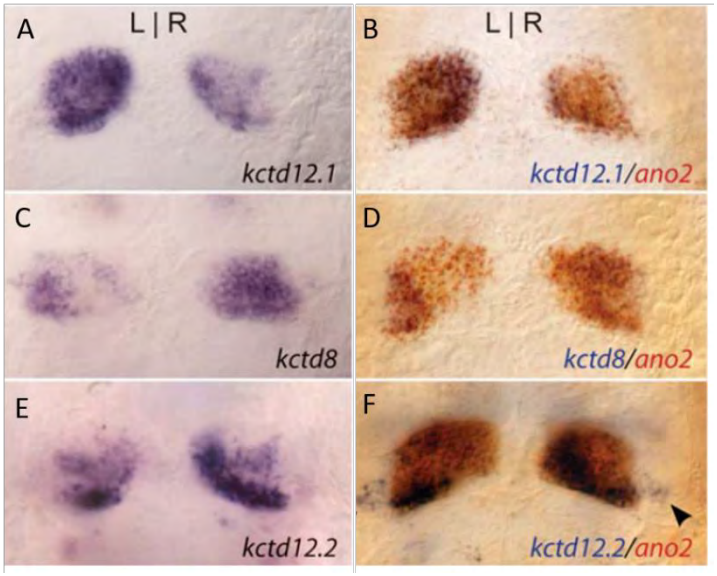

Figure 19 : Asymétries moléculaires dans les Hbd chez le poisson-zèbre. (A, B et C, bleu) Expressions asymétriques préférentiellement gauche ou droite, respectivement de, *kctd12.1, kctd8* et *kctd12,2, (*B, D et F) avec l'expression de *ano2.* (rouge). (deCarvalho et al., 2014).

L'étude de la distribution des neurotransmetteurs dans les populations neuronales des Hbd a mis en évidence de nouvelles asymétries entre les Hbd droite et gauche. Les populations neuronales cholinergiques sont plus étendues dans l'Hbd gauche, alors que les populations neuronales peptidergiques (substance P et somatostatine) sont plus étendues dans l'Hbd droite (deCarvalho et al., 2014) (Figure 20). Des traçages neuronaux ont aussi montré des asymétries entre les Hbd droite et gauche. Les Hbdm projettent préférentiellement sur l'IPN dorsal alors que l'Hbdl projette préférentiellement sur l'IPN ventral (Aizawa et al., 2005) (Figure 18).

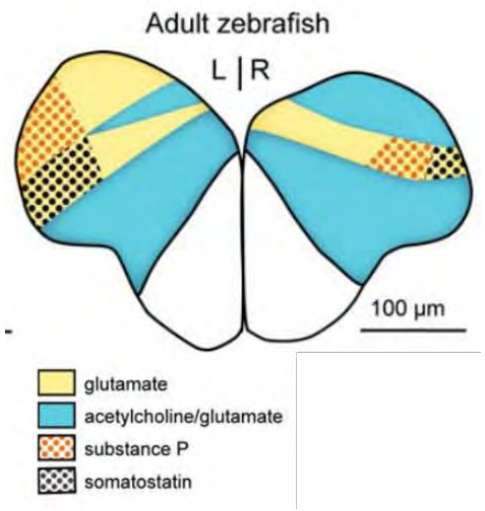

Figure 20 : Asymétries de nature des neurotransmetteurs dans les Hbd du poisson-zèbre. Asymétries de distributions des neurotransmetteurs entre HbdG et HbdD de poisson zèbre adulte en vue transverse. (deCarvalho et al., 2014)

Plus récemment, la caractérisation des Hb de poisson-zèbre par séquençage ScRNA-seq uniques évoqué plus haut (voir : I.1.c) a permis de détecter de nombreux gènes supplémentaires exprimés de façon asymétrique et de préciser les territoires concernés. Les hybridations *in situ* réalisées avec les marqueurs signatures des 15 clusters identifiés conduit à la cartographie de 6 d'entre eux dans des localisations asymétriques : 2 préférentiellement enrichis dans l'Hbd droite (Hb01 et Hb02) et 4 préférentiellement enrichis dans l'Hbd gauche (Hb07, Hb08, Hb09 et Hb10) (Pandey et al., 2018) (Figure 20). Ces nouveaux territoires d'expressions subdivisent les Hbdl et et Hbdm et ne se superposent pas de façon évidente à la carte de neurotransmetteurs établie par deCarvalho et al. 2014, ce qui montre que les asymétries habénulaires sont plus complexes que ce qui était attendu par les premières descriptions moléculaires des asymétries de l'organe.

I-3-b. Asymétries fonctionnelles

Plusieurs études ont montré une asymétrie de traitement des données sensorielles entre les habénulas gauche et droite. L'habénula gauche projette préférentiellement sur les régions ventrales des rétines de poisson-zèbre via les éminences thalamiques. Des lésions de l'Hb gauche induisent une perte du comportement de phototaxie positive observable chez les individus adultes sauvages (Cheng, Krishnan, Lin, Kibat, & Jesuthasan, 2017; Bai bing Zhang, Yao, Zhang, Kawakami, & Du, 2017). En revanche l'habénula droite innerve préférentiellement les bulbes olfactifs (Miyasaka et al., 2009). En accord avec cela, des imageries calciques de l'activité neuronale des populations de neurones des Hbd chez le poisson-zèbre montre des asymétries d'activité neuronale en fonction de la nature du stimulus environnemental : L'exposition des individus à un stimulus lumineux induit une activité de la majorité des neurones de l'Hbd gauche, alors que l'exposition à un stimulus olfactif induit l'activité de la plupart des neurones de l'Hbd droite. Des poissons mutés présentant un isomérisme droit des habénulas présentent un nombre de neurones répondant aux stimulus lumineux significativement inférieur aux types sauvages alors que les poissons présentant un isomérisme gauche des habénulas possèdent significativement moins de neurones activés par un stimulus olfactif (Dreosti, Vendrell Llopis, Carl, Yaksi, & Wilson, 2014b) (Figure 21).

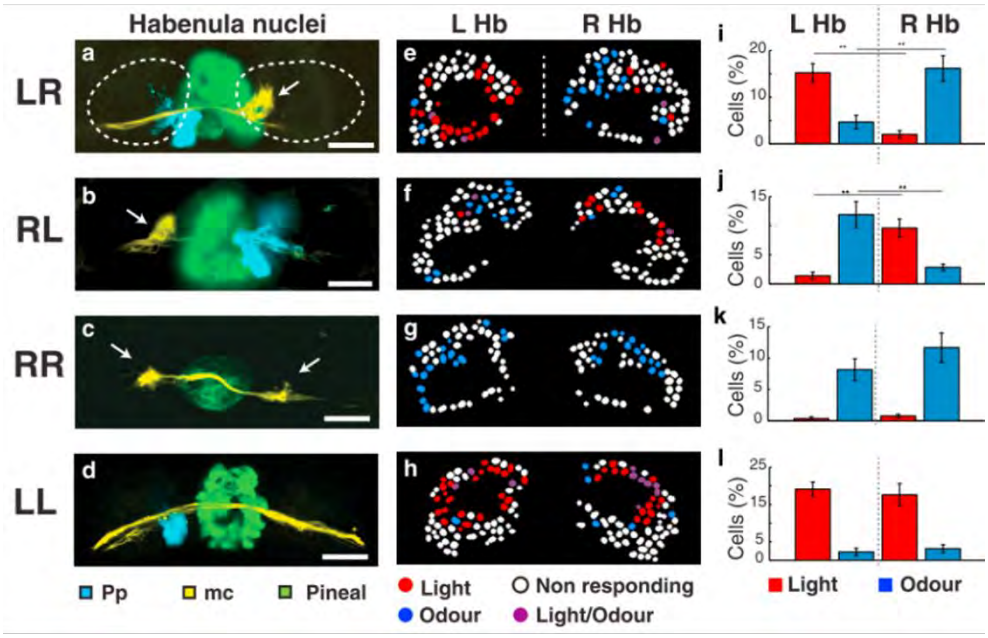

Figure 21 : La perte des asymétries des Hbd entraîne une diminution du nombre de neurones répondant à des stimuli lumineux ou olfactif. (A-D) Imagerie confocale de l'épithalamus sauvage (A), suite à un choc hypothermique (B), après ablation de la parapinéale (C), ou après traitement pharmacologique avec IWR-1-endo (D) d'une larve de poisson-zèbre Tg (*foxD3:* GFP x lhx2a:Gap43-YFP) au stade 4 dpf qui génèrent respectivement des Hb d'identités gauche-droite (A), droite-gauche (B), droite-droite (C) et gauche gauche (D). (E-H) Exemple d'un plan z des Hbd d'épithalamus sauvage (E), à la suite d'un choc hypothermique (F), après ablation de la parapinéale (G), ou encore après traitement pharmacologique avec IWR-1-endo (H) qui montre l'effet des traitements sur les identités habénulaires et la latéralisation des réponses neuronales au stimuli olfactifs et lumineux. (I-L) Histogrammes du pourcentage des neurones répondant au stimuli lumineux (rouge) et olfactifs (bleu) (normalisé par le nombre total de neurones de l'Hbd) dans l'HbG et l'HbD sur 2 plans z (à une profondeur de 7 à 14µm) de plusieurs poissons de chaque catégorie (Dreosti, Vendrell Llopis, Carl, Yaksi, & Wilson, 2014).

La perte ou l'inversion des asymétries habénulaires provoquent également la diminution du comportement exploratoire chez le poisson zèbre. Le comportement exploratoire de ces mutants peut être restauré à la suite d'un traitement avec un anxiolytique, la buspirone. Ces données ont conduit à la suggestion que les asymétries habénulaires régulent des processus émotionnels comme l'anxiété chez le poisson- (Facchin, Duboué, & Halpern, 2015) (Figure 22).

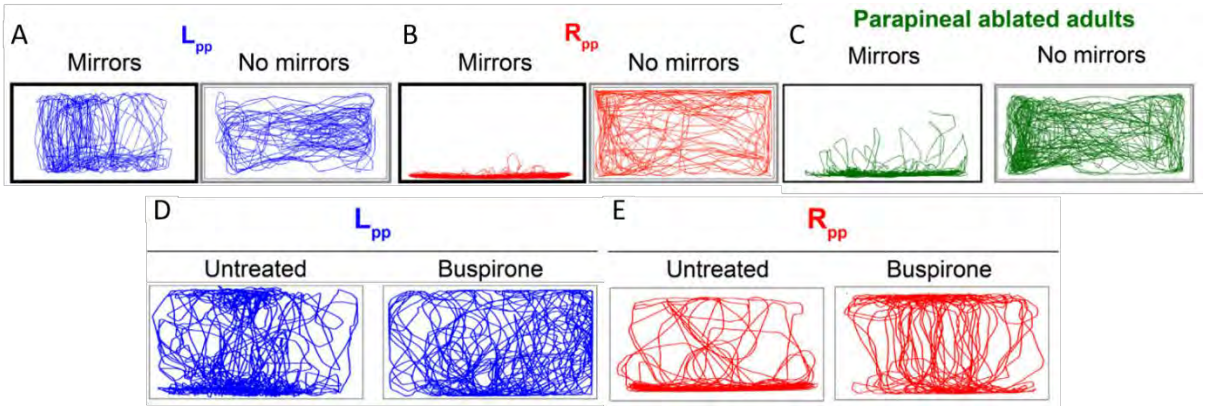

Figure 22 : Impact de la perturbation des asymétries habénulaire sur le comportement exploratoire du poisson-zèbre. (A-C) Représentation du trajet natatoire d'un même individu sur une durée de 5 minutes

ayant une migration gauche (sauvage) de la parapinéale (A), une migration droite de la parapinéale (B) ou une ablation de la parapinéale (C) en présence ou absence de miroir. (D-E) Représentation du trajet natatoire d'individu traité ou non à la buspirone et ayant une migration gauche (D) ou droite de la parapinéale (Facchin, Duboué, & Halpern, 2015).

I-3-c. Evolution des asymétries (mammifères, téléostéens, lamproies)

Les asymétries habénulaires sont détectées chez certaines espèces de tous les grands groupes de vertébrés, mais avec des variations importantes de leur degré (Concha & Wilson, 2001). La plupart des études se sont restreintes à des descriptions morphologiques ou des analyses de projection, des caractérisations moléculaires n'ayant été conduites que chez la souris, le poisson-zèbre et plus récemment la roussette et la lamproie. Les latéralités en taille varient même entre espèces relativement proches. Au sein des actinoptérygiens, l'habénula droite est plus grande en taille que la gauche chez le poisson roseau, *Erpetoichthys calabaricus* (Nieuwenhuys, 1998a), l'esturgeon, *Acipenser baeri* (Adrio, Anadón, & Rodríguez-Moldes, 2000), le lépisostée osseux, *Lepisosteus osseus* (Braford et al., 1983) et le poisson castor, *Amia calva* (Concha & Wilson, 2001). Chez les téléostéens, comme vu ci-avant, l'habénula gauche est plus importante en taille que la droite chez le poisson-zèbre, *Danio rerio*. Cette asymétrie en taille est aussi présente chez le medaka, *Oryzias latipes* (Signore et al., 2009). Mais aucune asymétrie n'est détectée chez certains téléostéens (Concha & Wilson, 2001). Chez les sarcoptérygiens, le cœlacanthe, *Latimeria chalumnae*, présente une taille plus importante de l'habénula gauche (Nieuwenhuys, 1998b). Chez les tétrapodes, des études morphologiques et de connectivité ont démontré la présence d'asymétries chez certaines espèces de tous les grands groupes. Les habénulas sont asymétriques chez le lézard à flancs maculés, *Uta stansburiana* (Engbretson, Reiner, & Brecha, 1981), le xénope, *Bombina tropicalis* (Freudenmacher, Twickel, & Walkowiak, 2020) ou encore le poulet, *Gallus gallus* (Gurusinghe & Ehrlich, 1985). Récemment, chez l'homme, des analyses volumétriques des habénulas montrent que l'habénula gauche a un volume plus important. (Ahumada-Galleguillos et al., 2016). Chez les cyclostomes, groupe frère des gnathostomes, la lamproie (*Petromyzon marinus*) possède une habénula droite qui est drastiquement plus importante en taille que l'habénula gauche. (Stephenson-Jones et al., 2012; Villar-Cheda et al., 2002). Chez les chondrichtyens, les habénulas sont asymétriques comme chez la petite roussette, *Scyliorhinus canicula,* (Rodriguez-Moldes et al., 1990) l'anguillat, *Squalus acanthias,* (Smeets et al., 1983 : ref Neuwhenhuys) ou encore la grande roussette, *Scyliorhinus stellaris*. (Kemali and Miralto, 1979) (Figure 23).

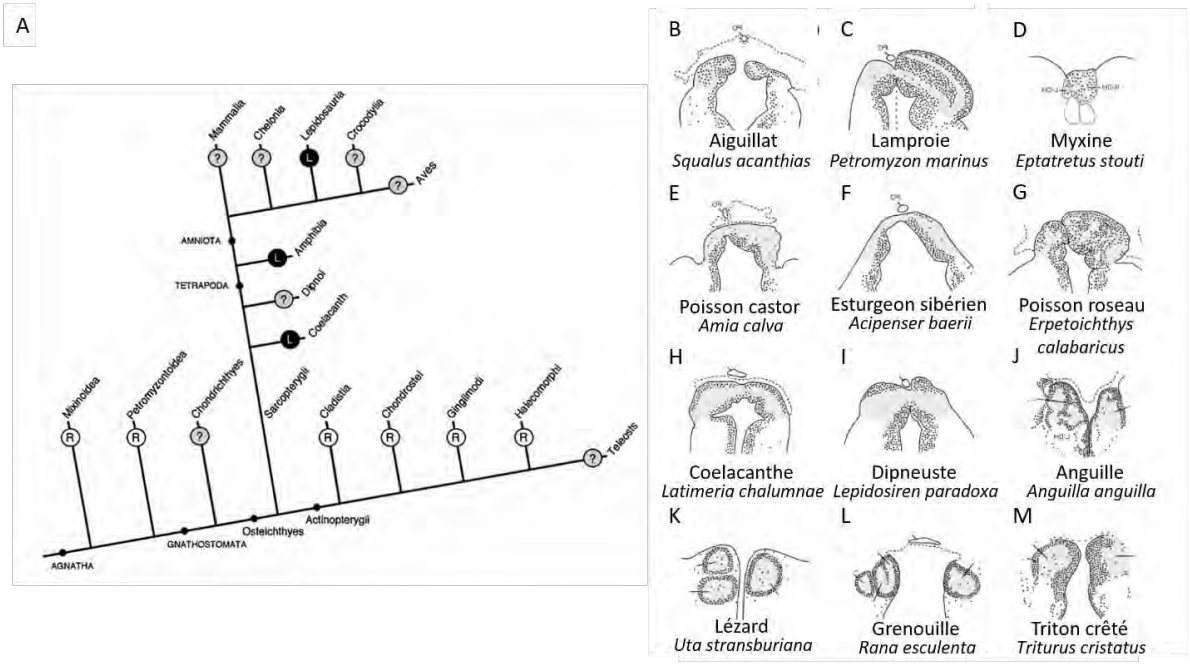

Figure 23 : Latéralité des asymétries habénulaires chez tous les grands groupes de vertébrés. (A) Etat ancestrale des asymétries épithalamiques à chaque nœud des grands groupes des vertébrés. (B-M) Chaque panneau correspond à une section transverse de l'épithalamus chez différentes espèces de différents groupes de vertébrés. Les régions grisées correspondent aux composants habénulaires asymétriques. Les pointillés délimitent la toile choroïdienne (3eme et 4eme ventricules). (Concha & Wilson, 2001)

II. Mécanismes de formation des asymétries habénulaires

II-1. Formation des habénulas

II-1-a. Modèle prosomérique du cerveau antérieur

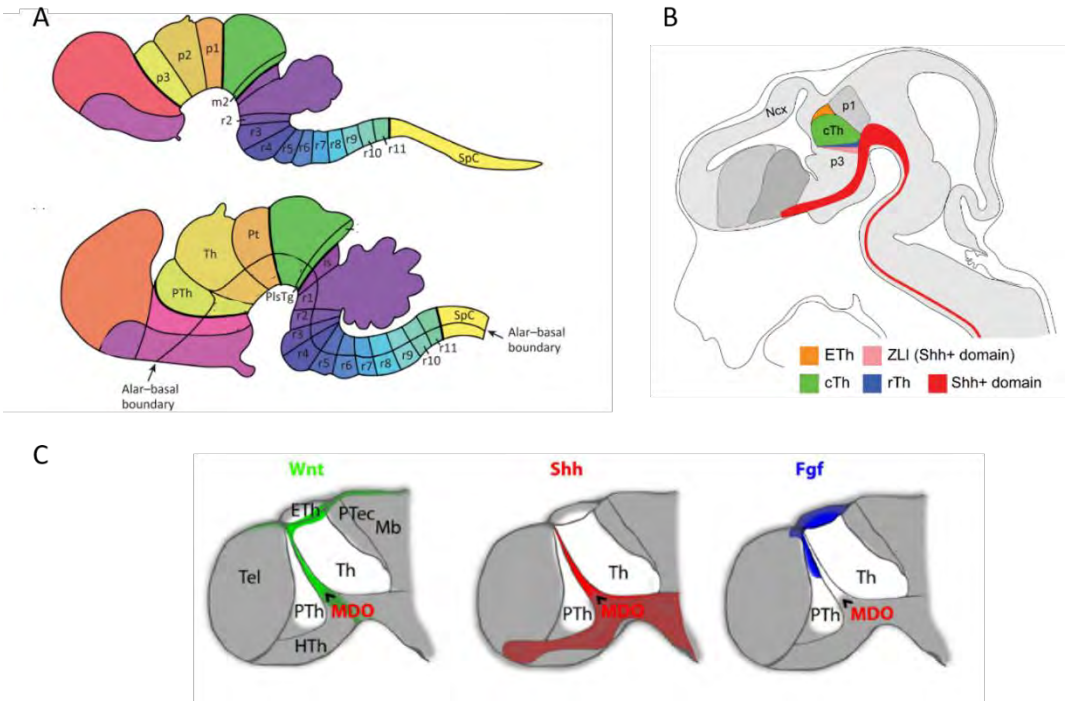

Figure 24 : Modèle prosomérique et voies de signalisations impliquées dans la formation des subdivisions du prosomère 2. (A) Vues latérales du cerveau embryonnaire de souris montrant les subdivisions en prosomères E15.5 (en haut) et E18.5 (en bas). PTh : Préthalamus ; Pt : Prétectum ; SpC : moelle épinière ; Th : Thalamus. (Puelles, Harrison, Paxinos, & Watson, 2013). (B) Vue latérale montrant les principaux dérivés du prosomère 2 chez l'embryon de souris à E12.5. cTh : thalamus caudal Eth : epithalamus ; rTh : thalamus rostral. (Mallika & Li, 2012). (C) Schéma montrant les zones d'expression des ligands Wnt (vert), Shh et Fgf (bleu), dans le cerveau embryonnaire des vertébrés. Hth : hypothalamus ; Mb : mésencéphale ; pTec : pretectum ; Tel : télencéphale. (Hagemann & Scholpp, 2012)

Le modèle prosomérique propose des subdivisions conservées du cerveau antérieur des vertébrés. Ce modèle qui fait aujourd'hui consensus repose sur l'observation d'expressions régionalisées, avec des bornes très nettes, de combinaisons de gènes codant pour des facteurs de transcription. Dans ce modèle, le prétectum dérive de p1, le thalamus et l'épithalamus (et donc les habénulas) de p2 et le préthalamus et l'*eminentia thalami* de p3 (Puelles & Rubenstein, 2003). La formation de ces territoires est sous le contrôle de centres de signalisation bien caractérisés, dont la *zona limitans intrathalamica* (ZLI ou MDO « mid-diencephalic organiser ») qui exprime notamment sonic hedgehog (shh) (Zeltser, 2005; Zeltser, Larsen, & Lumsden, 2001), et se retrouve chez l'ensemble des vertébrés (Barth & Wilson, 1995; Osorio, Mazan, & Rétaux, 2005; Puelles & Martinez-de-la-Torre, 1987; Ruiz i Altaba, 1998). L'établissement des bornes entre prosomères est sous le contrôle de signaux complexes, dont pour les plus étudiés les voies de signalisation Wnt, Shh et Fgf. Ces signaux proviennent de différentes sources tout au long de l'axe antéro-postérieur du SNC. p2 en contient 2, la frontière antérieure neurale (ANB) et le MDO, qui forme la frontière entre p2 et p3. (Hagemann & Scholpp, 2012). (Figure 24).

II-1-b. Spécification de l'épithalamus

Plusieurs voies de signalisation contrôlent la spécification des habénulas dans le prosomère 2. Le rôle de la voie Shh, sécrété par le MDO, a été bien établi. Ainsi, chez la souris, le territoire présomptif des habénulas est étendu chez des lignées *Shh*$^{SG/SG}$, codant pour une forme inactive de la protéine shh. En revanche, chez la souris comme chez le poisson-zèbre, le territoire de *Shh* dans le MDO présente une expansion dorsale chez des mutants pour le gène *Pax6*, et l'épithalamus n'est pas spécifié. Ces données indiquent que Shh est nécessaire à la spécification de l'épithalamus, sous le contrôle de *Pax6*. (Chatterjee & Li, 2012; Scholpp & Lumsden, 2010) (Macdonald et al., 1994; Walther & Gruss, 1991) (Mallika, Guo, Weber, Scholpp, & Li, 2014) (Figure 25)

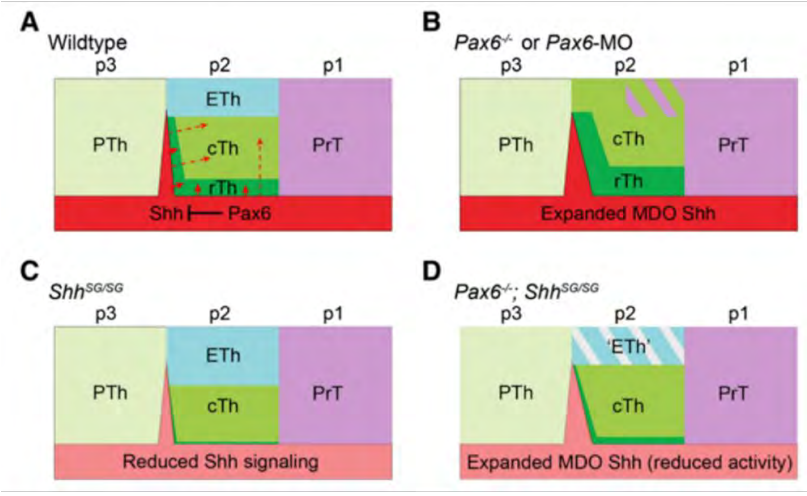

Figure 25 : Les subdivisions du prosomère 2 à l'origine de l'épithalamus et du thalamus sont sous le contrôle de *Pax6* et *Shh*. (A-D) schémas des partitions du diencéphale des génotypes indiqués. Chez les embryons sauvages (A), *Pax6* restreint le domaine d'expression de *Shh* dans le MDO. Une forte signalisation de Shh (flèches) induit le thalamus rostral (rTh). Shh a un effet à longue portée (flèches en pointillés) en induisant le thalamus caudal (cTh) et en inhibant l'épithalamus (ETh). Chez les mutants *Pax6*$^{-/-}$ (B), le domaine d'expression de *Shh* et du MDO est élargi dans les embryons de souris et de poisson zèbre, et sa formation est accélérée chez la souris. L'activité accrue de Shh entraîne une expansion des rTh, cTh et du préthalamus (PrT) aux dépens de l'épithalamus. Dans les embryons avec une fonction *Shh* réduite ou un gain de fonction de Pax6 (C), le domaine épithalamique est agrandi aux dépens du cTh. Chez les mutants Pax6$^{-/-}$ avec une activité Shh réduite (D), même si l'expression de *Shh* et le MDO sont élargis, l'épithalamus est partiellement restauré. PTh, préthalamus ; p1-3, prosomères 1-3. (Mallika et al., 2014).

La voie Wnt est également essentielle à la ségrégation entre thalamus et habénula, comme démontré par l'étude mutants de souris pour *Tcf7l2*, qui code pour un facteur de transcription de la famille Lef/Tcf et active l'expression des gènes cibles de la voie Wnt. Chez ces mutants, l'expression de marqueurs habénulaires, comme *Id4, Irx1, Pou4f1* devient ectopique. Le rôle du gène dans le maintien des identités neuronales habénulaires a également été démontré par l'étude de mutants conditionnels, chez lesquels l'activité post-natale du gène est abolie (M. Lee et al., 2017; Lipiec et al., 2020). Par ailleurs, *Gbx2*, un marqueur de précurseurs neuronaux du thalamus (L. Chen, Guo, & Li, 2009; Li, Zhang, & Li, 2012), est essentiel au maintien de l'identité thalamique des neurones post-mitotiques, qui en son absence d'expression prennent une identité habénulaire. On observe en effet des expressions ectopiques de marqueurs habénulaires (*Irx1, Nrp2, Robo3, Pou4f1*) dans le thalamus caudal, chez des lignées murines mutantes *Gbx2*$^{creER/-}$. (Mallika, Guo, & Li, 2015) (Figure 26). Des marqueurs du prétectum rostral, présentent également des expansions de leur territoire d'expression chez les mutants *Gbx2*$^{creER/-}$ (Mallika et al., 2015) ainsi que chez les mutants *Tcf7l2*$^{-/-}$. (M. Lee et al., 2017).

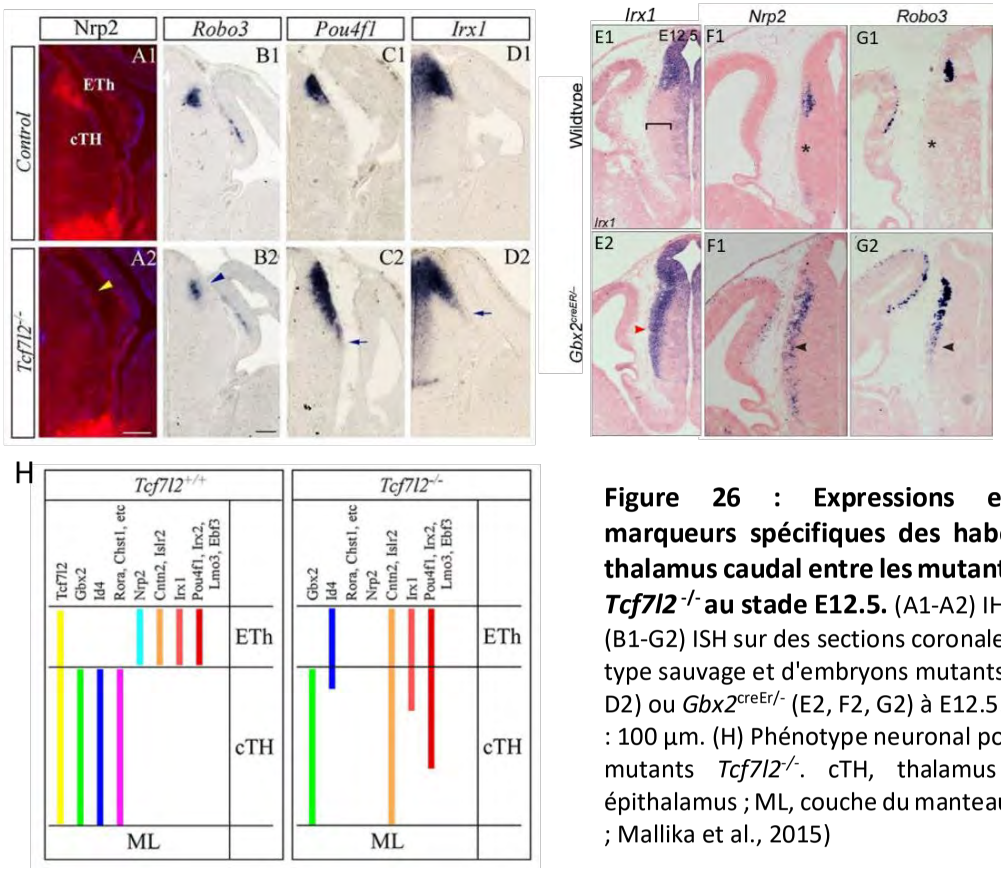

Figure 26 : Expressions ectopiques de marqueurs spécifiques des habénulas dans le thalamus caudal entre les mutants *Gbx2* $^{creER/-}$ *ou Tcf7l2* $^{-/-}$ au stade E12.5. (A1-A2) IHC contre Nrp2 et (B1-G2) ISH sur des sections coronales d'embryons de type sauvage et d'embryons mutants *Tcf7l2*$^{-/-}$ (B2, C2, D2) ou *Gbx2*$^{creEr/-}$ (E2, F2, G2) à E12.5. Barres d'échelle : 100 µm. (H) Phénotype neuronal post-mitotique des mutants *Tcf7l2*$^{-/-}$. cTH, thalamus caudal ; Eth, épithalamus ; ML, couche du manteau. Lee et al., 2017 ; Mallika et al., 2015)

En accord avec cela, la reconstruction des trajectoires cellulaires du diencéphale par séquençage de cellules uniques au stade E12.5 chez la souris montre que les cellules d'identité habénulaires sont plus proches de celles du prétectum rostral que celles du thalamus caudal. (Figure 27). (Guo & Li, 2019). *Gbx2* et *Tcf7l2* sont donc indispensables pour les choix de destins cellulaires entre thalamus, habénula et prétectum rostral.

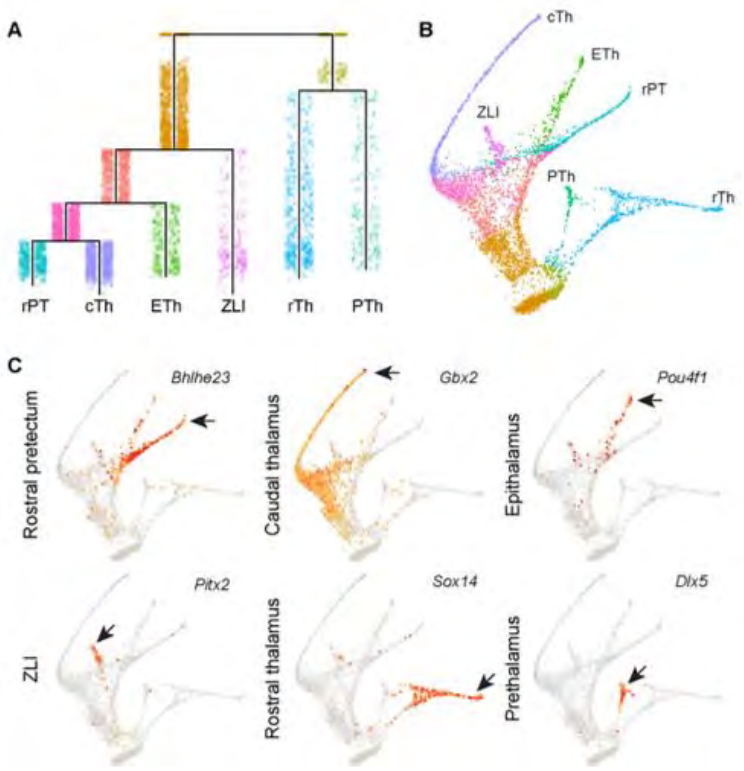

Figure 27 : Projections statistiques des trajectoires développementales du diencéphale. (A) Arbre hiérarchique des lignées diencéphaliques déduit de la reconstruction des trajectoires développementales ramifiées (URD). (B) Disposition dirigée par la force de l'arbre de trajectoire coloré par les segments comme indiqué en A. (C) Expression des marqueurs des sous-régions diencéphaliques superposée à l'arbre de trajectoire. Les flèches indiquent une expression robuste dans chaque lignée spécifique. cTh, thalamus caudal ; ETh, épithalamus ; PTh, préthalamus ; rPT, pretectum rostral ; rTh, thalamus rostral ; ZLI, zona limitans intrathalamica. (Guo & Li, 2019)

II-1-c. Formation de la subdivision dorso/ventrale des habénulas chez le poisson-zèbre

L'étude des mécanismes de formation des subdivisions des habénulas n'a à ce jour été effectuée que chez le poisson-zèbre. Chez cette espèce, les progéniteurs des Hbv et Hbd proviennent de populations de progéniteurs distinctes. Les neurones constituant l'Hbd sont issues de progéniteurs exprimant *dbx1b* localisés dans le diencéphale dorsal au st 24-28hpf. Le suivi du lignage cellulaire de ces progéniteurs *dbx1b*$^{+}$ montre que ces cellules expriment plus tardivement *elavl3* (ex *HuC*), marqueur de neurones post-mitotiques, et *cxcr4b, cadps2* ou *ano2*, marqueurs de l'Hbd, mais aucune expression de marqueurs de l'Hbv, tels que *aoc1,* n'est détectée (Dean, Erdogan, Gamse, & Wu, 2014; Roberson & Halpern, 2017) (Figure 28).

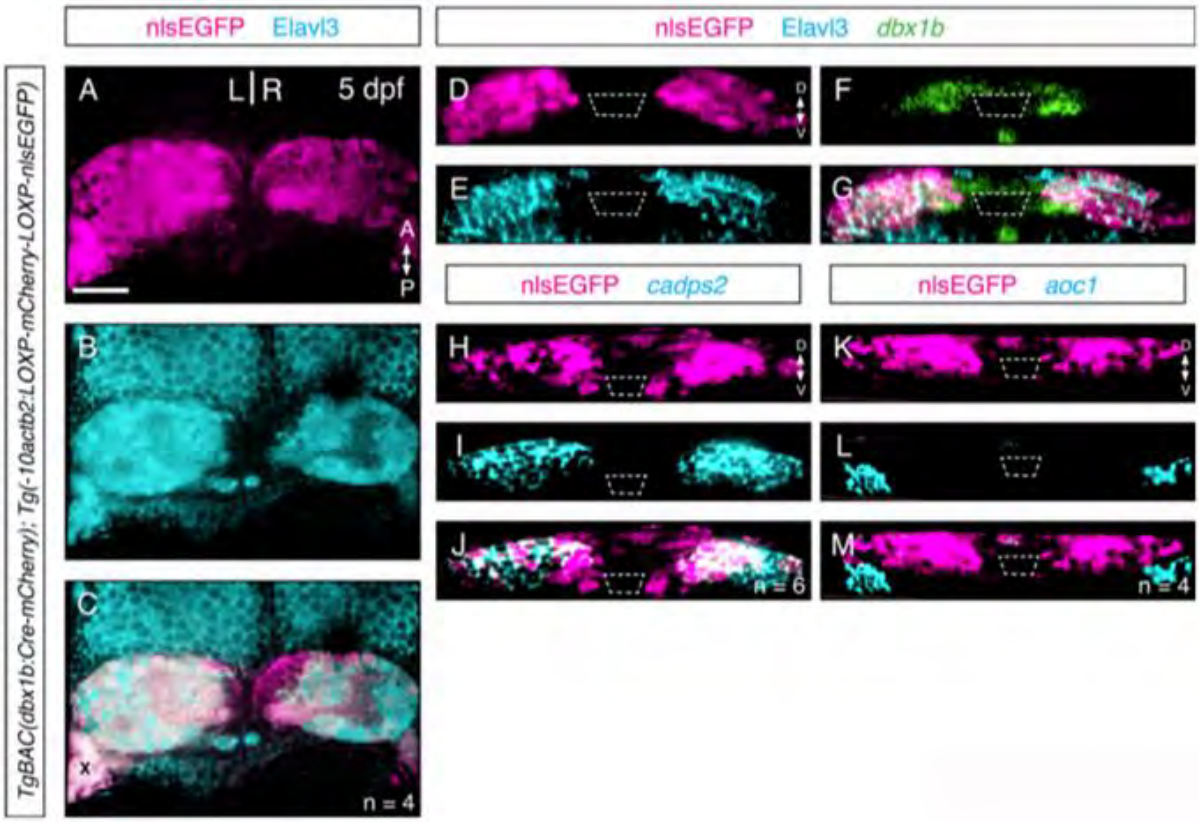

Figure 28 : Les progéniteurs diencéphalique *dbx1b*⁺ contribuent uniquement à la formation des Hbd. (A-C) Lignée transgénique *dbx1bBAC:cre* (magenta) marquant presque tous les neurones Elavl3-positifs dans les Hb (cyan). X = débris piégés, aucun un signal réel. (D-G) Domaine Elavl3-négatif correspondant au domaine des progéniteurs habénulaires, qui est marqué par l'expression de *dbx1b* (vert) sur des coupes coronales (H-J) Les cellules *dbx1b*⁺ sont limitées au domaine habenulaire dorsal *cadps2*⁺, dans la zone ventriculaire. (K-M) Les cellules marquées par le lignage sont exclues des habenulas ventrales *aoc1*⁺. Barres d'échelle = 50 µm (Dean, Erdogan, Gamse, & Wu, 2014; Roberson & Halpern, 2017).

Les expériences d'imagerie en temps réel montrent que les progéniteurs de l'Hbv proviennent d'une population distincte, constituée de cellules postérieures et latérales aux progéniteurs de l'Hbd, appelée « thalamic-epithalamic early projecting cluster (ThEPC) », qui migrent au voisinage des Hbd au cours du développement des habénulas. L'ablation de ces populations cellulaires avant leur migration résulte en des Hb plus petites, montrant la contribution des ThEPC à la formation des Hb. (Beretta, Dross, Bankhead, & Carl, 2013).

En ce qui concerne les mécanismes, les voies de signalisation Wnt, Fgf et Shh ont été impliquées dans la formation de cette subdivision. La voie Wnt est nécessaire à la migration des ThEPC. Chez la lignée mutante de poisson-zèbre *tcf7l2*$^{exl/exl}$, la migration des cellules du ThEPC vers le territoire des Hbv présomptives n'a pas lieu. (Beretta et al., 2013)(Figure 29).

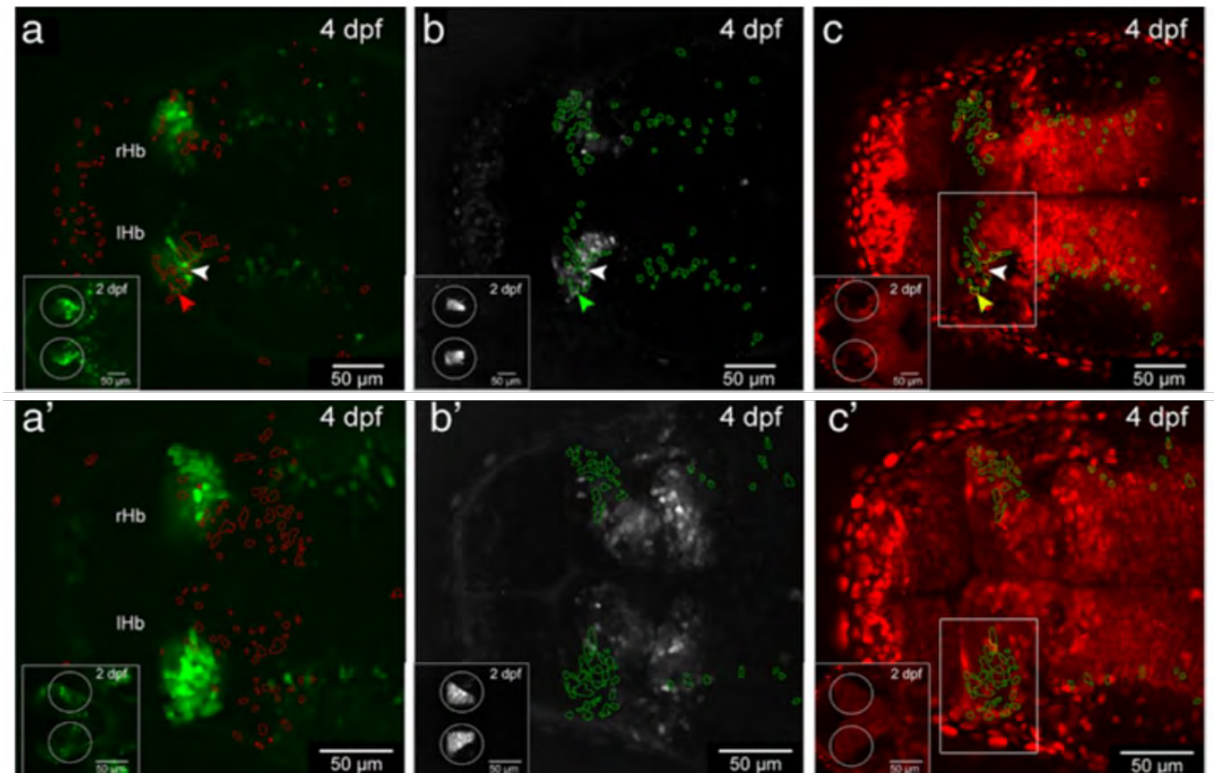

Figure 29 : La formation des Hbv nécessite la migration de cellules thalamiques ThEPC sous le contrôle de *Tcf7l2*. (a-c') Vues dorsales de coupes optiques d'embryons de poisson-zèbres à 4 jours après fécondation de lignée transgénique. Antérieur à gauche. (a-c) sans (Et(−1.0otpa:mmGFP)hd1)et (a'-c') avec KO *tcf7l2*(*tcf7l2*$^{exl/exl}$ *x Et(−1.0otpa:mmGFP)hd1*) après photoconversion des cellules positives H2B-PSmOrange dans le thalamus à 2 dpf (encarts). Les cercles mettent en évidence la zone de photoconversion. Toutes les cellules ciblées expriment la protéine photoconvertie et se trouvent au centre des cercles. (a-a') Les ROIs rouges montrent la position des cellules photoconverties dans le canal vert. (b-b') Les ROIs vertes montrent la position des cellules positives GFP. (c-c') Les ROIs rouges et vertes ont été combinés dans le canal rouge pour visualiser en jaune la position des neurones ThEPC photoconvertis GFP dans les noyaux habénulaires. (a-c) Les pointes de flèches colorées marquent une cellule positive GFP dérivée d'une cellule du ThEPC photoconvertie dans l'habenula. Les pointes de flèches blanches marquent une cellule négative GFP photoconverties dans l'Hb. (a'-c') Les cellules photoconverties ne sont pas retrouvées dans les Hb des mutants *tcf7l2* $^{exl/exl}$ (Beretta et al., 2013).

La voie Wnt est aussi impliquée dans la formation des Hbd. Chez des mutants *wls*, chez lesquels l'activité de la voie Wnt est perturbée, on peut observer une réduction des territoires d'expressions de marqueurs exprimés dans l'Hbd (kctd*12.2, cxcr4b, dbx1b*) comme dans l'Hbv (*aoc1*) (Kuan et al., 2015) (Figure 30).

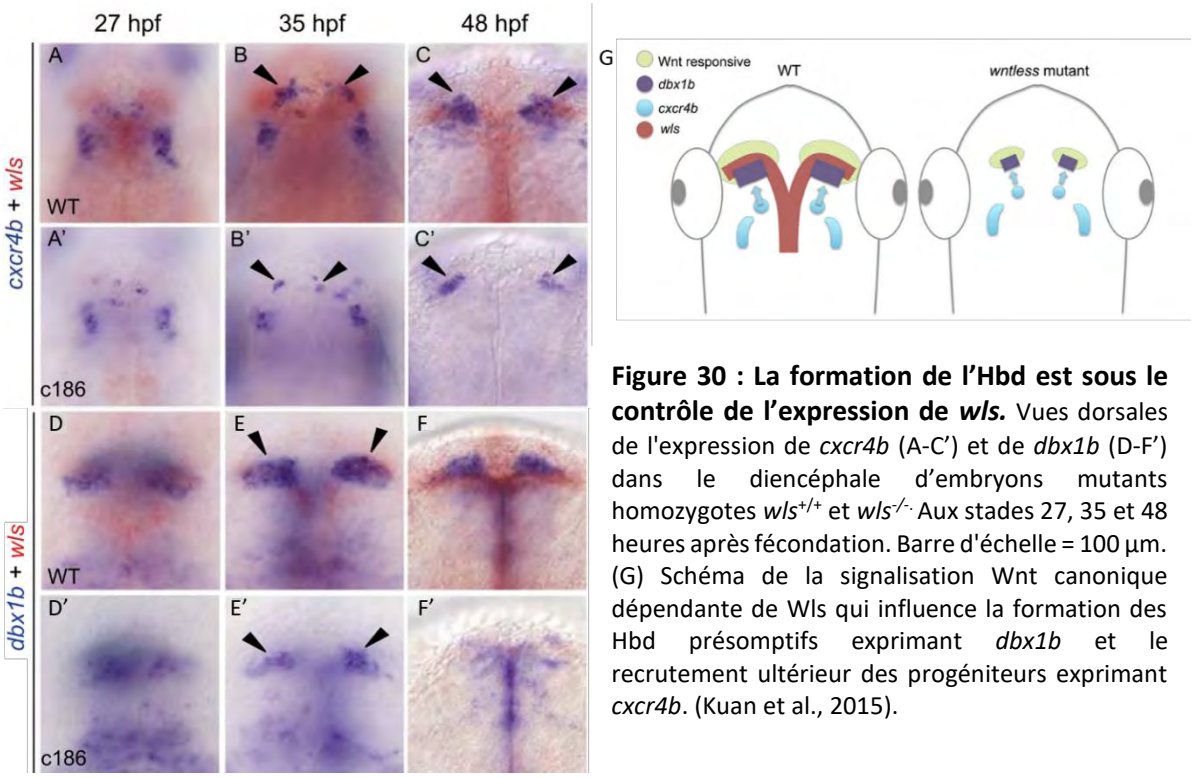

Figure 30 : La formation de l'Hbd est sous le contrôle de l'expression de *wls.* Vues dorsales de l'expression de *cxcr4b* (A-C') et de *dbx1b* (D-F') dans le diencéphale d'embryons mutants homozygotes *wls*$^{+/+}$ et *wls*$^{-/-}$. Aux stades 27, 35 et 48 heures après fécondation. Barre d'échelle = 100 µm. (G) Schéma de la signalisation Wnt canonique dépendante de Wls qui influence la formation des Hbd présomptifs exprimant *dbx1b* et le recrutement ultérieur des progéniteurs exprimant *cxcr4b*. (Kuan et al., 2015).

La voie « Hedgehog » (Hh) joue aussi un rôle dans la mise en place de ces subdivisions habénulaires. Chez des lignées de poisson-zèbre mutantes pour l'un des récepteurs de la voie de signalisation Hh, l'expression de *cxcr4b* et *dbx1b* est absente des habénulas dorsales. (Halluin et al., 2016; Roberson & Halpern, 2017). La voie Fgf est également nécessaire à la formation des Hbd, sous le contrôle de la voie Wnt. Le nombre de cellules *dbx1b*$^{+}$ sont réduites chez des mutants pour le gène *fgf8a* (Dean et al., 2014) et sont totalement absents chez des doubles mutants pour *wls* et *fgf8a* (Roberson & Halpern, 2017). Les voies de signalisations Wnt et Fgf sont toutes deux nécessaires à la formation des progéniteurs de l'Hbd sous le contrôle de *mediator subunit 12* (*med12*), qui code une protéine qui intervient dans la liaison entre l'ARN polymérase II et les facteurs de transcriptions. Chez des mutants n'ayant pas d'expression de *med12*, on observe une absence de cellules dbx1b^{+} comme chez les doubles mutants *wls* et *fgf8a* (Roberson & Halpern, 2018; S. Y. Wu, de Borsetti, Bain, Bulow, & Gamse, 2014).

II-2. Mécanismes d'établissement des asymétries épithalamiques

Le poisson-zèbre étant le seul organisme modèle génétique qui présente des asymétries épithalamiques marquées, c'est sur cette espèce que se sont concentrées les analyses des mécanismes contrôlant leur établissement. L'apparition des asymétries dans les habénulas différenciées est précédée par une séquence d'asymétries observées beaucoup plus tôt au cours du développement diencéphalique. Ces différentes phases et leurs interdépendances sont aujourd'hui bien connues. (Figure 31)

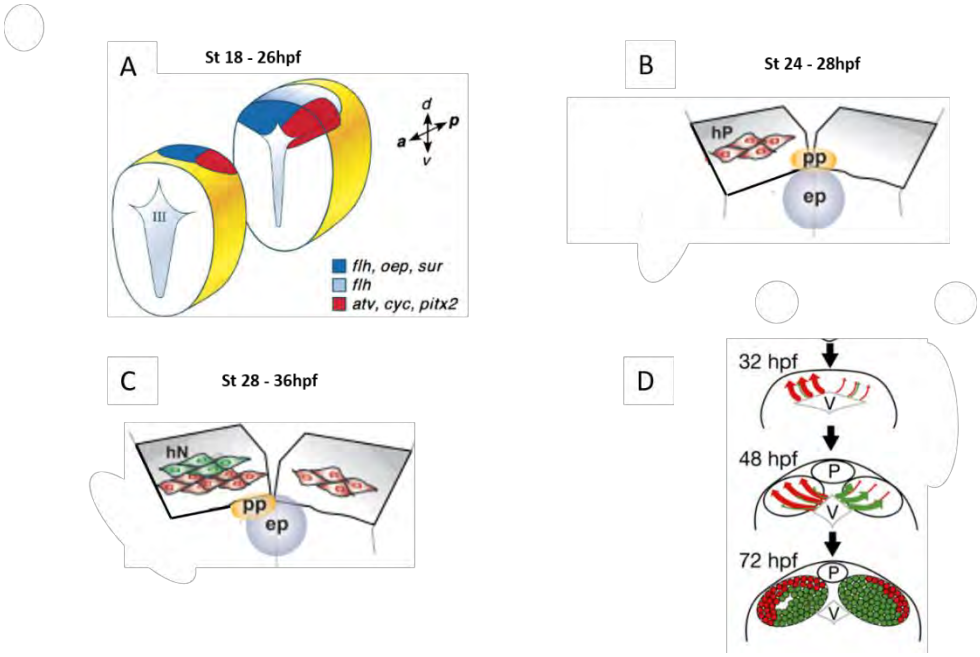

Figure 31 : Asymétries observées au cours du développement des habénulas. (A) Schéma montrant l'expression des différents gènes asymétriques exprimés dans le diencéphale dorsal entre les stades 18 et 26 hpf. Abréviations, III, troisième ventricule. (B) Schéma représentant l'initiation gauche de la différenciation neuronale, avant la migration de la parapinéale (pp) entre les stades 24 à 28 hpf. ep : épithalamus ; hP : précurseurs habénulaires. (C) Induction de l'identité de l'HbdG par un signal sécrété par la parapinéale une fois sa migration à gauche de la ligne médiane effectuée entre les stades 28 à 36 hpf. hN : neurones habénulaires. (D) Génération des précurseurs neuronaux pour les sous-noyaux médiaux dorsaux (vert) et latéraux dorsaux (rouge) aux stades 32 et 48 hpf selon une organisation asymétrique entre la gauche et la droite au stade 72 hpf. P : organe pinéal ; V : 3eme ventricule (Aizawa, Goto, Sato, & Okamoto, 2007; Concha et al., 2000a, 2003; Roussigne et al., 2009).

II-2-1. Asymétries précoces : diencéphale dorsal

II-2-1-a. Une fenêtre d'activité asymétrique de la voie Nodal

Une première asymétrie apparaît très précocement dans le diencéphale dorsal, peu après la fermeture du tube neural (18-26 hpf). A ce stade, on observe une expression asymétrique gauche de plusieurs composants et régulateurs de la voie Nodal : *atv,* un gène codant pour un antagoniste de la voie de signalisation Nodal, ndr2 (anciennement cyclops), codant pour l'un des 3 ligands paralogues de Nodal chez le poisson-zèbre (Dougan, 2003), *pitx2,* un facteur de transcription connu comme une cible la voie de signalisation Nodal. (Concha, Burdine, Russell, Schier, & Wilson, 2000b; Liang et al., 2000). (Figure 32).

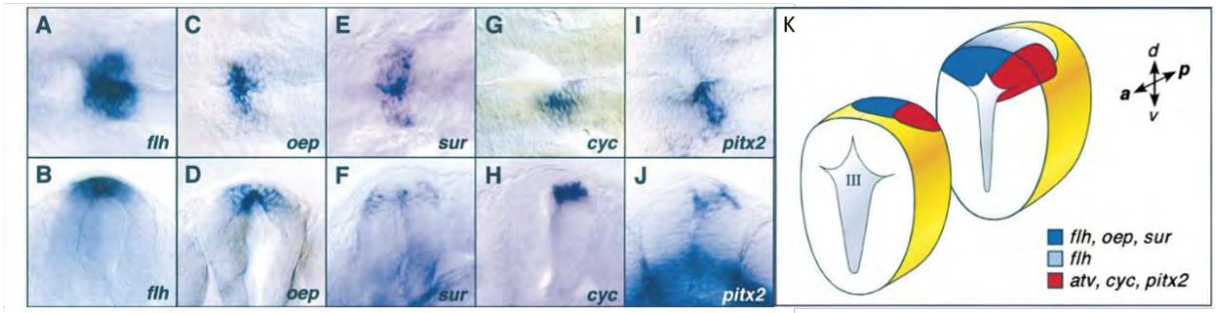

Figure 32 : Asymétries d'expressions de composants de la voie Nodal dans le diencéphale dorsal au stade 18 à 26 hpf. (A-N) Vues dorsales, antérieur à gauche (A, C, E, G, I) et frontales montrant l'expression gauche des gènes dans le diencéphale dorsal d'embryons de stades 24 à 26 somites (A,B,C,D,G,H,I,J) 18 somites (E et F). La gauche est sur la droite de la photo dans (B,D,F,H,J) et en bas dans (A,C,E,G,I). Schéma montrant la localisation relative des domaines d'expression des composants de la voie Nodal dans le diencéphale dorsal. Abréviations : III, troisième ventricule. (Concha et al., 2000b).

La perturbation de l'expression asymétrique de ces marqueurs est observée dans des lignées mutantes pour des composants de la voie Nodal, soit : *LZoep*$^{-/-}$, *ndr2*$^{-/-}$, *sur*$^{-/-}$ ou encore *ntl*$^{-/-}$. Pour les mutants *LZoep*$^{-/-}$ et *sur*$^{-/-}$, l'expression de *ndr2* et *pitx2* est perdue, alors que dans les mutants *ndr2*$^{-/-}$ et *ntl*$^{-/-}$ leur expression est bilatérale symétrique (Figure 33). Ces données confirment que la voie Nodal est active dans le diencéphale dorsal dans une fenêtre temporelle qui suit la fermeture du tube neural.

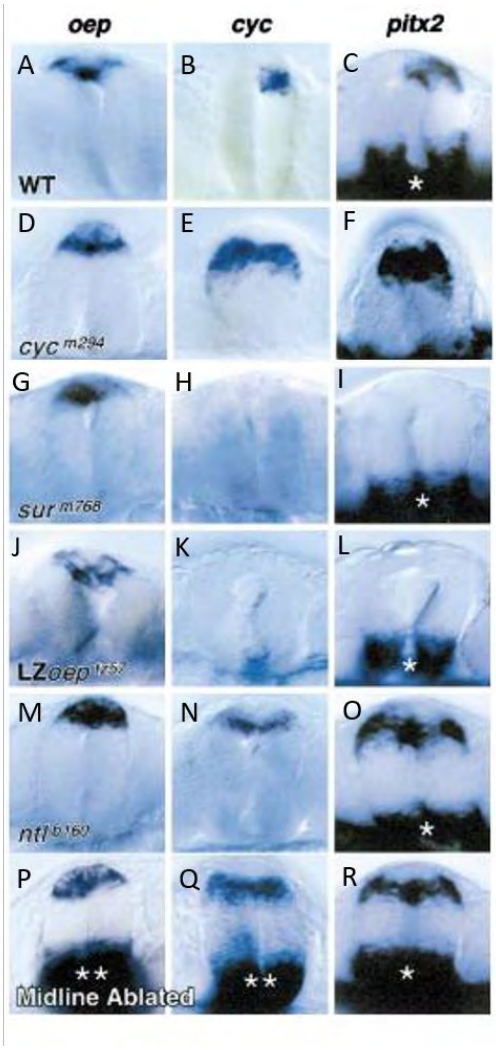

Figure 33 : Asymétries du diencéphale dorsale sous le contrôle de Nodal. Vues transversales d'embryons de type sauvage (A-C), cyc$^{-/-}$ (D-F), *ndr2*$^{-/-}$(*cyc*$^{-/-}$) (G-I), LZoep$^{-/-}$ (J-L), ntl$^{-/-}$ (M-O), et ablation de la ligne médiane (P-R) de l'expression diencéphaliques des gènes *oep, ndr2* et *pitx2* aux stades 24s-26s. L'astérisque indique l'expression de pitx2 dans le diencéphale ventral, présent dans les embryons sans défauts axiaux sévères. Le double astérisque indique l'expression de shh dans le cerveau ventral des embryons avec ablation de la ligne médiane. (Concha et al., 2000b).

II-2-1-b. Rôle de la voie Nodal dans la formation des asymétries habénulaires

Le rôle de la voie Nodal sur la formation des asymétries habénulaires a été étudié par l'étude de mutants pour des composants de la voie. Ces mutations n'abolissent pas la formation des asymétries épithalamiques mais conduisent à une randomisation de leur latéralité. (Figure 34). La formation des asymétries dans les habénulas ne dépend donc pas de l'activité de la voie Nodal mais leur latéralité est biaisée vers la gauche par la voie.

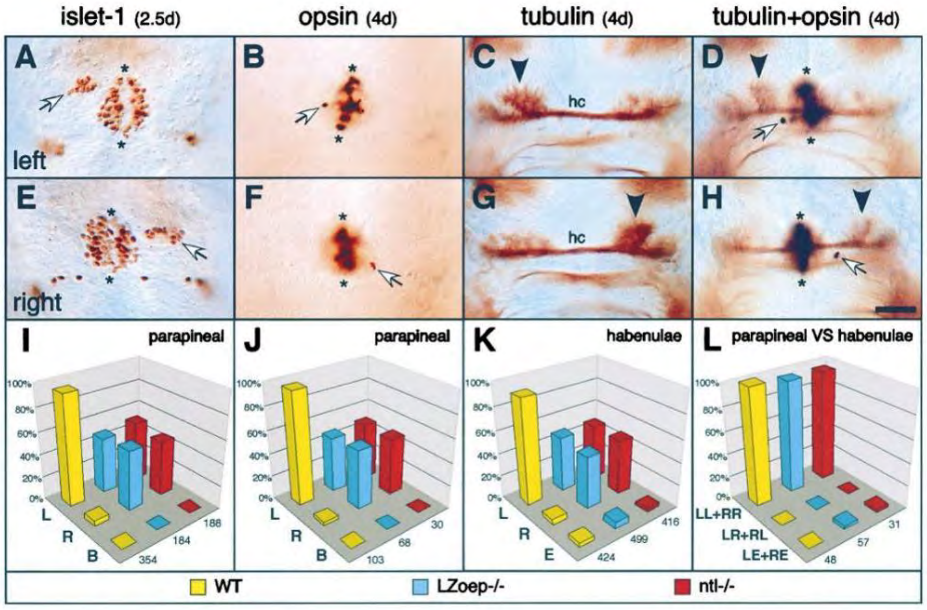

Figure 34 : l'absence ou la perte d'asymétries de composants de la voie Nodal dans le diencéphale dorsal conduit à une randomisation des asymétries habénulaires. (A-H) Vues dorsales du diencéphale d'embryons marqués avec des anticorps anti-Islet marquant la parapinéale (A et E), anti-opsine marquant la pinéale (B et F), anti-tubuline acétylée (C et G), ou anti-tubuline acétylée plus anti-opsine (D et H). Les astérisques délimitent les limites antérieures et postérieures de l'épiphyse le long de la ligne médiane dorsale, hc : commissure habénulaire (A-D) Embryons de types sauvages montrant le noyau parapinéal à gauche ([A, B et D], flèche) et le noyau habénulaire élargi gauche ([C et D], tête de flèche). (E-H) Exemples d'embryons mutants montrant le noyau parapinéal droit ([E, F et H], flèche) et le noyau habénulaire élargi droit ([G et H], tête de flèche). (I-L) Graphiques montrant la latéralité des asymétries épithalamiques chez les larves de type sauvage (jaune), LZoep$^{-/-}$ (bleu) et ntl$^{-/-}$ (rouge). Chez les larves LZoep$^{-/-}$ et ntl$^{-/-}$, la latéralité du cerveau est randomisée (I-K). Dans pratiquement tous les cas, le noyau habénulaire est plus gros du côté de la parapinéale (L). Abréviations : B, deux côtés ; E, taille égale ; L, côté gauche ; R, côté droit ; LL+RR, habenula et parapinéale de grande taille tous deux à gauche ou tous deux à droite ; LR+RL, parapinéale et habénula de grande taille sur des côtés opposés ; LE+RE, parapinéale au centre et habénulas de tailles égales. (Concha et al., 2000b).

II-2-2. Asymétries neurogénétiques

Des marquages de la prolifération cellulaire utilisant la bromodésoxyuridine (BrdU) et des études d'expression de marqueurs précoces de différenciation neuronale, montrent que la neurogénèse s'initie à gauche au stade 28hpf. (Aizawa et al., 2007; Roussigne et al., 2009). (Figure 35). Au stade 28 hpf, ces premières cellules différenciées de l'Hbd sont identifiées par l'expression de HuC/D et *cxcr4b*, des marqueurs de différenciation qui présentent une expression asymétrique gauche, peu avant le stade 28hpf jusqu'aux stades tardifs (Figure 35). Cette asymétrie gauche de différenciation neuronale est dépendante de l'activité de la voie Nodal (Roussigne et al., 2009). (Figure 35).

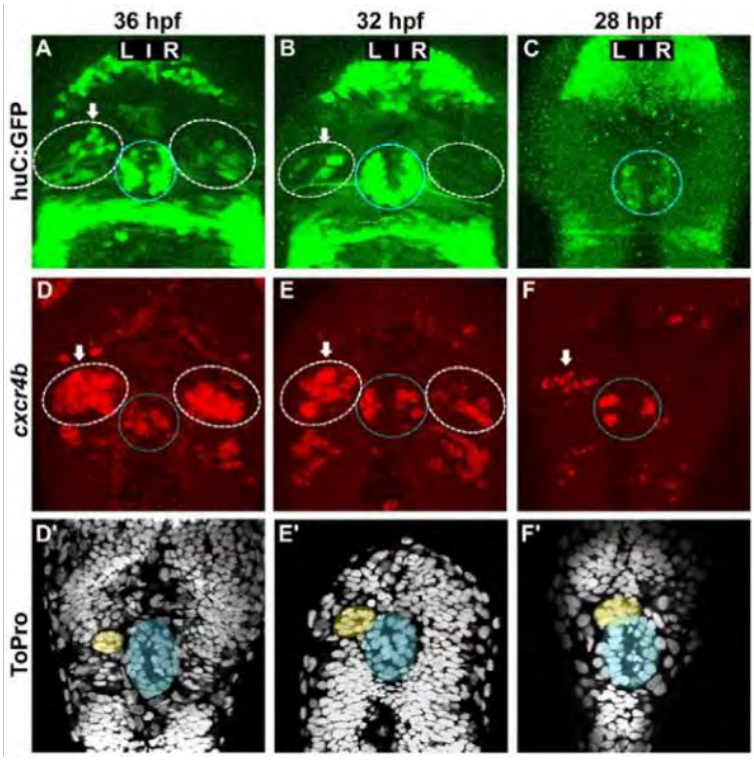

Figure 35 : Initiation asymétrique gauche de l'expression de *cxcr4b.* (A-C) Projections confocales des embryons de poisson zèbre Tg(huC:gfp) (vert) à 36 (A), 32 (B) et 28 (C) hpf. (D-F′) Hybridations in situ fluorescentes de *cxcr4b* (D-F) et coloration nucléaire au ToPro (D′-F′) aux stades 36 (D-D′), 32 (E,E′), ou 28 hpf (F,F′). Parapinéale en jaune et le pinéale en bleu. ligne blanche pointillée = Hb ; ligne bleue = épiphyse. Les flèches indiquent l'habenula avec le plus grand nombre de neurones habenulaires huC:GFP^{+} ou de cellules exprimant cxcr4b. (Roussigne, Bianco, Wilson, & Blader, 2009).

En effet, elle est perdue à la suite des traitements pharmacologiques utilisant la drogue SB431542, qui inhibe l'activité de la voie Nodal, juste avant l'initiation de l'expression asymétrique gauche de *ndr2* dans l'épithalamus dorsal (stade 16hpf à 34-38hpf) (Figure 36).

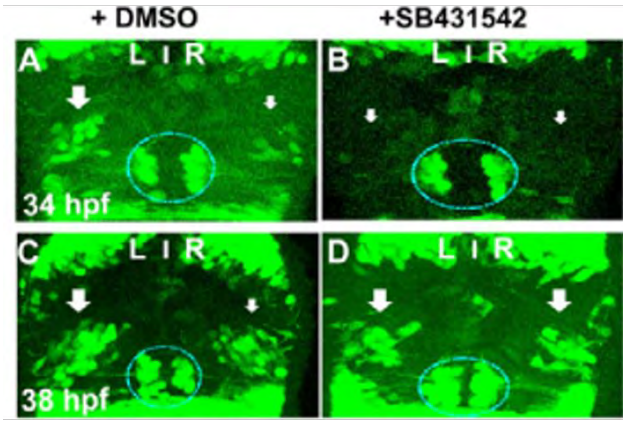

Figure 36 : L'initiation asymétrique gauche de la différenciation neuronale est sous le contrôle de la voie Nodal. (A-D) Projections confocales d'embryons de poissons zèbres transgéniques Tg(huC:gfp) incubés avec du DMSO (A,C) ou avec du SB431542 (B,D) à partir de 10 hpf et fixés à 34 (A,B) ou 38 (C,D) hpf. Les flèches indiquent que les pools de neurones HuC+ de gauche sont plus grands que ceux de droite dans les embryons traités au DMSO (A,C), alors que les pools de gauche et de droite sont symétriques dans les embryons incubés avec le SB431542 (B,D). Ligne bleue = épiphyse. (Roussigne, Bianco,

II-2-3. Asymétries de migration de la parapinéale

II-2-3-a. Migration gauche des cellules de la parapinéale

La 3e asymétrie observée lors du développement de l'épithalamus est une migration latéralisée des cellules qui vont former la parapinéale, localisée à gauche chez le poisson-zèbre. Cela a été montré par l'étude de lignées transgéniques codant pour des protéines de marqueurs spécifiques de la parapinéale (*flh* et *foxD3*). On observe chez ces embryons que des cellules de l'épithalamus antéro-dorsal s'agrègent pour former la parapinéale et migrent à gauche de la ligne médiane pour se positionner ventralement et à gauche de l'organe pinéal, à proximité de l'Hbd gauche. Cette migration se déroule entre les stades 24hpf et 60hpf (Concha et al., 2003; Gamse et al., 2003). (Figure 37).

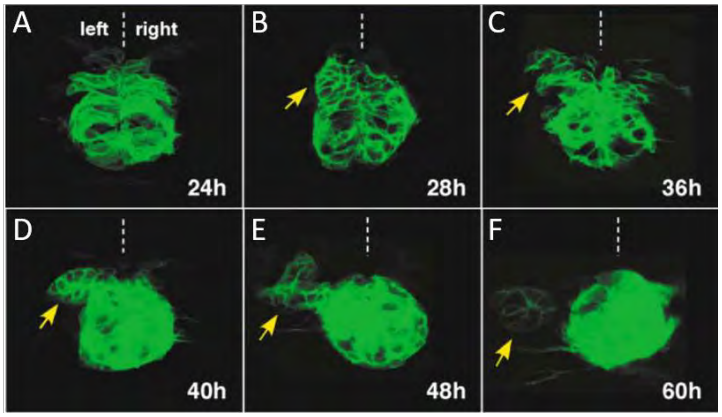

Figure 37 : Migration de la parapinéale à gauche lors du développement. (A-F) Images confocales montrant les premières phases de la morphogenèse asymétrique de l'organe parapinéal chez le poisson zèbre Tg(flh:eGFP). Les flèches indiquent la position de l'organe parapinéal. (Concha et al., 2003).

II-2-3-b. Mécanismes impliqués

La migration de la parapinéale est sous le contrôle de plusieurs voies de signalisation. Tout d'abord, chez des mutants ayant une expression symétrique de *ndr2, lft1* et *pitx2* au stade 20hpf, la latéralité de la migration de la parapinéale est randomisée (Halpern, Liang, & Gamse, 2003). (Halpern, Liang, & Gamse, 2003). La voie Nodal contrôle donc la latéralité de cette asymétrie. L'activité de la voie

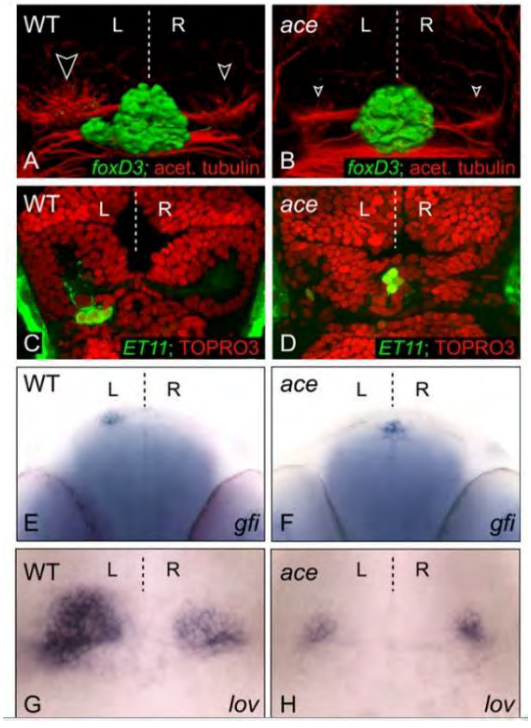

Figure 38 : La migration gauche de la parapinéale est régulée par l'expression de *fgf8*. (A-D) Vues dorsales de l'épithalamus chez des embryons de types sauvages et *ace* à 3 jours post-fécondation. (A-B) Reconstructions 3D des noyaux et des axones pinéaux/parapinéaux [vert, Tg(foxD3:GFP)] et du neuropile des noyaux habénulaires (rouge, anti-tubuline acétylée ; pointes de flèche à bordure blanche). (C-D) Les cellules parapinéales Tg(ET11:GFP) (vert) restent sur la ligne médiane dans l'embryon *ace* par rapport à celles de l'embryon de type sauvage à 3 dpf. Marquage nucléaire au TOPRO3 (rouge). Une seule coupe z est présentée pour chaque exemple. (E-F) Vue frontale de l'expression de *gfi*, marqueur de la parapinéale, chez des embryons de type sauvage et *ace* à 3 jours post-fécondation. (Regan et al., 2009).

Fgf est par ailleurs nécessaire à la migration de la parapinéale. Celle-ci ne se produit pas chez les poissons mutants *ace (fgf8-/-).* (Figure 38) ou suite à des traitements pharmacologiques dirigés contre le récepteur aux Fgfs, SU5402. (Figure 39). (Regan, Concha, Roussigne, Russell, & Wilson, 2009).

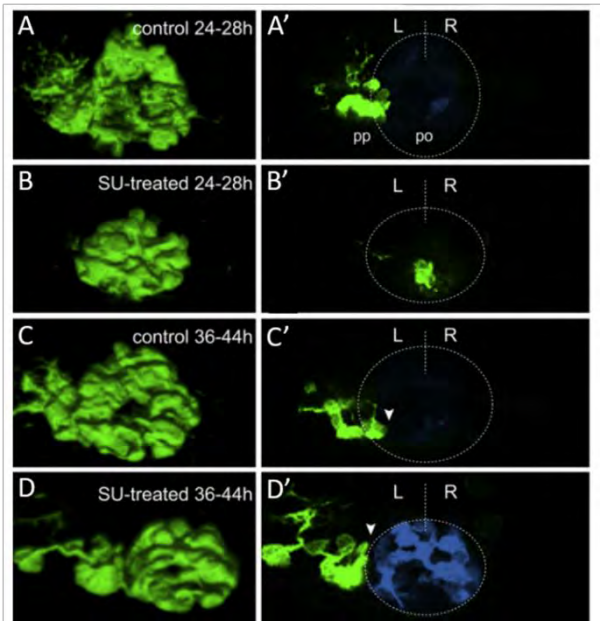

Figure 39 : Effet de l'inactivation de la voie Fgf a différentes fenêtres temporelles sur la migration la parapinéale. (A-D) Reconstitutions 3D et (A'-D') coupe optique de vues dorsales de l'épithalamus chez des embryons Tg(foxD3:GFP) traités au DMSO (A, A', C et C') et au SU5402 (B, B', D et D') à 4 jours post-fécondation. Antérieur vers le haut. Les cellules pinéales apparaissent en bleu. Lignes pointillées = pinéale et ligne médiane (A'-D'). Le traitement au SU5402 à 24-28 hpf (A-B') et à 36-44 hpf (C-D') aboli la translocation de la parapinéale vers des positions ventrales et médianes de la pinéale, et restent à des positions dorso-latérales.([D et D'], pointes de flèches blanches). L, gauche ; R, droite. (Regan et al., 2009).

Enfin, l'utilisation d'un rapporteur transgénique de l'activité de la voie Fgf, Tg*(dusp6 :d2EGFP)*^{pt6} a montré que la voie Fgf était active dans les cellules situées à l'extrémité menant le mouvement de migration, du stade 26 hpf à 36 hpf. L'activation localisée de la voie Fgf dans ces cellules chez le mutant *fgf8*$^{-/-}$, permet de restaurer la migration, ce qui montre que la voie Fgf est nécessaire et suffisante pour la migration de l'organe. (Roussigné et al., 2018). Dans le cas de l'inhibition de composant de la voie Nodal, la voie Fgf perd son activité spécifique dans les cellules menant le mouvement de migration. La voie Nodal est donc nécessaire pour la restriction de l'activité de la voie Fgf (Roussigné et al., 2018) mais elle intervient également dans la régulation du nombre de cellules de la parapinéale avant sa migration. L'inactivation de l'expression de *Pitx2c* à ce stade induit une augmentation du nombre de cellules de la parapinéale et le traitement au SB431542 de ces embryons traités, rétablit le nombre normal de cellules de la parapinéale (Garric et al., 2014). (Figure 40).

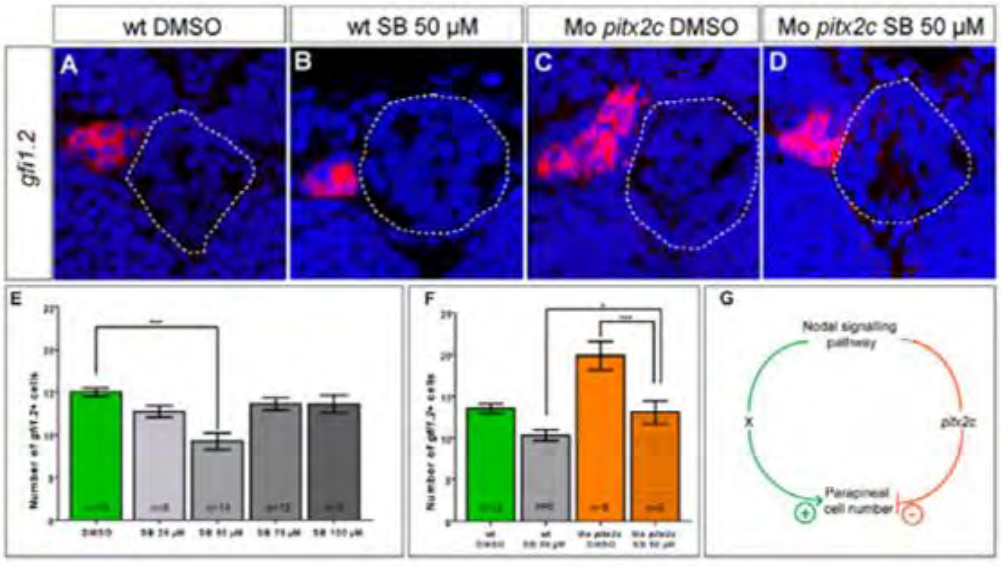

Figure 40 : la régulation du nombre de cellules de la parapinéale sont sous le contrôle de la voie Nodal. (A-D) Coupe optique du complexe pinéal montrant l'expression de *gfi1.2* chez des embryons traités au DMSO (A), traités par 50 µM de SB431542 (B), traités au DMSO/Mo *pitx2c* (C) et traités par 50 µM de SB431542/Mo *pitx2c* (D) à 72 hpf. Ligne pointillée = pinéale. (E) Comptage des cellules exprimant *gfi1.2* dans les embryons traités au DMSO ou au SB431542. Le nombre de cellules *gfi1.2*$^{+}$ est significativement diminué seulement chez les embryons traités avec 50 µM de SB431542 ; ***P<0,0,001 en utilisant un test t. barres d'erreur = SEM. (F) Comptage des cellules exprimant *gfi1.2* dans les embryons traités au DMSO et au SB431542 et injectés avec le *Mo pitx2c*. Augmentation du nombre de cellules de la parapinéale seulement chez les embryons traités au DMSO et Mo *pitx2c*; *P<0,05, ***P<0,0,001 en utilisant un test t .barres d'erreur = SEM. (G) Modèle de l'antagonisme entre Nodal et Pitx2c. La voie Nodal active l'expression de Pitx2c qui limite ensuite le nombre de cellules de la parapinéale. En parallèle, une seconde cible de la signalisation de Nodal (X) favorise une augmentation du nombre de cellules de la parapinéale. (Garric et al., 2014).

La voie de signalisation Notch, intervient dans la régulation du nombre de cellules de la parapinéale et sa migration. Chez le mutant *mib*^{ta52b}, chez qui la voie Notch est inactivée, la voie Fgf est active dans un plus grand nombre de cellules de la parapinéale que chez les individus sauvages et au stade 32hpf, la migration de la parapinéale n'a pas lieu. La voie Notch est donc nécessaire pour limiter l'activation de la voie Fgf dans les cellules de la parapinéale et dans la migration de la parapinéale mais ces deux rôles sont indépendants l'un de l'autre (Wei, Blader, & Roussigné, 2019).

II-2-3-c. Rôle dans la formation des asymétries habénulaires

Plusieurs approches démontrent que la migration de la parapinéale est nécessaire à la formation des asymétries habénulaires. Des expériences d'ablation de la parapinéale conduisent à un isomérisme droit (Figure 41)(Gamse, 2003). Le même phénotype est observé chez des

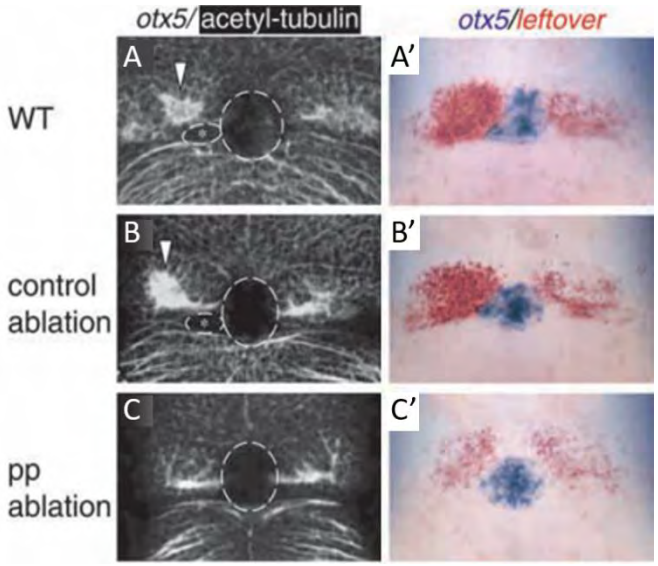

Figure 41 : La migration à gauche de la parapinéale est indispensable à la formation des asymétries habénulaires. (A,B,C) Immunomarquage de la tubuline acétylée (blanc) et (A',B',C') expression des marqueurs diencéphaliques *otx5* et *kct12.2* à 4 jours post-fécondation après ablation de la parapinéale (pp) ou controlatérale (contrôle) à 28-32h. L'ablation de la parapinéale a été confirmée par l'absence du domaine parapinéal *otx5*$^{+}$, et entraine (C) l'absence de neuropile dense dans l'habenula gauche et d'asymétrie du profil d'expression de *kctd12.2* (C'). (n=12/12). (Gamse et al. 2003).

mutants affectant la migration ou la différenciation de la parapinéale. Un mutant particulièrement intéressant est le mutant pour le gène sox1a , qui est exprimé dans la parapinéale des stades 20 hpf à 28 hpf. Chez ces derniers, la parapinéale est présente et sa migration vers la gauche a bien lieu. Un isomérisme droit des habénulas est néanmoins observé. Ces données ont suggéré que l'identité de Hbd gauche est induite par un signal sécrété provenant de la parapinéale sous le contrôle de l'expression de sox1a. (Faro, Nicolaou, Lekk, Blader, & Wilson, 2019).

En revanche, l'ablation de l'organe parapinéal n'affecte pas l'asymétrie d'initiation de la différenciation neuronale à gauche, qui précède le début de la migration de l'organe parapinéal. (Roussigne et al., 2009)(Figure 42).

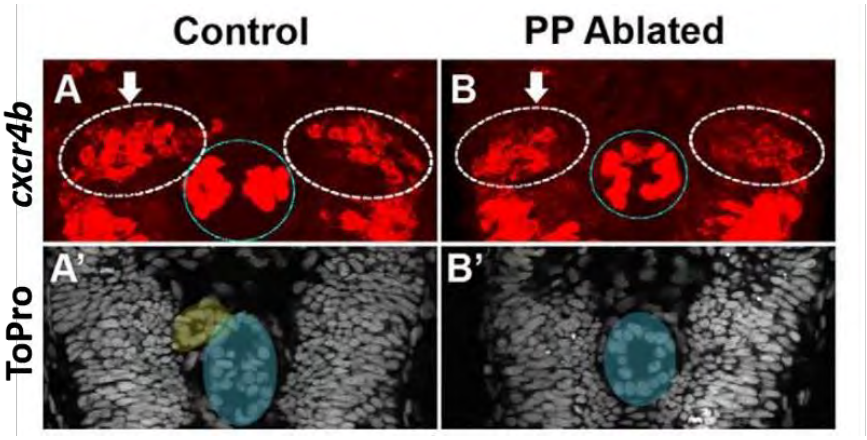

Figure 42 : Indépendance de l'asymétrie gauche d'initiation de la différenciation neuronale de la migration de la parapinéale. (A,B) Projection confocale d'immunohistochimie contre Elavl3/4 chez des embryons de poisson zèbre sans (A) et avec (B) ablation de la parapinéale à 36-38 hpf. Les flèches indiquent l'habenula avec le plus grand nombre de neurones HuC/D^{+}. Ligne blanche pointillée = Hb, ligne bleue = épiphyse. (A',B') Coloration nucléaire au ToPro des embryons en A,B révèle la parapinéale chez le témoin (jaune) mais pas chez l'embryon avec ablation; l'épiphyse apparaît en bleu (Roussigne et al., 2009).

II-2-4. Asymétries de la différenciation neuronale

II-2-4-a. Régulation temporelle asymétrique de la neurogenèse des territoires Hbdl et Hbdm

Comme indiqué ci-dessus, les asymétries habénulaires consistent en une différence de proportion relative entre la gauche et la droite des deux subdivisions Hbdl et Hbdm de l'Hbd. (voir I.3). (Figure 43).

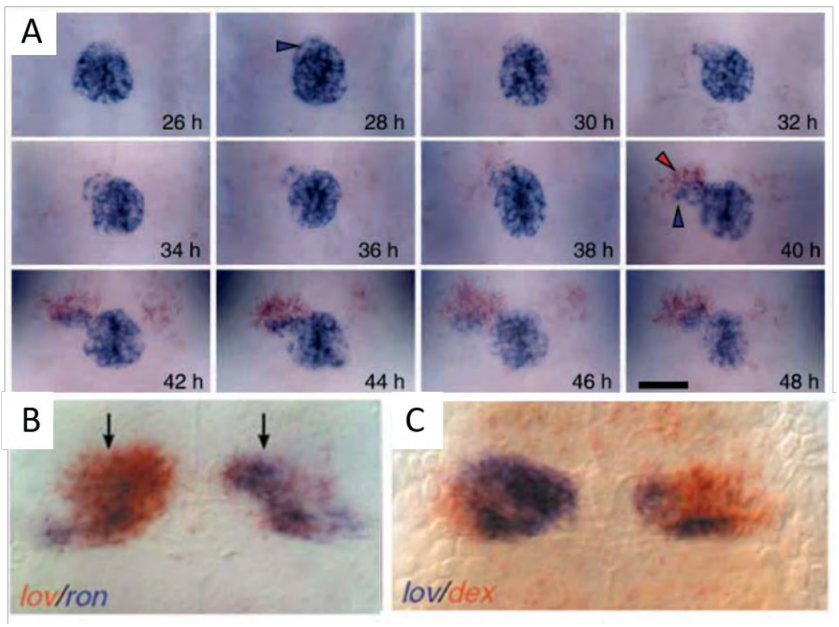

Figure 43 : Etablissement de l'expression asymétrique de *kctd12.1, kctd12.2* et *kctd8*. (A) Expression de *otx5* (bleu) et de *kctd12.1* (orange) dans des embryons type sauvage aux moments indiqués après la fécondation. (B) Double hybridation in situ montrant l'expression de *kctd12.1* (*ex-lov*, orange) et *kctd12.2* (*ex-ron,*bleu). (C) L'expression habénulaire de *kctd8* (*ex-dex*,orange) recouvrant partiellement celle de *kctd12.1* (bleu). B et C sont des vues dorsales avec l'antérieur orienté vers le haut. (Gamse et al., 2005a).

Les progéniteurs de ces deux populations de neurones sortent des cycles mitotiques avec une chronologie différente. Ce résultat a été obtenu par des expériences d'incorporation de l'analogue nucléotidique BrdU de type "pulse-chase" chez une lignée de poisson-zèbre exprimant une protéine Pou4f1 fluorescente (marqueur de l'Hbdm). Les cellules l'Hbdl sont préférentiellement observées à gauche et sortent des cycles mitotiques plus précocément (dès le stade 24hpf) que les cellules de l'Hbdm, préférentiellement observées à droite, à partir du stade 32hpf seulement (Aizawa et al., 2007). (Figure 44).

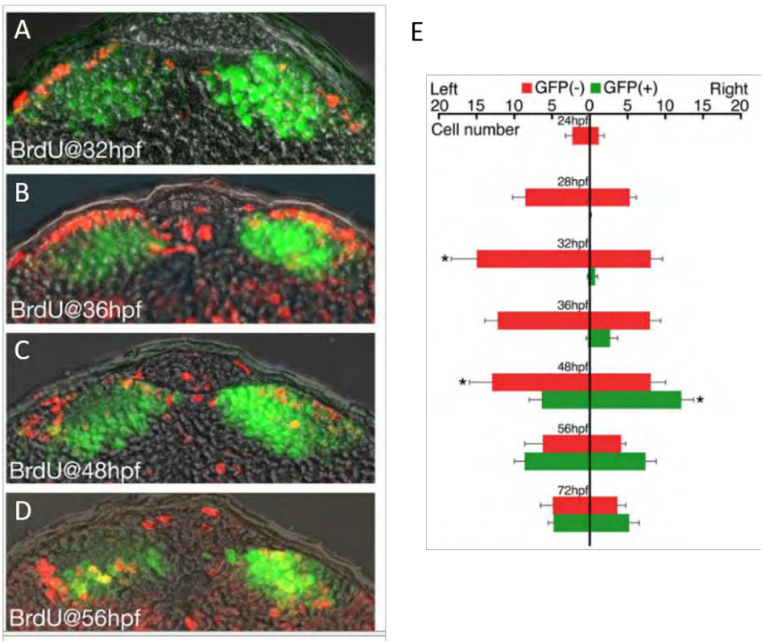

Figure 44 : Régulation temporelle asymétrique des choix de destins cellulaires de l'Hbdl et Hbdm. (A-D) Coupes transversales des habenulas montrant la distribution des cellules marquées par pulse au BrdU (rouge) et GFP (vert) chez les poissons transgéniques Tg(brn3a- hsp70:GFP)^{rw0110b} de 5 jours post-fécondation. (E) Changements dans le nombre de cellules marquées au BrdU dans HbG et HbD des poissons Tg(brn3a-hsp70:GFP)rw0110b après le pulse au BrdU jusqu'au stade 5 jours post-fécondation. (Aizawa, Goto, Sato, & Okamoto, 2007).

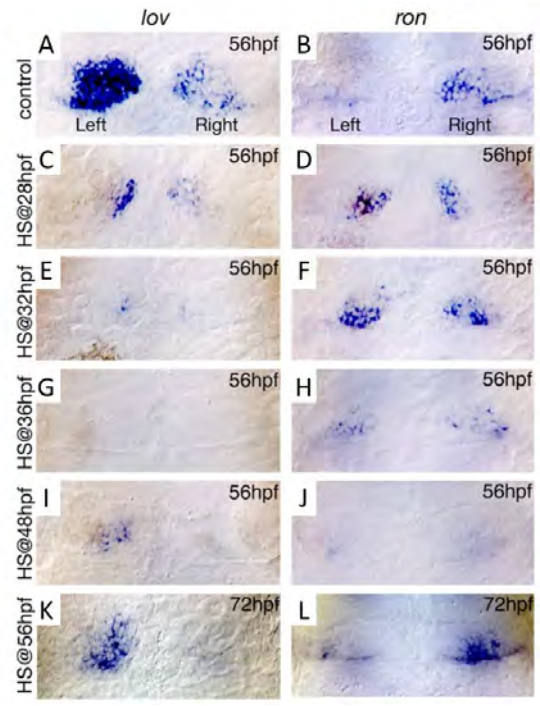

Figure 45 : Effet du retard de sortie des cycles mitotiques sur la régulation temporelle asymétrique des choix de destins cellulaires. Vues dorsales d'embryons de type sauvage (A-B) et notch1a $^{-/-}$ |Tg(hsp70:gal4)kca4;Tg(UAS : myc-notch1a-intra)kca3] (C-J) à 56 hpf (A-J) et 72 hpf (K-L) montrant l'expression de l'ARNm de *ktc12.1*, *kctd12.2* dans les habenulae. HS, stade auquel le choc thermique a été appliqué aux embryons. (Aizawa, Goto, Sato, & Okamoto, 2007).

La voie Notch, qui promeut la neurogenèse, modifie les asymétries, ce qui soutient l'hypothèse d'une implication de cette régulation temporelle dans leur formation (Figure 45).

II.2.4.b. Rôle de la voie Wnt dans le choix de différenciation neuronale Hbdl -Hbdm

L'analyse des mutants *tcf7l2-/-* montre que la voie Wnt est nécessaire à la formation des asymétries habénulaires et qu'elle promeut le choix d'identité Hbm versus dHbl. Les embryons mutants pour ce gène présentent en effet un isomérisme gauche au niveau des habénulas. Cette fonction agit de façon cellule autonome et le phénotype est indépendant de la migration de la parapinéale, indiquant que la voie agit en aval de ce processus (Figure 46). L'ensemble de ces données suggèrent que l'établissement des asymétries habénulaires chez le poisson-zèbre implique une répression à gauche de la voie Wnt, par un signal encore non identifié sécrété par la parapinéale. (Hüsken et al., 2014).

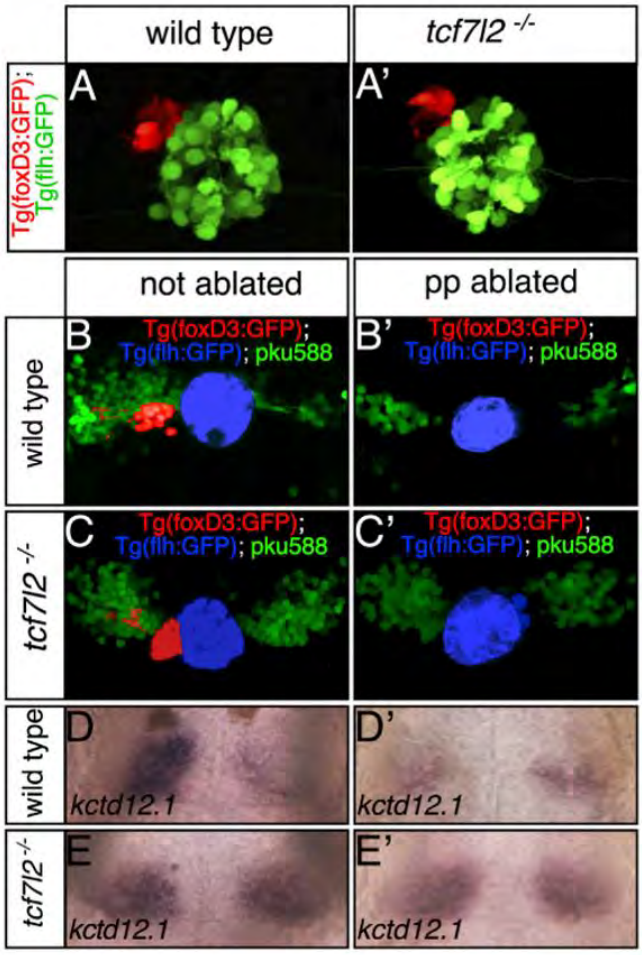

Figure 46 : La voie Wnt est nécessaire à l'établissement des asymétries habénulaires indépendamment de la migration de la parapinéale. Vues dorsales de l'épithalamus d'embryons de 2,5 (A et A') et de 4 jours post-fécondation (B-E'). (A et A') La parapinéale (rouge) est à gauche chez les embryons de type sauvage et les embryons mutants *tcf7l2*$^{-/-}$. (B-E') Dans les embryons triples transgéniques Et(gata2a:EGFP)pku588 ; Tg(foxD3:GFP) ; Tg(flh:eGFP) normaux et avec ablation de la parapinéale, les neurones dHbl (vert) et le complexe pinéal sont marqués. La pinéale est en bleu et la parapinéale et ses projections en rouge (B-C'). (D-E') L'expression de *kctd12.1* est observable sur les mêmes embryons que (B)-(C'). (Hüsken et al., 2014).

Au niveau cellulaire, le rôle de la voie Wnt pourrait passer par une régulation de la chronologie de la neurogenèse. L'activité de la voie Wnt est détectable dès le stade 22 hpf dans les cellules du diencéphale. Son activation à l'aide de traitement pharmacologique avant le stade 28hpf dans les cellules habénulaires, retardent l'initiation de la différenciation. Des expériences de perte de fonction de *wif1* (*Wnt inhibitory factor 1*), un inhibiteur de la voie Wnt, au stade 28hpf provoque également un retard d'initiation de la différenciation, ce qui montre que la répression de la voie Wnt dans les cellules habénulaires avant le stade 28hpf est sous le contrôle de *wif1*. *wif1* est donc nécessaire pour la différenciation des cellules en cellules de l'Hbdl. (Guglielmi et al., 2020).

III. Le modèle roussette dans l'étude des mécanismes de formation des asymétries habénulaires

III-1. Intérêts des chondrichtyens

III-1-a. Position phylogénétique

L'intérêt des chondrichtyens pour comprendre l'évolution des vertébrés tient d'abord et avant tout à leur position phylogénétique, en tant que groupe frère des ostéichthyens. En effet, tous les organismes modèles établis des vertébrés, et notamment les organismes génétiques (souris, poisson-zèbre) appartiennent aux ostéichtyens. L'étude d'un groupe externe est indispensable pour inférer l'état ancestral chez les gnathostomes, particulièrement importante pour pouvoir polariser des caractères quand ceux-ci divergent entre actinoptérygiens et sarcoptérygiens (Figure 47) (Coolen et al., 2008). Il s'agit donc de modèles importants pour les études de type évolution-développement.

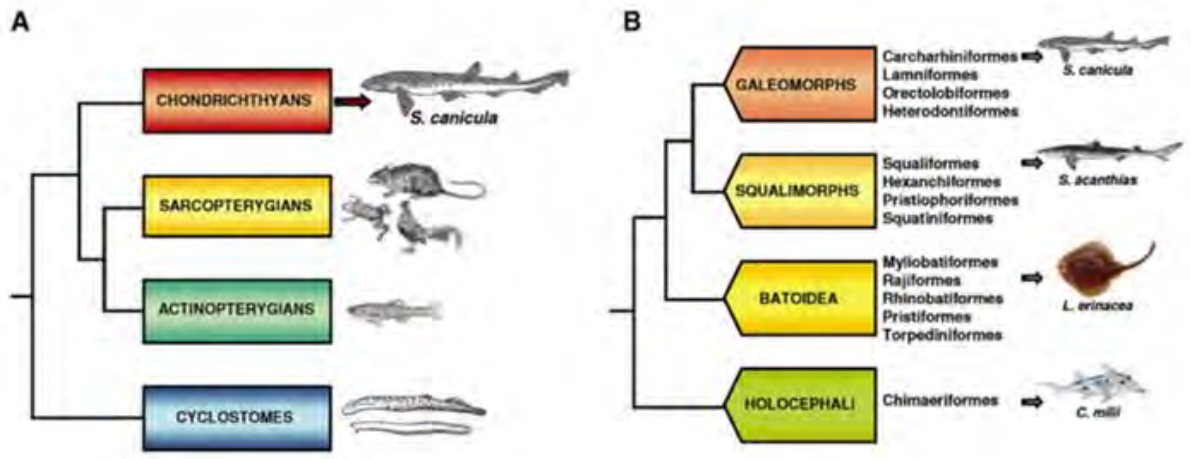

Figure 47 : Position de *S.canicula* chez les gnathostomes et les chondrichtyens. Position phylogénétique de la roussette parmi les vertébrés à mâchoires (A) et au sein des chondrichtyens (B). (A) Les chondrichtyens constituent le groupe frère des ostéichtyens (sarcoptérygiens et actinoptérygiens), un groupe comprenant les modèles vertébrés habituels (souris, grenouille, poussin). (B) Les modèles de chondrichtyens les plus couramment étudiés fournissent un bon échantillonnage phylogénétique du groupe. Les positions relatives des principaux groupes de chondrichtyens sont indiquées. (Coolen et al., 2008).

III-1-b. Outils génomiques

L'intérêt des génomes de chondrichtyens est qu'ils ont subi les duplications 2R qui ont eu lieu à l'origine des vertébrés, sans les polyploïdisations supplémentaires qui sont intervenues par exemple chez les téléostéens. Il est donc facile de résoudre les relations d'orthologie au sein des familles de gènes. Une difficulté pour le séquençage de leurs génomes a été leur taille généralement très élevée dans le groupe. Cette limitation a été aujourd'hui levée grâce à l'évolution des techniques de séquençage, et à ce jour, plusieurs génomes de chondrichtyens ont été séquencés outre celui de la roussette (Cf III.2). Le premier à avoir été entièrement séquencé est celui de la chimère (*C.milii*), un membre de la sous-classe des holocéphales, en raison de la petite taille de son génome (0.9Gb). Le

génome actuellement disponible est de haute continuité (N50 = 46.6kbp) mais de faible couverture (1.4x). (Venkatesh et al., 2007, 2014). On dispose également des séquences des génomes de *S.* torazame, la roussette japonaise aussi nommée « cloudy catshark », de *C. punctatum*, le requin chabot-bambou, de *R. typus*, le requin baleine , de *C. carcharias,* le requin blanc et de la petite raie *R. erinacea* (Hara et al., 2018; Marra et al., 2019; Wang et al., 2012). Ces séquences sont de continuité et de couverture variables mais certains génomes sont de continuité élevée. La disponibilité de ces génomes ouvre de nouvelles perspectives pour l'étude des chondrichtyens par des approches transcriptomiques ou épigénomiques.

III-1-c. Thèmes étudiés

Les études chez les chondrichtyens se sont principalement centrées soit sur des caractéristiques morphologiques qui leur sont spécifiques, soit sur des caractères des gnathostomes afin de préciser leur origine, soit encore sur des processus pour l'étude desquels ils fournissent un modèle pertinent. En ce qui concerne les premiers, les études se sont par exemple centrées sur la formation des ampoules de Lorenzini (Freitas, Zhang, Albert, Evans, & Cohn, 2006), le mécanisme très particulier de régénération des dents et denticules (Martin et al., 2016), l'apparition et l'évolution du système immunitaire adaptatif (Criscitiello, 2014). Les réseaux génétiques ancestraux contrôlant la formation des caractères morphologiques des gnathostomes ont été étudiés pour mieux comprendre l'apparition des appendices pairs (Tanaka et al., 2002)(Freitas, Zhang, & Cohn, 2007) ou de la mâchoire (Depew & Simpson, 2006), la minéralisation du squelette (Debiais-Thibaud et al., 2019), l'organisation en sous-domaines du cerveau (Rodríguez-Moldes, 2009) ou encore la spécification de l'axe embryonnaire (Coolen et al., 2007). Les chondrichtyens fournissent également des modèles pertinents pour l'étude de la formation des tissus extra-embryonnaires (Godard et al., 2014). A cela, s'ajoutent des études visant à mieux comprendre l'origine et l'évolution des systèmes physiologiques : le contrôle hormonal de la reproduction (Gaillard et al., 2018), le métabolisme du glucose, la physiologie du cœur et des muscles (Park-Holohan et al., 2012; Thébault et al., 2005) ou la nature des neurotransmetteurs du SNC (Adrio et al., 2000; Carrera, Molist, Anadón, & Rodríguez-Moldes, 2008; Rodríguez-Moldes et al., 2008).

III-2. Le modèle roussette

III-2-a. Biologie de l'espèce

La petite roussette est une espèce que l'on trouve dans le nord de l'océan Atlantique, le long des côtes européennes, de la Norvège au Sénégal, ainsi que dans la mer Méditerranée et au sud de la côte d'Ivoire, à 100 mètres de profondeurs environ (Compagno, 1966). Cette espèce est ovipare, et les femelles possèdent des spermathèques, ce qui leur permet de pondre au maximum 2 œufs tous les 15 jours pendant une période d'au moins 6 mois après accouplement. Une population de femelles adultes peut être maintenue en aquarium et les œufs peuvent être récupérés de cette manière pendant plusieurs mois. L'embryon de roussette se développe pendant environ 4 mois à 16°C avant éclosion. Les stades de développement de l'embryon de roussette ont été caractérisés. (Ballard, Mellinger, & Lechenault, 1993). (Figure 48).

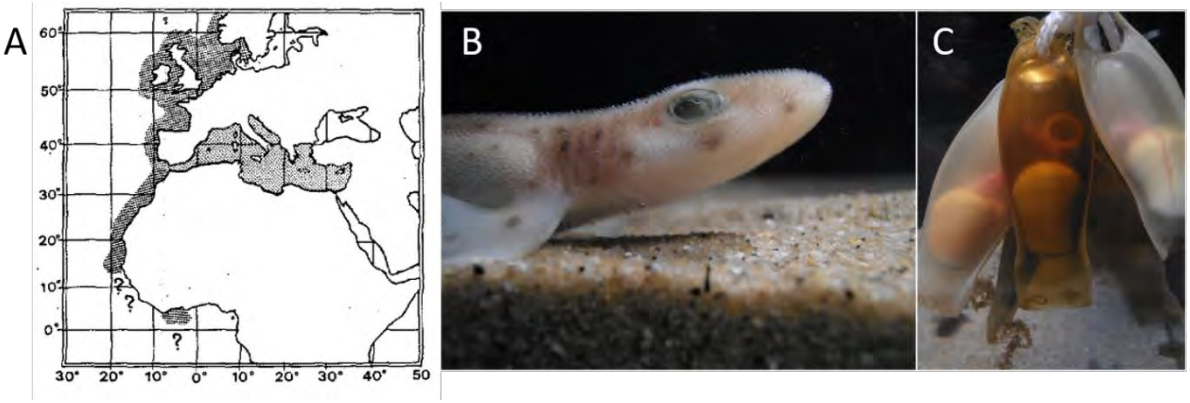

Figure 48 : Habitat de *S.canicula,* stade juvénile et embryons dans l'oeuf. (A) cartographie des côtes européennes et africaines où vit la petite roussette (champ grisé). (B) Photo d'une petite roussette juvénile. (C) Photo d'embryons de roussettes aux stades 30-31 dans leurs œufs.

III-2-b. Ressources génomiques et transcriptomiques

Les outils génomiques disponibles chez la roussette ont connu une avancée considérable au cours des 5 dernières années. Une avancée majeure a été permise par l'acceptation en 2019 d'un projet de séquençage génomique à haute continuité par le Sanger Institute. Ce projet a permis l'obtention d'un génome annoté de très haute continuité (717 scaffolds ; N50 de 198 Mb).

De nombreuses données transcriptomiques, obtenues à partir de tissus adultes ou stades embryonnaires variés, sont également disponibles.

III-2-c. Approches expérimentales

Plusieurs outils expérimentaux sont utilisés en routine chez la roussette. Les marquages histologiques mais aussi les techniques d'immunohistochimie et d'hybridation in situ sont utilisés depuis de nombreuses années chez cette espèce, que ce soit sur l'embryon entier ou sur des coupes histologiques selon le stade. Le développement des embryons dans des œufs permet d'utiliser ces derniers en tant que chambre d'incubation pour des traitements pharmacologiques et des approches par application de billes imprégnées sont également réalisables aux stades où l'embryon peut se développer en-dehors de la coque (à partir du stade 26). J'ai également réalisé des analyses impliquant l'incorporation de BrdU (essais de type "pulse" ou "pulse-chase"; Cf chapitres 2 et 3). Des approches de type scRNA-seq et ATAC-seq impliquant notre équipe sont également en cours, en collaboration avec plusieurs équipes (J. Tena, Séville, H. Kaessman, Heidelberg).

III-3 Intérêt du modèle roussette dans l'étude du développement des asymétries habénulaires

III-3-a. Asymétries habénulaires chez la roussette

La roussette apparaissait, a priori, un modèle d'intérêt pour l'étude des asymétries épithalamiques non seulement du fait de sa position phylogénétique mais également du fait de la différence de taille très marquée entre les habénulas droite et gauche. Cette asymétrie en taille apparaît en outre au cours de l'embryogenèse, dès le stade 31 (environ 2 mois après fécondation). La réalisation d'études d'expression ciblées sur les gènes de la famille *Kctd* a confirmé l'existence de ces asymétries. En effet, les orthologues *ScKctd8* et *ScKctd12b* (orthologue de *DrKctd8* et *DrKctd12.1*) chez la roussette présentent des expressions bilatérales mais très asymétriques dans les habénulas, avec un territoire d'expression dans l'habénulas gauche plus étendu que dans l'habénula droite. Le gène *ScKctd12a* (orthologue de *DrKctd12.2*) présente une expression restreinte à gauche. Un autre marqueur asymétrique identifié par le laboratoire est la forme phosphorylée de Erk (P-Erk), exprimée sélectivement à droite (Lagadec et al., 2015). (Figure 49 et 50).

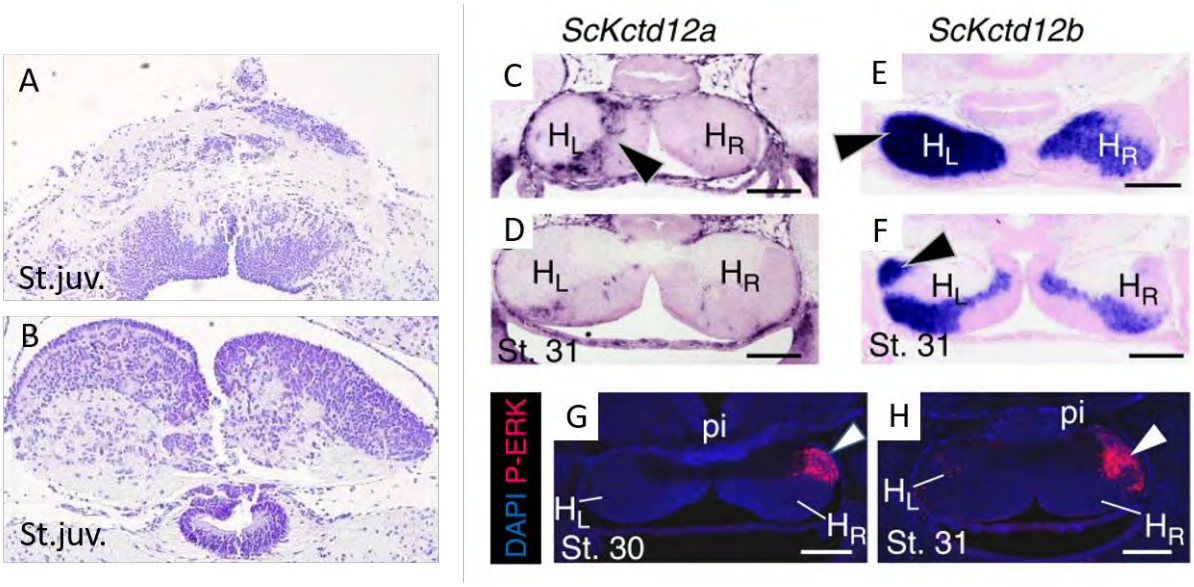

Figure 49 : Asymétries morphologiques et moléculaires chez la roussette. (A) Coloration histologique d'un plan transverse (A) et horizontal (B) de coupes d'habénulas de la petite roussette au stade juvénile. (C-F) Hybridation *in situ* de *ScKctd12a* (C-D) et *ScKctd12b* (E-F) sur des coupes transverses antérieures (C-E) et médianes (D-F) d'habénulas au stade 31. (G-H) Immunohistochimie contre P-Erk (rouge) aux stades 30 (G) et 31 (H) sur des coupes transverses d'habénulas. (Lagadec et al., 2015).

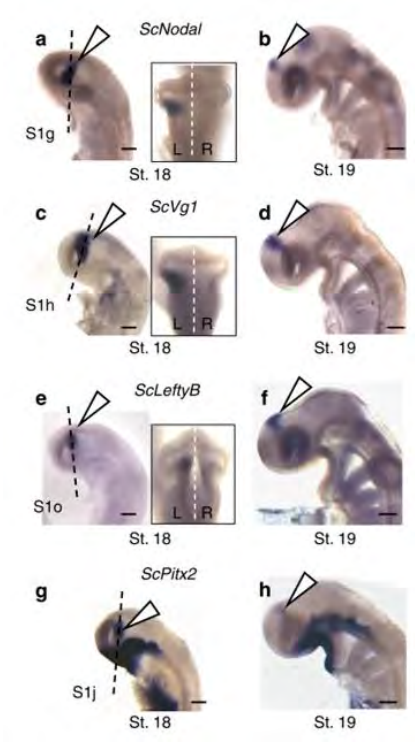

Figure 50 : Expression asymétrique gauche de la cascade de signalisation *nodal-lefty-pitx* chez la roussette. (a-h) Représentation de vues latérales gauches d'embryons de catshark après hybridation avec les sondes *ScNodal* (a,b), *ScVg1* (c,d), *ScLeftyB* (e,f) et *ScPitx2* (g,h). (a,c,e,g) et (b,d,f,h) montrent des embryons de stade 18 et 19, respectivement. Les encarts montrent des vues dorsales de la région de la tête des embryons présentés en (a,c,e), confirmant l'expression diencéphalique restreinte à gauche de chaque gène. (Lagadec et al., 2015).

III-3-b. Comparaison des mécanismes avec le poisson-zèbre

L'étude des mécanismes impliqués, ciblée dans un premier temps sur la voie Nodal, a confirmé l'intérêt de la roussette. Celle-ci partage avec le poisson-zèbre une fenêtre asymétrique d'activité de la voie Nodal, peu après la fermeture du tube neural (Figure 50). Toutefois, les asymétries habénulaires chez la roussette sont indépendantes de la migration de la parapinéale, contrairement au poisson-zèbre, puisque cet organe n'existe pas chez la roussette. De plus, la voie Nodal est indispensable à la formation des asymétries habénulaires chez la roussette, alors que chez le poisson-zèbre, elle n'impacte que la latéralité des asymétries hormis la première asymétrie gauche d'asymétrie (Lagadec et al., 2015). Des traitements pharmacologiques dirigés contre la voie de signalisation Nodal au stade 15-16, avant l'initiation de l'expression asymétrique gauche de Pitx2 dans le système nerveux central conduisent en effet à un isomérisme droit des habénulas chez la roussette (Figure 51). Ce rôle de la voie Nodal pourrait refléter l'état ancestral des vertébrés, puisqu'il est partagé par la lamproie.

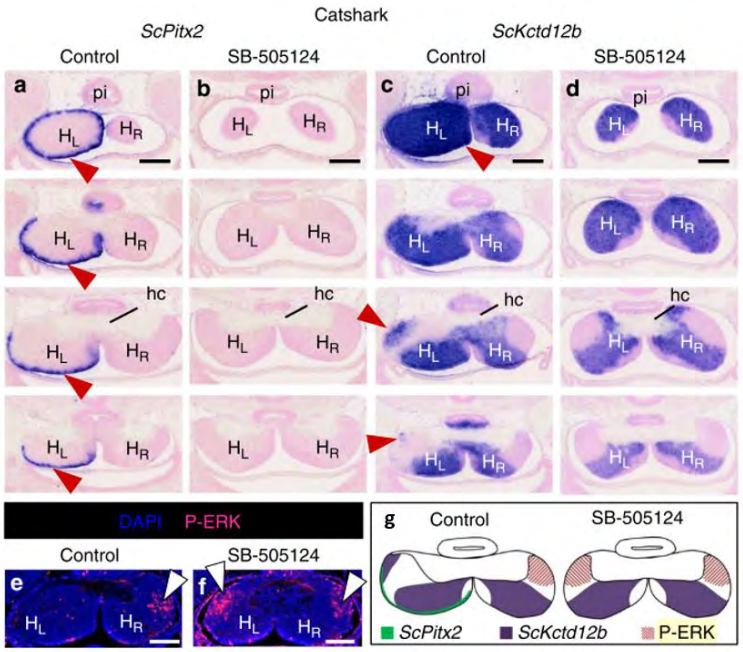

Figure 51 : L'inhibition de la voie Nodal induit un isomérisme droit des habénulas chez la roussette. (a-f)Coupes transversales d'embryons contrôles de stade 31 (a,c,e) et d'embryons traités au SB-505124 (b,d,f), après hybridation avec les sondes *ScPitx2* (a,b) et *ScKctd12b* (c,d), ou après immunohistochimie à l'aide d'un anticorps dirigé contre φ-ERK (e,f). Dans (a-d), des plans de coupes successifs sont montrés du niveau antérieur au niveau postérieur. (e,f) sections à un niveau médian. Les pointes de flèches rouges dans (a,c) indiquent l'expression gauche présente dans les embryons témoins mais perdus dans les embryons traités au SB-505124. Les pointes de flèches blanches en (e) indiquent les signaux P-ERK, limités à la droite chez les embryons non traités ou injectés au DMSO, mais présents des deux côtés chez les embryons traités au SB-505124 (f). Une différence de taille est observée entre les habenulae gauche et droite aux niveaux antérieurs (plus grande à gauche) chez les embryons témoins. Les embryons traités présentent une réduction de la taille de l'habenula gauche. (Lagadec et al., 2015).

III-4 Objectifs du travail

L'objectif de mon travail de thèse a tout d'abord été d'étendre la caractérisation des asymétries dans les habénulas embryonnaire de roussette. Mon étude a été centrée sur (1) la recherche d'asymétries neurogénétiques (chapitre I) et (2) l'organisation en sous-domaines des habénulas en utilisant une approche transcriptomique non biaisée (chapitre II). J'ai ensuite cherché à évaluer la conservation de cette organisation et des asymétries détectées chez la roussette chez un échantillonnage large de gnathostomes et à préciser les mécanismes impliqués (chapitre II). Une troisième partie de mon travail a été une contribution à une caractérisation transcriptomique en 3D du cerveau embryonnaire de roussette, qui sera utilisée pour rechercher des gènes candidats cibles de la voie Nodal pendant sa fenêtre d'activité diencéphalique gauche, peu après la fermeture du tube neural (chapitre III).

CHAPITRE I - Description des asymétries neurogénétiques au cours du développement des habénulas chez la roussette

I-1. Objectif, principaux résultats et conclusions

Ce travail était engagé lors de mon arrivée au laboratoire et je l'ai poursuivi en collaboration étroite avec R. Lagadec (IR CNRS) lors de mon Mastère et de ma première année de thèse. Son objectif était de caractériser la neurogénèse au cours du développement des habénulas chez la roussette, afin de rechercher la présence d'asymétries neurogénétiques. De telles asymétries ont en effet été décrites chez le poisson-zèbre, sous le contrôle de la voie Nodal. Pour cela, j'ai pris part à une étude des patrons de prolifération-différenciation par des approches immunohistochimiques et par hybridation in situ, à l'aide de marqueurs de progéniteurs neuraux et de marqueurs de différenciation neuronale précoce. J'ai également participé à la quantification du taux de prolifération par incorporation de l'analogue nucléotidique BrdU. Enfin nous avons évalué la présence d'asymétries de l'apoptose. Ce travail nous a permis de démontrer la présence d'asymétries neurogénétiques très marquées au cours du développement des habénulas de roussette, listées ci-dessous.

(1) Une initiation gauche de la différenciation neuronale est observée chez la roussette, comme c'est le cas chez le poisson-zèbre.

(2) Nous avons identifié 2 territoires de progéniteurs neuronaux distincts, à la fois sur la base de leur organisation cellulaire et de leur chronologie d'apparition : un neuroépithélium pseudo-stratifié (PNE) localisé dans la région médiane des habénulas, qui régresse au cours de leur différenciation, et une population cellulaire qui apparaît plus tardivement dans la continuité du PNE, dans les régions latérales de la zone ventriculaire (LVZ).

(3) Le maintien de ces deux pools de progéniteurs est régulé de façon différentielle et asymétrique. Au stade 31, le PNE est ainsi plus étendu, et compte plus de cellules, à droite qu'à gauche. En revanche, dès le stade 29, la morphologie des progéniteurs de la LVZ est différente entre la droite et la gauche et les cellules sont plus nombreuses à gauche qu'à droite. Cette régulation asymétrique est sous le contrôle de la voie Nodal.

(4) Aucune asymétrie significative du taux de prolifération cellulaire n'est détectée, sauf, de façon transitoire, au niveau de la LVZ, au stade où elle s'individualise morphologiquement (stade 29). A ce stade, le taux de prolifération cellulaire est plus important à gauche qu'à droite.

Aucune indication d'asymétrie de l'apoptose n'a été identifiée, le nombre de cellules apoptotiques dans les habénulas embryonnaires étant quasi-nul aux stades étudiés.

Ces données démontrent l'existence d'asymétries neurogénétiques complexes au cours du développement des habénulas de roussette. La plupart sont démontrées pour la première fois chez un vertébré. Seule une initiation à gauche de la différenciation neuronale conservée chez la roussette, avait précédemment été mise en évidence chez le poisson-zèbre. Les modalités d'implication de ces asymétries neurogénétiques dans la génération d'asymétries en taille, très fortes chez la roussette, reste à évaluer. De même, si le maintien asymétrique des progéniteurs de la LVZ et du PNE est sous le contrôle de la voie Nodal, les réseaux génétiques et le détail des régulations impliqués restent à caractériser.

J'ai obtenu au cours de l'analyse transcriptomique décrite dans le chapitre 2 des données qui indiquent que l'identité moléculaire des progéniteurs (1) est différente entre la droite et la gauche, (2) est dynamique au cours du développement et (3) diffère entre la LVZ et le PNE (Figure ci-dessous). Ces

marqueurs pourraient constituer une base de départ d'études mécanistiques, par exemple par traitements pharmacologiques (Figure 52).

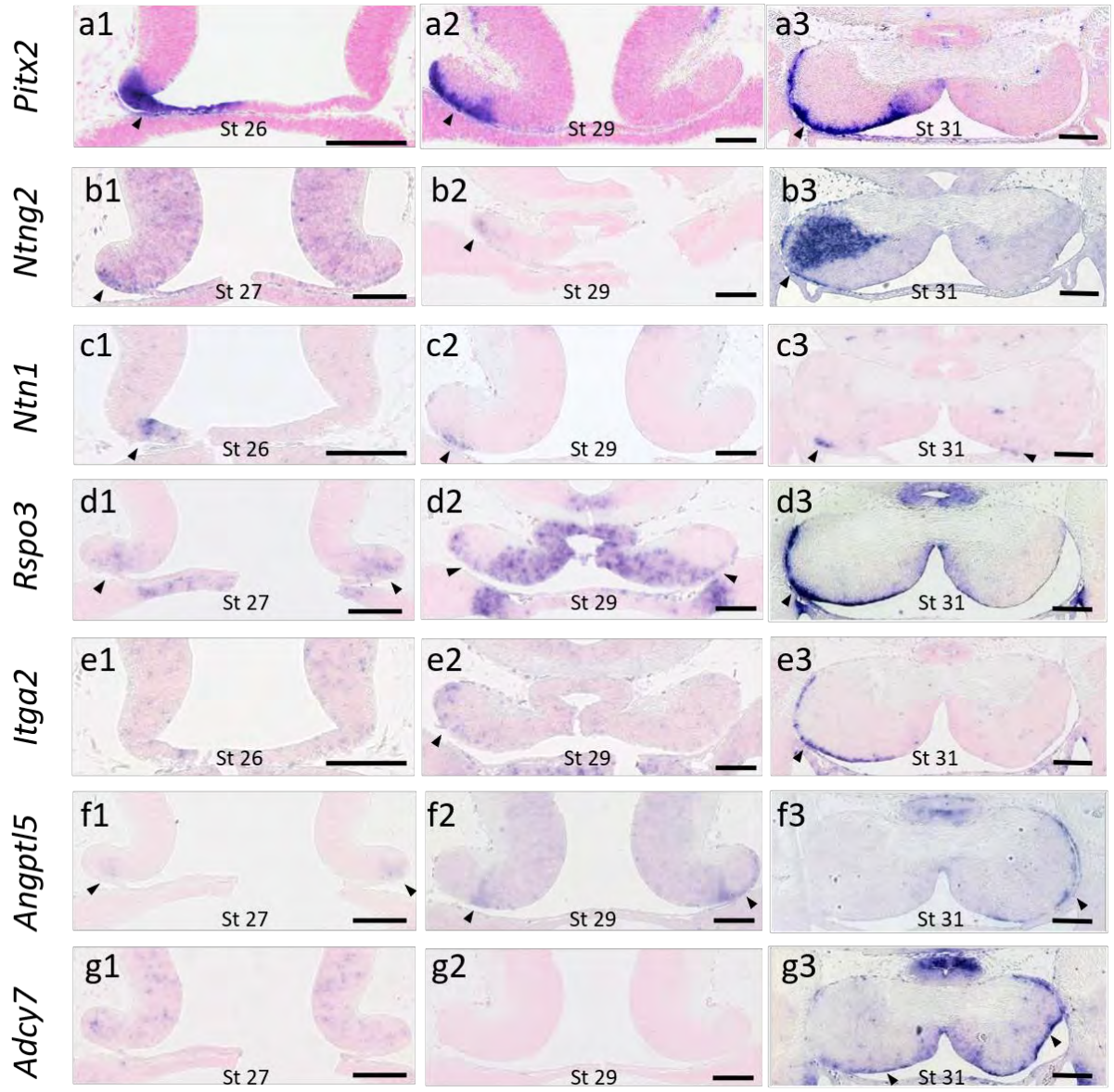

Figure 52 : Dynamique d'expressions asymétriques de marqueurs des territoires de progéniteurs habénulaires chez la roussette. **a-g**. Expression des gènes *Pitx2* (a), *Ntng2* (b), *Ntn1* (c), *Rspo3* (d), *Itga2* (e), *Angptl5* (f), *Adcy7* (g) au stades 26 (a1,c1,e1), 27 (b1, d1, f1, g1), 29 (a2-g2) et 31 (a3-g3) sur des sections transverses d'habénulas de roussette. Tous les marqueurs étudiés présentent des expressions asymétriques préférentiellement dans la LVZ gauche (*Pitx2, Ntng2, Ntn1, Rspo3, Itga2*) ou droite (Angptl*5, Adcy7*) au stade 31. A ce stade, l'expression de *Ntn1* est restreinte à la partie de la LVZ au voisinage immédiat du PNE. Une expression de *Pitx2* dans la partie la plus latérale du PNE est également visible. L'initiation d'expression de ces différents marqueurs s'effectue avec des chronologies différentes, dès les stades 26-27 pour *Pitx2, Ntng2, Ntn1, Rspo3* et *Angptl5*, à partir du stade 29 pour *Itga2* et du stade 30 pour *Adcy7*. Elles sont dynamiques: *R-Spo3* est ainsi exprimée de façon bilatérale dans le PNE jusqu'au stade 29 avant de se restreindre à la LVZ gauche; une expression de *Angptl5* est visible dans la zone latérale du PNE au stade 29 mais elle disparait ensuite, seule l'expression dans la LVZ droite étant maintenue. Les têtes flèches indiquent les expressions des gènes dans la LVZ et le PNE. Région dorsale en haut et gauche représentée à gauche à gauche. Barre d'échelle : 100µm.

I-2. Publication

Neurogenetic asymmetries in the catshark developing habenulae: mechanistic and evolutionary implications.

Ronan Lagadec[1], Maxence Lanoizelet[1], Nuria Sánchez-Farías[2], Fanny Hérard[1], Arnaud Menuet[3], Hélène Mayeur[4], Bernard Billoud[5], Isabel Rodriguez-Moldes[2], Eva Candal[2] & Sylvie Mazan[1]

[1]CNRS, Sorbonne Université, Biologie Intégrative des Organismes Marins, UMR7232, F66650, Banyuls-sur-Mer, France.

[2]Departmento de Bioloxía Funcional, Universidade de Santiago de Compostela, Santiago de Compostela, E 15782, Spain.

[3]CNRS Université d'Orléans, UMR7355, F45071, Orléans, France. 4CNRS, Sorbonne Université, Station Biologique, FR2424, F29680, Roscoff, France.

[5]CNRS, Sorbonne Université, Laboratoire de Biologie Intégrative des Modèles Marins, UMR8227, F29680, Roscoff, France.

SCIENTIFIC REPORTS

OPEN

Neurogenetic asymmetries in the catshark developing habenulae: mechanistic and evolutionary implications

Received: 20 October 2016
Accepted: 1 March 2018
Published online: 15 March 2018

Ronan Lagadec[1], Maxence Lanoizelet[1], Nuria Sánchez-Farías[2], Fanny Hérard[1], Arnaud Menuet[3], Hélène Mayeur[4], Bernard Billoud[5], Isabel Rodriguez-Moldes[2], Eva Candal[2] & Sylvie Mazan[1]

Analysis of the establishment of epithalamic asymmetry in two non-conventional model organisms, a cartilaginous fish and a lamprey, has suggested that an essential role of Nodal signalling, likely to be ancestral in vertebrates, may have been largely lost in zebrafish. In order to decipher the cellular mechanisms underlying this divergence, we have characterised neurogenetic asymmetries during habenular development in the catshark *Scyliorhinus canicula* and addressed the mechanism involved in this process. As in zebrafish, neuronal differentiation starts earlier on the left side in the catshark habenulae, suggesting the conservation of a temporal regulation of neurogenesis. At later stages, marked, Alk4/5/7 dependent, size asymmetries having no clear counterparts in zebrafish also develop in neural progenitor territories, with a larger size of the proliferative, pseudostratified neuroepithelium, in the right habenula relative to the left one, but a higher cell number on the left of a more lateral, later formed population of neural progenitors. These data show that mechanisms resulting in an asymmetric, preferential maintenance of neural progenitors act both in the left and the right habenulae, on different cell populations. Such mechanisms may provide a substrate for quantitative variations accounting for the variability in size and laterality of habenular asymmetries across vertebrates.

Epithalamic asymmetries provide an interesting model system to address the molecular and cellular bases for morphological variations across vertebrates. Asymmetries between the left and right habenulae, bilateral epithalamic structures, are widespread across vertebrates including humans[1,2], but with highly variable degrees in their magnitude. Analyses of the mechanisms involved in their formation in a teleost fish, the zebrafish[1,3,4], an agnathan, the lamprey *P. marinus*, and a cartilaginous fish, the catshark *S. canicula*[5], have highlighted a remarkable divergence between these three species. In the zebrafish, the formation of habenular asymmetries is strictly dependent on a secreted signal from the parapineal, a small group of neurons, which migrate from the dorsal midline to the left of the epithalamus and play an instructive role in the elaboration of left habenular identity[6]. Although a left sided Nodal activity is the first asymmetry observed in the developing diencephalon, inactivation of the pathway does not abolish habenular asymmetry formation and has only minor effects on their elaboration[3,6,7]. The catshark and lamprey share an early left restricted diencephalic Nodal activity with the zebrafish. However, no evidence for a conservation of a parapineal dependent mechanism can be found in these species and a pharmacological treatment abolishing the early window of Nodal activity also results in the loss of later habenular asymmetries[5].

Comparisons between the cellular mechanisms controlling habenular asymmetry formation in the catshark and lamprey with those dependent on the parapineal in the zebrafish, are essential to understand the molecular basis for this mechanistic divergence. In the latter, habenular asymmetries essentially consist in different size

[1]CNRS, Sorbonne Université, Biologie Intégrative des Organismes Marins, UMR7232, F66650, Banyuls-sur-Mer, France. [2]Departmento de Bioloxía Funcional, Universidade de Santiago de Compostela, Santiago de Compostela, E 15782, Spain. [3]CNRS Université d'Orléans, UMR7355, F45071, Orléans, France. [4]CNRS, Sorbonne Université, Station Biologique, FR2424, F29680, Roscoff, France. [5]CNRS, Sorbonne Université, Laboratoire de Biologie Intégrative des Modèles Marins, UMR8227, F29680, Roscoff, France. Ronan Lagadec and Maxence Lanoizelet contributed equally to this work. Correspondence and requests for materials should be addressed to S.M. (email: mazan@obs-banyuls.fr)

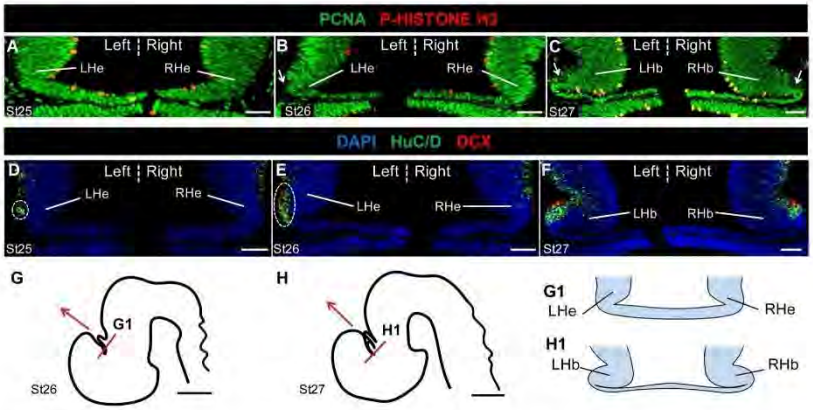

Figure 1. Early neuronal differentiation is asymmetric in the developing catshark habenulae. Transverse sections of catshark habenulae following IHC using antibodies against PCNA (**A**–**C**, green), PH3 (**A**–**C**, red), HuC/D (**D**–**F**, green) and DCX (**D**–**F**, red). DAPI stained nuclei are shown in blue in (**D**–**F**). (**G**,**H**) are schemes of the catshark embryonic brain (lateral views; **G**, stage 26; **H**, stage 27), with a red line indicating the location and plane of the sections analysed and a red arrow showing the antero-posterior axis (arrow pointing towards anterior). (G1,H1) show schemes of the habenula sections at the levels respectively indicated by the red line in (**G**,**H**). Stages are as indicated: (**A**,**D**), stage 25; (**B**,**E**), stage 26; (**C**,**F**) stage 27. White arrows in (**B**,**C**) point to lateral PCNA negative territories of habenular evaginations. Dotted circles in (**D**,**E**) highlight asymmetric HuC/D positive territories. Abbreviations: LHe and RHe, left and right habenular evaginations; LHb and RHb, left and right habenulae. Scale bars = 50 μm in (**A**–**F**), 500 μm in (**G**,**H**).

ratios between two domains of distinct neuronal identities (dHbm, or dorsal medial habenula, and dHbl, or dorsal lateral habenula). The cellular mechanism underlying this difference between the left and the right sides relies on a Wnt and parapineal dependent asymmetric regulation of the corresponding cell fate choices[8,9]. Despite the absence of major effects of Nodal inactivation on habenular asymmetry formation, both direct and indirect roles of the pathway have also been demonstrated in the zebrafish developing epithalamus. Neurogenesis is subject to an asymmetric temporal regulation during habenular development, with a Nodal dependent and parapineal independent delay of the onset of neuronal differentiation in the right habenula relative to the left one[9,10]. The contribution of this process to the establishment of final habenular asymmetries in the zebrafish remains unclear but this observation has led to the suggestion that an ancestral role of Nodal in epithalamic asymmetry formation may involve an asymmetric regulation of neurogenesis[5]. Nodal also regulates parapineal cell number, thus indirectly impacting the elaboration of habenular asymmetries[11]. Here, we show that neurogenesis and the maintenance of neural progenitors are subject to asymmetric regulations in the developing catshark habenulae and that these asymmetries are lost following a pharmacological treatment known to inhibit the early left restricted diencephalic Nodal activity. Unexpectedly, the effects observed differ depending on the progenitor pool considered, neural progenitors appearing preferentially maintained on the left side in a lateral territory, but on the right one in a more medial territory. These data shed light on asymmetrically regulated cellular processes in the catshark developing habenulae and prompt novel hypotheses to account for the variability of habenular size asymmetries across vertebrates.

Results

Early neuronal differentiation is asymmetric in the developing catshark habenulae. Catshark habenulae first become visible at stage 25 as two lateral diencephalic evaginations, which expand laterally at subsequent stages (Fig. 1A–F; Fig. S1A–D). To characterise the timing of neurogenesis in the catshark, we first analysed the distribution of proliferation markers, PCNA (proliferating cell nuclear antigen) and PH3 (phospho-histone H3), and neuronal differentiation markers, HuC/D (Hu antigens) and DCX (doublecortin), respectively expressed in post-mitotic and migrating neurons[12,13]. At stages 25 to 27, most cells in the habenular evaginations are positive for PCNA, except for a small number at the lateral tip of the organ from stage 26 onwards (Fig. 1A–C). Expression of HuC/D is first observed in the left habenular evagination at stage 25. No signal is present on the right at this stage (Fig. 1D). At stage 26, HuC/D and DCX expressions overlap in a broader lateral territory of the left habenula, while only a few expressing cells become visible on the right (Fig. 1E). At stage 27, these asymmetries are no longer detectable, HuC/D and DCX positive territories appear established in both developing habenulae, without obvious size difference (Fig. 1F). These data highlight an early, transient asymmetry of neuronal differentiation in the developing catshark habenulae, reminiscent of the unilateral, left presence of habenular neurons observed at the onset of neuronal differentiation in the zebrafish[9,10].

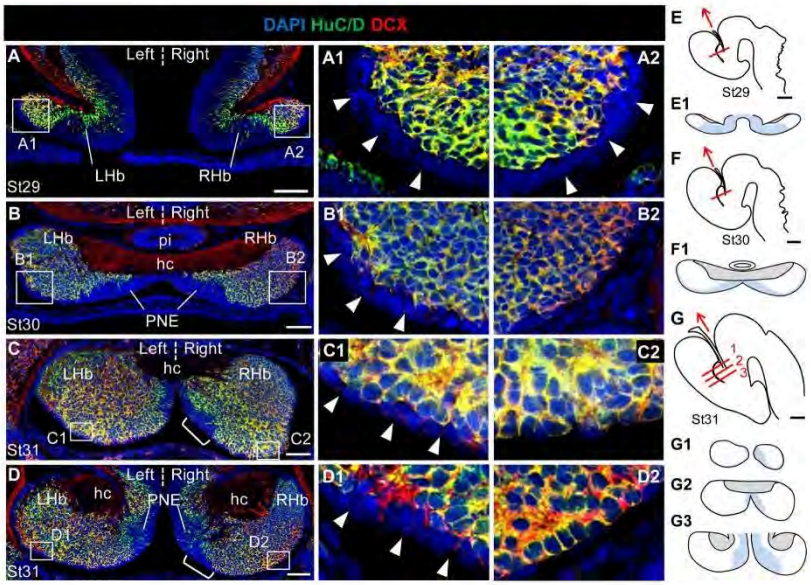

Figure 2. Neuronal differentiation in the LVZ is asymmetric. Transverse sections of catshark habenulae following IHC using antibodies against HuC/D (green) and DCX (red) at stages 29 (**A**), 30 (**B**) and 31 (**C**,**D**). DAPI stained nuclei are shown in blue. (**C**) and (**D**) are located at medial and posterior levels of the habenulae, respectively. (**E**–**G**) are schemes of the catshark embryonic brain (lateral views; **E**, stage 29; **F**, stage30; **G**, stage 31), with a red line indicating the location and plane of the sections analysed and a red arrow showing the antero-posterior axis (arrow pointing towards anterior). (**E1**,**F1**,**G1**-**3**) show schemes of the habenula sections at the levels respectively indicated by the red line in (**E**,**F**,**G**), with the proliferative neuroepithelium shaded in light blue. (**G1**), (**G2**) and (**G3**) respectively correspond to sections at anterior, medial and posterior levels, labelled 1, 2 and 3 in (**G**). (**A1**,**A2**), (**B1**,**B2**), (**C1**,**C2**), and (**D1**,**D2**) show higher magnifications of LVZ territories boxed in (**A**), (**B**), (**C**) and (**D**), respectively. Brackets in (**C**,**D**) delineate a size extension of the PNE on the right compared to the left. White arrowheads in (**A1**,**A2**,**B1**,**C1**,**D1**) point to LVZ HuC/D and DCX negative cells that are maintained on the left but not the right at stages 30–31. Abbreviations: LHb and RHb, left and right habenulae; hc, habenular commissure; pi, pineal stalk; PNE, pseudo-stratified neuroepithelium. Scale bars = 100 μm in (**A**–**D**), 500 μm in (**E**–**G**).

Neural progenitors are preferentially maintained in the left, versus right, lateral ventricular zone (LVZ). We next extended analysis of HuC/D and DCX expression to stages 29 to 31, when marked size asymmetries appear between the left and right habenulae (Fig. 2). From stage 27 onwards, two territories exhibiting distinct cell organisations are observed on histological sections: a medial ventricular one, showing a typical pseudostratified neuroepithelium cell organisation (PNE), and a lateral one, containing dispersed, round shaped cells, which expands as development proceeds (Fig. S1). At all stages analysed, expression of HuC/D and DCX is mainly restricted to the latter, except for a few HuC/D scattered cells in the PNE (Fig. 2A–D). Higher magnification views show that starting from stage 29, the labelling also excludes a thin layer of cells lining the ventricular zone laterally to the PNE, referred to as lateral ventricular zone (LVZ: Fig. 2A1,A2). No evidence for HuC/D or DCX positive cells is observed at this level either on the left or on the right at stage 29 (Fig. 2A,A1,A2). In contrast, at stage 30, discrete HuC/D and DCX cell clusters appear on the right, while the left LVZ remains unlabelled (Fig. 2B,B1,B2). At stage 31, most cells are HuC/D and DCX immunoreactive in the right LVZ, while they remain largely unlabelled in the left LVZ (Fig. 2C,C1,C2,D,D1,D2). These data suggest that neuronal differentiation in the LVZ is differentially regulated between the left and right habenulae. In order to test whether LVZ neural progenitors may be differentially maintained between the left and right habenulae, we analysed expression of *ScSox2*, the catshark orthologue of *Sox2*, a maintenance factor of neural progenitor identity[14,15], and Pax6, a marker of neural progenitors[16], from stages 28 to 31 (Fig. 3). A strong, bilateral signal is observed for both markers in the LVZ at all stages studied (Fig. 3A–I). *ScSox2* and Pax6 are strongly expressed in the LVZ when it becomes visible at stage 29 (Fig. 3B,H). At stage 30, while the LVZ *ScSox2* signal is maintained as a continuous and strongly labelled territory on the left, it becomes patchy, with a fainter intensity on the right (Fig. 3C,C1,C2). This difference is maintained at stage 31 (Fig. 3D–F). Similarly, at stages 30–31, Pax6 positive cells form a dense ventricular layer in the left LVZ, while they appear dispersed along the right LVZ, only few cells remaining at late stage 31 (Fig. 3I,I1,I2,J,K,K1,K2).

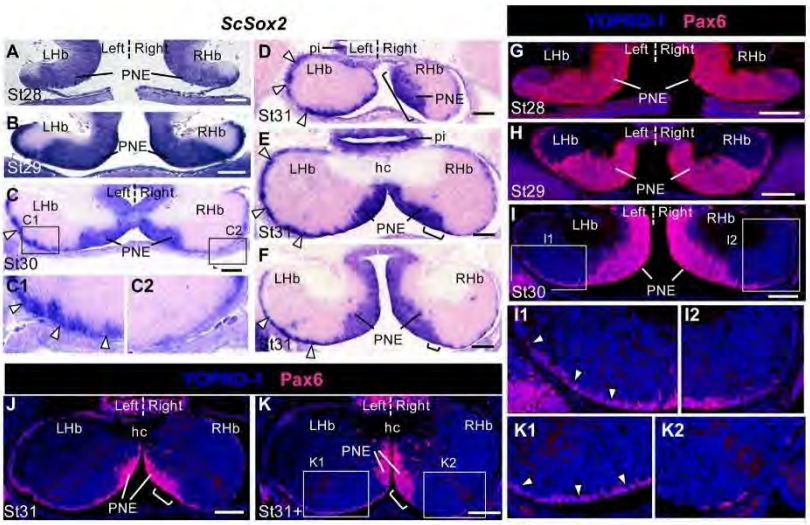

Figure 3. Asymmetric maintenance of neural progenitors in the LVZ and the PNE. Transverse sections of catshark habenulae following ISH using a *ScSox2* probe (**A**–**F**) and IHC using antibodies against Pax6 (red) with a YOPRO-1 nuclei staining in blue (**G**–**K**). Stages are as indicated: (**A**,**G**), stage 28; (**B**–**H**), stage 29; (**C**,**I**), stage 30; (**D**–**F**,**J**), stage 31; (**J**), late stage 31 (**K**). Section levels and planes are as depicted in Figs 1 and 2, with (**D**), (**E**,**J**,**K**) and (**F**) being respectively located at anterior, medial and posterior levels of the habenulae, as defined in Fig. 2G,G1-3. (**C1**,**C2**), (**I1**,**I2**) and (**K1**,**K2**) show higher magnifications of LVZ territories boxed in (**C**), (**I**) and (**K**).Brackets in (**D**–**F**,**J**,**K**) show the size extension of the PNE on the right relative to the left. Arrowheads in (**C**,**C1**,**D**,**E**,**F**,**I1**,**K1**) point to left LVZ territories showing stronger *ScSox2* expressions (**C**,**C1**,**D**,**E**,**F**) or more Pax6 expressing cells (**I1**,**K1**) than their right counterparts (**C2**,**I2**,**K2**). Abbreviations are as in Fig. 2. Scale bars = 100 μm.

These data support the conclusion that habenular neural progenitors are preferentially maintained in the left, versus right LVZ.

The PNE exhibits a larger size in the right habenula than in the left one at stage 31. From stages 29 to late 31, the PNE becomes restricted to the medial part of the habenulae, while differentiating HuC/D and DCX positive territories expand in lateral regions (Fig. 2A–D; Fig. S1C,D,F,G). *ScSox2*, PCNA and PAX6 are strongly expressed in this territory at these stages, supporting its proliferative neuroepithelial nature (Fig. 3A–K; Fig. 4A–H). From stages 27 onwards, the PNE also expresses *ScNgn2* and *ScNeuroD1*, the catshark orthologues of the proneural genes *Ngn2* and *NeuroD1*[17]. Expression of the latter is restricted to the peripheral PNE, suggesting that the two territories may correspond to different stages of the neurogenic process (Fig. S2A–J). No asymmetry in the *ScSox2*, *ScNgn2*, Pax6 and PCNA expressing PNE territories is observed from stages 26 to 30 (Fig. 3A–C,G–I; Fig. 4A,B; Fig. S2B–D). In contrast, at stages 31-31+, expressions of *ScSox2* (Fig. 3D–F; see also Fig. S5), *ScNgn2* (Fig. S2E), Pax6 (Fig. 3J,K), PCNA (Fig. 4C–E,D1; Fig. S3F–H) extend further laterally in the PNE on the right than the left. This asymmetry is most obvious in the anterior habenulae (Fig. 3D,E; Fig. 4C,D; Fig. S5) and maintained at late stage 31 (Fig. 3K; Fig. 4F–H), as assessed by PCNA and Pax6 labelling. At stage 32, PCNA immunoreactivity has withdrawn from the ventricular zone except for a few scattered cells in its medial part (Fig. S2M). This dynamic expression profile is consistent with an asymmetric regulation of the maintenance of PNE neural progenitors, which persist in a broader territory in the left habenula than in the right one at stage 31-31+.

Cell proliferation is asymmetrically regulated in the LVZ. In order to address whether cell proliferation may be asymmetrically regulated in the PNE or LVZ, we compared the total number of neural progenitors and relative proportion of dividing cells in each of these territories between the left and the right. The statistical significance of differences between the left and the right habenulae was assessed at the level of individual embryos or at the level of the group of embryos analysed, respectively using X^2 tests on cell counts or paired Student's t-tests on the mean difference of the variable analysed (cell counts or ratios). Both tests were used when applicable. In the PNE, there is no evidence for a difference in cell density between the left and the right from stage 27 to 31 (X^2 tests on cell counts from individual embryos; $n > 46$; p-values between 0.42 and 0.92; Table S1). The count distribution of PH3 positive, mitotic cells also exhibits no statistically significant difference between the left and the right PNE at stages 27 ($n = 8$), 29 ($n = 8$) and 30 ($n = 6$) (paired Student's t-tests; p-values comprised between

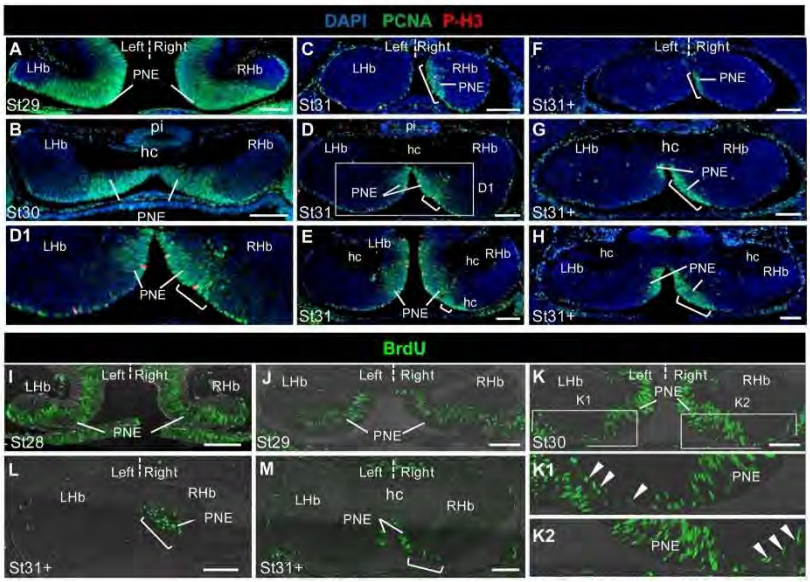

Figure 4. Cell proliferation asymmetries in the LVZ and the PNE. Transverse sections of catshark habenulae following IHC using antibodies against PCNA (green) and PH3 (red) with a DAPI nuclei staining in blue (**A**–**H**) or following a BrdU pulse labelling (**I**–**M**). Stages are as indicated: (**I**), stage 28; (**A**,**J**), stage 29; (**B**,**K**), stage 30; (**C**–**E**) stage 31; (**F**–**H**,**L**,**M**), late stage 31. (**C**,**F**,**L**), (**D**,**G**,**M**) and (**E**,**H**) are respectively located at anterior, medial and posterior levels of the habenulae,as defiend in Fig. 2G,G1-3. (**K1**,**K2**) show higher magnifications of left and right LVZ territories boxed in (**K**). (**D1**) shows a higher magnification of the PNE territories boxed in (**D**). Brackets in (**C**-**H**,**L**,**M**) show the size extension of the PNE on the right relative to the left. Arrowheads in (**K1**,**K2**) point to BrdU labeled cells in the LVZ. Abbreviations are as in Fig. 2. Scale bars = 100 μm.

0.1 and 0.6). Mean AI (asymmetry index) values do not exceed +/−10% at these stages (Fig. 5A; Tables S2 and S3). Similarly, no significant difference in counts of BrdU (5-bromo-2-deoxyuridine) positive cells can be detected between the left and right PNE of the embryos analysed at stages 28 (n = 3), 29 (n = 3) and 30 (n = 3) following BrdU pulse labelling (X^2 tests on cell counts from individual embryos; n > 500; p-values comprised between 0.399 and 0.976; AI values comprised between −0.7 and 1.7%; Fig. 5B; Table S4). In contrast, at stage 31, the count distribution of PH3 positive cells in the PNE appears significantly asymmetric (n = 10; paired Student's t-test; p-value = 4.0810E-04; Fig. 5A; Table S3), with higher values on the right than on the left in all embryos tested (AI values ranging from −12% to −36%) and with statistically significant asymmetries in 7 out of 10 embryos analysed (X^2 tests on cell counts from individual embryos; Table S2). In order to test whether the PNE size, larger on the right than on the left at stage 31, could account for this asymmetry, we directly counted PH3 positive cells in the right PNE expansion for three embryos (Table S5). No significant difference is detected between the left and the right sides if this expansion is excluded from the counts, in either one of the three embryos analysed (X^2 tests on cell counts from individual embryos; n > 52; p-values comprised between 0.785 and 0.966; Table S5). In the absence of overt difference in cell density between the left PNE and the right one, this suggests that the difference in PH3 counts observed at stage 31 is not related to an asymmetry in proliferation rate and only reflects the larger PNE size on the right than on the left. In the LVZ, the count distribution of PH3 positive cells at stage 31 highlights a significant asymmetry between the right and the left sides (n = 10; paired Student's t-test; p-value = 4.16E-05), with fewer labelled cells on the right than on the left in all embryos analysed and AI values comprised between 18 and 61% (Fig. 5C; Tables S2 and S3). An asymmetric distribution of cell counts is also detected at stage 29, albeit with lower AIs including positive and negative values (AIs comprised between −7% and 31%) and a lower statistical support (n = 8; Student's t-test; p-value = 1.5950E-02), but not at stage 30 (n = 6; Student's t-test; p-value = 0.4017) (Fig. 5C; Tables S2 and S3). In view of the low number of PH3 labelled cells in the LVZ and of the absence of significant asymmetries for most individual embryos analysed with regard to this parameter (X^2 test p-values > 5E-02 except for one embryo; Table S2), we conducted BrdU incorporation experiments in order to further assess cell proliferation asymmetries in this cell population. Pax6 immuno-detection was also used in this analysis to estimate the number of neural progenitors in the left and right LVZ and normalise counts of BrdU labelled cells. This analysis was focused on stages 29 and 30, when no overt size asymmetry is detected between the left and right habenulae. A significantly higher number of Pax6 expressing neural progenitors is observed in the left LVZ than in the right one in all embryos analysed not only at stage 30, in line with

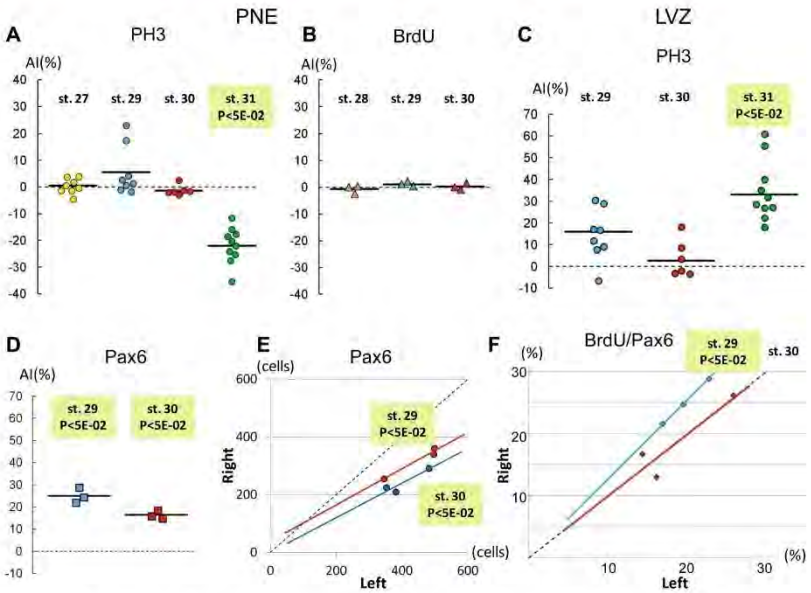

Figure 5. Quantified analysis of proliferation asymmetries in the LVZ and PNE. (**A**–**D**) Plots showing asymmetry indexes (**AI**) in the PNE (**A**,**B**) and in the LVZ (**C**,**D**), with regard to counts of PH3 (**A**,**C**), BrdU (**B**) and Pax6 (**D**) positive cells at stages 27 to 31. Dots in (A,C), triangles in (**B**) and squares in (**D**) correspond to AIs obtained for individual embryos at stages 27 (yellow), 28 (orange), 29 (blue), 30 (red) and 31 (green). For each group of embryos analysed (same marker, same stage, same zone), horizontal black lines show the median AI value. (**E**,**F**) Plots showing Pax6 positive cell counts (**E**) and ratios (in %) of BrdU to Pax6 positive cell counts (**F**) in the right and in the left LVZ at stages 29 and 30. Blue and red dots correspond to individual embryos respectively at stage 29 and at stage 30. Best-fit regression lines (blue at stage 29, red at stage 30) are shown, together with the symmetry reference (dotted black line). Light green shading in (**A**,**C**–**F**) with the indication ($P < 5E-02$) highlight embryo groups exhibiting a significant asymmetry in the distribution of cell counts between the left and the right, based on paired Student's t-tests on AIs (**A**,**C**,**D**) and ratios of BrdU to Pax6 cell counts (**F**). In (**E**), this indication refers to X^2 tests conducted on all individual embryos analysed. Abbreviation used: P, p-value.

the broader *ScSox2* and Pax6 expression territories observed (see above; Fig. 3), but also at stage 29 (X^2 tests on cell counts from individual embryos; $n > 200$; p-values comprised between 2.582E-12 and 2.83E-04; Fig. 5E; Table S6). A paired Student's t-test confirms an asymmetric distribution of counts of Pax6 expressing cells at these stages, with a higher statistical support and a higher mean AI value at stage 30 than at stage 29 (paired Student's t-test; $n = 3$; p-value = 1.257E-02 at stage 29 and 2.315E-02 at stage 30; Fig. 5D; Table S6). In view of this asymmetry, we next focussed on the ratio of BrdU to Pax6 expressing cell count in order to assess proliferation rate asymmetries between the left and right LVZ (Fig. 5F). In all embryos analysed, this ratio appears higher on the right than on the left, with a significant asymmetry in distribution at stage 29 ($n = 3$; paired Student's t-test; p-value = 5.859E-03), not observed at stage 30 (Fig. 5F; Table S6). These data highlight a transient asymmetry of the cell proliferation rate, higher in the left LVZ than in the right one at stage 29. In order to assess the contribution of apoptosis to the PNE and LVZ size asymmetries, we also conducted TUNEL assays on habenula sections at stages 27, 29, 30, 31 and 32. Very low numbers of apoptotic cells were detected whether on the right or left side, whatever the territory considered (respectively at most 3, 1 and 4 apoptotic cells per habenula in the PNE, LVZ and other territories; Fig. S2K,L; Table S7), suggesting that apoptosis does not play a major part in the formation of the asymmetries observed.

Left and right territories of neural progenitors become symmetric following pharmacological treatment with SB-505124. We previously showed in the catshark that an *in ovo* injection of SB-505124, an antagonist of the TGF-β type I receptors Alk4/5/7[18], prior to the onset of Nodal activation in the diencephalon, results in a loss of the early left sided Nodal activity, as well as of later habenular asymmetries in size and regional marker expression[5]. In order to test whether the treatment could similarly abolish the neurogenetic asymmetries observed in the PNE and the LVZ, we analysed its effect on the maintenance of these territories at stages 30 to 31. In stage 31 control embryos, HuC/D and DCX immunoreactivity is observed in the right LVZ but largely excluded from the left one (Fig. 6A,C,C1,C2), as observed in untreated embryos. Following SB-505124 treatment,

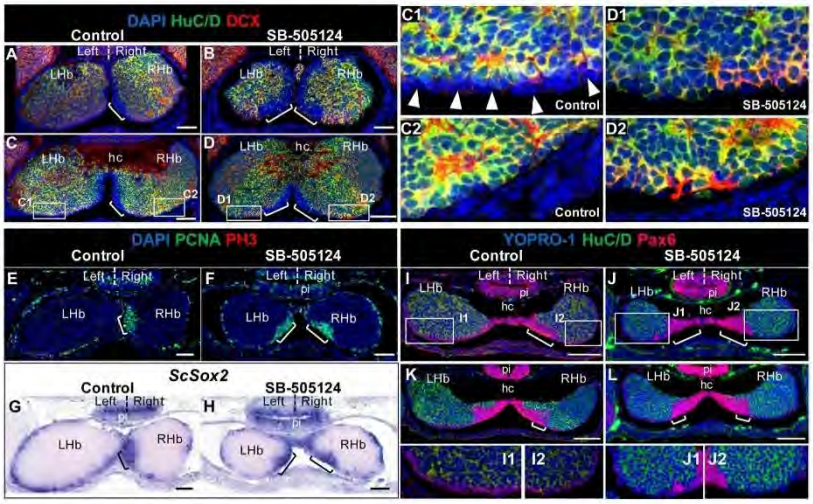

Figure 6. LVZ and PNE neurogenetic asymmetries are dependent on Nodal signalling. Transverse sections of stage 30–31 catshark habenulae following IHC using antibodies against HuC/D and DCX (**A**–**D**), PCNA and PH3 (**E**,**F**), HuC/D and Pax6 (**I**–**L**), or following ISH using a *ScSox2* probe (**G**,**H**). (**A**,**C**,**E**,**G**,**I**,**K**) and (**B**,**D**,**F**,**H**,**J**,**L**) show sections of control and SB-505124-treated embryos, respectively. (**A**,**B**,**E**,**F**,**G**,**H**,**I**,**J**) and (**C**,**D**,**K**,**L**) are respectively located at anterior and medial levels of the habenulae, as defined in Fig. 2G,G1,G2. (**A**–**D**), (**E**–**H**) and (**I**–**L**) respectively correspond to stage 31+, 31 and 30+ embryos. (**C1**,**C2**), (**D1**,**D2**), (**I1**,**I2**) and (**J1**,**J2**) show higher magnifications of LVZ territories boxed in (**C**), (**D**), (**I**) and (**J**) respectively. Symbols and abbreviations are as in Fig. 2. Scale bars = 100 μm.

HuC/D and DCX expression appears similar between the left and right LVZ, and comparable to that observed in the right LVZ of control embryos (Fig. 6B,D,D1,D2). *ScSox2* and Pax6 LVZ expression, more patchy on the right than on the left in control embryos (Fig. 6G,I,K,I1,I2), also becomes very similar following SB-505124 treatment (Fig. 6H,J,L,J1,J2). In the PNE, the PCNA positive, HuC/D and DCX negative territory exhibits a marked size asymmetry in control embryos, similar to untreated ones (Fig. 6A,C,E). This asymmetry is lost following SB-505124 treatment, with the left PNE expanding to a size comparable to its counterpart on the right and becoming visible at anterior-most levels (compare Fig. 6B,D,F). Analyses of *ScSox2* and Pax6 PNE expression lead to the same conclusions (compare Fig. 6G–L). These data show that the asymmetric regulation of neural progenitor maintenance in the PNE and LVZ is abolished by the pharmacological treatment. Expression of *Pitx2*, a canonical target of Nodal in left-right asymmetry formation, has been shown to be lost in the catshark following SB-505124 treatment[5]. In order to assess whether this gene may be a candidate to mediate the drug effect, we analysed its expression from stage 27 to 31. *ScPitx2* expression is restricted to the left habenula at all stages analysed (Fig. S3). The signal spans the distal part of the evagination at stage 27 (Fig. S3A,A1). When the LVZ appears, at stage 29, it becomes restricted to the left LVZ and adjacent lateral-most territory of the PNE (Fig. S3B,B1). At stage 31, the signal persists in the left LVZ and lateral PNE (Fig. S3C–E), extending to the whole PNE at medial organ levels (Fig. S3D; compare Fig. S3C–G).

Discussion

Our solid understanding of the cellular mechanisms involved in habenular asymmetry formation in the zebrafish contrasts with the paucity of data available in other vertebrates. Our analysis addresses this issue for the first time in a non-teleost model, the catshark, which as a chondrichthyan, provides an excellent reference to infer gnathostome ancestral traits via comparisons with the zebrafish[19]. These data highlight two main neurogenetic asymmetries, which may contribute to the elaboration of habenular asymmetries in the catshark (Fig. 7). We first find a left restricted initiation of neuronal differentiation, observed at stage 25 (Fig. 7A). At later stages, we also detect marked asymmetries in neural progenitor territories, with a higher number of LVZ neural progenitors on the left than on the right starting from stage 29 (Fig. 7B), and a consistent PNE size expansion in the right habenula relative to the left one starting from stage 31 (Fig. 7C). The cellular mechanisms responsible for this differential maintenance between the left and the right habenulae remain to be explored but our analysis provides insight into this question. An asymmetric regulation of apoptosis, known to regulate the number of neural progenitors in the mammalian brain[20,21] seems unlikely to play a major role, in view of the very small number of apoptotic cells detected at the stages studied. Our analysis also failed to detect significant asymmetries in cell proliferation rate, except for a significantly higher rate observed in the right LVZ at stage 29. This transient cell proliferation asymmetry may contribute to the decrease in magnitude of the LVZ asymmetry with regard to the number of Pax6

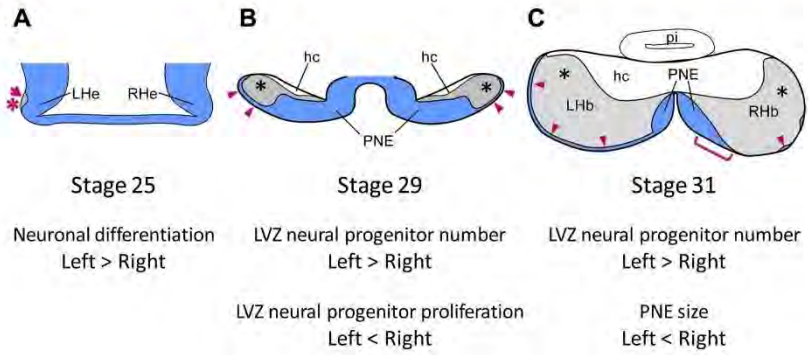

Figure 7. Scheme summarising the neurogenetic asymmetries detected in the catshark developing habenulae. Transverse sections are schematised at stages 25 (**A**), 29 (**B**) and 31 (**C**). Neural progenitor territories are coloured in blue and an asterisk shows territories expressing early neuronal differentiation markers. The red arrow and asterisk in (**A**) indicate a left restricted differentiated territory. Black asterisks in (**B**,**C**) indicate differentiated territories. Red arrowheads in (**B**,**C**) point to LVZ neural progenitors and a red bracket in (**C**) delineates the PNE right size expansion relative to the left.

positive neural progenitors between stage 29 and 30. However, it cannot explain the preferential maintenance of the LVZ on the left already observed at stage 29 and is difficult to relate to the right PNE extension observed at stage 31. Taken together, these data suggest that another cellular mechanism, such as an asymmetric regulation of cell cycle exits between the left and the right, may be responsible for the differential maintenance of LVZ and PNE neural progenitors. The difference in size of *ScNeuroD1* territory between the left and right habenulae supports this possibility, which will have to be assessed by quantified analyses of the rates of cell cycle exits as neurogenesis proceeds.

We previously observed that *in ovo* injection of the pharmacological inhibitor SB-505124 after neural tube closure, just prior to the onset of a left sided Nodal expression in the diencephalon, results in a loss of habenular asymmetries in size and molecular regionalisation in the catshark, with a right isomerism[5]. Similarly, this pharmacological treatment abolishes the asymmetric maintenance of LVZ and PNE neural progenitors, with a right side phenotype observed in both habenulae. Whether these neurogenetic asymmetries may be dependent on the earlier Nodal diencephalic activity is difficult to formally address in the catshark. However, in support of this hypothesis, the catshark orthologue of *Pitx2*, whose habenular expression is lost following SB-505124 treatment, is selectively expressed in the left LVZ and lateral part of the PNE at the time when neurogenetic asymmetries are detected at this level. This gene, known as a canonical target of Nodal signalling in left-right asymmetry formation, thus appears as a candidate to mediate possible effects of Nodal on the formation of habenular neurogenetic asymmetries in the catshark. An unexpected result of this study is that the injection of the pharmacological inhibitor SB-505124 in the conditions described above has opposite effects on the LVZ and PNE, resulting in an increased cell number in the former, but a smaller size of the latter in the left versus right habenula. Several distinct yet non-mutually exclusive mechanisms could account for these differential effects. First, we cannot formally exclude that the treatment may affect not only the early, left restricted window of Nodal activity immediately following the drug injection, but also other yet unidentified phases of Alk4/5/7 mediated signalling activities, also known to be inhibited by SB-505124[18], in the right habenula. A bilateral expression of the FoxH1 forkhead activin transducer has thus been observed in the zebrafish[22]. Another possibility may be related to differential sequential effects in the LVZ and the PNE, related to asymmetric modifications of the habenula environment as differentiation proceeds. Temporal regulations of the identity of neural progenitors have indeed been shown to involve dynamic extrinsic signals, such as those secreted by previously generated neurons in a variety of model systems[23]. The asymmetries first observed at stage 25 and detected in the LVZ at stage 29, may similarly modulate those later arising in the PNE in a cell non-autonomous manner. Finally, cell intrinsic genetic programs, possibly differentially interpreting the early phase of Nodal activity, may also differ between the LVZ and PNE. In line with this hypothesis, we observe a prominent left expression of *ScPitx2* in the LVZ, but not in the PNE, prior to stage 31. Further dissections of the mechanisms acting cell autonomously and non-cell autonomously in asymmetry formation in the catshark developing habenulae will be crucial to resolve these issues. Comparisons of the neurogenetic asymmetries identified here in the catshark with the zebrafish also provide insights into the evolution of the mechanisms of habenular asymmetry formation. The early left restricted neuronal differentiation observed in the catshark as in the zebrafish[9,10], suggests that the asymmetric temporal regulation of neuronal differentiation demonstrated in the latter, may reflect the conservation of an ancestral characteristic of jawed vertebrates. In contrast, neither size asymmetries of neural progenitor territories, nor differences in cell proliferation rate between the left and right developing habenulae as observed in the catshark, were reported in the zebrafish. Whether these traits may correspond to ancestral gnathostome features, or to more recent adaptations of chondrichthyans, remains unknown. Changes in the regulation of neurogenesis have been identified as a driving force of cortical

evolution in amniotes[24] and suggested to contribute to the diversification of habenular asymmetries across vertebrates[1,25]. Our data, which highlight both conserved and divergent neurogenetic asymmetries between the catshark and the zebrafish, support this view. Furthermore, a noticeable feature of the catshark is that the preferential maintenance of proliferating neural progenitors, a process potentially affecting organ size[26], is not a unilateral one but is observed in the right habenula as well as in the left one, depending on the progenitor pool considered, PNE or LVZ. This provides a rationale to reconcile the apparent discrepancy between the conservation of a left restricted Nodal activity and variations of the laterality of size asymmetries, as observed between the lamprey and catshark[1,5,25]. Evolutionary variations affecting the size ratio between two such progenitor pools, or their temporal regulation, could indeed result in changes in the laterality of habenular size asymmetries across vertebrates. Finally, an important remaining question concerns the contribution of the neurogenetic asymmetries characterised in the catshark to the differences in molecular organisation between the left and right habenulae. The coupling of marked neurogenetic asymmetries, as observed here, and of a temporal regulation of cell fate choices, as frequently encountered in the central nervous system[27] and as reported in the zebrafish developing habenulae[9,10], may be the major mechanism controlling habenular asymmetry formation in the catshark. However, we cannot exclude that an additional asymmetric regulation of cell fate choices, involving a left repression of Wnt signalling as reported in the zebrafish[8], may contribute to this process, possibly under the control of Nodal rather than a parapineal secreted signal. Direct perturbations of neurogenesis, for instance by manipulations of Notch activity as described in the zebrafish[9], and analyses of the regulation of cell fate choices will be crucial to resolve this issue.

Methods

Embryo collection. *Scyliorhinus canicula* eggs were obtained from Roscoff and Banyuls sur Mer Marine Stations. Embryos were dissected, fixed and staged as described previously[5].

***In situ* hybridization (ISH).** ISH of sections were conducted using digoxigenin-labelled antisense RNAs as previously described[28,29]. Probes were obtained from collections of embryonic *S. canicula* cDNA recombinants, characterized by Sanger sequencing and described in[30]. Clone identities were confirmed by phylogenetic analyses (Fig. S4). Accession numbers for the sequences used in this study are listed in Table S10. Following ISH, nuclei were counterstained using Nuclear Fast Red (Sigma N3020). For all probes analysed, the orthogonality of section planes to the antero-posterior axis (as depicted in Figs 1 and 2) was checked using symmetrical morphological references (eyes, olfactory epithelium) and sections were systematically analysed at all organ levels (at least one section every three successive sections at stages 27–28 and one every four sections at stages 29–31; see example in Fig. S5).

Immunohistochemistry (IHC). The antibodies used and their concentration are listed in Supplementary Information (Table S9). Fluorescent immunohistochemical analyses of sections were conducted as previously described[5] for PCNA, PH3, Pax6, HuC/D and DCX IHC. BrdU pulse labelling were conducted by incubating catshark embryos in 10 mg/ml BrdU in oxygenated artificial sea water after opening the egg shell. Incubations were conducted for 30, 45, 120 and 150 minutes respectively at stages 27, 28, 29 and 30 respectively. For detection of BrdU, sections were incubated in 2 N HCl for 30 minutes at 50 °C prior to fluorescent IHC analysis in the conditions described above. Embryo sections were imaged with a Leica SP8 confocal laser-scanning microscope and images processed using ImageJ. As for ISH, at least one section every three (stages 27–28) or four (stages 29–31) successive sections was analysed, over the whole organ.

TUNEL assays. Apoptosis was detected on paraffin-embedded sections with the *In Situ* Cell Death Detection Kit (Roche, 11684809910) according to the supplier's instructions. In short, slides were pretreated in 0.1 M citrate buffer pH6.0 with a 350 W microwave irradiation for 5 minutes, incubated in the TUNEL reaction mixture for 1 h at 37 °C prior to DAPI nuclear staining. For positive controls, a DNase I treatment (1000 U/mL) was added for 10 min at room temperature prior to the labeling procedure. For negative controls, slides were treated as described above, except that terminal transferase was omitted in the reaction.

Countings and data analysis. Following fluorescent IHC and DAPI staining, PH3 positive nuclei in the PNE and LVZ were counted manually on adjacent habenular transverse sections using an epifluorescence Olympus IX51. Countings were restricted to the habenular evaginations, taking into account all sections (10 µm thick) starting from the anterior part of the organ (total number of sections = 25 at stage 27, 32 at stage 29, 35 at stage 30, 40 at stage 31). The same methodology was used to estimate the number of PH3 positive nuclei in the right PNE expansion, defined by comparisons between the left and the right habenulae on sections submitted to fluorescent IHC using antibodies directed against PCNA and PH3. For statistical analyses, these counts were systematically corrected and divided by a factor of 2, in order to take into account the relative thickness of nuclei and sections according to[31]. BrdU and Pax6 positive cells were counted in the whole habenular evaginations as described above, except that only one section was taken into account every three (stage 28) or four (stages 29–30) successive sections. No correction for section thickness was applied in this case before statistical analysis. Ratios of BrdU to Pax6 expressing cell counts were calculated using counts in the whole habenula, obtained as described above. X^2 statistical tests were conducted for individual embryos using the count data obtained as described above, following correction in the case of PH3 labelling, the null hypothesis for each embryo analysed being that cell counts are identical in the right and in the left habenulae. For Student's t-tests, counts obtained for replicates of the same condition (same zone, same stage, same side) were taken into account in order to assess the probability of occurrence of the observed distribution against a symmetry null hypothesis (same mean number of cell counts or ratios on the left and on the right for the group of embryos considered). All statistical tests were performed using the R statistical software[32] with the following parameters ($\alpha = 5\%$; for X^2 test $df = 1$).

Pharmacological treatments. Catshark embryos were treated by *in ovo* injection of SB-505124, a selective inhibitor of TGF-β type I receptors Alk4/5/7[18], as previously described[5]. The same protocol was applied to control embryos, except for the absence of the drug in the injected solution.

Data availability statement. The data, probes and protocols used in this study are available upon request to SM.

References

1. Concha, M. L. & Wilson, S. W. Asymmetry in the epithalamus of vertebrates. *J. Anat.* **199**, 63–84 (2001).
2. Ahumada-Galleguillos, P. *et al.* Directional asymmetry in the volume of the human habenula. *Brain Struct Funct.* **222**, 1087–1092 (2016).
3. Concha, M. L., Signore, I. A. & Colombo, A. Mechanisms of directional asymmetry in the zebrafish epithalamus. *Semin. Cell Dev. Biol.* **20**, 498–509 (2009).
4. Roussigné, M., Blader, P. & Wilson, S. W. Breaking symmetry: The zebrafish as a model for understanding left-right asymmetry in the developing brain. *Dev. Neurobiol.* **72**, 269–281 (2012).
5. Lagadec, R. *et al.* The ancestral role of nodal signalling in breaking L/R symmetry in the vertebrate forebrain. *Nat. Commun.* **6**, 6686 (2015).
6. Gamse, J. T., Thisse, C., Thisse, B. & Halpern, M. E. The parapineal mediates left-right asymmetry in the zebrafish diencephalon. *Development* **130**, 1059–1068 (2003).
7. Concha, M. L., Burdine, R. D., Russell, C., Schier, A. F. & Wilson, S. W. A nodal signaling pathway regulates the laterality of neuroanatomical asymmetries in the zebrafish forebrain. *Neuron* **28**, 399–409 (2000).
8. Hüsken, U. *et al.* Tcf7l2 is required for left-right asymmetric differentiation of habenular neurons. *Curr. Biol.* **24**, 2217–2227 (2014).
9. Aizawa, H., Goto, M., Sato, T. & Okamoto, H. Temporally Regulated Asymmetric Neurogenesis Causes Left-Right Difference in the Zebrafish Habenular Structures. *Dev. Cell* **12**, 87–98 (2007).
10. Roussigné, M., Bianco, I. H., Wilson, S. W. & Blader, P. Nodal signalling imposes left-right asymmetry upon neurogenesis in the habenular nuclei. *Development* **136**, 1549–1557 (2009).
11. Garric, L. *et al.* Pitx2c ensures habenular asymmetry by restricting parapineal cell number. *Development* **141**, 1572–1579 (2014).
12. Marusich, M. F., Furneaux, H. M., Henion, P. D. & Weston, J. A. Hu neuronal proteins are expressed in proliferating neurogenic cells. *J. Neurobiol.* **25**, 143–155 (1994).
13. Reiner, O. *et al.* DCX's phosphorylation by not just another kinase (JNK). *Cell Cycle* **3**, 747–751 (2004).
14. Graham, V., Khudyakov, J., Ellis, P. & Pevny, L. SOX2 functions to maintain neural progenitor identity. *Neuron* **39**, 749–765 (2003).
15. Bylund, M., Andersson, E., Novitch, B. G. & Muhr, J. Vertebrate neurogenesis is counteracted by Sox1–3 activity. *Nat. Neurosci.* **6**, 1162–1168 (2003).
16. Osumi, N., Shinohara, H., Numayama-Tsuruta, K. & Maekawa, M. Concise Review: Pax6 Transcription Factor Contributes to both Embryonic and Adult Neurogenesis as a Multifunctional Regulator. *Stem Cells* **26**, 1663–1672 (2008).
17. Huang, C., Chan, J. A. & Schuurmans, C. Proneural bHLH genes in development and disease. *Curr. Top. Dev. Biol.* **110**, 75–127 (2014).
18. DaCosta Byfield, S., Major, C., Laping, N. J. & Roberts, A. B. SB-505124 is a selective inhibitor of transforming growth factor-beta type I receptors ALK4, ALK5, and ALK7. *Mol. Pharmacol.* **65**, 744–752 (2004).
19. Coolen, M. *et al.* The dogfish Scyliorhinus canicula: A reference in jawed vertebrates. *Cold Spring Harb. Protoc.* **3**, 1–14 (2008).
20. Kuan, C., Roth, K., Flavell, R. & Rakic, P. Mechanisms of programmed cell death in the developing brain. *Trends Neurosci.* **21**, 4752–4760 (2000).
21. Depaepe, V. *et al.* Ephrin signalling controls brain size by regulating apoptosis of neural progenitors. *Nature* **435**, 1244–1250 (2005).
22. Boggetti, B. *et al.* Cloning and expression pattern of a zebrafish homolog of forkhead activin signal transducer (FAST), a transcription factor mediating Nodal-related signals. *Mech. Dev.* **99**, 187–190 (2000).
23. Syed, M. H., Mark, B. & Doe, C. Q. Playing well with others: extrinsic cues regulate neural progenitor temporal identity to generate neuronal diversity. *Trends Genet.* **33**, 933–942 (2017).
24. Nomura, T., Murakami, Y., Gotoh, H. & Ono, K. Reconstruction of ancestral brains: Exploring the evolutionary process of encephalization in amniotes. *Neuroscience Research* **86**, 25–36 (2014).
25. Villalón, A. *et al.* Evolutionary plasticity of habenular asymmetry with a conserved efferent connectivity pattern. *PLoS One* **7**, e35329 (2012).
26. Bielen, H., Pal, S., Tole, S. & Houart, C. Temporal variations in early developmental decisions: an engine of forebrain evolution. *Curr. Opin. Neurobiol.* **42**, 152–159 (2017).
27. Rossi, A. M., Fernandes, V. M. & Desplan, C. Timing temporal transitions during brain development. *Curr. Opin. Neurobiol.* **42**, 84–92 (2017).
28. Derobert, Y. *et al.* Structure and expression of three Emx genes in the dogfish Scyliorhinus canicula: functional and evolutionary implications. *Dev. Biol.* **247**, 390–404 (2002).
29. Plouhinec, J. L. *et al.* Comparative analysis of gnathostome Otx gene expression patterns in the developing eye: implications for the functional evolution of the multigene family. *Dev. Biol.* **278**, 560–575 (2005).
30. Coolen, M. *et al.* Evolution of axis specification mechanisms in Jawed vertebrates: Insights from a chondrichthyan. *PLoS One* **2**, e374 (2007).
31. Abercrombie, M. Estimation of nuclear population from microtome sections. *Anat. Rec.* **94**, 239–247 (1946).
32. R Core team. R Core Team. *R: A Language and Environment for Statistical Computing. R Foundation for Statistical Computing, Vienna, Austria. ISBN 3-900051-07-0*, http://www.R-project.org/. **55**, 275–286 (2015).

Acknowledgements

We thank David Pecqueur and Sophie Le Panse for providing access to the imaging platforms at the OOB (Observatoire Océanologique de Banyuls) and SBR (Station Biologique de Roscoff), Pascal Romans (OOB), Sébastien Henry (SBR), and OOB and SBR Marine Model Services (EMBRC-France) for collecting catshark eggs. We are grateful to Patrick Blader and Anne-Marie Genevière for helpful comments on the manuscript. The work was funded by CNRS, Université Pierre et Marie Curie, grant N° ANR-16-CE13-0013-02 to S.M., and grants from the Spanish Dirección General de Investigación-FEDER (BFU2014-58631-P), Xunta de Galicia-FEDER (ED341D R2016/032) to E.C. R.L. and M.L. were supported was supported by CNRS and Région Occitanie doctoral fellowships.

Author Contributions

S.M., E.C., I.R.M. and R.L. designed the study; R.L., M.L., N.S.F., F.H. and A.M. conducted the experiments, H.M. and B.B. performed phylogenetic analyses and statistical analyses; all authors analysed the data; S.M. wrote the manuscript with inputs from all authors.

Additional Information

Supplementary information accompanies this paper at https://doi.org/10.1038/s41598-018-22851-3.

Competing Interests: The authors declare no competing interests.

Publisher's note: Springer Nature remains neutral with regard to jurisdictional claims in published maps and institutional affiliations.

Neurogenetic asymmetries in the catshark developing habenulae: mechanistic and evolutionary implications

Ronan Lagadec, Maxence Lanoizelet, Nuria Sánchez-Farías, Fanny Hérard, Arnaud Menuet, Hélène Mayeur, Bernard Billoud, Isabel Rodriguez-Moldes, Eva Candal and Sylvie Mazan

LEGENDS TO SUPPLEMENTARY FIGURES

Fig. S1. Histological structure of developing habenulae in the catshark *S. canicula*
Transverse sections through the catshark habenulae at stages 27 (A), 28 (B), 29 (C), 30 (D) and 31 (F,G) following hematoxylin staining (12 μm sections). (E) Scheme showing a lateral view of the developing catshark brain at stages 31 indicating the plane, level and tissue organisation (boxed) of the sections shown in (F-G). (C1) is a higher magnification of a stage 29 left habenula (5 μm section), showing the difference in cell organisation between the PNE and lateral territory of dispersed rounded cells. A thin layer of distinct ventricular cells (LVZ) extends laterally to the PNE, adjacent to rounded cells (see Figure 2). (F1) and (G2) show higher magnifications of the PNE territories boxed in (F) and (G), respectively. (G1) is a higher magnification of the lateral territory boxed in (G). This territory is labelled by asterisks in (A-D,F,G). Black arrowheads in (A-D,F,G) point to the boundary between the habenulae and the forming choroid plexus. Abbreviations used: Cp, choroid plexus; hc, habenular commissure; LVZ, lateral ventricular zone; LHb, left habenula; RHb, right habenula; pi, pineal stalk; PNE, pseudo-stratified neuroepithelium. Scale bars=100μm.

Fig. S2. Expression of neurogenetic genes and proliferation-differentiation markers in the developing catshark habenulae
Transverse sections through the catshark habenulae following ISH with probes for *ScNgn2* (A-E) and *ScNeuroD1* (F-J), a TUNEL assay for apoptosis detection (K-L) or IHC using antibodies directed against PCNA and PH3 (M; PCNA in green and PH3 in red). (K-M) nuclei were counterstained with DAPI (blue). Stages are; 25 (A,F), 26 (B,G), 27 (C,H), 29 (D,I,K), 31 (E,J,L) and 32 (M). Section planes in (E,J,L-M) are the same as in Fig. S1. (M), (E,J) and (L) correspond to anterior, medial and posterior levels of the organ, respectively. The bracket in (E,K,L) delineates an extension of the PNE in the right but not the left habenula. Black arrows in (J) delimit the boundaries of *ScNeuroD1* expression territory outside the PNE: the labelled territory is broader on the left than on the right at stage 31. This difference is already observed at stage 30 (not shown). White arrows in (K,L) point cells positive for the TUNEL assay. Symbols and abbreviations are the same as in Fig. S1. Scale bars=100μm.

Fig. S3. Comparison of *ScPitx2* and *ScPNCA* expressions in the catshark developing habenulae
Transverse sections of catshark habenulae following ISH with a *ScPitx2* probe at stages 27 (A), 29 (B) and 31 (C-E). (F-H) transverse sections of the same embryo, adjacent to those shown in (C-E), following ISH with a *ScPCNA* probe. (C,F), (D,G) and (E-H) correspond to sections at anterior, medial and posterior levels of the organ, respectively. (A1,A2) and (B1,B2) show higher magnifications of the territories boxed in (A) and (B), respectively. The bracket in (F-H) shows the lateral extension of the PNE observed in the right habenula but not the left. *ScPCNA* and *ScPitx2* territories overlap on the left at lateral levels of the PNE. *ScPitx2* also shows strong expression in the left LVZ. These *ScPitx2*

territories exhibit neurogenetic asymmetries at stage 31. Abbreviations are the same as in Fig. S1. Scale bars=100μm.

Fig. S4. Phylogenetic analyses

Maximum-likelihood phylogenetic trees for Neurogenin (A), Sox1/2/3 (B), NeuroD (C) and PCNA (D). Amino acid sequences of gene family members were extracted from Genbank or Ensembl protein databases, or inferred from cDNA sequences. Alignments were obtained using the MUSCLE package [Elgar 2004] and BioEdit [Tippmann 2004] was used for manual corrections. Trees were constructed using PhyML (version 3.0), integrated into Seaview 4.2, using the Maximum Likelihood method and the LG-F+Γ_{12}+I substitution model. SPR was used to compute the trees. The trees were viewed and edited with the TreeExplorer program in MEGA 6.0 [Kumar et al. 2008]. Posterior probabilities for each node were calculated *a posteriori* and are displayed (in %) when higher than 80%. Accession numbers and nomenclature for the sequences used in the phylogenetic reconstructions are listed in Table S10. Abbreviations used: Ac, *Anolis carolinensis*; Bf, *Branchiostoma floridae*; Cm, *Callorhinchus milii*; Dr, *Danio rerio*; Gg, *Gallus gallus*; Hs, *Homo sapiens*; Lc, *Latimeria chalumnae*; Le, *Leucoraja erinacea*; Lo, *Lepisosteus oculatus*; Ol, *Oryzias latipes*; Pm, *Petromyzon marinus*; Ps, *Pelodiscus sinensis*; Sc, *Scyliorhinus canicula*; Xt, *Xenopus tropicalis*.

Fig. S5. Transverse sections of stage 31 catshark habenulae following ISH with a *ScSox2* probe.

(A-B) and (C-V) show transverse sections of the head and of the habenulae respectively (section plane shown in Fig. S1). (C) to (V) correspond to different levels of the organ, from anterior to posterior. (D) and (O) are magnifications of the habenula territory boxed in (A) and (B). Only one every two sections was submitted to ISH and the *ScSox2* profiles thus obtained are shown for all sections analysed. A bracket delineates the expansion displayed by the right habenula compared to the left one. Schemes describing the morphological of habenulas at this stage are presented in Fig. S1. Abbreviations: same as in Fig.S1; Mes, mesencephalon; OB, olfactory bulb; OE, olfactory epithelium. Scale bars=100μm.

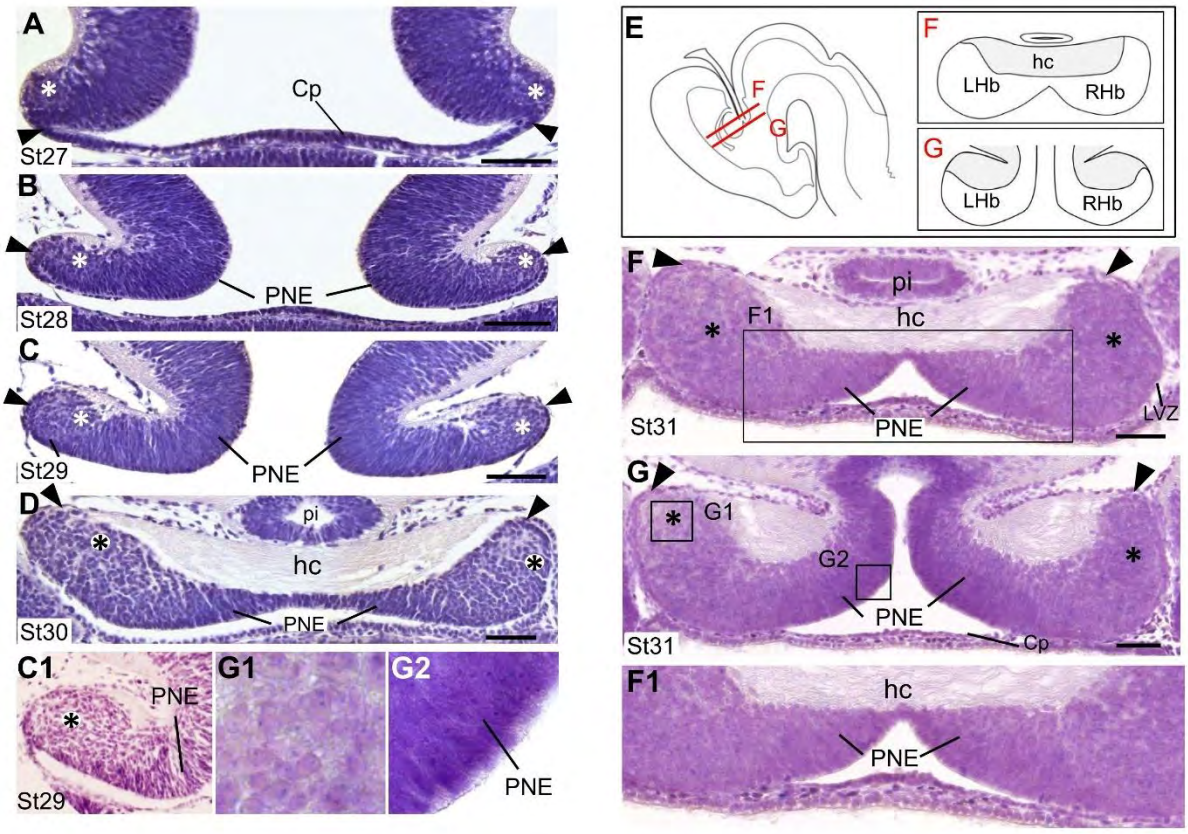

Figure S1

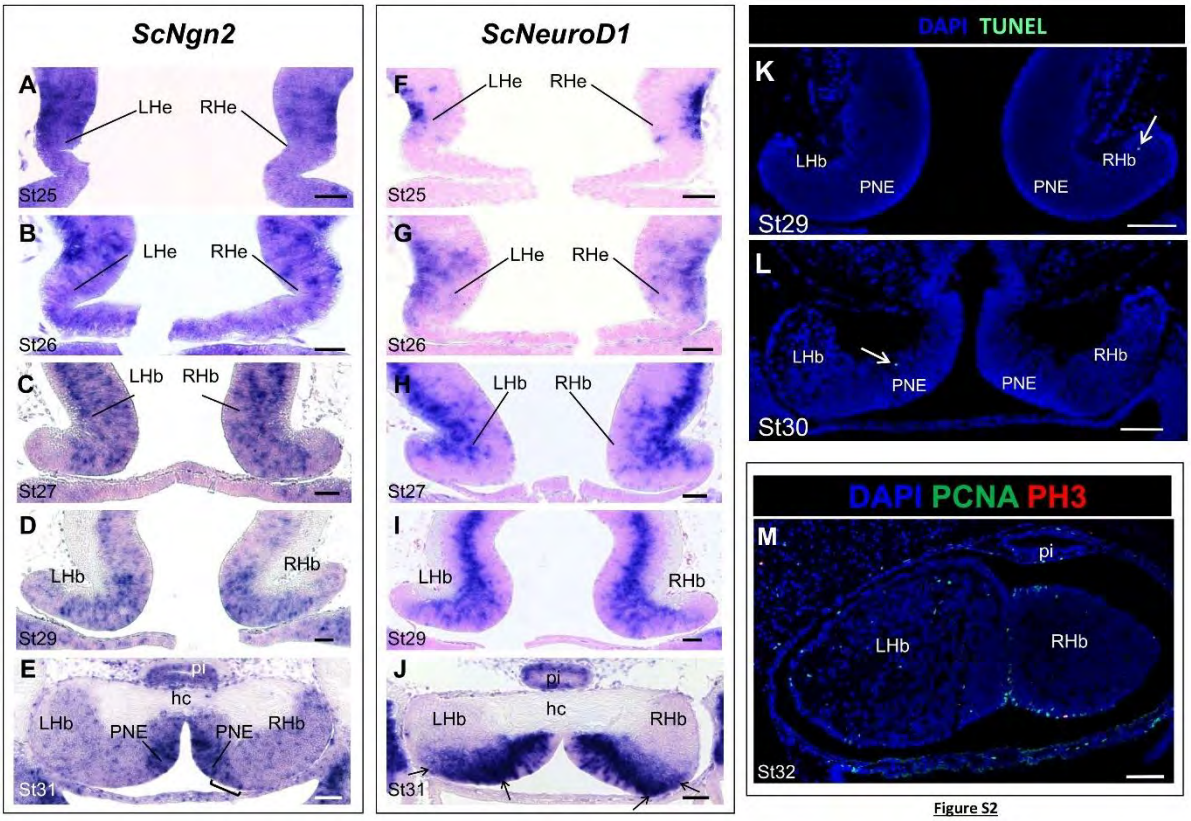

Figure S2

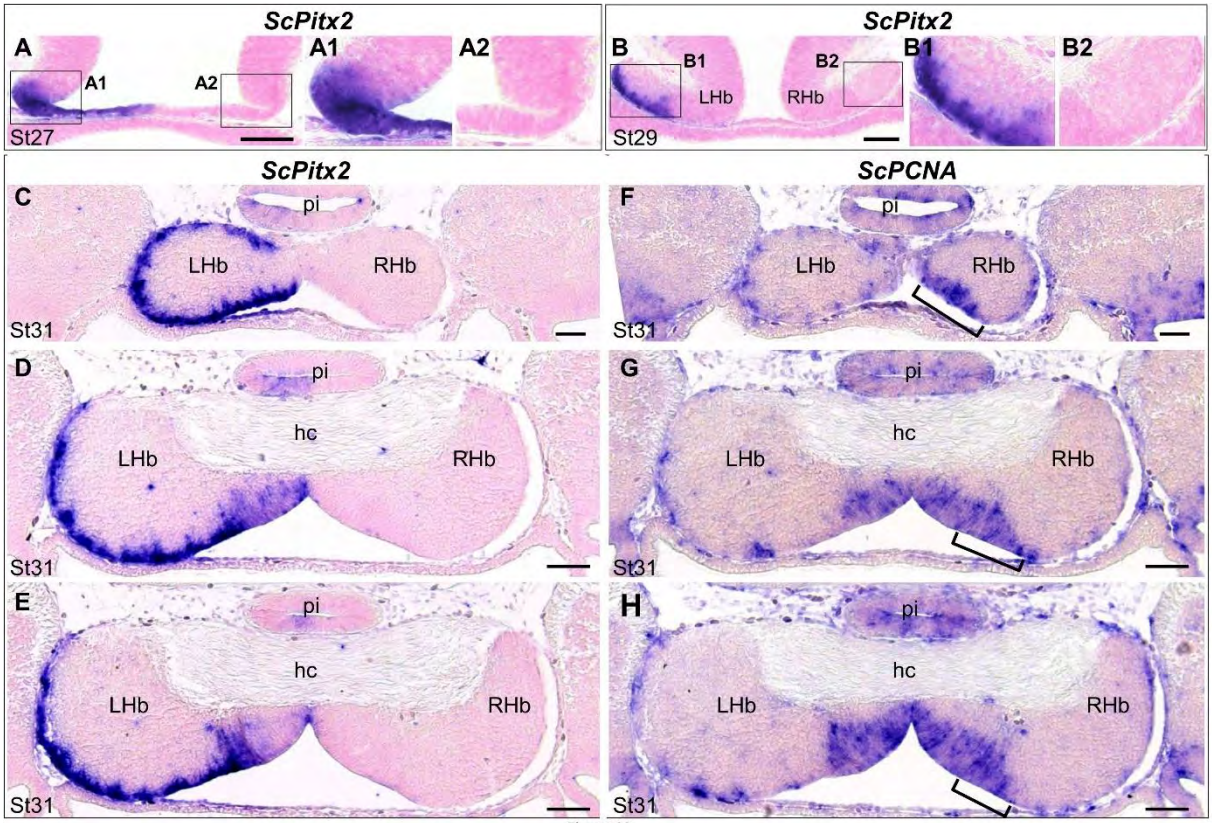
ScPitx2
A
A1
A2
St27
ScPitx2
B
B1
B2
LHb
RHb
St29
ScPitx2
ScPCNA
C
D
E
F
G
H
pi
hc
LHb
RHb
St31

Figure S3

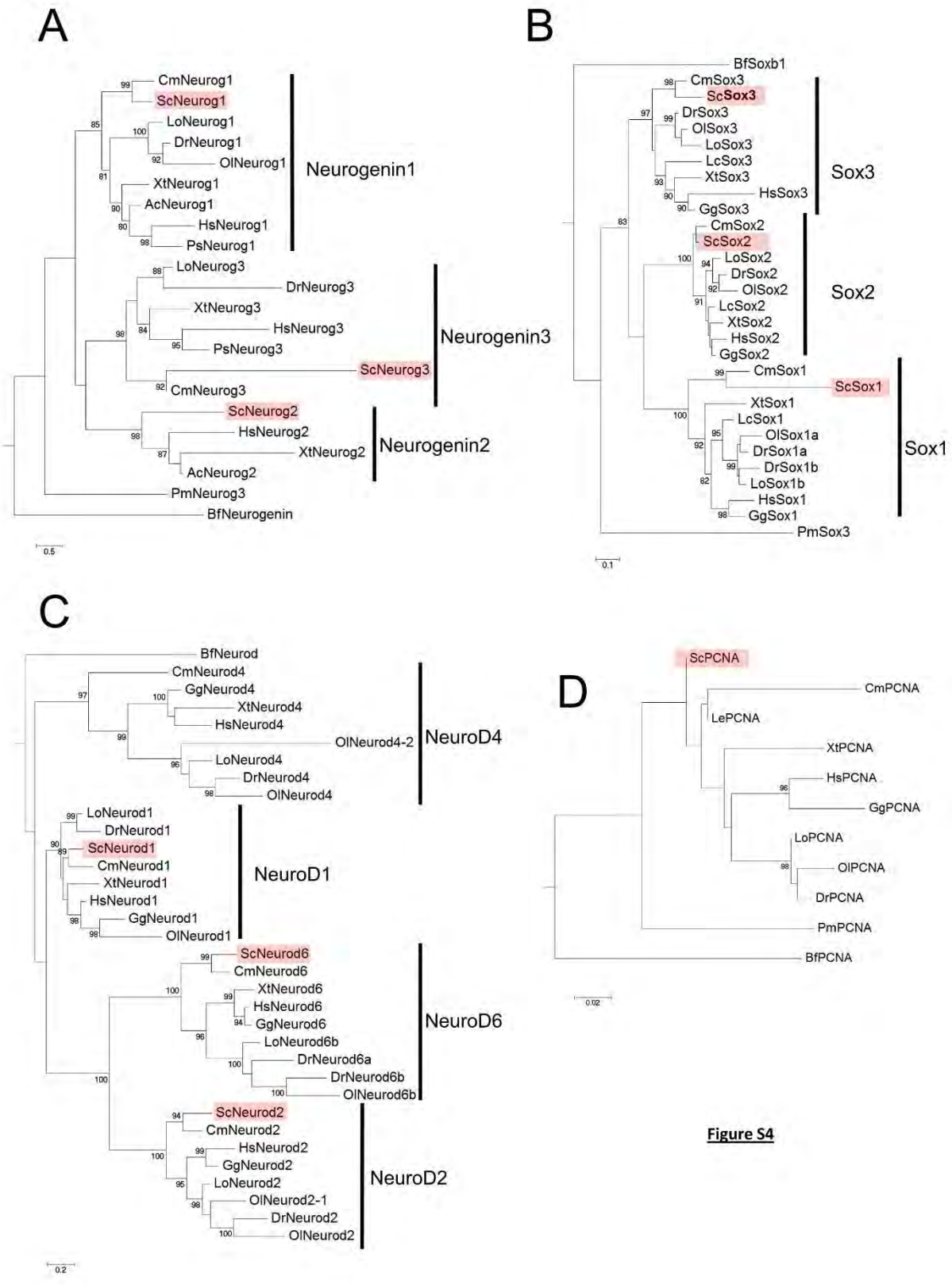
A
CmNeurog1
ScNeurog1
LoNeurog1
DrNeurog1
OlNeurog1
XtNeurog1
AcNeurog1
HsNeurog1
PsNeurog1
Neurogenin1
LoNeurog3
DrNeurog3
XtNeurog3
HsNeurog3
PsNeurog3
ScNeurog3
CmNeurog3
Neurogenin3
ScNeurog2
HsNeurog2
XtNeurog2
AcNeurog2
Neurogenin2
PmNeurog3
BfNeurogenin
0.5
B
BfSoxb1
CmSox3
ScSox3
DrSox3
OlSox3
LoSox3
LcSox3
XtSox3
HsSox3
GgSox3
Sox3
CmSox2
ScSox2
LoSox2
DrSox2
OlSox2
LcSox2
XtSox2
HsSox2
GgSox2
Sox2
CmSox1
ScSox1
XtSox1
LcSox1
OlSox1a
DrSox1a
DrSox1b
LoSox1b
HsSox1
GgSox1
Sox1
PmSox3
0.1
C
BfNeurod
CmNeurod4
GgNeurod4
XtNeurod4
HsNeurod4
OlNeurod4-2
LoNeurod4
DrNeurod4
OlNeurod4
NeuroD4
LoNeurod1
DrNeurod1
ScNeurod1
CmNeurod1
XtNeurod1
HsNeurod1
GgNeurod1
OlNeurod1
NeuroD1
ScNeurod6
CmNeurod6
XtNeurod6
HsNeurod6
GgNeurod6
LoNeurod6b
DrNeurod6a
DrNeurod6b
OlNeurod6b
NeuroD6
ScNeurod2
CmNeurod2
HsNeurod2
GgNeurod2
LoNeurod2
OlNeurod2-1
DrNeurod2
OlNeurod2
NeuroD2
0.2
D
ScPCNA
CmPCNA
LePCNA
XtPCNA
HsPCNA
GgPCNA
LoPCNA
OlPCNA
DrPCNA
PmPCNA
BfPCNA
0.02

Figure S4

ScSox2, stage 31

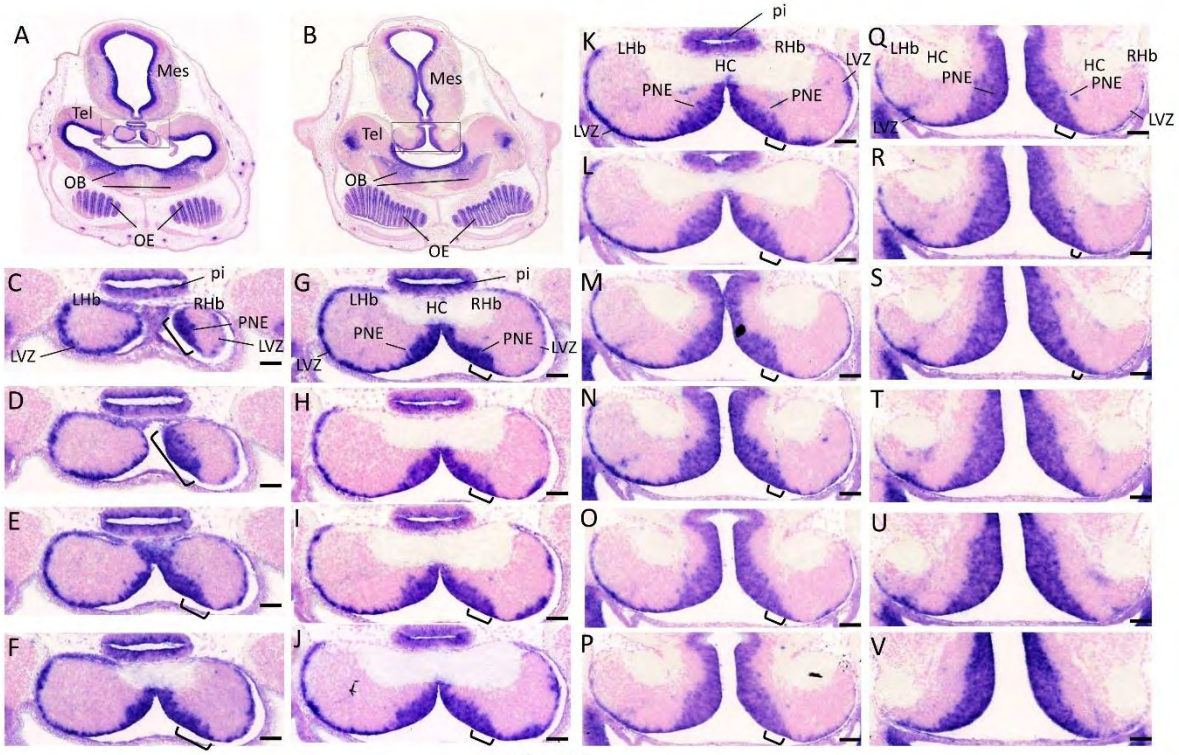

Figure S5

SUPPLEMENTARY TABLES

Stage 27				Stage 28				Stage 29			
Embryo	Left	Right	p-value	Embryo	Left	Right	p-value	Embryo	Left	Right	p-value
n°27.6	60	61	0.93	n°28.1	51	47	0.69	n°29.9	50	53	0.77
n°27.7	59	63	0.72	n°28.2	47	48	0.92	n°29.10	46	54	0.42
n°27.8	64	57	0.52	n°28.3	46	48	0.84	n°29.11	49	50	0.92

	Stage 30				Stage 31		
Embryo	Left	Right	p-value	Embryo	Left	Right	p-value
n°30.7	53	56	0.77	n°31.11	60	62	0.86
n°30.8	56	55	0.92	n°31.12	61	64	0.79
n°30.9	54	53	0.92	n°31.13	67	63	0.73

Table S1. Estimation of cell densities in the left and right developing habenulae

Quantifications were performed using images of habenula sections following DAPI or YOPRO-1 nuclear staining. For each embryo analysed (n=3 at each stage), a 10µm section was selected at a medial level of the developing habenulae and the total number of nuclei contained within a squared area of the PNE (50µm x 50µm) was counted on the left and on the right. These counts are indicated in the table, for each embryo analysed. X^2 tests, performed on cell counts for each individual embryo, showed no difference between the left and the right sides (p-values comprised between 0.4 and 1.0).

Stage 27								
	PNE				LVZ			
	Left	Right	AI (%)	X^2 p-value	Left	Right	AI (%)	X^2 p-value
n°27.1	235	218	3.8	0.5722	-	-	-	-
n°27.2	193	194	-0.3	0.9713	-	-	-	-
n°27.3	107	117	-4.5	0.6366	-	-	-	-
n°27.4	107	99	3.9	0.6935	-	-	-	-
n°27.5	246	252	-1.2	0.8492	-	-	-	-
n°27.6	190	183	1.9	0.7977	-	-	-	-
n°27.7	212	209	0.7	0.9177	-	-	-	-
n°27.8	142	146	-1.4	0.8676	-	-	-	-
Stage 29								
	PNE				LVZ			
	Left	Right	AI (%)	X^2 p-value	Left	Right	AI (%)	X^2 p-value
n°29.1	229	143	23.1	1.616E-03	14	16	-6.7	0.7963
n°29.2	389	273	17.5	1.433E-03	30	16	30.4	0.1444
n°29.3	297	303	-1.0	0.3768	29	16	28.9	0.1706
n°29.4	320	316	0.6	0.9107	24	17	17.1	0.4395
n°29.5	230	238	-1.7	0.7937	21	15	16.7	0.4795
n°29.6	221	215	1.4	0.839	14	12	7.7	0.7815
n°29.7	289	266	4.1	0.49	24	20	9.1	0.6698
n°29.8	285	270	2.7	0.6525	19	15	11.8	0.6276
Stage 30								
	PNE				LVZ			
	Left	Right	AI (%)	X^2 p-value	Left	Right	AI (%)	X^2 p-value
n°30.1	180	171	2.6	0.7341	13	9	18.2	0.5465
n°30.2	293	311	-3.0	0.6045	24	25	-2.0	0.9195
n°30.3	181	187	-1.6	0.825	14	15	-3.4	0.8955
n°30.4	151	155	-1.3	0.8715	19	16	8.6	0.7199
n°30.5	88	91	-1.7	0.874	15	16	-3.2	0.8989
n°30.6	199	207	-2.0	0.7789	15	14	3.4	0.8955
Stage 31								
	PNE				LVZ			
	Left	Right	AI (%)	X^2 p-value	Left	Right	AI (%)	X^2 p-value
n°31.1	127	267	-35.5	6.123E-07	33	19	26.9	0.1698
n°31.2	72	103	-18.7	9.752E-02	33	8	61.0	5.766E-03
n°31.3	162	223	-15.8	2.793E-02	41	26	22.4	0.195
n°31.4	108	163	-20.3	1.815E-02	18	10	28.6	0.285
n°31.5	72	113	-22.2	3.305€-03	21	9	40.0	0.1213
n°31.6	84	148	-27.6	2.967E-03	25	12	35.1	0.1307
n°31.7	81	136	-25.3	8.289E-03	28	16	27.3	0.2008
n°31.8	79	115	-18.6	6.761E-02	13	9	18.2	0.5465
n°31.9	52	85	-24.1	4.62E-02	14	4	55.6	9.558E-02
n°31.10	141	178	-11.6	0.143	29	15	31.2	0.1356

Table S2. Counts of PH3 positive nuclei and asymmetry index in the developing habenulae of stage 27 to 31 catshark embryos

For each individual embryo (1st column), PH3 positive nuclei were counted in the PNE at stages 27, 29, 30 and 31 (n=8,8,6 and 10 respectively), and in the LVZ at stages 29, 30 and 31 (n=8,6 and 10 respectively) from serial 10µm habenular sections. All habenular sections were taken into account in these counts. For each embryo analysed, the degree of asymmetry with regard to the number of PH3 positive cells in the PNE and in the LVZ was quantitatively expressed as an asymmetry index (AI), defined as the difference between counts of PH3 positive cells on the left versus the right side, normalised to the total number of PH3 positive cells. AI values in % are shown in the 4th column (PNE) and the 8th column (LVZ), respectively. Following count correction to take section thickness into account, X^2 test p-values were calculated for each embryo in order to detect statistically significant count differences between the left and the right (threshold =5E-02, green shading).

	Student's t-test (count data)	
	PNE	LVZ
stage 27	5,9050E-01	-
stage 29	1,1240E-01	1,5950E-02
stage 30	2,1900E-01	4,0170E-01
stage 31	4,0810E-04	4,1650E-05

Table S3. Statistical analysis of habenular asymmetry with regard to PH3 cell counts in the PNE and LVZ of stage 27 to 31 catshark embryos

The table shows the results of statistical tests of habenular asymmetry in the PNE (stages 27 to 31; column 2) and in the LVZ (stage 29 to 31; column 3), with regard to corrected PH3 cell counts of Table S2. For each condition (same zone and same stage), a paired Student's t-test was conducted in order to test whether the distribution of PH3 positive nuclei counts significantly differed between the left and the right. The corresponding p-values are shown in columns 3 and 6. P-values lower than 5E-02 were considered as indicative of a significant asymmetry and are shaded in green.

Stage 28				Stage 29				Stage 30			
Embryo n°	Left	Right	AI (%)	Embryo n°	Left	Right	AI (%)	Embryo n°	Left	Right	AI (%)
n°28.1	507	502	0.5	n°29.9	954	931	1.2	n°30.7	898	896	0.1
n°28.2	563	562	0.1	n°29.10	1171	1161	0.4	n°30.8	1018	1032	-0.7
n°28.3	629	659	-2.3	n°29.11	736	704	2.2	n°30.9	917	887	1.7

Table S4. Counts of BrdU labeled nuclei and asymmetry index in the PNE of catshark developing habenulae at stage 28-30

For each individual embryo (1st, 5th and 9th columns respectively at stages 28, 29 and 30), BrdU positive nuclei were counted and summed in the PNE following IHC with an antibody directed against BrdU. For each embryo analysed, the degree of asymmetry was quantitatively expressed as an asymmetry index (AI), defined as the difference between the number of BrdU positive cells on the left (2nd, 6th and 10th columns) versus the right (3rd, 7th and 11th columns) side, normalised to the total number of BrdU positive cells. AI values in % are shown in the 4th (stage 28), 8th (stage 29) and 12th (stage 30) columns. All X^2 tests, performed on individual embryos, showed an absence of significant difference in the number of labelled nuclei between the left and the right (p-values comprised between 0.399 and 0.976).

PNE, stage 31					
	Left, total	**Right, total**	**Right, expansion**	**Right, total - Right, expansion**	**X^2 p-value right (total - expansion) vs left (total)**
n°31.8	79	115	37	78	0.955
n°31.9	52	85	29	56	0.7855
n°31.10	141	178	36	142	0.9665

Table S5. Contribution of the right PNE expansion to the counts of PH3 positive cells in the right PNE

For each of the three stage 31 embryos shown, (1st column), PH3 positive nuclei were counted in the left and right PNE (2nd and 3rd columns). The expansion of the right PNE relative to the left was delineated based on PCNA immunoreactivity and PH3 positive nuclei were counted in this domain (4th column). The counts shown in the 5th column show the difference between the total count of PH3 cells in the right PNE and the latter value. X^2 tests, performed for each individual embryo on cell counts in the left PNE (2nd column) and the corresponding territory on the right (5th column), showed no statistically significant difference, supporting the conclusion that the higher number of PH3 positive cells in the right versus left PNE is due to the larger size of the former.

Stage 29								
	Left			Right			Pax6 AI (%)	X^2 p-value Pax6
	BrdU	Pax6	BrdU/Pax6 ratio (%)	BrdU	Pax6	BrdU/Pax6 ratio (%)		
n°29.9	74	380	19.5	52	210	24.8	28.8	2.582E-12
n°29.10	80	352	22.7	65	225	28.9	22.0	1.243E-07
n°29.11	81	481	16.8	63	292	21.6	24.5	1.062E-11
Stage 30								
	Left			Right			Pax6 AI (%)	X^2 p-value Pax6
	BrdU	Pax6	BrdU/Pax6 ratio (%)	BrdU	Pax6	BrdU/Pax6 ratio (%)		
n°30.7	80	498	16.1	47	362	12.9	15.8	3.525E-06
n°30.8	89	345	25.8	67	256	26.2	14.8	2.83E-04
n°30.9	71	496	14.3	57	341	16.7	18.5	8.434E-08

Table S6. Counts of BrdU and Pax6 labeled nuclei in the LVZ of catshark developing habenulae at stages 29-30

For each individual embryo (1st column), nuclei positive for the presence of BrdU (left, 2nd column; right, 5th column) and Pax6 (left, 3rd column; right, 6th column) were counted in the LVZ at stages 29 and 30 following IHC with antibodies respectively directed against BrdU and Pax6. The corresponding ratio (percentage of BrdU positive cells to Pax6 expressing ones) is shown in 4th (left) and 7th (right) columns. The degree of asymmetry with respect to Pax6 positive cell counts is quantitatively expressed as the asymmetry index (AI) shown in the 8th column, defined as the difference between the number of positive cells on the left versus the right side, normalised to the total number of positive cells. X^2 tests, performed for each individual embryo on Pax6 positive cell counts (9th column) show a statistically significant difference in Pax6 positive cell counts between the left and the right LVZ in all embryos analysed at stage 29 and 30. An asymmetry in the distribution of Pax6 positive cell counts is also supported by paired Student's t-tests at stage 29 (p-value=0.01257) and at stage 30 (p-value=0.02315). Paired Student's t-tests show a statistically significant asymmetry in the distribution of BrdU/Pax6 ratios at stage 29 (p-value=0.005869) but not at stage 30 (p-value=0.9551).

	PNE		LVZ		Other		Total	
	Left	**Right**	**Left**	**Right**	**Left**	**Right**	**Left**	**Right**
Stage 27	0	0	0	0	0	0	0	0
Stage 29	0	3	1	0	1	1	2	5
Stage 30	1	0	1	0	4	4	6	4
Stage 31	1	1	0	1	3	2	4	4
Stage 32	0	0	0	0	4	3	4	3

Table S7. Counts of apoptotic cells in the developing habenulae of stage 27 to 31 catshark embryos

For each stage (1st column), apoptotic cells were counted in the PNE (2nd and 3rd columns), LVZ (4th and 5th columns) and in the other territories (6th and 7th columns) of the left (2nd, 4th and 6th columns) and right (3rd,5th and 7th columns) habenulae of a single embryo following a TUNEL assay. For each stage, the total number of apoptotic cells in the left and right habenulae is shown in the 8th and 9th columns respectively. The TUNEL assay was done on 10µm habenular sections. At each stage, all habenular sections were taken account.

	PNE St. 31			LVZ St. 30 and St. 31		
	Untreated	Control	SB-505124	Untreated	Control	SB-505124
	Asymmetric phenotype	Asymmetric phenotype	Right isomerism	Asymmetric phenotype	Asymmetric phenotype	Right isomerism
ScSox2	1/1	3/3	2/2	4/4	3/3	2/2
ScNgn2	1/1	1/1	1/1	-	-	-
ScNeuroD1	1/1	2/2	1/1	-	-	-
ScPCNA	1/1	-	-	-	-	-
PCNA	9/9	1/1	1/1	-	-	-
HuC/D	2/2	1/1	1/1	2/2	1/1	1/1
DCX	1/1	1/1	1/1	4/4	1/1	1/1
Pax6	3/3	1/1	1/1	3/3	1/1	1/1
Embryos analysed, total	17/17	7/7	6/6	11/11	5/5	4/4

Table S8. Number of embryos analysed and habenular phenotypes observed in the PNE and LVZ
For each marker tested (1st column), ratios show the number of embryos exhibiting the phenotypes indicated in the 3rd line relative to the total number of embryos analysed. These ratios are shown for phenotypes observed in the PNE at stage 31 (2nd, 3rd and 4th columns) and in the LVZ at stages 30-31 (5th, 6th and 7th columns), in three conditions: untreated embryos (2nd and 5th columns), control, DMSO-injected embryos (3rd and 6th columns) and SB-505124 treated embryos (4th and 7th columns). The asymmetric phenotype in the PNE refers to a right expansion relative to the left, as described in Fig. 3, Fig. S2 and S5. The asymmetric phenotype in the LVZ refers to the preferential maintenance of neural progenitors on the left relative to the right as described in Results and Fig. 2.

Anti-acetylated tubulin	**Sigma T-6793**	**1:1000**
Anti-proliferating cell nuclear antigen (PCNA)	**Sigma P8825**	**1:300**
Anti-Histone H3 (phospho-S10)	**Abcam ab5176**	**1:400**
Anti-human HuC/D	**Molecular Probes A-21271**	**1:200**
Anti-doublecortin (DCX)	**Santa Cruz Biotechnology**	**1:300**
Anti-Pax6	**Abcam ab6326**	**1:200**
Anti-BrdU	**Abcam ab6326**	**1:100**

Table S9. Antibodies used
For each antibody (1st column), the reference and concentration used are shown in 2nd and 3rd columns respectively.

NEUROGENIN		NEUROD		SOX1/2/3	
CmNeurog1	XM_007901395.1	BfNeurod	XM_002586803.1	BfSoxb1	DQ644541.1
ScNeurog1	KX592193	CmNeurod4	XM_007886134.1	CmSox3	XM_007892868.1
LoNeurog1	ENSLOCT00000014228	GgNeurod4	ENSGALT00000041276	ScSox3	KX592197
DrNeurog1	ENSDART00000078563	XtNeurod4	ENSXETT00000014760	DrSox3	ENSDART00000075617
OlNeurog1	ENSORLT00000025439	HsNeurod4	ENSG00000123307	OlSox3	ENSORLT00000002213
XtNeurog1	ENSXETT00000017331	OlNeurod4-2	ENSORLT00000024677	LoSox3	ENSLOCT00000021635
AcNeurog1	ENSACAT00000001181	LoNeurod4	ENSLOCT00000022352	LcSox3	ENSLACT00000007556
HsNeurog1	ENST00000314744	DrNeurod4	ENSDART00000145072	XtSox3	ENSXETT00000016558
PsNeurog1	ENSPSIT00000004407	OlNeurod4	ENSORLT00000009362	HsSox3	ENST00000370536
LoNeurog3	ENSLOCT00000014195	LoNeurod1	ENSLOCT00000021971	GgSox3	AB011803.1
DrNeurog3	ENSDART00000002863	DrNeurod1	ENSDART00000011837	CmSox2	XM_007907767.1
XtNeurog3	ENSXETT00000055709	ScNeurod1	KX592190	ScSox2	KX592196
HsNeurog3	ENST00000242462	CmNeurod1	XM_007884678.1	LoSox2	ENSLOCT00000021488
PsNeurog3	ENSPSIT00000001125	XtNeurod1	ENSXETT00000030713	DrSox2	ENSDART00000104493
ScNeurog3	KX618851	HsNeurod1	ENST00000295108	OlSox2	ENSORLT00000014648
CmNeurog3	XM_007897988.1	GgNeurod1	ENSGALT00000014484	LcSox2	ENSLACT00000007461
ScNeurog2	KX592194	OlNeurod1	ENSORLT00000013242	XtSox2	ENSXETT00000004031
HsNeurog2	ENST00000313341	ScNeurod6	KX592192	HsSox2	ENST00000431565
XtNeurog2	ENSXETT00000052002	CmNeurod6	XM_007900862.1	GgSox2	ENSGALT00000014379
AcNeurog2	ENSACAT00000026370	XtNeurod6	ENSXETT00000050601	CmSox1	XM_007891764.1
PmNeurog3	ENSPMAT00000006843	HsNeurod6	ENST00000297142	ScSox1	KX618852
BfNeurogenin	XM_002596198.1	GgNeurod6	ENSGALT00000019978	XtSox1	ENSXETT00000004030
		LoNeurod6b	ENSLOCT00000015959	LcSox1	ENSLACT00000006057
PCNA		DrNeurod6a	ENSDART00000098859	OlSox1a	ENSORLT00000015157
ScPCNA	KX592195	DrNeurod6b	ENSDART00000018150	DrSox1a	ENSDART00000102021
CmPCNA	scaffold_5357	OlNeurod6b	ENSORLT00000022267	DrSox1b	ENSDART00000010894
LePCNA	LS-transcriptB2-ctg95554	ScNeurod2	KX592191	LoSox1b	ENSLOCT00000021941
XtPCNA	ENSXETT00000017963	CmNeurod2	XM_007901456.1	HsSox1	ENST00000330949
HsPCNA	ENST00000379143	HsNeurod2	ENST00000302584	GgSox1	AB011802.1
GgPCNA	ENSGALT00000000225	GgNeurod2	ENSGALT00000045217	PmSox3	ENSPMAT00000010751
LoPCNA	ENSLOCT00000019283	LoNeurod2	ENSLOCT00000021660		
OlPCNA	ENSORLT00000003670	OlNeurod2-1	ENSORLT00000004277		
DrPCNA	ENSDART00000076304	DrNeurod2	ENSDART00000002078		
PmPCNA	ENSPMAT00000008605	OlNeurod2	ENSORLT00000010417		
BfPCNA	XM_002588834.1				

Table S10. Accession numbers for sequences used for the phylogenies shown in Fig. S4

Novel catshark sequences were taken from Illumina transcriptomic or genomic datasets and are shown shaded in blue.

SUPPLEMENTARY REFERENCES

R Core Team (2015) R: A Language and Environment for Statistical Computing, *R Foundation for Statistical Computing*, https://www.R-project.org.

Edgar RC.(2004) MUSCLE: a multiple sequence alignment method with reduced time and space complexity. BMC Bioinformatics5:113

Kumar, S., Nei, M., Dudley, J., Tamura, K. (2008). MEGA: a biologist-centric software for evolutionary analysis of DNA and protein sequences. Brief Bioinform. *9*, 299-306.

Tippmann, H.F. (2004). Analysis for free: comparing programs for sequence analysis. Brief Bioinform. 5, 82-87.

CHAPITRE II – Origine et diversification des asymétries habénulaires chez les vertébrés : la roussette comme référence

II-1. Objectif, principaux résultats et conclusions

L'objectif de ce travail, qui a constitué l'essentiel de mon travail de thèse, était d'utiliser le modèle roussette en tant que référence pour comprendre l'évolution des asymétries habénulaires et des mécanismes de leurs formations. Pour cela nous avons mis en œuvre une triple stratégie : (1) une recherche transcriptomique des asymétries habénulaires chez la roussette à un stade (stade 31) où la différenciation neuronale est bien engagée (avec néanmoins le maintien de pools de progéniteurs asymétriques) et j'ai mené la validation par hybridation in situ (fixation, histologie, synthèse de sondes, hybridation *in situ* sur lames, imageries) .(2) J'ai ensuite réalisé des comparaisons à partir des résultats obtenus chez la roussette, en incluant des espèces occupant des positions phylogénétiques d'intérêt chez les chondrichtyens, avec les actinoptérygiens et les tétrapodes. (3) Enfin, j'ai effectué une étude des mécanismes impliqués chez la roussette, ciblé sur la voie de signalisation Wnt (traitements pharmacologiques). Les résultats obtenus conduisent à trois conclusions principales :

(1) Les habénulas de roussette présentent, sur un axe médio-latéral, une organisation fortement asymétrique en trois grands sous-domaines, avec un domaine bilatéral médian (MHb, de taille différente à droite et à gauche) flanqué de deux domaines latéraux d'identité moléculaires très différentes quasi intégralement restreints à droite et à gauche (Right-LHb et Left-LHb). Le domaine médian présente lui-même des subdivisions sur l'axe médio-latéral, avec des identités moléculaires distinctes dans ses régions latérales gauche et droite

(2) Cette organisation tripartite est retrouvée chez les actinoptérygiens. Mais (1) cette organisation médio-latérale chez les chondrichtyens est convertie en une organisation dorso-ventrale chez les actinoptérygiens. Et (2) les localisations asymétriques chez les chondrichtyens des territoires apparentés aux domaines latéraux Left-LHb et Right-LHb de roussette sont perdues au cours de l'évolution des actinoptérygiens (mais conservées chez un polyptère, en accord avec leur caractère ancestral chez les gnathostomes et leur maintien à l'origine des actinoptérygiens). Cette conservation ne se retrouve pas clairement chez les tétrapodes étudiés, chez lesquels l'organisation des habénulas rappelle celle de l'habénula gauche des chondrichtyens

(3) l'étude des mécanismes de formation des asymétries des domaines latéraux de roussette (Left- and Right-LHb) met en évidence des similitudes avec le poisson-zèbre: régulation temporelle de la sortie des cycles mitotiques des progéniteurs des grands sous-domaines identifiés, rôle essentiel de la voie Wnt canonique dans le choix de l'identité neuronale droite (Right-LHb versus Left-LHb chez la roussette), régulation dynamique de la voie avec une répression à gauche pendant une fenêtre temporelle bien définie.

Plusieurs aspects de ce travail doivent être consolidés (caractérisation moléculaire du domaine ventral gauche du polyptère étudié et du domaine latéral du xénope; analyse d'un dipneuste; extension des caractérisations moléculaires des habénulas de roussette après traitement pharmacologique dirigé contre la voie Wnt; analyses fonctionnelles chez le

poisson-zèbre en vue d'évaluer les conservations de fonction de la voie Wnt) , Ces données fournissent néanmoins d'ores et déjà les premières indications moléculaires quant à l'origine et au mode de diversification des asymétries habénulaires chez les gnathostomes. Elles suggèrent également une implication de la voie Wnt dans ces deux aspects, sous le contrôle de la voie Nodal chez la roussette mais sous le contrôle de la parapinéale chez le poisson-zèbre. Ce travail fait l'objet d'un manuscrit en préparation (voir ci-après).

II-2. Publication

The formation and diversification of habenular asymmetries rely on a core, Wnt dependent mechanism shaping neuronal identities in the epithalamus

Maxence Lanoizelet[1], Ronan Lagadec[1], Hélène Mayeur[1], Léo Michel[1], Kyle Martin[2], Christophe Klopp[3], Sylvain Marcellini[4], Nicolas Pollet[5], Mélanie Debiais-Thibaud[6], Catherine Boisvert[7], Bernard Billoud[8], Patrick Blader[9], Sylvie Mazan[1]

[1]CNRS, Sorbonne Université, UMR7232-Biologie Intégrative des organismes marins (BIOM), Observatoire Océanologique, Banyuls sur Mer, France

[2]UK Research and Innovation, Biotechnology and Biological Sciences Research Council Affiliations, UK

[3]Plateforme Bioinformatique, Genotoul, BioinfoMics, UR875 Biométrie et Intelligence Artificielle, INRAE, Castanet-Tolosan, France

[4]Department of Cell Biology, Faculty of Biological Sciences, Universidad de Concepción, Concepción, Chile

[5]Université Paris-Saclay, CNRS, IRD, Évolution, Génomes, Comportement et Écologie, Université Paris-Saclay, Gif-sur-Yvette, France.

[6]ISEM, Université de Montpellier, CNRS, IRD, EPHE, Montpellier, France

[7]School of Molecular and Life Sciences, Curtin University, Perth, WA, Australia.

[8]UMR8227, CNRS-Sorbonne Université, Station Biologique, Place Georges Teissier, 29680 Roscoff, France

[9]Centre de Biologie Intégrative (CBI, FR 3743), Université de Toulouse, CNRS, UPS, France

Abstract

The presence of habenular asymmetries is a recurrent trait in vertebrates, albeit with a high variability in nature and degree. Whether a conserved regulatory logic may underlie their formation and diversification during evolution is currently unknown. To address this issue, we have characterised habenular asymmetries in a chondrichthyan, the catshark *Scyliorhinus canicula*, which by its phylogenetic position and marked habenular asymmetries, provides an excellent comparative reference. In this species, habenulae are organised into three territories characterised by distinct molecular identities, a bilateral medial one (MHb) exhibiting an asymmetric subdomain organisation, a lateral left-restricted one (Left-LHb) and a lateral right-restricted one (Right-LHb). Comparisons across a wide range of jawed vertebrates including the elephant shark, reedfish, spotted gar, zebrafish, xenopus, and mouse, indicate that this tripartite organisation is ancestral in jawed vertebrates. However, very different patterns of asymmetry are observed, territories related to the catshark Left- and Right-LHB appearing bilateral in all osteichthyans analysed except the reedfish. In the catshark, neurogenesis of the different habenula subdomains follows a temporal sequence and a repression of Wnt signaling on the left at the time when Left- and Right-LHb differentiates controls their respective neuronal identity choice, promoting Right- versus Left-LHb neuronal identity. These data point to Wnt signaling as a conserved mechanism controlling neuronal identities in the epithalamus of jawed vertebrates and indicate that variations of its regulation in time and space may be a driving force in habenular asymmetry diversifications across the taxon.

Introduction

Habenulae are bilateral epithalamic structures, present in all vertebrates, known to integrate information from multiple sources, including sensory organs and corticolimbic areas (Beretta et al., 2012), and to regulate complex behavioural (Andalman et al., 2019), cognitive (Mathis et al., 2017), and emotional responses (Matsumoto & Hikosaka, 2007; Alice M Stamatakis & Stuber, 2012). These functions develop sequentially during development, habenular neurons harbouring distinct functional properties depending on birthdate (Fore et al., 2020). An intriguing feature of this structure is that it displays asymmetries, which can considerably vary in nature -size, cellular or nuclei organisation, connectivity pattern and degree, in a recurrent manner across vertebrates (Concha & Wilson, 2001). The biological significance of these asymmetries has started to emerge in the zebrafish, the reference model for analyses of both their roles and mechanisms of formation (Roussigné, Blader, & Wilson, 2012). In this species, sensory cues are differentially processed between the right and left habenulae, and asymmetries have been shown to impact important adaptive responses such as exploratory (Facchin et al., 2015) and food-seeking behaviours (W. yu Chen et al., 2019), light preference (Dreosti, Vendrell Llopis, Carl, Yaksi, & Wilson, 2014a) or responses to fear (Duboué, Hong, Eldred, & Halpern, 2017). Their degree of conservation and mode of diversification across vertebrates remains unclear. Similarly, whether their pattern of

occurrence and the variations in degree, which they exhibit, reflects independent convergent processes, or parallel ones, related to conserved developmental constraints, is unclear. To date, detailed molecular characterisations of habenular asymmetries and analyses of underlying mechanisms have only been reported in the zebrafish, the only established model to exhibit a marked organ laterality (Concha, Signore, & Colombo, 2009; Roussigné et al., 2012). In this species, habenulae are partitioned into dorsal and ventral territories, asymmetries being restricted to the former and consisting in different relative proportions between two subdomains, the dorsal lateral (dHbl) and dorsal medial (dHbm) habenulae, respectively prevailing on the left and on the right (deCarvalho et al., 2014; Gamse, 2003; Gamse et al., 2005a). Their formation involves a left repression of Wnt signalling, the pathway promoting dHbm neuronal cell fate choices in this context (Hüsken et al., 2014). This repression takes place during a narrow time window, under the control of a yet unidentified signal secreted on the left by the parapineal (Faro et al., 2019) and Wnt effect on neuronal differentiation may be related to its capacity to delay neurogenesis in a changing habenular environment, therefore promoting late-born dHbm, versus early-born dHbl neuronal identities (Guglielmi et al., 2020). While a subdivision of habenulae into two domains (dorsal and ventral in the zebrafish, medial and lateral in the mouse) appears conserved in the mouse, albeit based on a very limited number of marker genes, there is no evidence of asymmetric territories equivalent to zebrafish dHbm and dHbl (Amo et al., 2010; Hashikawa et al., 2020a). Analyses of two non-conventional models harbouring marked habenular asymmetries in size, the lamprey and catshark, have highlighted bilateral asymmetric habenular expressions of Kctd family members, which mark different subdomains of the dorsal habenula in the zebrafish. However, this analysis provided no evidence for a conserved subdomain organisation. Furthermore, it highlighted a major mechanistic divergence with the zebrafish: in both species, Nodal signalling was required for asymmetry formation while it is dispensable in the zebrafish (Lagadec et al., 2015). To clarify the mode of evolution of habenular asymmetries across gnathostomes, we have taken as reference the catshark *Scyliorhinus canicula*, which, as a member of chondrichthyans (cartilaginous fishes), the closest outgroup of osteichthyans, provides a relevant reference to explore their origin (Coolen et al., 2008). We find that habenulae in this species display a tripartite subdomain organisation of habenulae, whose marked asymmetry is gradually lost in actinopterygians and, independently, in tetrapods. We also highlight a conserved regulatory logic for their formation, involving a flexible temporal and spatial regulation of Wnt signaling, which could account for the evolvability of habenular asymmetries across vertebrates.

Results

RNA-seq identifies novel habenular asymmetries in the catshark

In order to obtain an exhaustive characterisation of molecular asymmetries in the catshark developing habenulae, we conducted a transcriptomic comparison between stage 31 left and right habenulae. At this stage, a large fraction of the organ is differentiated but asymmetric progenitor pools persist (Lagadec et

al., 2018). Statistical analysis of about 362 million read pairs (PE100) obtained from three left versus right pools of dissected habenulae explants led to the identification of 614 differentially expressed gene models (373 left-enriched and 241 right-enriched), of which 538 can be annotated as protein coding (Supplementary Table 1). In order to explore their biological significance, we searched for over-represented GO terms for biological processes in the lists of left- and right-enriched genes, taking as reference the overall repertoire of habenula expressed genes (Supplementary Table 2). The analysis of the corresponding list, to be presented in Figure 1 is in progress.

Catshark habenulae exhibit an asymmetric, lateral to medial subdomain organisation

In order to characterise the spatial organisation of asymmetries in stage 31 habenulae, we conducted in situ hybridisation (ISH) for 43 genes, selected on statistical support or fold change from the list of left- or right-enriched genes obtained by the transcriptomic analysis (Suppl. Table 3). Highly specific expression territories, restricted to well-defined habenular subdomains and prevailing either on the left or on the right as predicted by the transcriptomic analysis, were obtained for 35 genes, 3 of them restricted to neural progenitors and the remaining 32 expressed in differentiated domains (Fig.2, Suppl. Fig. 1-5). ISH analysis was restricted to the latter. Unexpectedly, most 29 out of these 32 genes can be classified into no more than five broad categories, based on expression profile (Fig. 1q; Suppl. Fig. 1-5). Among left-enriched genes, three (*ScKctd12b*, *ScNrp2*, *ScStac*) are expressed in a broad bilateral medial territory (MHb, or medial habenula), larger on the left than on the right, also expressing previously characterised *ScKctd8* (Lagadec et al., 2015)(Fig. 2b,e,h-k; Suppl. Fig. 1b). This territory is itself divided into two subdomains, forming together bilateral radial bands restricted to its outer part. The left one (Left-MHb), identified by *ScPde1a*, *ScKctd12a*, *ScPtprm*, *ScSpon1*, *ScStk32c*, *ScTrhr2* and *ScTrhde* co-expressions, is restricted to the anterior part of the left radial band (Fig. 2c,h; Suppl. Fig. 1d). The other one (Right-MHb), defined by *ScEnpp2* and *ScEya2* expressions, is restricted posteriorly on the left, complementary to Left-MHb, and spans the whole right radial band in the outer part of MHb (Fig. 2d,k; Suppl. Fig. 1e). Two additional broad subdomains occupy the lateral parts of the habenulae, complementary to MHb, Left-LHb co-expressing *ScSox1*, *ScNtng2* and *ScPcdh17* on the left, and Right-LHb co-expressing *ScAk5*, *ScGng14*, *ScKiss1*, *ScPrkcb*, *ScPrkcq*, *ScProx1, ScRergl*, *ScShh*, *ScSlc5a7*, *ScStxbp6*, *ScTrib1*and *ScWisp1* on the right (Fig. 2f,g,j,k; Suppl. Fig. 1a and 1c). While these genes are almost completely restricted to one side of the habenulae, minor territories can be noted on the contralateral side, in the posterior part of habenulae (Fig 2o; Suppl. Fig.2b-f; Suppl. Fig. 3b-f). These broad expression characteristics are maintained in juveniles (Fig. 2l-p; Suppl. Fig. 4-5).

A tripartite habenula organisation is retained in chondrichthyans and actinopterygians

To explore how habenular asymmetries diversify in jawed vertebrates, we next assessed the conservation of the habenular organisation in the three main gnathostome taxa, chondrichthyans, actinopterygians and sarcopterygians, taking the catshark as reference. Analysis was focussed on orthologues of markers

of Left-LHB (*Sox1*, *Ntng2*, *Pcdh17*), Right-LHB (*Prox1*, *Kiss1*, *RORa*), and MHb (*Kctd8/12/12b*) and on four species selected for their phylogenetic position, the elephant shark *Callorhinchus milii* (holocephalan), the frog *Xenopus tropicalis*, and two non-teleost ray-finned fishes, the reedfish *Erpetoichthys calabaricus* (bichir) and the spotted gar *Lepisosteus oculatus*, which both diverged from the teleost lineage prior to the 3R genome duplication. All except xenopus exhibit marked habenular asymmetries in size, the right habenula appearing larger than the left one, unlike the catshark and zebrafish. In the elephant shark, habenula organisation into almost completely left or right-restricted lateral domains (respectively expressing *Sox1/Pcdh17/Ntng2*, and *Prox1/ Kiss1/Rorα*: Fig. 3e-h, Suppl. Fig. 6) complementary to a *Kctd8/12b* medial territory is largely conserved with the catshark. Only minor differences are observed with the catshark, including a left expansion of *CmKiss1* in a dorsal medial territory of relatively low *CmKctd12b* expression (Suppl. Fig. 6f-g). In both actinopterygians analysed, complementary territories respectively expressing members of the *Kctd8/12* gene familly, *Prox1* and *Sox1* were also identified, albeit with different relative organisations and asymmetry patterns. In the spotted gar, *Kctd12b* and *Prox1*/*Kiss1* span adjacent, respectively dorsal and ventral territories (Fig. 3m,o; Suppl. Fig. 7e-g). Ventrally, the latter largely excludes a minor *Sox1/Pcdh17* territory, which prevails in the anterior ventral part of the habenulae (Fig. 3n; Suppl. Fig. 7c,d,). While habenulae exhibit a major size difference (with a larger right habenula), these three territories are bilateral, occupying similar relative proportions of the organ on the left and the right. In the reedfish, *Kctd12a* and *Kctd12b* exhibit bilateral expressions as in the catshark and spotted gar, but only the former is restricted to a well delimited dorsal subdomain (Fig. 3i; Suppl. Fig. 8e-f). An anterior ventral territory co-expressing orthologues of catshark Left-LHb markers (*Sox1*, *Ntng2*, *Pcdh17*) and complementary to the *Kctd12a/12b* domain, also exists but contrary to the spotted gar, it is restricted to the left as in the catshark (Fig. 3j, Suppl. Fig. 8b-d). *Prox1* expression spans most of the right habenula, largely overlapping with *Kctd12a*/*12b* dorsally but only concerns a minor ventral domain, adjacent to *Sox1*/*Ntng2*/*Pcdh17* expressing cells on the left (Fig. 3k; Suppl. Fig. 8g). In order to further clarify the evolution of habenular asymmetries in the actinopterygian lineage, we also examined whether catshark Left- and Right-LHb markers have orthologues within the lists of signature genes of regionalised cell clusters, as inferred from a scRNA-sequencing of zebrafish larval and adult habenulae (Pandey et al., 2018). Seven markers of catshark LHbs fulfill this criterion (*Ak5*, *Gng14*, *Kiss1*, *Prkcq*, *Rergl*, *Prox1* and *Sox1*). Zebrafish orthologues for the former five ones are retrieved from the list of top markers for larval Hb15 or adult VHb01, two cell clusters spanning broad ventral habenula territories, an occurrence having a low probability on a random basis. Both zebrafish *Sox1* paralogues (*sox1a*/*sox1b*) are also found in a ventrally restricted cell cluster, concerning a more discrete territory (Hb11), while *prox1a,* the only *Prox1* paralogue retained in the zebrafish, is a marker of a cell clusters mapping to a broad, right enriched territory spanning both ventral and dorsal habenulae (Hb01). In sarcopterygians, xenopus *Kctd8* is restricted to a medial habenula subdomain, overlapping with *Kctd12b* and *Prox1* territories posteriorly, and complementary to a *Sox1* lateral territory laterally, without evidence for any asymmetry

(Fig. 3q-s; Suppl. Fig. 9b-e). This organisation is reminiscent of the one reported in the mouse, with medial habenulae expressing *Kctd* gene family members (Metz, Gassmann, Fakler, Schaeren-Wiemers, & Bettler, 2011) and lateral ones expressing *Sox1*(Kan et al., 2007). In summary, these data show that chondrichthyans and actinopterygians share a tripartite organisation of habenulae, albeit with highly variable asymmetry patterns. This organisation is lost in tetrapods.

Asymmetries within medial/dorsal habenulae vary extensively across jawed vertebrates

We next examined the conservation of the partitioning and asymmetry patterns within the medial (chondrichthyans and tetrapods) or dorsal (actinopterygians) territories related to catshark MHb. In the elephant shark as in the catshark, a partitioning of the *Kctd8/Kctd12b* territory into medial and lateral components, themselves subdivided along the dorso-ventral and antero-posterior axes, is observed, albeit with a number of differences. In the elephant shark, *Kctd12a* thus defines a medial left, rather than lateral left subdomain of MHb as in the catshark (Fig. 4f-h; data not shown). Its domain largely overlaps with the *Trhde* one as in the catshark, but not with the *Trhr2* one, transcribed in the right side contrary to the catshark (right dorsal MHb subdomain) (Fig. 4h,i,j; compare Fig. 4c-e with Fig. 4h-j). In the spotted gar, *Kctd12a* delimits a medial subdomain of *Kctd8/12b* territories (compare Fig. 4k,l with Fig. 4m) as in chondrichthyans but contrary to them, this domain is bilateral. While no habenular *Trhr2* signal could be detected (Fig. 4o), *Trhde* is preferentially expressed in a small dorsal *Kctd8* negative territory strongly expressing *Kctd12b* (Fig. 4k,m,n,d). Finally in *Xenopus tropicalis*, no *XtKctd12a* is detected, *XtKctd8* is broadly expressed in the medial habenula while *XtKctd12b* is excluded from anterior regions of the organ (Fig. 4p-r; Suppl. Fig 9d-e). Rather than being restricted to dorsal/medial habenula subdomains as in chondrichthyans and actinoperygians, *Trhde* and *Trhr2* are also both broadly expressed in the medial habenula with very similar patterns to *Kctd8* (Fig. 4s-t). These data do not highlight any clear conservation between the species studied either in terms of subdomain organisation, or asymmetry pattern, suggesting a rapid divergence of the partitioning within the dorsal/medial habenula across gnathostomes.

Wnt signaling promotes Right-LHb identity in the catshark lateral habenulae

In the zebrafish, Wnt signaling is required both for asymmetry formation and for expression of ventral habenula markers, whose orthologues are restricted to Right-LHb in the catshark, such as *Kiss1* (Beretta et al., 2013). β-catenin distribution appears dynamic during habenula development in the catshark, with a bilateral nuclear accumulation of β-catenin in most nuclei of differentiating territories of the forming habenulae at stage 27 (Suppl. Fig. 10a), which largely disappears at stage 28 (Suppl. Fig. 10b). Starting from stage 29, distribution becomes markedly asymmetric, with a nuclear accumulation restricted to the right habenula, in its lateral parts (Suppl. Fig. 10c-d). To directly test the involvement of the pathway in

asymmetry formation, we inhibited its activity by *in ovo* injection of the Wnt antagonist IWR-1 (Fig. 5, Suppl. Fig. 11). A single injection of the drug at stage 29 results in the loss of *ScProx1* along a radial band contained within the gene territory (compare Fig. 5c-d with Fig. g-h). A concomitant right expansion of *ScSox1* is consistently observed, in territories exactly superimposable to those where *ScProx1* expression is lost, suggesting that Wnt signaling is required for the establishment of habenula right identity (compare Fig. 5a-b with Fig. 5e-f and Fig. 5g-h). In contrast, expressions of *ScEnpp2* and *ScPde1a* were maintained in expected territories treated embryos (Suppl. Fig. 11). In order to assess whether inhibition of Wnt signaling can compensate for the loss of Nodal signaling during its diencephalic left restricted window of activity, we next conducted Wnt loss of function in the conditions described above in control or SB-505124 treated embryos as described previously (Lagadec et al., 2015)(Fig. 5i-p; Suppl. Fig. 12). In ovo injection of SB-505124 results in a complete loss of Left-LHb *ScSox1* expression, concomitant with an expansion of *ScProx1* at this level, confirming the essential role of Nodal in left habenula identity formation (compare Fig. 5i-j with 5m-n; Suppl. Fig.12a-b with Suppl. Fig. 12e-f). In double-treated embryos, Left-LHb *ScSox1* expression is restored, suggesting that Nodal role in the formation of Left-LHb is mediated by a Wnt repression (compare Fig. 5m-n with 5o-p; Suppl. Fig.12e-f with 12g-h). A left expansion of the profile of β-catenin nuclear accumulation is accordingly observed following SB-505124 treatment (compare Suppl. Fig. 10e and 10f).

Left- and Right-LHb progenitors exit cell cycles prior to stage 29

In order to address when Left- and Right-LHb progenitors exit cell cycles and assess neurogenesis status at the time of Wnt loss of function in the conditions described above, we conducted BrdU (5-bromo-2'-deoxyuridine) pulse chase assays, with BrdU incorporations at stages 26, 27, 28, 28+ and 29 and analysis of the distribution of labelled cells at stage 31 (Fig. 6; Suppl. Fig. 13). At all stages analysed, the signal maximal intensity is observed along radial bands, which gradually regress from lateral to medial habenula levels (compare Fig. 6a1-6 to 6d1-6). Except at anterior-most levels after a pulse at stage 26 (Fig. 6a1) asymmetric distributions of labelled cells are also visible following incorporations from stages 26 to 28+, with higher cell densities on the right than on the left (Fig. 6b1,c1,a3,b3,c3,a5,b5,c5). To analyse the neuronal identity of these cells at stage 31, we mapped their location relative to Left-LHb, MHb and Right-LHb, visualised on adjacent sections by fluorescent ISH. Following incorporation at stage 26, BrdU positive cells are excluded from the lateral-most parts of Left- and Right-LHbs (*ScKctd12b* negative), as well as the dorso-lateral left expansion of *ScKctd12b* domain, also expressing *ScPde1a* and absent from the right (Fig. 6a; Suppl. Fig. 13a). The lateral border of this BrdU negative territory regresses from lateral to medial levels of the organ with incorporations conducted at 28, 28+ and 29 (compare Fig. 6b1-6 to 6d1-6). Labelled cells become undetectable in Left- and Right-LHbs following pulses at stage 28+ on the left and at stage 29 on the right (Fig. 6c and 6d). This temporal regulation of neuronal birth dates from lateral to medial habenula levels also takes place within the bilateral MHb territories (excluding the early-born left-restricted *ScPde1a* dorso-lateral region

mentioned above). BrdU positive cells are found within both Left-MHb (*ScPde1a* positive) and Right-MHb (*ScEnpp2* positive) when BrdU is incorporated at stage 28+ but this labelling disappears when incorporation is conducted at stage 29 (compare Suppl. Fig. 14 a and 14b).

Discussion

The characterisation of asymmetries in the catshark habenulae is the first unbiased one in another species than the zebrafish to our knowledge. It reveals a highly asymmetric, lateral to medial organisation, with a partitioning into three broad territories expressing a number of distinct signature genes, two lateral ones (Left- and Right-LHb) and a bilateral medial one (MHb).

Ancestral tripartite organisation of habenulae in jawed vertebrates

Comparisons with an holocephalan, two non-teleost actinopterygians and an amphibian highlight partial similarities to this tripartite organisation, which makes it possible to outline the gnathostome ancestral state. A bilateral medial (tetrapods and chondrichthyans) and dorsal (actinopterygian) territory expressing at least one *Kctd* family member is shared by all species analysed in this study, as well as by the mouse and the zebrafish. This strong conservation is consistent with the homology previously proposed between the medial habenula of mammals and dorsal habenula of teleosts (Amo et al., 2010; Hashikawa et al., 2020a), and is consistent with connectivity analyses, suggesting an ancient origin of this habenular territory in vertebrates (Schmidt & Pasterkamp, 2017). Expression of *Trhr2* or *Trhde* in all or part of this territory, as observed in the catshark, the elephant shark, the spotted gar (this study) or the mouse (O'dowd et al., 2000), supports this conclusion, although we find that this characteristic has been differentially retained dependent on species. Concerning Left- and Right-LHb, they are unambiguously conserved between the catshark and the elephant shark, based on lateral location and several signature markers, indicating that the partitioning observed in the catshark reflects the chondrichthyan ancestral state (Fig. 7a). Unexpectedly, two distinct ventral territories sharing several gene signatures with the former two can be identified in actinopterygians. In the reedfish, while expression analysis of catshark Right-LHb orthologues has to be expanded, the presence of a ventral (rather than lateral), Left-LHb related territory is strongly supported both by its left restriction and expression of *Sox1/Pcdh17/Ntng2* as in the catshark. It can also be inferred in the spotted gar, based on *Sox1/Pcdh17* expression and an anterior ventral location very similar to the reedfish. Similarly, a bilateral ventral territory expressing *Prox1* and *Kiss1*, largely excluding and complementary to both the *Kctd* positive dorsal habenula and the *Sox1/Pcdh17* anterior ventral domain, can be observed in the spotted gar (Fig. 7a). An overlap between these three territories is difficult to exclude with a cellular resolution based on ISH in the reedfish and spotted gar. However the identification in the zebrafish of distinct ventrally restricted cell clusters, Hb11 and Hb15 (Pandey et al., 2018) respectively including *Sox1* orthologues, or *Ak5/Gng14/Kiss1/Prkcq/Rergl* (albeit not *Prox1*), in their list of top markers,

suggests that these domains are also present in the zebrafish, and that these markers are relevant to discriminate between their respective cell types. Taken together, these data suggest that a partitioning into three subdomains is an ancestral characteristic of habenulae in jawed vertebrates, retained in chondrichthyans but also recognizable in polypterids, holosteans and teleosts, three taxa occupying key phylogenetic positions in actinopterygians (Fig. 7a). Concerning sarcopterygians, we find that *Sox1* is a lateral habenula marker, with a territory complementary to the *Kctd* positive medial habenula, in xenopus (these data) as reported in the mouse (Kan et al., 2007) This organisation is reminiscent of the catshark left habenula. More detailed analyses will be needed to clarify evolutionary trends of territories related to Right-LHb in the taxon but neither *Kiss1*, *Prox1* or *RORα*, three markers of Right-LHb in the catshark, harbour habenular expression in the mouse, suggesting a loss of their habenular territory in the tetrapod lineage (Fig. 7a) (Clarkson, d'Anglemont de Tassigny, Colledge, Caraty, & Herbison, 2009; Galeeva, Treuter, Tomarev, & Pelto-Huikko, 2007; Nagalski et al., 2016a).

Independent asymmetry losses in actinopterygians and sarcopterygians

Asymmetry patterns extensively vary, albeit with a phylogenetic logic for the three broad domains related to catshark Left-LHb, Right-LHb and MHb. The almost complete left restriction of the *Sox1/Ntng2/Pcdh17* territory observed in chondrichthyans as well as in the reedfish, which belongs to the sister group of all other ray-finned fishes, thus evokes a retention of an ancestral asymmetry, lost in the spotted gar and in the zebrafish. The same pattern of asymmetry variation is observed for territories related to catshark Right-LHb based on *Prox1* expression, restricted to the right in the reedfish. Taken together these data suggest that an asymmetric location of catshark Left- and Right-LHb related territories may be an ancestral gnathostome characteristic, maintained in ancestral actinopterygians but lost in the actinopterygian lineage after the split of polypterids (Fig. 7a). We also report a strongly asymmetric subdomain organisation of the catshark medial habenula. While the homologous dorsal territory of actinopterygians is also asymmetric, we could not identify clear conservations of asymmetries or even subdomain organisation between these groups. Divergent organisations and patterns of MHb asymmetry were even observed between the two chondrichthyans analysed, suggesting a relatively rapid variation of asymmetries within the medial (chondrichthyans)/dorsal (actinopterygians) habenula.

Wnt signaling as core mechanism underlying asymmetry formation

Even though catshark lateral habenulae and zebrafish dorsal habenulae (medial in the catshark) are unrelated from a phylogenetic standpoint, we find that Wnt signaling is similarly involved in asymmetry formation in these territories, promoting a right identity in both cases (Fig. 7b1 and 7b3). Furthermore, in the catshark, phenotypes are observed as a result of a pathway inactivation conducted after Right-LHb neurons have exited cell cycles, suggesting that it controls the elaboration of neuronal identity of differentiating neurons, promoting a Right-LHB versus Left-LHb neuronal fate choice. This is

reminiscent of the Wnt role reported in the zebrafish, which promotes right prevalent dHbm versus left prevalent dHbl neuronal identity choices (Hüsken et al., 2014). Another similarity is that in both species, the pathway is repressed on the left during a well identified temporal window, which allows the development of left neuronal identities (Guglielmi et al., 2020). A major difference is that while this repression is under parapineal control in the zebrafish (Faro et al., 2019). we find that it is dependent on Nodal in the catshark, in line with the essential role of the pathway in the catshark (Lagadec et al., 2015). Taken together, these data suggest that an ancestral Nodal dependent mechanism responsible of left repression of Wnt activity may have been recruited under parapineal control in the actinopterygian lineage. However, we cannot exclude those other Nodal dependent mechanisms may shape asymmetries in the catshark. For instance, some asymmetries lost upon Nodal inactivation, such as differences in cell densities between Left- and Right-MHb, were maintained in our Wnt loss-of-function analyses. Whether this may be related to the timing of the pharmacological treatments used to inactivate Wnt signaling, an incomplete pathway inactivation at the drug concentrations used, or more fundamentally because Wnt independent regulatory networks are controlled by Nodal, remains an opened question. It is also intriguing to note that zebrafish mutant larvae for tc*f7l2,* a component of Wnt pathway, exhibit a loss of ventral habenula *kiss1 e*xpression, reminiscent of the loss of Right-LHb marker expression observed in the catshark following Wnt inhibition (Beretta et al., 2013). This supports the relationship proposed between catshark Right-LHb and part of the zebrafish ventral habenula, suggesting that the mechanisms involved in Left- versus Right-LHb identity choice may reflect those shaping neuronal identities within the ventral habenula of teleosts. This hypothesis will have to be further tested by more exhaustive analyses of neuronal identity changes in the zebrafish ventral habenula following Wnt inactivation (Fig. 7b3). A related mechanism may also shape neuronal identities across the epithalamic-thalamic border in the mouse, as suggested in this species by the loss of expression of *Prox1* and *Rorα* (orthologues of catshark Right-LHB markers) in *Tcf7l-/-* embryos (Fig. 7b3) (Lipiec et al., 2020).

A conserved regulatory logic prone to variations underlies the development of vertebrate habenulae

Which mechanisms could underlie the evolutionary switch in asymmetry status of related habenula subdomains, such as the strongly asymmetric lateral habenulae of chondrichthyans, and their symmetric proposed ventral homologues in teleosts? In the zebrafish, the left Wnt repression crucial for asymmetry formation depends on a parapineal secreted signal and is restricted to a narrow time window (Faro et al., 2019; Guglielmi et al., 2020). This regulation in time and space has been suggested to contribute to the absence of asymmetry in the ventral habenula, since its precursors originate from a thalamic-epithalamic region of prosomere 2 located at a distance from the forming dorsal habenula and may escape parapineal signals (Beretta et al., 2013). Several key aspects of Wnt regulation are conserved in the catshark. First, neurogenesis of the broad territories identified similarly takes place in a sequential manner, progenitors of medial domains exiting cell cycles later than those of more lateral ones. We also obtain evidence for

a dynamic regulation of Wnt activity, with an initial bilateral nuclear accumulation of β-catenin at the onset of neuronal differentiation, a subsequent withdrawal until LHb progenitors have completed cell cycle exits, and a later phase of asymmetric nuclear accumulation selectively on the right, which in the catshark lasts for several weeks, at least until stage 31, when asymmetric lateral territories are established. The temporal window of left Wnt repression is in this casefully consistent with the role of the pathway in promoting Right-LHb neuronal identities. Taken together, our data suggest that Wnt signaling is part of a core, dynamic regulatory network, prone to variations in time and space, and acting as a substrate for habenular asymmetry formation and diversification across jawed vertebrates.

Materials and Methods

RNA isolation, library construction and sequencing

Left and right habenulae were manually dissected from a total of 45 anaesthetised stage 31 catshark embryos and stored in RNAlater (Ambion) until RNA extraction. Three left pools, each containing 15 left habenulae and three right ones, containing the corresponding 15 right habenulae, were made from these explants. Total RNA was extracted from these pools using the Ribopure Kit (Ambion). RNA quantities and integrity indexes (RINs) were controlled using a Bioanalyzer 2100 (Agilent). RNA quantities ranging between 1.1 and 2.4 µg and RIN values comprised between 7.4 and 9.6 were obtained for each pool analysed. Illumina cDNA libraries were generated using the NEBNext Ultra II RNA Library kit for Illumina and sequenced by Illumina Hi-seq 1500 paired sequencing.

Mapping and expression profiling

Reads obtained from each one of the three left and right habenula pools were pseudo-mapped onto an annotated database of reference gene models (described in Mayeur et al, manuscript in revision) and pseudo-counted using a k-mer quantification method, kallisto (Bray, Pimentel, Melsted, & Pachter, 2016). Contigs exhibiting statistically significant count differences between the left and right habenulae were identified using the Wald test implemented in sleuth ((Pimentel, Bray, Puente, Melsted, & Pachter, 2017); q-value threshold 5E-02).

Gene ontology (GO) analysis

Left versus right habenulae GO term enrichment gene analysis was conducted using the ConsensusPathDB on-line tool ((A Kamburov et al., 2011; Atanas Kamburov, Wierling, Lehrach, & Herwig, 2009) http://cpdb.molgen.mpg.de/) with the whole set of genes expressed in the habenulae as background reference. It was restricted to levels 2-5 GO terms related to biological processes (p-value cut-off of 5E-02, further curated to a q-value threshold of 5E-02).

Embryo collection

Scyliorhinus canicula eggs were provided by the Aquariology Service of the Banyuls sur Mer Oceanological Observatory.. Embryos were dissected, fixed and staged as described previously (Lagadec et al., 2015). Juvenile of *Lepisosteus oculatus* and *Erpetoichthys calabaricus* were provided from commercial sources (https://www.poisson-or.com/). Juveniles of *Callorhincus milii* were provided by C. Boisvert (Curtin University, Australia) and *Xenopus tropicalis* by S. Marcellini (University of Concepcion, Chile).

***In situ* hybridization (ISH) and IHC.**

Probes were obtained from collections of embryonic *S. canicula* cDNA recombinants (Coolen et al., 2008), or obtained from synthetic double-stranded DNA. Following ISH, nuclei were counterstained using Nuclear Fast Red (Sigma N3020). Chromogenic ISHs of paraffin sections were conducted using digoxigenin-labelled antisense RNAs as previously described (Derobert et al., 2002; Plouhinec et al., 2005). Fluorescent ISHs were conducted using digoxigenin-labelled antisense RNAs and fluorescein-labelled antisense RNAs as described in (Hauptmann, Lauter, & Söll, 2016; Lauter, Söll, & Hauptmann, 2011; Tuan & Lo, 1999). Fluorescent immunohistochemical detection of β-catenin (Abcam, Ab97959, 1/1000) on sections was conducted as previously described for (Lagadec et al., 2015). For fluorescent ISHs and IHCs, sections were imaged with a Leica SP8 confocal laser-scanning microscope.

BrdU pulse chase analysis.

BrdU pulse labelling and BrdU detection were conducted as described in Lagadec et al. 2018 with the following modifications. Catshark embryos were removed from the egg case, incubated in oxygenated filtrated sea water containing 5 mg/ml BrdU (16.2mM) for 16 hours and for the chase, transferred to filtrated sea water at 16°C until desired stages were reached. Following incubation of sections with the anti-BrdU primary antibody, detection was conducted using m-IgGκ BP-HRP (Santa Cruz; 1/100) and the TSA Plus Cyanine 3 kit (Akoya Bioscience) following suppliers' instructions.

Pharmacological treatments.

For Nodal inhibition, catshark embryos were treated by in ovo injection of 100 µl of a 50µm SB-505124, a selective inhibitor of TGF-β type I receptors Alk4/5/718, at stage 16 as previously described (Lagadec et al., 2015). For Wnt inactivation, 100 µl of a DMSO solution containing 1mM IWR-1-endo, a selective inhibitor of tankyrase known to inhibit β-catenin cytoplasmic accumulation through stabilization of the destruction complex member AXIN2, were injected into the egg case at stage 29 and eggs were maintained in oxygenated sea water (16°C) until reaching the desired stage. The same protocol was applied to control embryos, except for the absence of the drug in the injected solution.

Legends

Figure 1. Functional annotation of asymmetrically expressed genes in the catshark developing habenulae. This Figure is in progress (taken in charge by H. Mayeur, engineer in bioinformatics, and S. Mazan).

Figure 2. Asymmetric lateral to medial organisation of catshark habenulae. a Left: Schemes showing left lateral views of catshark stage 31 and juvenile brains (top and bottom respectively), with the habenulae boxed; middle and right: schemes showing left lateral views of the habenulae (middle: stage 31; right: juvenile), with lines indicating the planes and levels of the sections shown in (b-p). **b-p** Transverse sections of habenulae (b-k: stage 31; l-p: juveniles) after ISH with probes for *ScKctd12b* (b,e,l), *ScPde1a* (c,m), *ScSox1* (f,o), *ScEnpp2* (d,n), *ScProx1* (g,p) or after fluorescent double ISH with *ScPde1a*/*ScKctd12b* (magenta/green: h), *ScKctd12b*/*ScEnpp2* (green/magenta: i), *ScSox1*/*ScKctd12b* (magenta/green: j) and *ScKctd12b*/*ScProx1* (green/magenta: k). Arrowheads in (c,d) point to the boundary between *ScPde1a* and *ScEnpp2* complementary territories along their left radial band of expression. Asterisks in (k,o) indicate minor territories of *ScProx1* in the right habenula (k) and *ScSox1* in the left habenula (o). **q** Schemes showing the subdomain organisation of habenulae on sections at a medial organ level (scheme on the left, stage 31) or at an anterior organ level (scheme in the middle, juvenile). Abbreviations: ant., anterior; post., posterior; MHb, medial habenula; LHb, lateral habenula; hc, habenular commissure; pi, pineal stalk. Scale bar=100μm.

Figure 3. An asymmetric, tripartite organisation of habenulae is ancestral in jawed vertebrates. a-c,e-g,i-k,m-o,q-s Transverse sections of habenulae in catshark (*S. canicula*: a-c), elephant shark (*C. milii*: e-g), reedfish (*E. calabaricus*: i-k), spotted gar (*L. oculatus*: m-o) and xenopus (*X. tropicalis*: q-s) juveniles, following ISH with probes for orthologues of catshark MHb (a,e,i,m,q), Left-LHb (b,f,j,n,r) and Right-LHb (c,g,k,o,s) markers. Probe identity is indicated on each view. Dotted lines in (i-k,m-o) delineate the boundary between dorsal and ventral habenula in actinopterygians, and between medial and lateral habenula in tetrapods. Arrowheads in (r,s) point to a thalamic *Prox1* expression in xenopus. **d,h,p,l,t** Schemes showing relationships in habenula subdomain organisation between the catshark (d), the elephant shark (h), the reedfish (l), the spotted gar (p) and the xenopus (t), with territories related to catshark Left-LHb, MHb and Right-LHb in yellow, purple and blue respectively. Abbreviations : same as in Figure 2; dHb, dorsal habenula; vHb, ventral habenula. Scale bar=200μm in (a-c,m-o), 500μm in (e-g), 150μm in (i-k), 100μm in (q-s).

Figure 4. Variations in subdomain organisation within the dorsal /medial habenula. a-t Habenula **s**ections of habenulae of catshark (a-e), elephant shark (f-j), spotted gar (k-o) and xenopus (p-t) juveniles

following ISH with probes for orthologues of *Kctd8* (a,f,k,p), *Kctd12b* (b,g,l,q), *Kctd12a* (c,h,m,r), *Trhde* (d,i,n,s) and *Trhr2* (e,j,o,t). All sections are transverse ones, from juvenile specimens, except (d) (horizontal, stage 31). Sections are shown at a medial organ level, except (a,f) and (d,p-t), respectively shown at anterior and posterior levels. Arrowheads in (k,m,n) point to a left dorsal territory showing a high signal intensity for *LoKctd12a* and *LoTrhde* but excluded from the *LoKctd8* left dorsal domain. An asterisk in (g,e) shows a *CmTrhr2* positive territory of lower *CmKctd12b* relative signal intensity. No signal was observed for *Trhr2* and *Trhde* in *E. calabaricus* (not shown). Histologies and signals are sub-optimal in (a,c,d,e) and experiments are underway to improve these data. Same abbreviations as in Figure 2. Scale bars= 200µm in (a-o), 50µm in (p-t).

Figure 5. Wnt signaling promotes Right-LHb identity under the control of Nodal in the catshark lateral habenulae. a-h Transverse sections of catshark stage 31 habenulae after ISH with probes for *ScSox1* (a,b,e,f,i,m,k,o) and *ScProx1* (c,d,g,h,j,n,l,p). (a,c,e,g) and (b,d,f,h,i-p) are respectively shown at anterior and medial organ levels. (a-d) and (e-h) respectively show control and treated embryos for IWR-1 treatment. (i,j), (k,l), (m,n) and (o,p) respectively show control, IWR-1 treated, SB-505124-treated and IWR-1/SB505124 double-treated embryos for SB-505124/IWR-1 double treatments. Arrowheads in (e,f,k,o) show a right expansion of *ScSox1*, (g,h,l,p) show a loss of *ScProx1* in the same territory. Asterisks in (m,n) show the loss of left *ScSox1* expression (m, black asterisk) and the expansion on the right of *ScProx1* (n, white asterik). Same abbreviations as in Figure 2. Scale bar=100µm.

Figure 6. Neurons of habenula territories exit cell cycles following a temporal regulation from lateral to medial organ levels. a-d Transverse views of catshark stage 31 habenulae from embryos exposed to a BrdU pulse at stage 26 (a), 28 (b), 28+ (c) and 29 (d). (a1,a3,a5,b1,b3,b5,c1,c3,c5,d1,d3,d5) show confocal images following BrdU detection (magenta). (a2,a4,a6,b2,b4,b6,c2,c4,c6,d2,d4,d6) show confocal images of adjacent sections after double ISH with probes for *ScKctd12b* (green) and *ScProx1* (red). DAPI stained nuclei are shown in blue. (a1) to (a6), (b1) to (b6), (c1) to (c6) and (d1) to (d6) are numbered from anterior to posterior levels of the same embryo. Habenulae left and right sides are respectively shown on the left and on the right on all views, dorsal to the top. White dotted lines delimit the *ScKctd12b* positive territory (inferred from adjacent sections for sections showing BrdU accumulation). Asterisks show LHb territories, negative for *ScKctd12b* expression (eft for Left-LHb, right for Right-LHb). Arrowheads in (a-d3) and (a-d4) point to an early born, lateral dorsal *ScKctd12b* and *ScPde1a* positive territory, only observed on the left. For each embryo, three section levels (anterior, medial, posterior) are shown as indicated. Scale bar=100µm.

Figure 7. Evolution of habenula asymmetries in gnathostomes. a. Evolution of habenula organisation and asymmetries in jawed vertebrates. Territories proposed to be homologous to the lateral left (Left-LHb), lateral right (Right-LHb) and medial (MHb) territories of chondrichthyans are respectively shown

in yellow, blue, and purple. The former two have become ventral in actinopterygians. Their asymmetric location has been lost in the actinopterygian lineage after the split of polypterids. The ancestral sarcopterygian state is less clear and is currently addressed in the laboratory by analysis of the lungfish *Protopterus annectens*. Bilateral symmetric thalamic expression of mouse orthologues of catshark Right-LHb markers (Clarkson et al., 2009; Galeeva et al., 2007; Lavado & Oliver, 2007; Nagalski et al., 2016b) as well as *Prox1* expression changes observed in xenopus, suggest a loss from habenulae. A; loss of asymmetries of ancestral lateral domains may have also taken place in tetrapods. **b** Loss-of-function phenotypes in the catshark (b1), mouse (b2) and zebrafish (b3) habenulae. An expression loss of Right-LHb markers (blue) markers is observed in the catshark, concomitantly with an expansion of Left-LHb markers. In the mouse, expression of orthologues of several Right-LHb markers (*Prox1, Ror*α) in thalamic nuclei, adjacent to the habenulae, is lost following inactivation of *Tcf7l2,* a member of the Lef/Tcf7l2 family (Lipiec et al., 2020). In the zebrafish, similarly, the bilateral ventral expression of *Kiss1,* whose catshark orthologue is a Right-LHb marker, is lost in Wnt loss-of-function analyses (Beretta et al., 2013). In the two latter species, whether an expression expansion of orthologues of Left-LHb markers, such as *Sox1*, concomitantly takes place, as predicted by our model, remains to be addressed.

Supplementary Table 1. List of differentially expressed gene models between catshark stage 31 left and right habenulae. Differentially expressed gene models are listed in column A, with left- and right-enriched ones shaded in yellow and blue respectively. Curated annotation and automated annotation against Swissprot are indicated in columns B and C. P-values, q-values and fold changes (FC) are given in columns D, E and G. Genes previously identified as asymmetrically expressed in the catshark developing habenulae are present in this list. For instance *ScPitx2* (q-value=0.0001, FC=13.6), known to be left-restricted, and *ScKctd12b* (q-value=5.7E-13, FC=1.9), which exhibits a broader left, relative to right territory at stage 31, are both retrieved as left-enriched with significant statistical supports (Lagadec et al., 2015).

Supplementary Table 2. Over-represented biological processes in left versus right habenulae.

Supplementary Table 3. List of genes analysed by ISH in the catshark. The genes analysed were retrieved from the transcriptomic comparison between stage 31 left and right habenulae except *ScKctd8*, *ScKctd12a* and *ScRora*, selected by a candidate gene approach (Lagadec et al., 2015).Gene names are indicated in column A, the corresponding identification in column B, the laterality of the enrichment predicted by the transcriptomic analysis in column C, the rank in the list of differentially expressed genes in column D (ranking on increasing p-values), the corresponding expression characteristics in column E and the sequence of the probe in column F. Colours indicate the expression characteristics of genes exhibiting regionalised expression in differentiated habenula territories with the same colour code

as in Fig. 1 (yellow, Left-LHb; purple, MHb and subdomains; blue, Right-LHb). Genes expressed in combinations of these domains are shaded in grey.

Supplementary Figure 1. Expression profiles of genes retrieved from the transcriptomic analysis and showing regionalised expression in stage 31 catshark habenulae. **a** Left-LHb markers. **b** MHb markers. **c** Right-LHb markers. **d** Left-MHb markers. **e** Right-LHb markers. **f** Genes expressed in combinations of LHb and MHb territories. **g** Lateral ventricular zone (LVZ) progenitors. For each gene, a transverse section is shown at a medial level of the organ, with the left and right sides on the left and right respectively. A scheme of a section, showing the location of neural progenitors (in red; PNE, pseudo-stratified neuroepithelium; LVZ, lateral ventricular zone), the pineal stalk (pi) and the habenular commissure (hc) is shown on the left, at the bottom of the Figure. Scale bar=100μm.

Supplementary Figure 2. Expression of *ScSox1* (b), *ScPde1a* (c), *ScKctd12b* (d), *ScEnpp2* (e) and *ScProx1* (f) in transverse sections of stage 31 catshark habenulae. a Schematic lateral view of stage 31 catshark habenulae (a1) with the section planes indicated by dottted lines and scheme showing the subdomain organisation of stage 31 habenulae on a section at a medial organ level (a2). **b-f** Transverse sections of stage 31 habenulae after ISH with probes for *ScSox1* (b), *ScPde1a* (c), *ScKctd12b* (d), *ScEnpp2* (e) and *ScProx1* (f). (b1-f1), (b2-f2), (b3-f3), (b4-f4), (b5-f5) each show adjacent successive sections from anterior to posterior; (b1-5), (c1-5), (d1-5), (e1-5), (f1-5) each show sections from anterior to posterior. All sections are shown with left and right sides on the left and on the right respectively, dorsal to the top. Arrowheads in (c2,c3,e2,e3) point to the boundary between *ScPde1a* and *ScEnpp2* complementary territories in the left habenula. Asterisks in (b5) and (f4) show *ScSox1* and *ScProx1* minor territories respectively in the right and left habenulae. Same abbreviations as in Figure 2. Scale bar=100μm.

Supplementary Figure 3. Expression of *ScSox1* (a), *ScPde1a* (b), *ScKctd12b* (c), *ScEnpp2* (d) and *ScProx1* (e) in horizontal sections of stage 31 catshark habenulae. a Schematic lateral view of stage 31 catshark habenulae (a1) with the section planes indicated by dottted lines and scheme showing the subdomain organisation of stage 31 habenulae on sections at a medial organ level (a2). **b-f** Horizontal sections of stage 31 habenulae after ISH with probes for *ScSox1* (b), *ScPde1a* (c), *ScKctd12b* (d), *ScEnpp2* (e) and *ScProx1* (f). (b1-f1), (b2-f2), (b3-f3), (b4-f4) each show adjacent successive sections from dorsal to ventral (b1-4), (c1-4), (d1-4), (e1-4) each show sections from dorsal to ventral. All sections are shown with left and right sides on the left and on the right respectively, anterior to the top. Arrowheads in (c3,c4, e3,e4) point to the boundary between *ScPde1a* and *ScEnpp2* complementary territories in the left habenula. Asterisks in (b4) and (f3) show *ScSox1* and *ScProx1* minor territories respectively in the right and left habenulae. Same abbreviations as in Figure 2. Scale bar=100μm.

Supplementary Figure 4. Expression of *ScSox1* (a), *ScPde1a* (b), *ScKctd12b* (c), *ScEnpp2* (d) and *ScProx1* (e) in transverse sections of juvenile catshark habenulae. **a** Schematic lateral view of juvenile catshark habenulae (a1) with the section planes indicated by dottted lines and scheme showing the subdomain organisation of juvenile habenulae on sections at a medial organ level (a2). **b-f** Transverse sections of juvenile habenulae after ISH with probes for *ScSox1* (b), *ScPde1a* (c), *ScKctd12b* (d), *ScEnpp2* (e) and *ScProx1* (f).(b1-f1), (b2-f2), (b3-f3), (b4-f4) each show adjacent successive sections from anterior to posterior; (b1-4), (c1-4), (d1-4), (e1-4) each show sections from anterior to posterior. All sections are shown with left and right sides on the left and on the right respectively, dorsal to the top. Asterisks in (b1,b2) and (f3) show *ScSox1* and *ScProx1* minor territories respectively in the right and left habenulae. Same abbreviations as in Figure 2. Scale bar=100μm.

Supplementary Figure 5. Expression of *ScSox1* (a), *ScPde1a* (b), *ScKctd12b* (c), *ScEnpp2* (d) and *ScProx1* (e) in horizontal sections of juvenile catshark habenulae. a Schematic lateral view of juvenile catshark habenulae (a1) with the section planes indicated by dottted lines and scheme showing the subdomain organisation of juvenile habenulae on sections at a medial organ level (a2). **b-f** Transverse sections of juvenile habenulae after ISH with probes for *ScSox1* (b), *ScPde1a* (c), *ScKctd12b* (d), *ScEnpp2* (e) and *ScProx1* (f).(b1-f1), (b2-f2), (b3-f3), (b4-f4) each show adjacent successive sections from dorsal to ventral (b1-4), (c1-4), (d1-4), (e1-4) each show sections from dorsal to ventral. Each section is shown with left and right sides on the left and on the right, anterior to the top. Arrowheads in (c3,c4,e3,e4) point to the boundary between *ScPde1a* and *ScEnpp2* complementary territories in the left habenula. Asterisks in (b5) and (f4,f5) show *ScSox1* and *ScProx1* minor territories respectively in the right and left habenulae. Same abbreviations as in Figure 2. Scale bar=100μm.

Supplementary Figure 6. Tripartite organisation of the habenulae in the elephant shark. a Schemes showing a lateral view of the elephant shark brain, with the location of habenulae in red and dotted lines indicating section planes (left) and a posterior section along this plane (right), with the habenular commissure in grey. **b-i** Transverse sections of *C. milii* juvenile habenulae after ISH with probes for *CmPcdh17* (b), *CmNtng2* (c), *CmSox1* (d), *CmKctd8* (e), *CmKctd12b* (f), *CmKiss1* (g), *CmRorα* (h) and *CmProx1* (i). (d,f,i), (f') and (d',f'',i') respectively show sections at anterior, medial and posterior organ levels. All sections are shown with left and right sides on the left and on the right respectively, dorsal to the top. Black arrowheads in (b) point to *CmPcdh17* MHb subdomains, labeled in addition to Left-LHb. Asterisks in (f,f',f'') and in (g) indicate a dorsal MHb right territory where *CmKctd12b* expression is relatively faint and where *CmKiss1* is expressed in addition to Right-LHb. Completion of analysis of *CmKctd8* profile is not yet completed and is in progress. Scale bar=500μm.

Supplementary Figure 7. Tripartite organisation of the habenulae in the spotted gar. a Schemes showing a left lateral view of the spotted gar brain, with the location of habenulae in red and dotted lines indicating section planes (left) and a medial section along this plane (right), with tract zones in grey. **b-g** Transverse sections of *L. oculatus* juvenile habenulae after ISH with probes for *LoNtng2* (b), *LoPcdh17* (c), *LoSox1* (d), *LoKctd12b* (e), *LoKiss1* (f) and *LoProx1* (g). (b-g), (b'-g') and (b"-g") respectively show sections at anterior, medial and posterior organ levels. All sections are shown with left and right sides on the left and on the right respectively, dorsal to the top. Black arrowheads point to the boundary between ventral and dorsal habenulae, as respectively defined by *LoKctd12b* and *LoKiss1*/*LoProx1* territories. Asterisks indicate ventral territories co-expressing *LoPcdh17* and *LoSox1* (but not *LoNtng2*). Abreviations: dHb, dorsal habenula; vHb, ventral habenula. Scale bar=100µm.

Supplementary Figure 8. Tripartite organisation of the habenulae in the reedfish. a Schemes showing a left lateral view of the reedfish brain, with the location of habenulae in red and dotted lines indicating section planes (left) and a medial section along this plane (right), with tract zones in grey. **b-g** Transverse sections of *E. calabaricus* juvenile habenulae after ISH with probes for *EcPcdh17* (b), *EcNtng2* (c), *EcSox1* (d), *EcKctd12a* (e), *EcKctd12b* (f) and *EcProx1* (g). (b-g), (b'-g') and (b"-g") respectively show sections at anterior, medial and posterior organ levels. All sections are shown with left and right sides on the left and on the right respectively, dorsal to the top. Black arrowheads point to the boundary between ventral and dorsal habenulae, as defined by *EcKctd12a* profile. An asterisk in (b") labels a minor posterior right territory observed for *EcPcdh17*. Abbreviations: dHb, dorsal habenula; vHb, ventral habenula. Analysis are in progress to characterise the profile of other orthologues of catshark Right-LHb (*EcKiss1*), and to improve the section planes for the markers shown in (b,c,d). Scale bar=100µm.

Supplementary Figure 9. Medial to lateral organisation of habenulae in *Xenopus tropicalis.* a Schemes showing a left lateral view of the xenopus brain, with the location of habenulae in red and dotted lines indicating section planes (left) and a transverse section at a medial level along this plane (right). **b-f** Transverse sections of *X. tropicalis* juvenile habenulae after ISH with probes for *XtSox1* (b), *XtProx1* (c), *XtKctd8* (d), *XtKctd12b* (e) and *XtGbx2.1* (f). (b-g), (b'-g') and (b"-g") respectively show sections at anterior, medial, and posterior organ levels. All sections are shown with left and right sides on the left and on the right respectively, dorsal to the top. Dotted lines delineate the boundary between thalamus and habenula, based on morphology or *Sox1* expression, habenulae being only easily distinguished by their characteristic shape anteriorly. (b-d), (b'-d') and (b"-d") are adjacent sections of the same embryo, which allows accurate comparisons. Abbreviations: LHb, lateral habenula; MHb, medial habenula. Analysis are in progress to expand the list of markers to *XtNtng2*, *XtPcdh17* and *XtKiss1*. Scale bar=50µm.

Supplementary Figure 10. β-catenin nuclear accumulation becomes restricted to the right habenula starting from stage 29 and is regulated by Nodal and Wnt signaling. a-d Confocal images of transverse sections of catshark habenulae at stages 27 (a), 28 (b), 29 and (c) 31 following IHC with an antibody directed against β-catenin (magenta) and YOPRO-1 staining (blue). **e-f** Same as above but from stage 31 catshark embryos injected with DMSO (CTRL,e) or SB-505124 (f) following neural tube closure. All sections are shown with left and right sides on the left and on the right respectively, dorsal to the top. Magnifications of boxed areas in (a) to (f) are shown in (a1-4) to (d1-4), with the left boxed area in (a1-2) to (f1-2) and the right boxed area in (a3-4) to (f3-4). White arrowheads point to nuclear β-catenin signals. Scale bar=100μm.

Supplementary Figure 11. IWR-1 treatment at stage 29 has no effect on *ScPde1a* and *ScEnpp2* expression. Transverse sections of catshark stage 31 habenulae after ISH with probes for *ScPde1a* (a-a",c-c") and *ScEnpp2* (b-b",d-d"). (a-d), (a'-d') and (a"-d") are respectively shown at anterior, medial and posterior organ levels. (a-a",b-b") and (c-c",d-d") respectively show control and IWR-1 treated embryos. Medial signals are maintained in the latter in these treatment conditions. Same abbreviations as in Figure 2. Scale bar=100μm.

Supplementary Figure 12. Effect of double SB-505124 and IWR-1 treatments. a-h Transverse sections of catshark stage 31 habenulae after ISH with probes for *ScSox1* (a-a",c-c",e-e",g-g") and *ScProx1* (b-b",d-d",f-f",h-h") in control (a-a",b-b"), IWR-1 treated (c-c",d-d"), SB-505124 (e-e",f-f") and IWR-1/SB505124 double-treated (g-g",h-h") embryos. (a-g), (a'-g') and (a"-g") are respectively shown at an anterior, medial and posterior organ levels. Lft and right habenula sides are shown on the left and on the right respectively, dorsal to the top. Arrowheads in (c-c",g-g") show a right expansion of *ScSox1*, (d-d",h-h") show a loss of *ScProx1* in the same territory. Asterisks in (e-e",f-f") show the loss of left *ScSox1* expression (e-e", black asterisk) and the expansion on the right of *ScProx1* (f-f", white asterik). Same abbreviations as in Figure 2. The number of control and treated embryos (IWR-1,SB-505124) has to be expanded (analyses in progress). Scale bar=100μm.

Supplementary Figure 13. Neurons of habenula territories exit cell cycles following a temporal regulation from lateral to medial organ levels. a-d Horizontal views of catshark stage 31 habenulae from embryos exposed to a BrdU pulse at stage 26 (a), 28 (b) and 28+ (c). (a1,a3,a5,b1,b3,b5,c1,c3,c5) show confocal images following BrdU detection (magenta). (a2,a4,a6,b2,b4,b6,c2,c4,c6) show confocal images of adjacent sections after double ISH with probes for *ScKctd12b* (green). DAPI stained nuclei are shown in blue. (a1) to (a6), (b1) to (b6) and (c1) to (c6) are numbered from dorsal to ventral levels of the same embryo. Habenulae left and right sides are respectively shown on the left and on the right on all views, anterior to the top. White dotted lines delimit the *ScKctd12b* positive territory (inferred

from adjacent sections for sections showing BrdU accumulation). Asterisks show LHb territories, negative for *ScKctd12b* expression (Left for Lft-LHb, right for Right-LHb). Arrowheads in (a1-c1) and (a2-c2) point to an early born, lateral dorsal *ScKctd12b* and *ScPde1a* positive territory, only observed on the left. For each embryo, three section levels (anterior, medial, posterior) are shown as indicated. Scale bar=100µm.

Supplementary Figure 14. Timing of cell cycles exits of Left-MHb and Right-MHb neurons. a-b Transverse views of catshark stage 31 habenulae from embryos exposed to a BrdU pulse at stage 28+ (a) and 29 (b). (a1,a3,a5,a7,a9,a11,b1,b3,b5,b7,b9,b11) show confocal images following BrdU detection (magenta). DAPI stained nuclei are shown in blue. (a1) to (a12) and (b1) to (b12) are numbered from anterior to posterior levels of the same embryo. (a1-2), (a3-4), (a5-6), (a7-8), (a9-10), (a11-12), (b1-2), (b3-4), (b5-6), (b7-8), (b9-10), (b11-12) are adjacent sections. (a2,a4,a6,a8,a10,a12,b2,b4,b6,b8,b10,b12) show ISH with probes for *ScPde1a* (a2,a6,a10,b2,b6,b10) or *ScEnpp2* (a4,a8,a12,b4,b8,b12). Habenulae left and right sides are respectively shown on the left and on the right on all views, dorsal to the top. White dotted lines delimit the *ScPde1a* or *ScEnpp2* positive territories (inferred from adjacent sections for sections showing BrdU accumulation). Arrowheads in (a1,a2,a5,a6,b1,b2) point to an early born, lateral dorsal *ScKctd12b* and *ScPde1a* positive territory, only observed on the left. Scale bar=100µm.

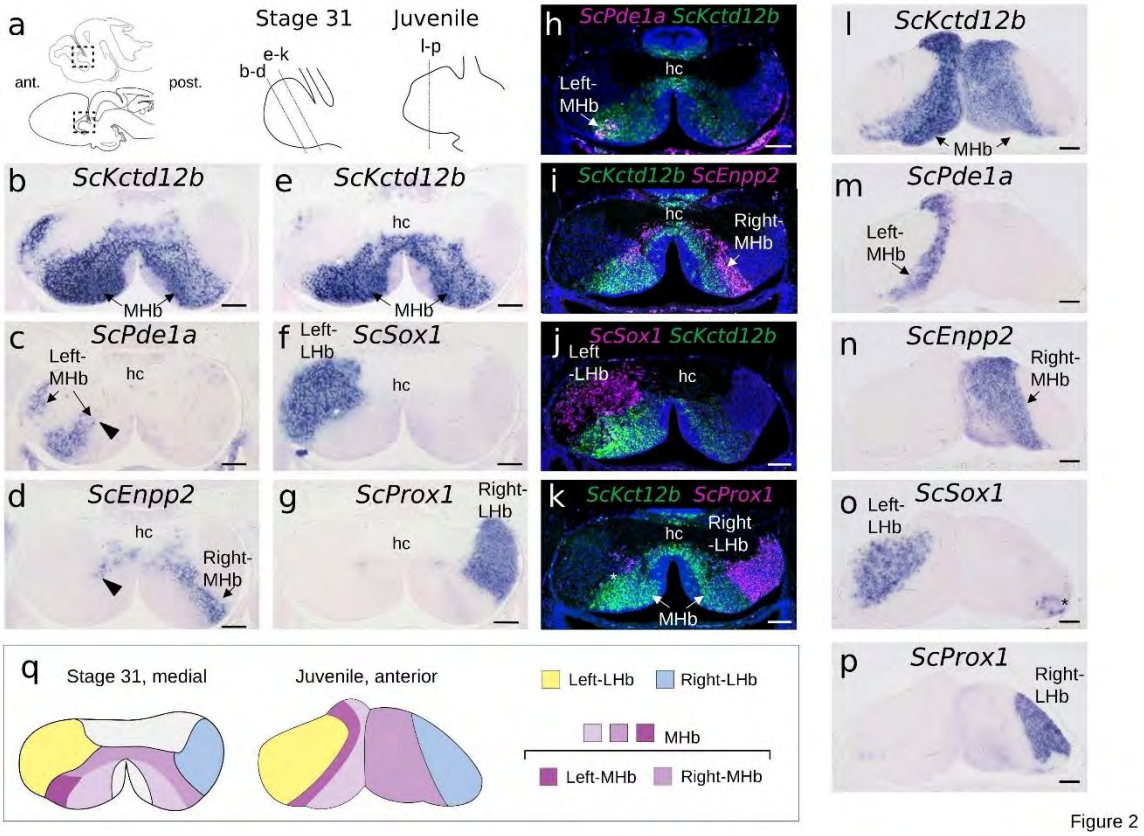

Figure 2

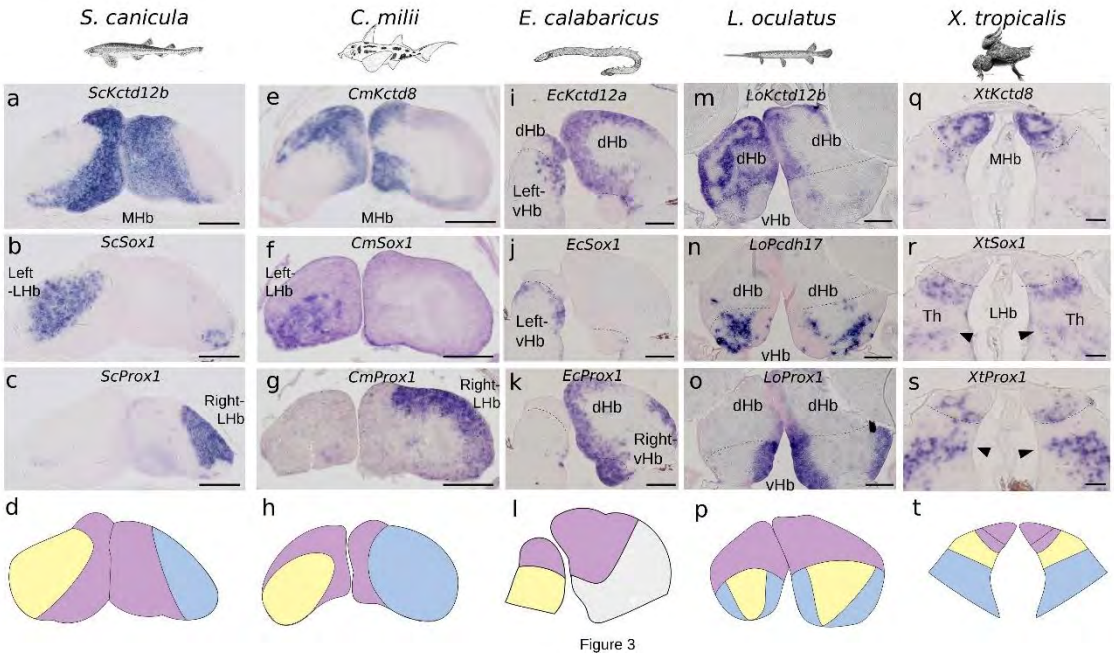

Figure 3

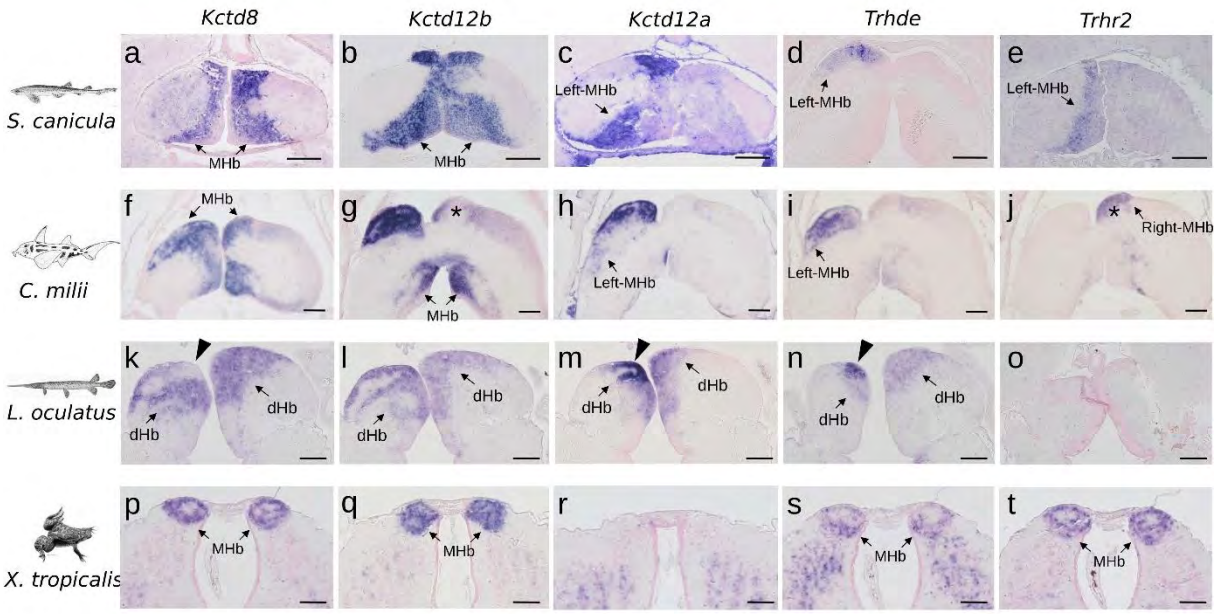

Figure 4

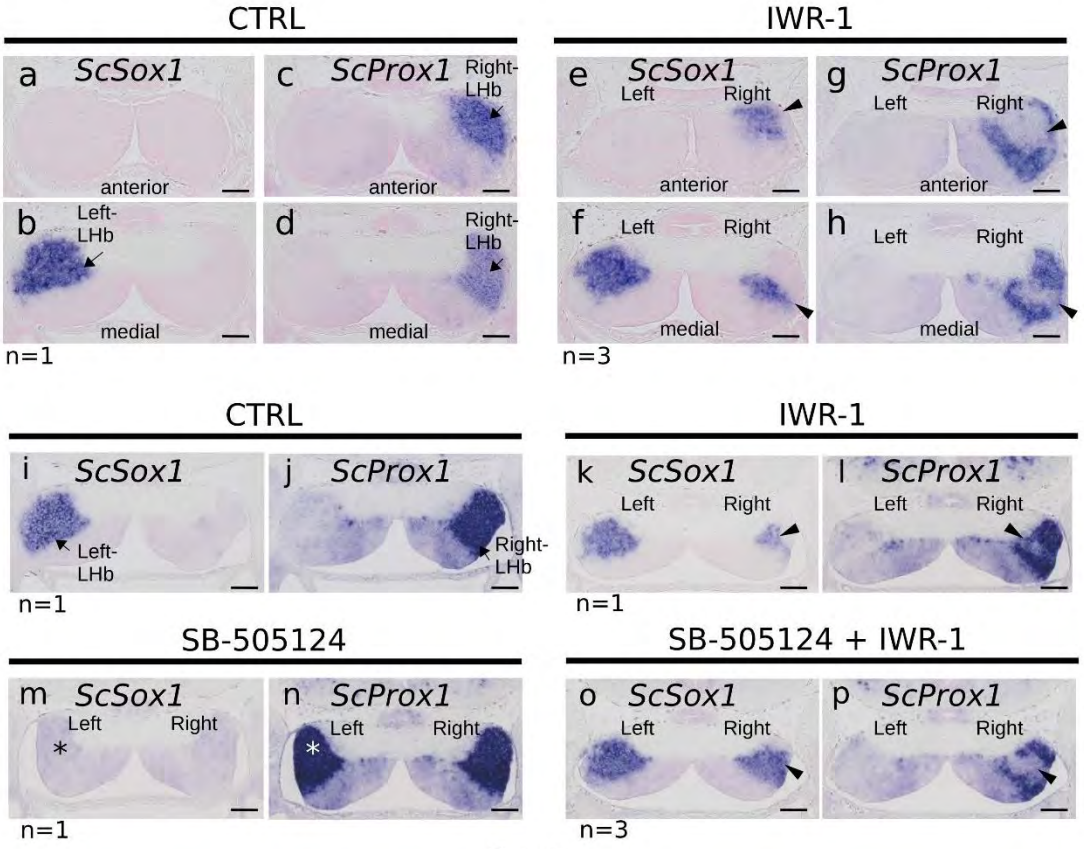

Figure 5

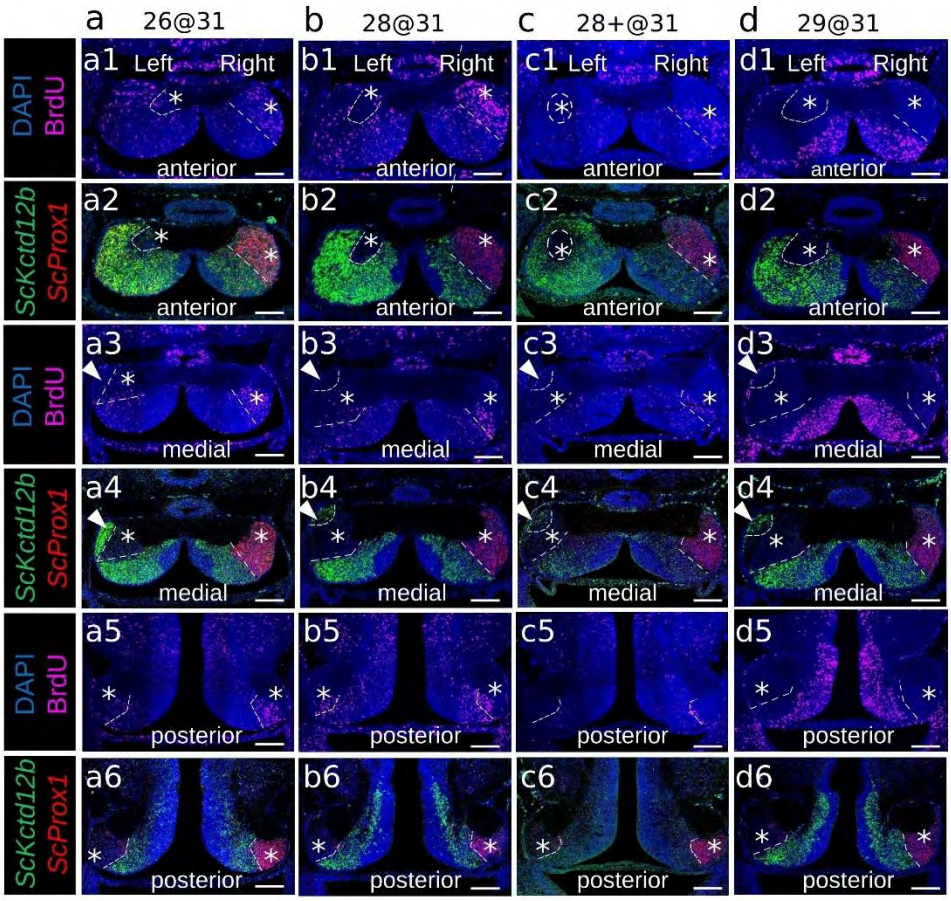

Figure 6

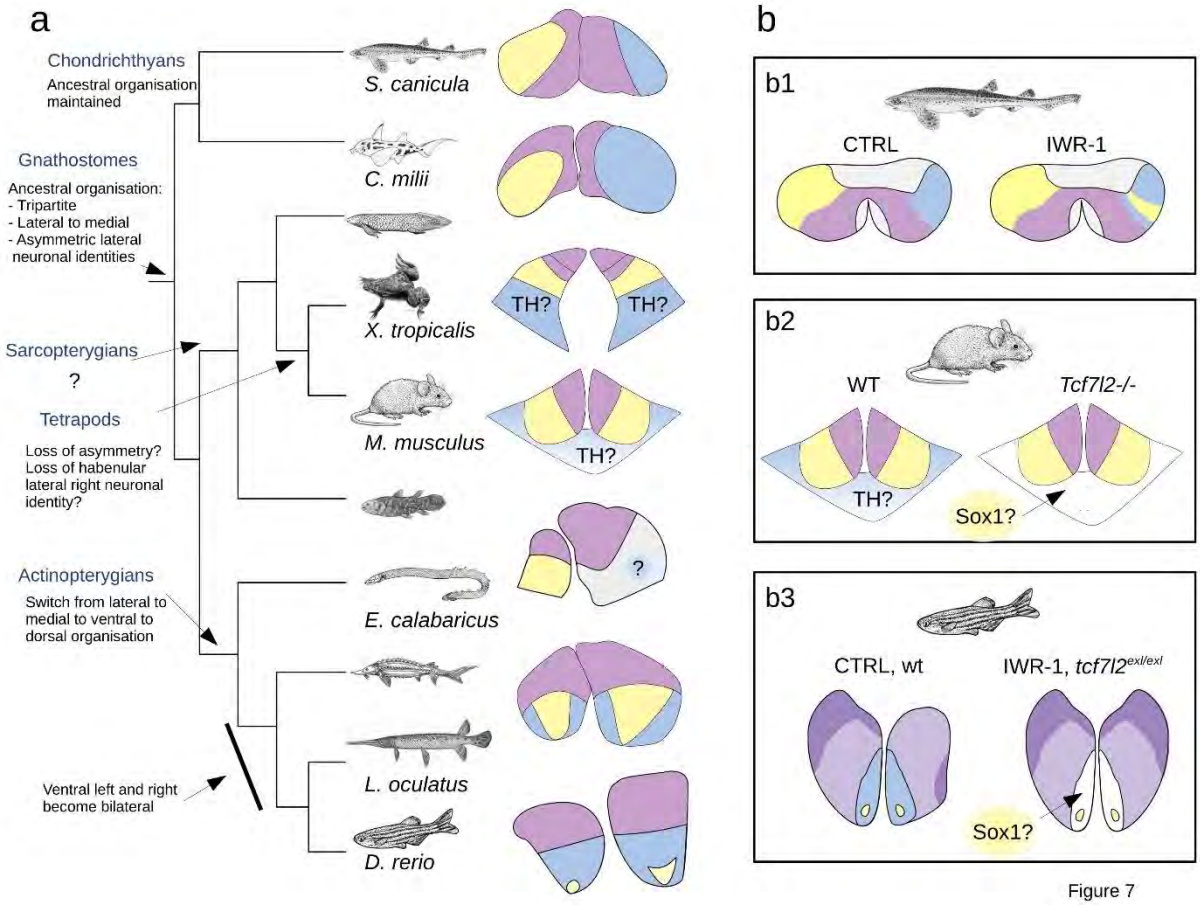

Figure 7

Supplementary Table 3

ScAk5	XM_038793757.1	Right	2	Right-LHb
ScAngptl5	XM_038811454.1	Right	26	Progenitors
ScCa8	XM_038809435.1	Right	6	Ubiquitous
ScEnpp2	XM_038809789.1	Right	39	Right-MHb
ScEya2	XM_038803556.1	Right	55	Right-MHb
ScFzd1	XM_038797926.1	Left	114	Ubiquitous
ScGng14	Cluster-19096.0	Right	47	Right-LHb
ScGpr78	XM_038792142.1	Left	10	Left-LHb, MHb
ScGrm2	XM_038810827.1	Left	70	No signal
ScItga2	XM_038790878.1	Left	126	Progenitors
ScKctd8		NA	undetected	MHb
ScKctd12a		NA	undetected	Left-LHb
ScKctd12b	XM_038775015.1	Left	69	MHb
ScKiss1	Cluster-5123.1	Right	1	Right-LHb
ScLhfpl5	XM_038820366.1	Left	32	Left-LHb, MHb
ScNrp2	XM_038787297.1	Left	30	MHb
ScNtng2	XM_038781563.1	Left	20	Left-LHb
ScPcdh17	XM_038817900.1	Left	21	Left-LHb
ScPde1a	XM_038789235.1	Left	106	Left-LHb
ScPrkcb	XM_038821090.1	Right	81	Right-LHb
ScPrkcq	XM_038811892.1	Right	56	Right-LHb
ScProx1	XM_038811423.1	Right	5	Right-LHb
ScPtprm	XM_038808713.1	Left	41	Left-LHb
ScRergl	XM_038811107.1	Right	19	Right-LHb
ScRor α		NA	undetected	Right-LHb
ScRspo3	XM_038799763.1	Left	128	Progenitors
ScSema3a	XM_038811983.1	Right	109	Ubiquitous
ScShh	XM_038798390.1	Right	158	Right-LHb
ScShisa3	XM_038791308.1	Left	107	Ubiquitous
ScSlc5a7	XM_038818584.1	Right	53	Right-LHb
ScSox1	XM_038818902.1	Left	34	Left-LHb
ScSox6	XM_038808084.1	Right	95	Ubiquitous
ScSpon1	XM_038807896.1	Left	14	Left-LHb
ScStac	XM_038809850.1	Left	22	MHb
ScStk32c	XM_038822141.1	Left	23	Left-LHb
ScStxbp6	XM_038786182.1	Right	3	Right-LHb
ScTmeff2	XM_038789119.1	Left	51	Left-LHb, MHb
ScTmcc3	XM_038775241.1	Right	147	Ubiquitous
ScTrhr2	XM_038806506.1	Left	7	Left-LHb
ScTrhde	XM_038780529.1	Left	90	Left-LHb
ScTrib1	XM_038810170.1	Right	76	Right-LHb
ScUpk1b	XM_038802384.1	Left	85	No signal
ScWisp1	XM_038808815.1	Right	15	Right-LHb

	Right-LHb
	Left-LHb
	MHb
	Right-MHb
	Left-LHb
	Combination
NA	Non applicable

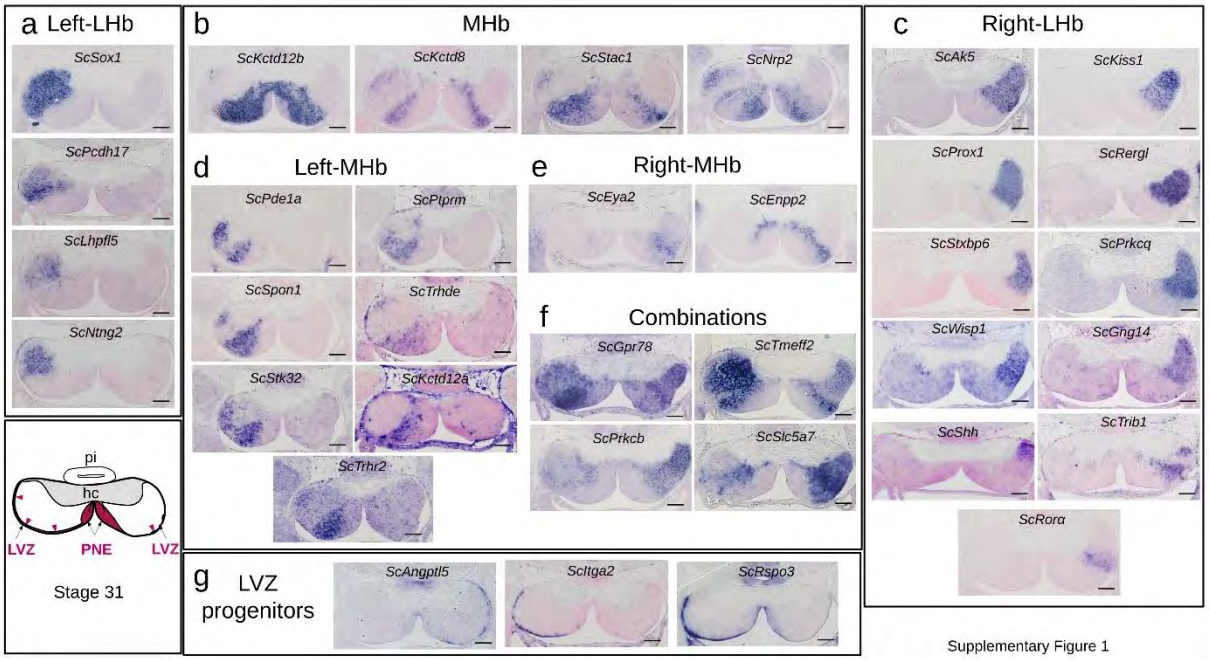

Supplementary Figure 1

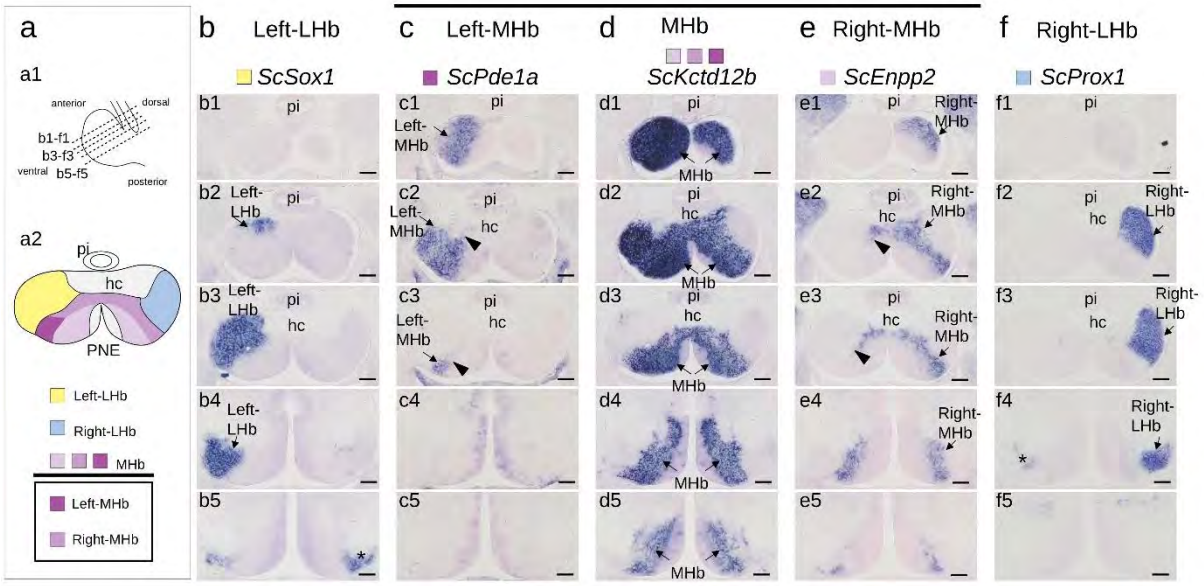

Supplementary Figure 2

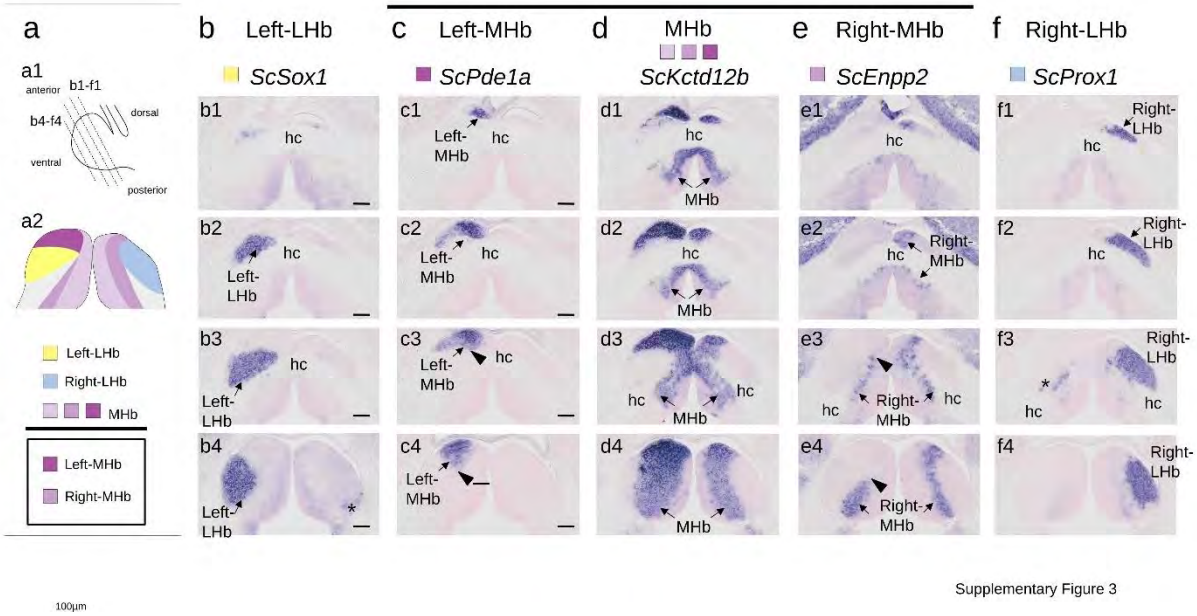

Supplementary Figure 3

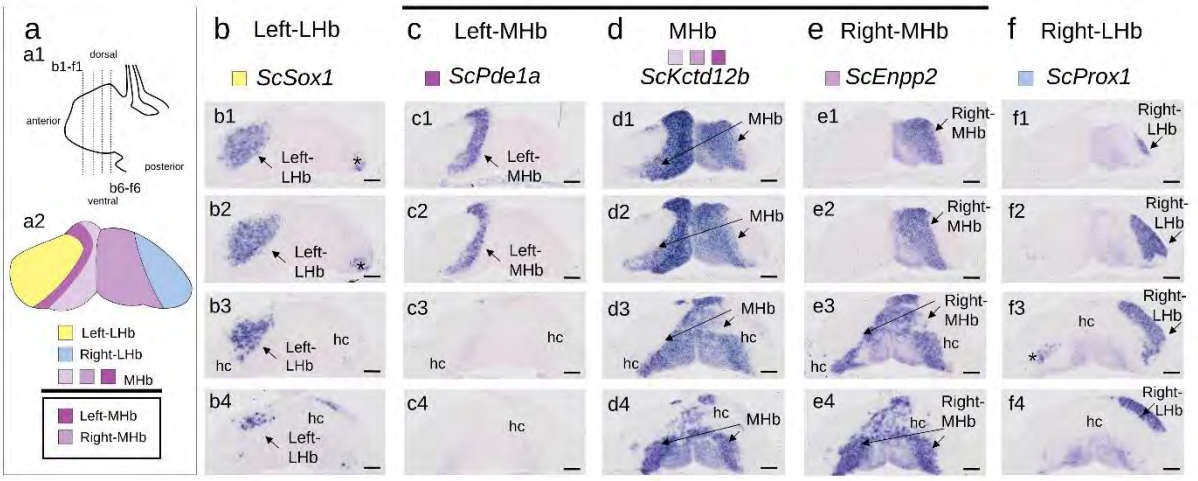

Supplementary Figure 4

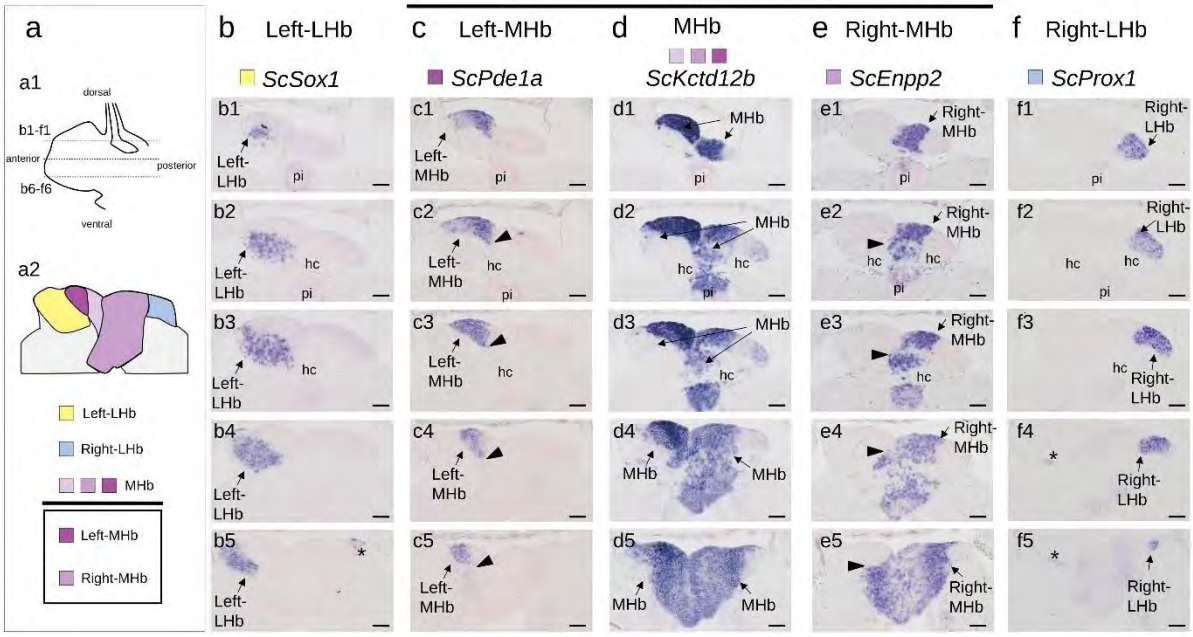

Supplementary Figure 5

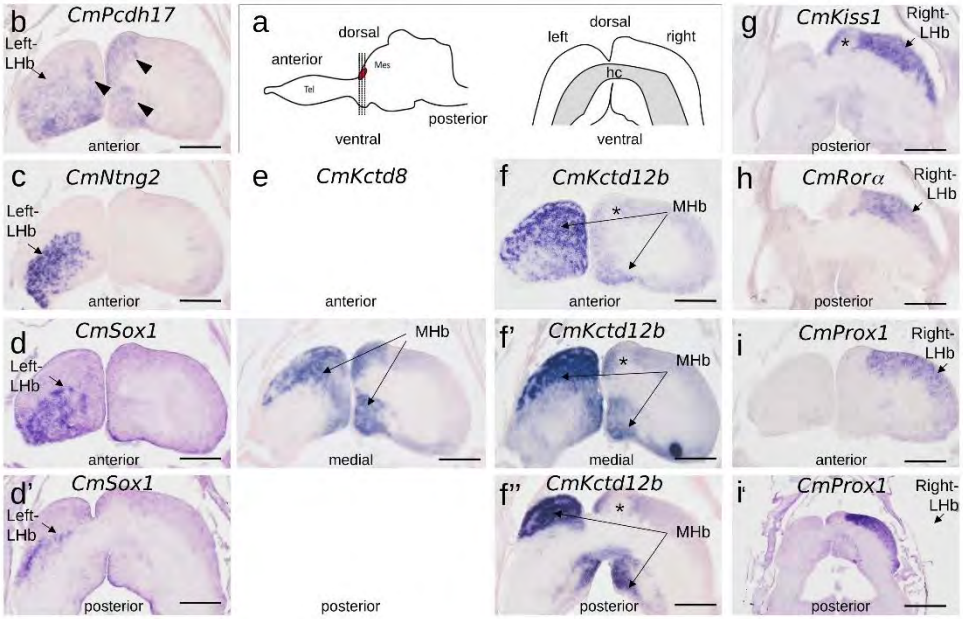

Supplementary Figure 6

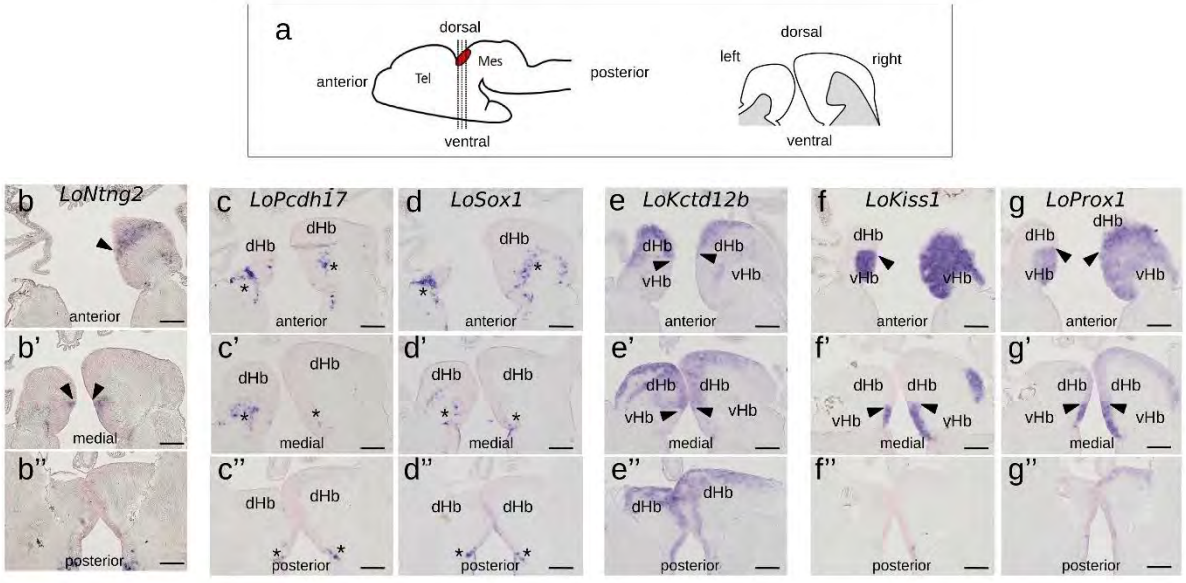

Supplementary Figure 7

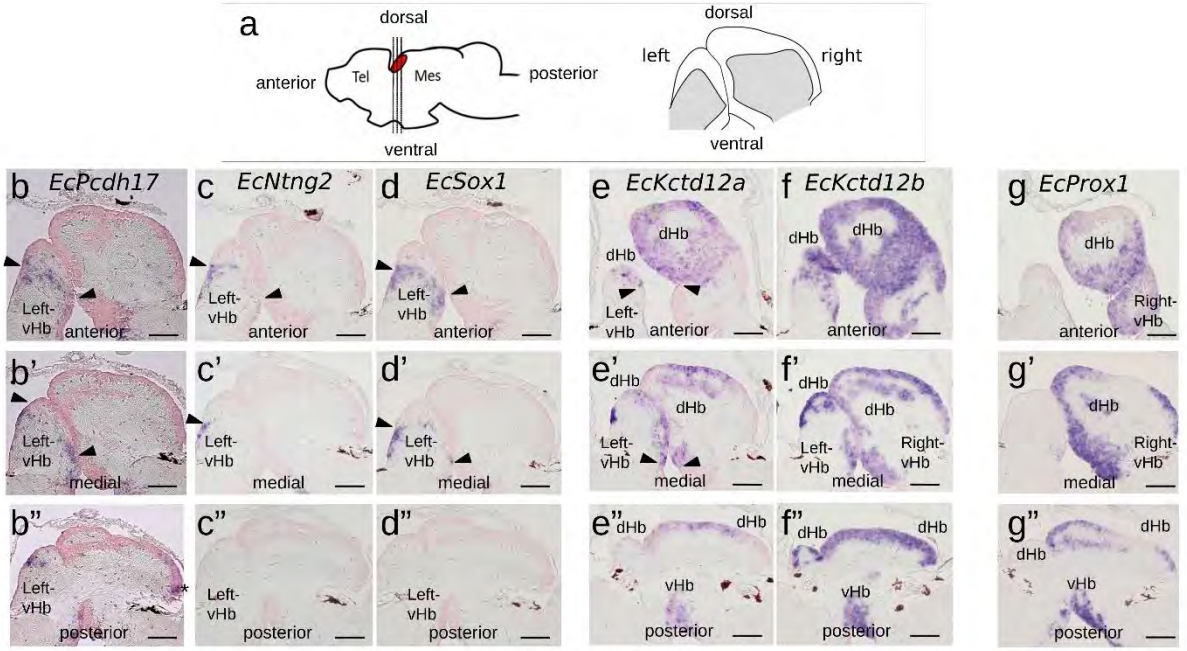

Supplementary Figure 8

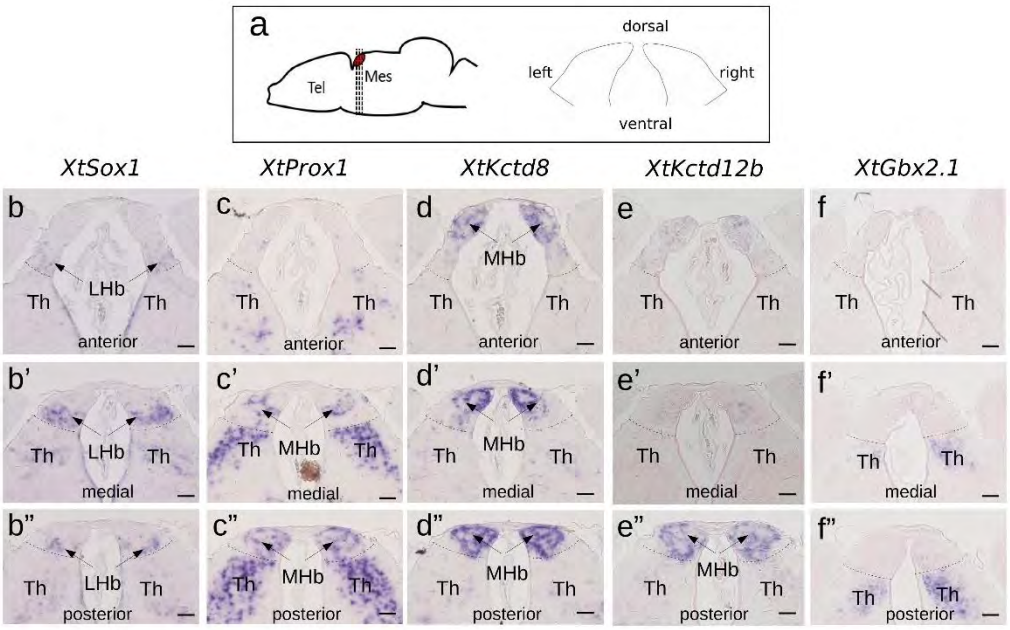

Supplementary Figure 9

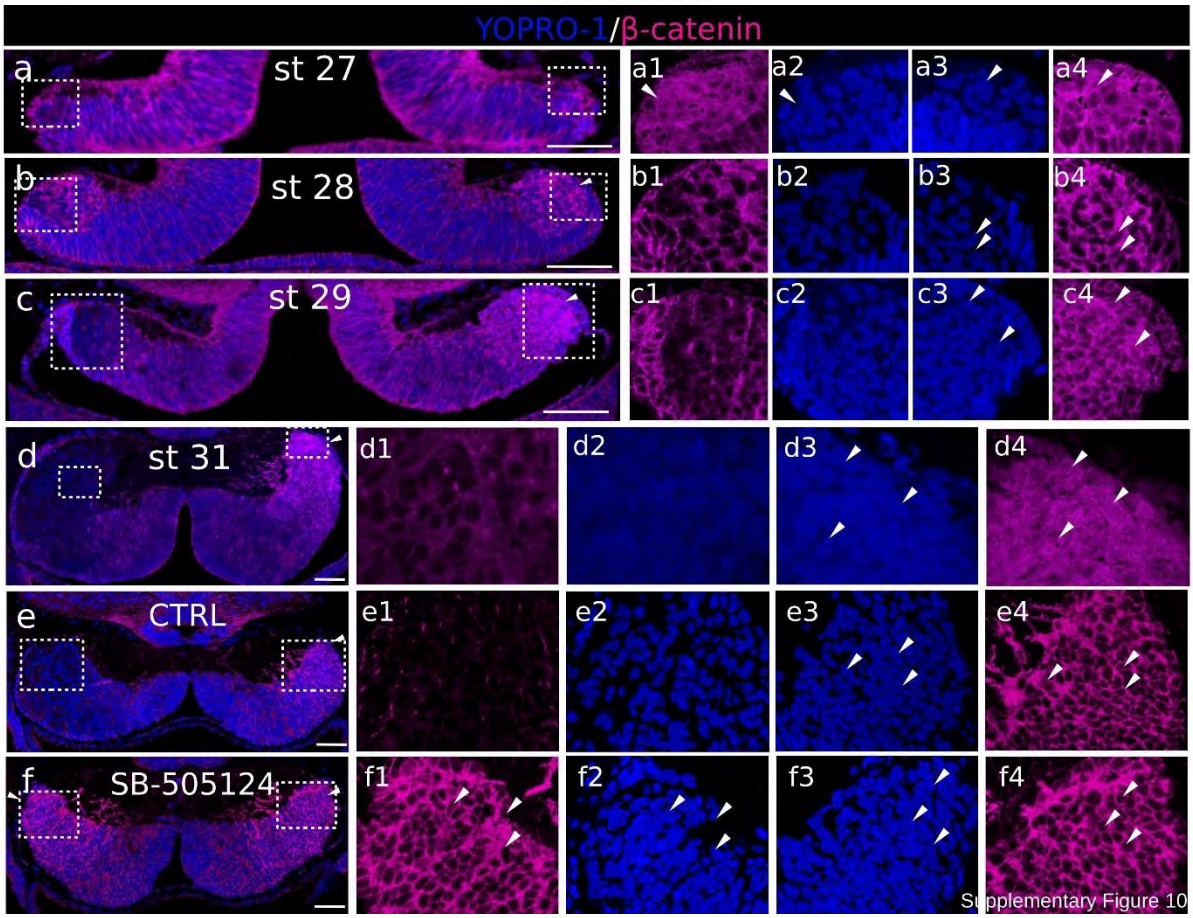

Supplementary Figure 10

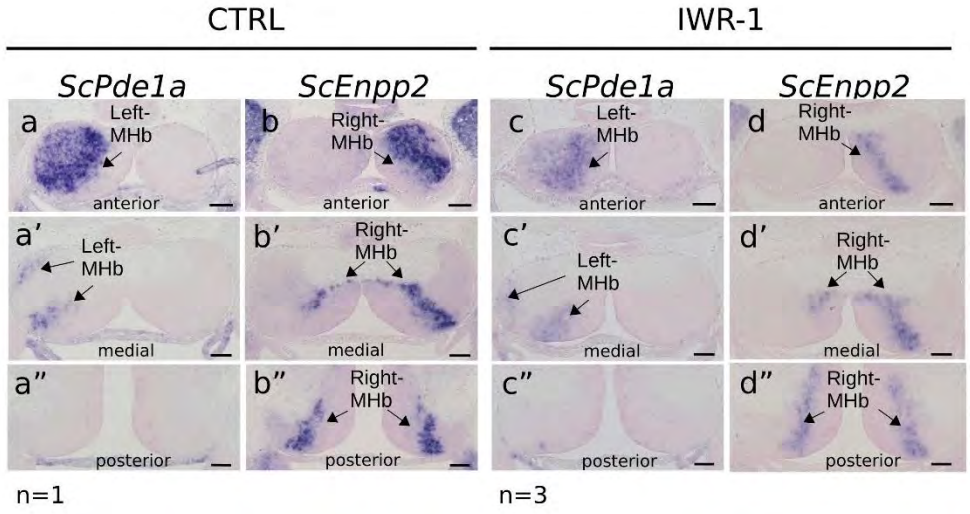

Supplementary Figure 11

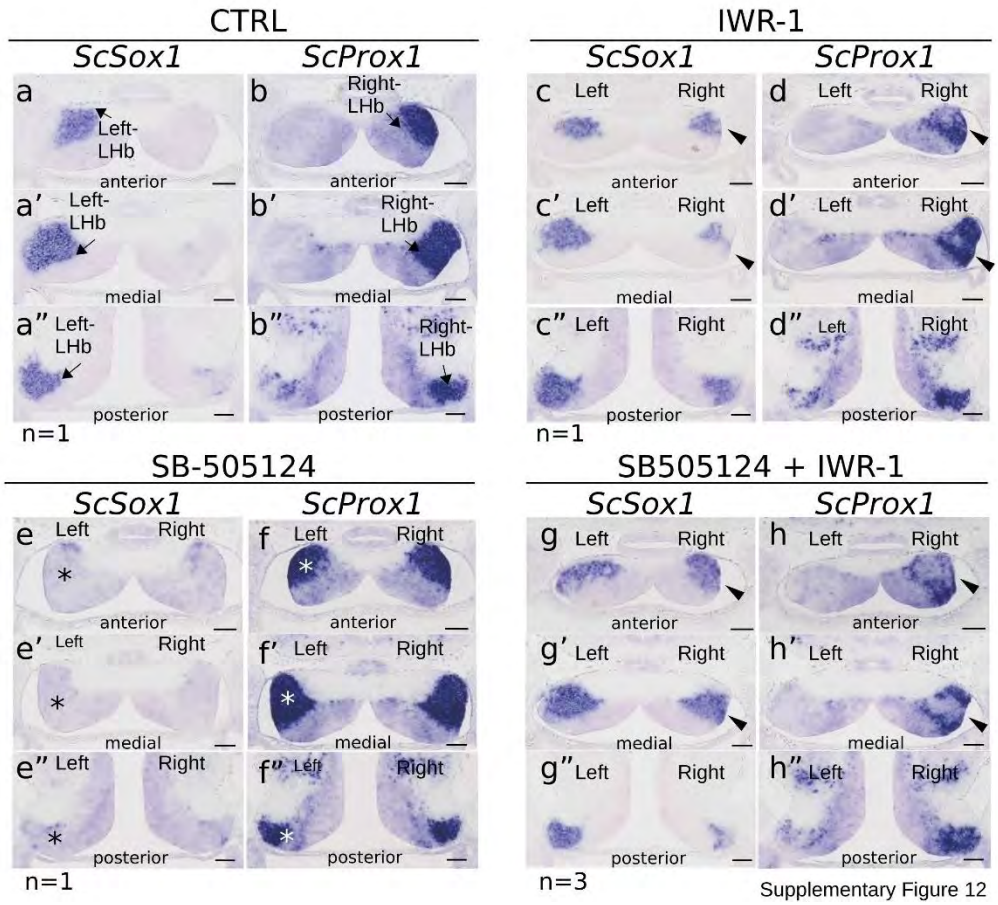

Supplementary Figure 12

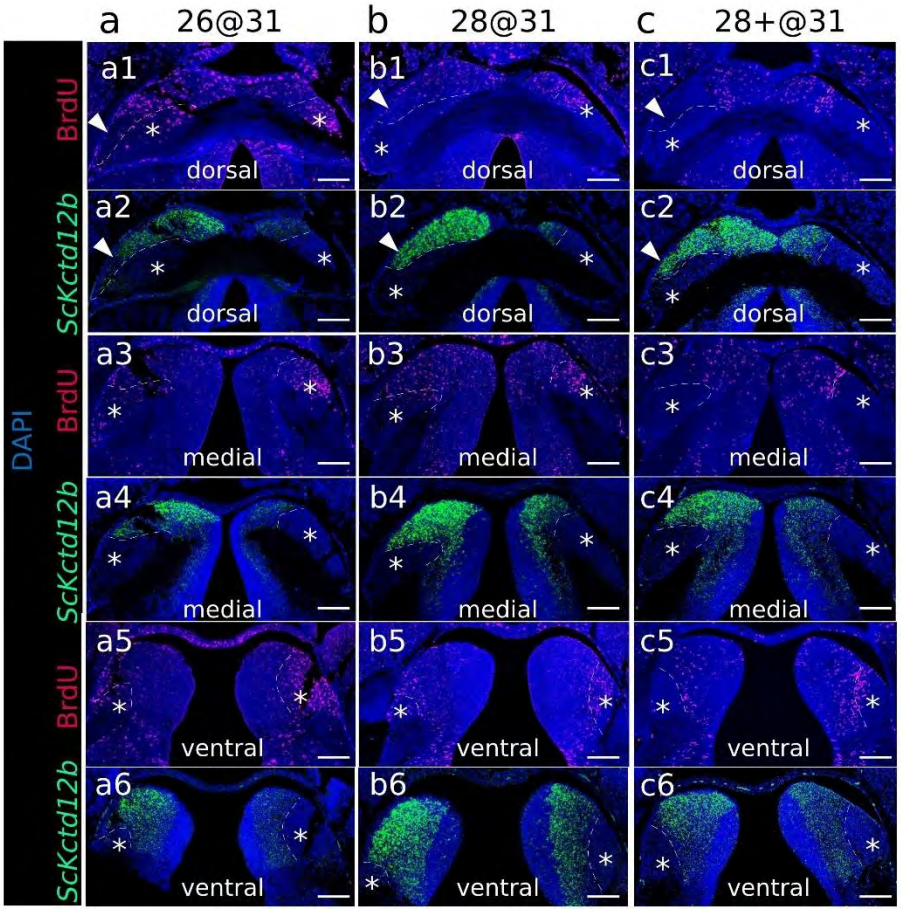

Supplementary Figure 13

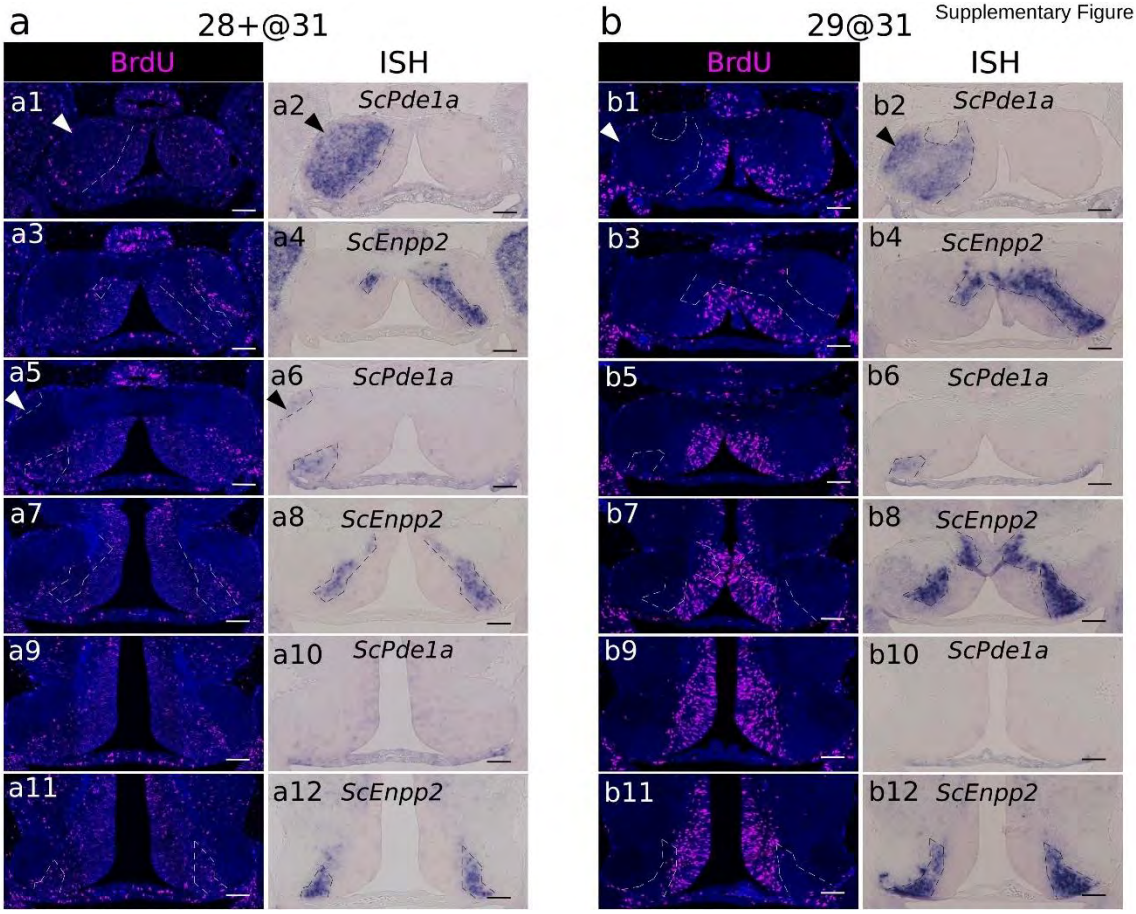

Supplementary Figure 14

CHAPITRE III – Caractérisation par tomographie ARN du cerveau embryonnaire de la petite roussette

III-1. Objectif, contexte et principaux résultats

Nous avons pu démontrer que la répression à gauche de la voie Wnt pendant la différenciation des habénulas dépend d'une fenêtre beaucoup plus précoce d'activité restreinte à gauche de la voie Nodal (Cf chapitre 2). Toutefois la possibilité que la voie Nodal contrôle d'autres mécanismes impliqués dans la formation des asymétries habénulaires complexes observées chez la roussette reste ouverte. Une façon d'aborder cette question est de rechercher les programmes génétiques et les cibles régulées par la voie Nodal, et cela pendant sa fenêtre d'activité restreinte à gauche, peu après la fermeture du tube neural. En vue de cet objectif, nous avons engagé une approche permettant d'obtenir un profilage ARN exhaustif en 3D de la région céphalique d'un embryon de stade 17 (stade correspondant à la fenêtre d'activité restreinte à gauche de la voie Nodal chez la roussette). Nous avons pour cela engagé une approche par tomographie ARN, consistant à séquencer des coupes sériées en cryostat selon trois plans orthogonaux, puis à reconstruire un modèle digital 3D contenant l'ensemble du répertoire génétique exprimé pour chacun des voxels. Ce travail a principalement reposé sur le travail de R. Lagadec (IR CNRS) pour l'obtention des séquences et celui de H. Mayeur (AI CNRS en bioinformatique) pour la production du modèle digital. Mon rôle a été une contribution aux hybridations in situ permettant de valider le modèle obtenu.

Nous avons pu obtenir par tomographie ARN un modèle transcriptomique en 3D de la région céphalique de l'embryon de roussette au stade 17. Ce modèle reproduit fidèlement les profils de gènes candidats d'expression connue dans le cerveau embryonnaire. En outre, en collaboration avec un collègue mathématicien, des outils statistiques exploitant les notions d'autocorrélation et corrélation ont été développés afin respectivement d'identifier des gènes d'expression régionalisée ou coexprimés avec un marqueur donné. Nous cherchons actuellement à exploiter ce modèle et ces outils statistiques (étendues à la notion de biais, ou "skewness" d'une distribution) pour identifier des gènes d'expression asymétrique dans le diencéphale dorsal. Des listes de gènes susceptibles de répondre à ce critère ont été générées et les hybridations in situ de validation sont en cours. Cette technique, qui contrairement aux approches de type scRNA-seq donne une information spatiale directe, est applicable à toute espèce, embryon ou tissu de taille suffisante, dès lors qu'un génome de bonne qualité est disponible. Elle est actuellement utilisée dans le laboratoire pour la même question que décrite ci-dessus chez la lamproie ainsi que pour des descriptions d'habénulas adultes de lamproie et roussette. Elle pourrait être mise en œuvre chez un spectre beaucoup plus large d'espèces, choisies par exemple à la fois pour leur position phylogénétique et sur la base des profils obtenus au chapitre 2, pour des caractérisations moléculaires exhaustives des habénulas, en complément d'approches scRNA-seq. Ce travail fait l'objet d'un manuscrit en cours de révision (ci-après).

III-2. Publication

When bigger is better: 3D RNA profiling of the developing head in the catshark *Scyliorhinus canicula*

Hélène Mayeur[1], Maxence Lanoizelet[1], Aurélie Quillien[2], Arnaud Menuet[3], Léo Michel[1], Kyle Martin[4], Sébastien Dejean[5], Patrick Blader[2], Sylvie Mazan[1], Ronan Lagadec[1]

[1]CNRS, Sorbonne Université, UMR7232-Biologie Intégrative des organismes marins (BIOM), Observatoire Océanologique, Banyuls sur Mer, France

[2]Centre de Biologie Intégrative (CBI, FR 3743), Université de Toulouse, CNRS, UPS, France

[3]UMR7355, Experimental and Molecular Immunology and Neurogenetics, CNRS and University of Orléans, Orléans, France

[4]Institut de Mathématiques de Toulouse, Université de Toulouse, CNRS, UPS, UMR 5219, Toulouse, France

[5]UK Research and Innovation, Biotechnology and Biological Sciences Research Council Affiliations, UK

1) Abstract

We report the adaptation of RNA tomography, a technique allowing 3D genome-wide expression profiling, to a non-conventional model organism occupying a key phylogenetic position in gnathostomes, the catshark *Scyliorhinus canicula*. We focused analysis on head explants at embryonic stage 17, which follows neural tube closure and is of interest for a number of developmental processes, including early brain patterning, placode specification or epithalamic asymmetry formation. As described in the zebrafish, we have sequenced RNAs extracted from serial sections along transverse, horizontal and sagittal planes, mapped the data onto a gene model reference taking advantage of the high continuity genome recently released in the catshark, and projected read counts onto a digital model of the head obtained by confocal microscopy. This results in the generation of a genome-wide 3D atlas, containing digital expression data for more than 20000 protein-coding genes in about 12000 voxels. The digital profiles obtained for candidate forebrain regional markers along antero-posterior, dorso-ventral and left-right axes reproduce those obtained by ISH, with expected relative organizations. We also apply the concepts of spatial autocorrelation or correlation to analysis of these data and show that they provide adequate statistical tools to extract novel expression information from the model. These data and tools allow exhaustive searches of genes exhibiting any predefined expression characteristics, thus providing

a reference for comparative analyses across gnathostomes. This methodology appears best suited to species endowed with large embryo sizes and opens novel perspectives to a wide range of non-conventional model organisms, traditionally counter-selected on size criterion.

2) Introduction

Unravelling spatially resolved gene expression information is crucial to address a variety of developmental biology problems, including patterning, regional identity specification and determination. These questions are currently revolutionised by emerging RNA-seq approaches and concomitantly developing analytical methods aimed at extracting relevant information from the resulting datasets (J. H. Lee et al., 2014; Sun, Zhu, & Zhou, 2020; Waylen, Nim, Martelotto, & Ramialison, 2020). One such approach is RNA tomography or tomo-seq, which was initially applied to the developing zebrafish (Junker et al., 2014). Briefly, this method relies on the sequencing of frozen sections along three orthogonal planes and subsequent reconstruction of a spatially resolved genome-wide RNA profile, using the iterative proportional fitting algorithm. This results in the generation of a digital 3D model of the tissue of interest, containing genome-wide expression information for every voxel of the model.While the sequencing of sections has been successfully used for the identification of genes exhibiting regionalised expression along a polarity axis, 3D reconstructions using tomo-seq have only been obtained in the zebrafish thus far to our knowledge (Junker et al., 2014).We have used this approach to generate a spatially resolved, genome-wide RNA profile of the embryonic head of a non-conventional model, the catshark *Scyliorhinus canicula*. As a chondrichthyan, this species occupies a key phylogenetic position to gain insight into gene regulatory network modifications, which have occurred concomitantly with the rise of gnathostome innovations, such as paired limbs, true teeth or articulated jaws, or to infer ancestral features, when discrepancies are observed between actinopterygians and sarcopterygians (Coolen et al., 2008). It is also amenable to experimental approaches during development and while genome size (4.2 Gb) has been for long an obstacle to whole genome sequencing projects, an annotated, chromosome-level genome assembly has been recently released in his species.We have focussed on stage 17, which shortly follows neural tube closure. A number of developmental processes of interest, such as the partitioning of the forebrain into its broad subdivisions (Santos-Durán et al., 2015), the appearance of the earliest diencephalic asymmetries (Lagadec et al., 2015), the specification of cephalic mesoderm components (Derobert et al., 2002), or the initiation of optic cup and otic placode formation (O'Neill, McCole, & Baker, 2007; Plouhinec et al., 2005), indeed take place in the developing head at this stage. Here, we report the generation of a genome-wide 3D profile of the cephalic region at this stage, as well as the use of correlation and other statistical analysis tools to extract novel information from this model. In addition to providing reference expression data at the stage analysed, this analysis validates the catshark as a relevant model organism for tomo-seq characterisations of embryogenesis.

3) Materials and Methods

3.1. Preparation of total RNA from sections

3.1.1. Explant dissection and cryostat sectioning

Eggs from the catshark *Scyliorhinus canicula* were obtained from the Aquariology Service of the Banyuls sur Mer Oceanological Observatory. Stage 17 embryos (Ballard et al., 1993) were manually dissected and truncated anterior to the first pair of pharyngeal pouches. The cephalic explant was transferred to OCT medium, frozen in liquid nitrogen prior to sectioning (18µm cryostat sections). Each frozen section was transferred into Trizol (200µL) immediately after collection.

3.1.2. RNA extraction

Total RNA was extracted using standard Trizol extraction protocol and purified on Macherey Nagel NucleoSpin RNA XS columns according to the manufacturer's instructions. 2µl (1:200000) spike-in RNA (ERCC) were added to each section prior RNA extraction as internal control.

3.2. Illumina library construction and sequencing

cDNA synthesis, amplification and Illumina library construction were conducted following (Holler & Junker, 2019) with the following modifications. Superscript II reverse-transcriptase was replaced by SuperScript IV (Invitrogen) and cDNA clean-up was done using Omega Bio-Tek's Mag-Bind TotalPure NGS. Sequencing was conducted on the DNB-seq platform (100 bp paired-end).

3.3. Read mapping and counting

Reads were mapped onto the reference gene model database (provided in Supplementary Table 1; annotation in Supplementary Table 2) complemented with spike-in sequences. Briefly, the construction of this database (to be reported elsewhere) involved building an isoform collapsed version of the NCBI gene models annotated from the catshark genome assembly (https://www.ncbi.nlm.nih.gov/assembly/GCF_902713615.1/#/st_Primary-Assembly) and a subsequent extension of 3' UTRs. Reference indexing, read mappings and quantifications were done using Kallisto v0.44.0 using the --bias parameter and bootstrapping 100 times. Read counts were aggregated for each gene and each sectioning plane, and normalized on the total spike-in read counts

for each section. Ratios between spike-in input and output were calculated for the sum of all sections along each section plane.

3.4. 3D model construction

To generate a 3D binary mask, a stage 17 head explant dissected as described above was fixed in PFA 4%, DAPI stained, dehydrated in methanol and cleared in Benzyl Alcohol/Benzyl Benzoate (1/2) prior to mounting and imaging with a SP8X confocal microscope (Leica). A 3D binary mask was built using Fiji to obtain a binary image of the tissues. It was then oriented transversally using Interactive Stack Rotation plugin and resized to match sectioning planes and section numbers along all three planes. The 3D expression genome-wide profile was reconstructed from normalized read counts for each gene and each section plane using the MATLAB code reported in (Junker et al., 2014). In short, following the virtual partitioning of the binary mask in serial digital sections as described above, an iterative process was applied to 1D profiles of each gene in each sectioning plane, multiplying the 3D expression of the gene by said profile in each plane in succession. 3D profiles of selected genes were then visualized using Fiji. A custom Fiji macro was also written in order to get all 3D profiles, each viewed in all three sectioning planes, in the AVI format and with more explicit filenames.

3.5. Statistical analyses

For the autocorrelation analysis, Moran's indexes were calculated for each gene model on a neighbourhood defined as the voxels on adjacent sections on all three section planes, giving a 3*3*3 cube centered on each voxel examined. Supports for the indexes thus obtained were estimated by statistical tests, consisting in calculating the Pearson correlation between the expression of a gene between all possible pairs of neighbouring voxels, using the R libraries spdep (especially moran.test) and ade4. Pearson correlations between the 3D expressions of each possible pair of genes in each voxel (18µm cube at the intersection of one section of each sectioning plane) were calculated using the R command cor with default parameters.

3.6. In situ hybridisation (ISH) of whole-mount embryos and sections

Whole-mount ISH and ISH of paraffin sections were conducted using standard protocols as described previously (Lagadec et al., 2015).

4) Results

4.1. Obtaining genome-wide RNA profiles for serial sections along AP, DV and LR axes

In order to obtain a digital transcriptomic map of the catshark stage 17 forebrain, we excised out an embryonic head explant truncated anterior to the first branchial pouch (Figure1A). Using cryostat sectioning along AP (antero-posterior), DV (dorso-ventral) and LR (left-right) axes, we obtained a total of 34 transverse, 33 horizontal and 30 sagittal 18 μm frozen sections (Figure 1B). We next synthesized cDNA for each individual section using barcoded primers, which allowed to pool cDNA samples for linear amplification and quality controls of amplified products (Supplementary Table 3). We next proceeded to Illumina library construction and sequencing to obtain about 210 million reads (PE-100). For the bioinformatic analysis (Figure 1C), reads were demultiplexed and mapped onto a gene model reference obtained taking advantage of the catshark genome NCBI annotation and of transcriptomic resources available in our laboratory (Supplementary Tables 1-2), which led to the assignment of 76% reads to a reference contig (Supplementary Figure 1B-C,E-F,H-I). For each section plane, a minimum of 4 reads in at least two sections were detected prior to normalisation for more than 13000 contigs (13354, 13501 and 14239 for sagittal, horizontal and transverse planes respectively). Read counts were then normalised, allowing the generation of expression profiles for any gene model along each section plane and of a genome-wide 3D digital model of gene expression (Figure 1D-E).

3.2. Expression traces along AP, DV and LR axes reflect expression restrictions of candidate regional markers

In order to test whether variations in read counts between serial sections along each axis reflect gene regional expressions, we focussed on forebrain markers previously characterised in the catshark (*Dlx5*, *Emx3*, *Gbx2*, *Pax3*, *Nkx2.1*, *Nodal*, *Lefty2*; Supplementary Table 5). Markedly higher *Dlx5* and *Emx3* read counts are found in anterior, versus posterior, transverse sections in line with their telencephalic expression. Read counts drop to basal levels from sections 1 to 27 for *Dlx5* and from sections 1 to 20 for *Emx3*, which accurately reflects the more restricted anterior territory of the former (Derobert et al., 2002; Santos-Durán et al., 2015) (Figure 2A). In contrast, read counts peak at posterior levels (sections 1 to 8) for *Gbx2*, a midbrain marker (Figure 2A). Along the DV axis, *Pax3* and *Emx3* read counts are high dorsally and return to basal levels in more ventral sections, with a more dorsal peak for the former, while *Nkx2.1* reads are only detected in ventral-most sections (22 to 33), in line with ISH profiles for these genes (Derobert et al., 2002; O'Neill et al., 2007; Santos-Durán et al., 2015) (Figure 2B). Along the left-right axis, sharp left restricted peaks are observed for *Nodal* and *Lefty2* (sections 7 to 10), consistent with the asymmetric left diencephalic territory reported at this stage (Lagadec et al., 2015) (Figure 2C). In contrast, the curve shows a plateau at the level of sections located on each side of the

midline (sections 10 to 18) for the symmetrically expressed hypothalamic marker *Nkx2.1* (Santos-Durán et al., 2015) (Figure 2C).

3.3. Construction of a 3D digital RNA profile reproducing ISH expression patterns

We next projected the sequence data obtained for each section onto a mask imaged by confocal microscopy (Figure 1E) to generate a 3D RNA profile. To do so, we used iterative proportional fitting (Fienberg, 1970), as described in Junker et al., 2014. This resulted in a digital 3D model, containing expression information computed by the algorithm, referred to hereafter as digital expression, for every reference gene model of the reference database and in every voxel identified by its (x, y, z) coordinates in the mask. In order to assess whether virtual expression patterns reflect expected ISH expression profiles, we focussed on forebrain regional markers along AP (antero-posterior), DV (dorso-ventral) and LR (left-right) axis (Figures 3-5; Supplementary Figure 2). Along the AP axis, we visualised digital profiles for *ScDlx5*, *ScEmx3*, *ScLhx5* and *ScGbx2*. *ScDlx5* and *ScEmx3* exhibit anterior digital expressions, while *ScLhx5* positive voxels are located in a more medial position, adjacent to a posterior *ScGbx2* territory, in line with ISH expressions (compare Figure 3C-D,C1-C3 with Figure 3E-H). Similarly, as observed in ISH, *ScEmx3* digital territory extends further laterally and posteriorly than the one of *ScDlx5* (Figure 3B,B1-B2) and *ScLhx5* digital expression exhibits a sharp posterior border, contrasting with its anterior extension (Figure 3B3,C3). Similarly, along the DV axis, *ScNkx2.2* positive voxels are restricted to a medial and ventral location relative to optic evaginations, within a broader *ScSix3* digital territory (Figure 4A,B,B2,B3). The latter overlaps with *ScEmx3* digital expression, which extends further posteriorly and is restricted dorsally (Figure 4A,B,B1-B2). These features reproduce those observed in whole-mount ISH (Figure 4C-E). Along the left-right axis, left-restricted (*ScNodal*, *ScVg1*) or left-enriched (*ScLefty2*) digital signals are observed dorsally and posteriorly to optic evaginations, at the interface between *ScSix3* anterior and *ScIrx1l* posterior digital territories, as in whole-mount ISH (compare Figure 5A-F to Figure 5G-K). Digital signals are primarily located dorsally as expected for *ScNodal*, *ScVg1* and *ScLefty2* (Figure 5A-C, G1-I1), but a few additional positive voxels, without clear counterparts in ISH, can be observed more ventrally at the level of optic evaginations (Figure 5A,C). The accuracy of the digital profiles was further assessed by analysis of digital expressions of additional markers including paralogous genes (Supplementary Figure 2). Comparison of *ScNkx2.1* and *Nkx2.2* digital profiles shows a broader expansion of the latter compared to its paralogue along the AP axis, as observed in ISH (Supplementary Figure 2A,A1,A2). Along the same line, the sharp dorsal and ventral boundaries of *ScSix6* territory and its relative location within the broader *ScSix3* domain are reproduced by the digital profiles of the paralogues (compare Supplementary Figure 2B,C,B1,C1), as well as the respective expression characteristics of *ScFgf17* (restricted to the anterior-most part of the forebrain) and *ScFgf8* (harbouring a major midbrain expression and a more diffuse

anterior signal) (compare Supplementary Figure 2D,D1,D2). The ventral expansion of forebrain markers such as *ScFoxg1* or *ScFezF2* relative to *ScEmx3* is also correctly predicted by digital profiles (compare Figure 3D, Supplementary Figure 2E,F,E1,E2,F1,F2).

3.4. Autocorrelation as estimate of the spatial restriction of digital profiles

In order to extract lists of genes exhibiting regionalised digital expressions, we applied the mathematical notion of spatial autocorrelation, commonly used to analyse the spatial structure of geographically distributed biological variables (Diniz-Filho, Nabout, Telles, Soares, & Rangel, 2009) to the analysis of our digital expression model (Figure 6, Supplementary Figure 4). The underlying rationale is that genes harbouring regionalised profiles should tend to exhibit similar digital expressions in neighbouring voxels within their expression territory and therefore harbour high autocorrelation values (Supplementary Figure 3A). Moran's index, which provides a measure of spatial autocorrelation, and the p-value evaluating its statistical support, were calculated for all gene models (Figure 6A; Supplementary Table 5). In order to assess the relevance of this notion to the identification of regionalised genes, we first surveyed Moran's indexes (i) and p-values obtained for a selection of the forebrain regional markers analysed above, exhibiting discrete digital territories of variable size (*ScFezF2*, *ScNkx2.2*, *ScEmx3*, *ScSix6*, *ScDlx5*, *ScFoxg1*, *ScVg1*, *ScIrx3*, *ScGbx2*, *ScFgf8*, *ScFgf17*, *ScNodal*: Fig. 6A). In all cases, indexes>0.1, supported by null p-values, were retrieved. The lowest index is obtained for *ScNodal* (i=0.11), which harbours a relatively low total digital expression (n=619 counts over all voxels), while highest indexes are obtained for *ScFezF2*, *ScScNkx2.2* and *ScEmx3*, three genes exhibiting high digital expressions (total digital expression summed over all voxels>14000) and a single, continuous territory. Reciprocally, we randomly selected gene models within 5 sectors of the p-value versus Moran's index graph (sector 1: 0<-ln(p-value)<50; sector 2: 100<-ln(p-value)<150, sector 3: 250<-ln(p-value)<300; sector 4: p-value=0 and i<0.2: sector 5: p-value=0 and 0.6<i<0.7; Figure 6A). All genes within sector 4 and 5 exhibited strongly regionalised digital territories, with a digital expression observed in all voxels in the former and a majority of voxels in the latter (Fig. 6E-F; Supplementary Figure 4D-E). In contrast, labelled voxels appeared more and more dispersed and generally less numerous from sector 3 to 1 (Fig. 6B-D; Supplementary Figure 4A-C). In general, gene models of low total digital expression were over-represented among those with low autocorrelations and high p-values (Supplementary Table 6). For instance, more than 19% of the gene models harbouring -log(p-value)<50 have a total digital expression<100 and this value drops to respectively 2.1 and 0.1% for gene models with i<0.1 and i>0.1, p-value=0. Of note, 12 100 gene models, i.e. more than 60% of annotated gene models, exhibit significant autocorrelation values (i>0.1, p-value=0; Supplementary Table 5; Supplementary Figure 3B).

3.5. A correlation statistical approach allows the detection of co-expressed genes

The availability of a spatially resolved genome-wide profile allows the search for genes harbouring specific expression criteria, for instance coexpression with selected subterritory markers. To exploit this possibility, we used a statistical approach relying on calculations of Pearson correlations (Cor) between pairs of gene models (Supplementary Figure 5A). We first calculated Pearson correlations between digital expressions of all coding gene model pairs taking over all voxels of our 3D model. Lists of genes ranked by correlation coefficient can then be extracted from this dataset for every single gene model. In order to assess the possibility to identify new genes coexpressed with a given candidate by this method, we focussed on correlations with *ScShh*, which harbours a highly specific expression in the ventral midline, faithfully reproduced by the digital pattern (Figure 7A-B; Supplementary Table 7). All 12 genes most strongly correlated to *ScShh* (Cor>0.4) harbour a ventral digital expression, largely overlapping with the one of *ScShh* (Figure 7A; Supplementary Figure 5B). This list contains the catshark orthologues of two midline markers, respectively coding for the Shh receptor Ptch1 and the extracellular matrix protein Slit3 (Ingham & Mcmahon, 2001; Yeo et al., 2001). In order to assess the possibility to identify novel genes coexpressed with *ScShh* by this approach, we conducted ISH for novel candidates retrieved from this list (*ScFoxa2*, *ScRrbp1*, *ScRop1l*, *ScIgfbp3*, *ScFoxb2*, *ScCcd39*). While no or very faint midline signals were observed for *ScRop1l* and *ScCcd39* (not shown), strong ventral restricted signals similar to the one of *ScShh* were retrieved for *ScFoxa2*, *ScRrbp1*, *ScIgfbp3* and *ScFoxb2* (Figure 7C-F). This validates both the predictive power of the 3D model and the possibility to extract novel information using a correlation approach.

5) Discussion

Since the initial description of RNA tomography in whole-mount zebrafish embryos (Junker et al., 2014), this technique has been applied to a limited number of model systems, including limbs, the regenerating or pathological heart and aorta formation, in established model organisms (Burkhard & Bakkers, 2018; Combs & Eisen, 2017; van den Brink et al., 2020; C. C. Wu et al., 2016; Yvernogeau et al., 2020). Most of these analyses have focussed on characterisations along a single plane of interest, which is sufficient to identify genes differentially expressed along a polarity axis but does not provide a 3D spatial resolution. Here, we have applied this technique for the first time to a non-conventional model, the catshark *Scyliorhinus canicula*, focussing on the developing head, shortly after neural tube closure. The resulting dataset is a digital model of this structure, containing expression information in each voxel of this volume for about 30 000 sequences, of which almost 20 000 correspond to coding ones.

By principle, a lower limit in resolution is imposed by section thickness, here 12 µm. The 3D reconstruction, which integrates data from three independent and necessarily non-identical biological

samples, is another factor potentially limiting the resolution of the model. However, we find that 3D digital expressions for known markers of broad forebrain subdivisions faithfully reproduce the broad characteristics observed by ISH, and the method was sensitive enough to allow the detection of regionalised expressions for transcription factors or signalling molecules. Digital profiles also correctly predicted expression details, such as expression differences between paralogues, such as *ScNkx2*.1 and *ScNkx2*.2, or *ScSix3* and *ScSix6*. The 3D digital model obtained in the catshark thus provides a reference atlas to rapidly identify profiles of interest from a list of candidate genes of interest.

An important perspective opened by the availability of this resource is the possibility to identify new genes characterised by a defined expression feature, such as co-expression with a territory marker. Established methodologies are still lacking for 3D tomo-seq datasets, which have been thus far only produced in the zebrafish. Junker et al., 2014 previously reported that an Euclidean distance-based method could lead to the detection of new genes harbouring expression similarity to an organiser marker. Here we used an alternative statistical method, relying on estimates of Pearson correlations between any pair of genes and over all voxels, to address this question. This approach leads to the identification of novel genes exhibiting clear similarities in digital profiles to *ScShh*, chosen as a test for its highly specific ventral-restricted expression. We also validate some of these profiles by ISH, which demonstrates the potential of this approach to gain insight into the whole expression repertoire of territories of interest.

Similarly, we used the concept of spatial autocorrelation for the search of genes exhibiting regionalised expression. The underlying formalism has been widely used in biology (Diniz-Filho et al., 2009), albeit not, to our knowledge, to tomo-seq data. Its adequacy in this context is related to the assumption that expression values per voxel are non-independent variables, neighbouring voxels, for instance around a peak or trough, tending to behave similarly. This characteristic is indeed observed for most regionalised genes, albeit not for those exhibiting pepper-and-salt expression patterns, such as Notch targets (Caprioli, Goitsuka, Pouget, Dunon, & Jaffredo, 2002). In line with the relevance of this indicator, strongly supported (p-value=0) positive autocorrelation values were obtained for all highly regionalised genes analysed, whether expressed in broad territories like most of the forebrain markers tested, or in highly restricted domains such as left-restricted *Vg1* or *Nodal*. Reciprocally, randomly selected patterns exhibit an expression dispersal per voxel, which increases inversely proportionally to their autocorrelation value. These data points to autocorrelation as a relevant indicator to identify genes of regionalised expression. Its use suggests that as previously proposed (Junker et al., 2014), regionalised genes (p-value=0, autocorrelation>0.1) represent an important fraction (>60%) of the total gene repertoire.

The combination of scRNA-seq, with its cellular resolution, and 3D RNA tomography, which directly provides spatial resolution, may be a powerful approach for comprehensive characterisation of tissue or

organ RNA profiling (van den Brink et al., 2020). The limitations of the latter in terms of resolution by the mere principle of a sectioning-based approach, are alleviated in the case of large organ, or embryo sizes, a characteristic shared by many non-conventional model organisms such as the catshark. This characteristic, necessarily counter-selected in the choice of genetic models, has generally been considered as a weakness of these species but could thus become an advantage in spatial transcriptomics approaches such as tomo-seq. Analyses of the 3D model reported here for biological questions such as forebrain regionalisation, sensory organ, placode or diencephalic asymmetry formation, will help to assess the potential of this approach.

Legends to Figures

Figure 1. Main experimental steps used to generate a 3D RNA profile of the catshark embryonic head (stage 17). (A) Explant dissection: left side photograph of a stage 17 catshark embryo with a blue arrowhead showing the dissected explant and a dotted line delimiting its posterior boundary (top panel) and higher magnification confocal view of the explant with the posterior dissection plane (bottom panel). **(B)** Cryo-sectioning: schemes show the planes used to generate series of cryo-sections (horizontal, pink; transverse, green; sagittal, blue). Section numbers along each plane are indicated. **(C)** Library contruction and sequencing resulting in RNA-seq data for a total of 97 sections. **(D)** Visualisation of expression traces along each axis for all gene models. **(E)** Generation of a genome-wide 3D profile with its three steps (generation of a confocal 3D image of the explant, of a digitized model and computation of digital expressions for each voxel and gene model). D, dorsal; V, ventral; Ant, anterior; Post, posterior.

Figure 2. Expression traces for selected genes along transverse (A), horizontal (B) and sagittal (C) planes. For each graph, section number and read counts are indicated along x- and y-axes respectively. Sections 1 to 34, 33 and 30 are respectively numbered from posterior to anterior in (A), dorsal to ventral in (B) and left to right in (C).

Figure 3. Digital profiles reproduce regional patterns along AP axis. **(A)** Scheme representing the digitized model of stage 17 catshark head with sagittal, transverse and horizontal digital section planes shown as white rectangles. **(A1)**, **(A2)** and **(A3)** show examples of digitized sections along these planes. **(B-D)** Digital horizontal (B) and sagittal (C-D) sections showing merged profiles of *ScDlx5* (magenta), *ScEmx3* (blue), *ScLhx5* (green) and *ScGbx2* (red). Sections are numbered from dorsal to ventral in (B) and from left to right in (C,D). **(B1-3) and (C1-3)** Digital sections showing the profiles for *ScDlx5* (B1,C1), *ScEmx3* (B2,C2) and *ScLhx5* (B3,C3) merged in (B) and (C) respectively. **(E-H)** Left lateral

views of stage 17 catshark embryonic heads after ISH with probes for *ScDlx5* (E), *ScEmx3* (F), *ScLhx5* (G) and *ScGbx2* (H). Scale bars=200µm.

Figure 4. Digital profiles reproduce regional patterns along DV axis. (A-B) Digital sagittal (A) and transverse (B) sections showing merged profiles of *ScSix3* (magenta), *ScEmx3* (blue), *ScNkx2.2* (yellow) and *ScGbx2* (red). Sections are numbered from left to right in (A) and from posterior to anterior in (B). **(B1-3)** Digital sections showing the profiles for *ScEmx3* (B1), *ScSix3* (B2) and *ScNkx2.2* (B3) merged in (B). **(C-E)** Left lateral views of stage 17 catshark embryonic heads after ISH with probes for *ScEmx3* (C), *ScSix3* (D) and *ScNkx2.2* (E). Scale bars=200µm.

Figure 5. Nodal signaling components exhibit left enriched profiles. (A-F) Digital transverse (A-C) and horizontal (D-F) sections showing merged profiles of *ScSix3* (magenta), *ScIrx1l* (yellow) and *ScNodal* (blue) (A,D), *ScVg1*(blue,) (B,E), *ScLefty2* (blue). Sections are numbered from posterior to anterior in (A-C) and from dorsal to ventral in (D-F). **(G-K)** Left lateral views of stage 17 catshark embryonic heads after whole-mount ISH with probes for *ScNodal* (G), *ScVg1* (H), *ScLefty2* (I), *ScIrx1l* (J) and *ScSix3* (K). **(G1-I1)** horizontal sections of the brain of stage 17 catshark embryos after hybridization with probes for *ScNodal* (G1), *ScVg1* (H1), *ScLefty2* (I1). Hybridisation signals are left-restricted in (G-I;G1-I1). Scale bars=200µm.

Figure 6. Autocorrelation as an indicator of profile regionalisation. (A) Graph showing autocorrelation values (y-axis) and their statistical support (-ln(p-value) on x-axis) for all gene models. Each dot corresponds to a single gene model, in grey if the corresponding total digital expression is below 100, in black otherwise. Gene models harbouring null p-values are shown on the right of the graph with -ln(p-value)=infinite (inf). Horizontal arrowheads point to dots corresponding to a selection of genes, exhibiting clearly regionalised expressions in ISH experiments. Colour codes for these genes are shown boxed in black. Coloured boxes delimit sectors of the graph numbered from 1 to 5 and containing gene models with decreasing p-values/increasing autocorrelations (green, sector 1; yellow, sector 2, cyan, sector 3; blue, sector 4; magenta, sector 5). **(B-F)** Digital transverse sections showing examples of profiles observed in sectors 1 (B), 2 (C), 3 (D), 4 (E) and 5 (F). The corresponding gene identities are indicated and sections are numbered from posterior to anterior.

Figure 7. Identification of genes harbouring expression correlation with *ScShh*. (A) Digital profiles on sagittal section number 15 (out of 30, from left to right) of a selection of genes showing a high

expression correlation to *ScShh* (red): *ScFoxA2* (green), *ScRrbp1* (blue), *ScPtch1*(cyan), *ScIgfbp3* (yellow) and *ScFoxb2* (purple). The rank of each gene in the list of gene models ordered by decreasing correlation to *ScShh* and the correlation value (Cor) are indicated below each section. **(B-F)** Left lateral views of stage 17 catshark embryonic heads after ISH using probes for *ScShh* (B), *ScFoxA2* (C), *ScRrbp1* (D), *ScIgfbp3* (E) and *ScFoxb2* (F). Scale bars=200µm.

Supplementary Figure 1. General sequence analysis of sections. (A,D,G) Input/output relationship for spike-in RNA, summed over all transverse (A), horizontal (D) and sagittal (G) sections. Each dot corresponds to a spike-in form. Linearity is observed, suggesting a minimal amplification bias. **(B-C,E-F,H-I)** Number of reads mapping onto the gene model reference without normalisation (B,E,H) or following normalisation on spike-in (C,F,I). (B,C), (E,F) and (H,I) correspond to transverse, horizontal sections and sagittal sections respectively. Sections are shown and numbered from posterior (Post.) to anterior (Ant.) in (B-C), from dorsal (Dors.) to ventral (Vent.) in (E-F) and from left to right in (H-I).

Supplementary Figure 2. Accuracy of 3D RNA profiles. (A-F) Digital sagittal sections showing merged profiles for: (A), *ScNkx2.1* (magenta) and *ScNkx2.2* (blue); (B), *ScSix3* (magenta) and *ScEmx3* (blue); (C), *ScSix6* (red) and *ScEmx3* (blue); (D), *ScFgf17* (magenta) and *ScFgf8* (blue); (E), *ScFoxg1* (blue) and *ScIrx1l* (red); (F), *ScFezF2* (blue) and *ScIrx3* (magenta). Sections are numbered from left to right. **(A1,A2,B1,C1,D1,D2,E1,E2,F1,F2)** Left lateral views of stage 17 catshark embryonic heads after ISH with probes for respectively *ScNkx2.1*, *ScNkx2.2*, *ScSix3*, *ScSix6*, *ScFgf8*, *ScFgf17*, *ScFoxg1, ScIrx1l, ScFezF*2 and *ScIrx3*. Scale bars=200µm.

Supplementary Figure 3. Autocorrelation as a measure of expression regionalisation. (A) Schemes illustrating how local variations affect autocorrelation values. **(B)** Histogram showing the distribution of gene models depending on autocorrelation values for null p-values.

Supplementary Figure 4. Typical digital profiles obtained for gene models chosen randomly in selected sectors of the autocorrelation versus p-value graph. Digital sections showing the profiles of gene models found in sectors 1, 2, 3, 4 and 5 (as defined in Figure 6) are presented in (A), (B), (C), (D) and (E) respectively. Voxels harbouring digital expressions appear clustered in sector 1 and 2, but more and more dispersed in sectors 3 to 1. Only one expression is observed (*ScZn234*, sector 3), expression being ubiquitous in this case.

Supplementary Figure 5. Correlation as a measure of expression profile similarity. (A) Schemes illustrating positive, null and negative correlations between two genes. **(B)** Digital sagittal sections (section 15, from left to right) showing the profiles of genes showing high expression correlations to ScShh. The rank in the list of gene models ordered by decreasing correlation is shown, as well as the correlation value obtained for each gene shown. All gene models share a ventrally restricted signal similar to the one observed for *ScShh*.

Supplementary Table 1. Fasta file of the gene models database used for read mapping. The table contains the identity and sequence of the 30348 gene models used as reference in this study.

Supplementary Table 2. Annotation file of the gene models. THe table contains 20554 gene models that could be annotated. For each gene model (column A), the identity of the best Blastx hit in Swissprrot is indicated in column B. Columns C and D respectively contain the query deduced amino acid and hit protein sequence contained within the alignment.

Supplementary Table 3. Primers used for library constructions and read counts obtained per section. For each section (column A), the names and sequences of the barcoded primers used for reverse transcription are indicated in columns B and C. The names and sequences of Illumina indexes used for Illumina library construction are listed in columns D and E. The read counts obtained after sequencing are indicated for each section in column F.

Supplementary Table 4. Identifiers of analysed selected genes.

Supplementary Table 5. Autocorrelation values for all gene models. Gene models are listed in column A, with their annotation in column B. The autocorrelation value and corresponding statistical support (p-value) are shown in columns C and D respectively. The total digital expression (summed over all voxels) is given in column E.

Supplementary Table 6. Effect of total digital expression level on autocorrelation. The table shows the number of gene models exhibiting a total digital expression <100 or >100 (columns B and C respectively; total in column C) depending on their autocorrelation/p-value (column A). Corresponding ratios are shown in columns E and F respectively.

Supplementary Table 7. Correlations with ScShh. For all gene models (column A, annotation in column B), 3D profile correlations with *ScShh* are shown in column C.

Supplementary Video 1. Zip file containing digital profiles for all gene models along serial horizontal sections. Serial sections 1 to 33 are shown and numbered from dorsal to ventral in one .avi file per gene model. Annotation and gene model identity are indicated in the name of each file (format: Annotation_Gene Model identity_horizontal.avi). Individual files can be opened in Fiji and visualised following appropriate size adjustment (interpolation: none).

Supplementary Video 2. Zip file containing digital profiles for all gene models along serial sagittal sections. Serial sections 1 to 30 are shown and numbered from left to right in one .avi file per gene model. Annotation and gene model identity are indicated in the name of each file (format: Annotation_Gene Model identity_sagittal.avi). Individual files can be opened in Fiji and visualised following appropriate size adjustment (interpolation: none).

Supplementary Video 3. Zip file containing digital profiles for all gene models along serial transverse sections. Serial sections 1 to 34 are shown and numbered from posterior to anterior in one .avi file per gene model. Annotation and gene model identity are indicated in the name of each file (format: Annotation_Gene Model identity_transverse.avi). Individual files can be opened in Fiji and visualised following appropriate size adjustment (interpolation: none).

Supplementary Videos 4 and 5. Avi files containing merged digital profiles for *ScDlx5* (magenta), *ScEmx3* (blue), *ScLhx5* (green) and *ScGbx2* (red) along serial horizontal sections 1 to 33 (numbered from dorsal to ventral; Suppl. Video 4) and along serial sagittal sections 1 to 30 (numbered from left to right; Suppl. Video 5).

Supplementary Videos 6 and 7. Avi files containing merged digital profiles for *ScSix3* (magenta), *ScEmx3* (blue), *ScNkx2.2* (yellow) and *ScGbx2* (red) along serial sagittal sections 1 to 30 (numbered from left to right; Suppl. Video 6) and along serial transverse sections 1 to 34 (numbered from posterior to anterior; Suppl. Video 7).

Supplementary Videos 8-13. Avi files containing merged digital profiles for *ScSix3* (magenta), *ScIrx1l* (yellow), *ScNodal* (blue, Suppl. Videos 8 and 9), ScVg*1* (blue, Suppl. Videos 10 and 11) and *ScLefty2* (blue; Suppl. Videos 12 and 13). Suppl. Videos 8, 10 and 12 show serial transverse sections 1 to 34, numbered from posterior to anterior. Suppl. Videos 9, 11 and 13 show serial horizontal sections 1 to 33 (numbered from dorsal to ventral).

Supplementary Videos 14-19. Avi files containing merged digital profiles along serial sagittal sections 1 to 30 (from left to right) for: Suppl. Video 14, *ScNkx2.1* (magenta) and *ScNkx2.2* (blue); Suppl. Video 15, *ScSix3* (magenta) and *ScEmx3* (blue); Suppl. Video 16, *ScSix6* (red) and *ScEmx3* (blue); Suppl. Video 17, *ScFgf17* (magenta) and *ScFgf8* (blue); Suppl. Video 18, *ScFoxg1* (blue) and *ScIrx1l* (red); Suppl. Video 19, *ScFezF2* (blue) and *ScIrx3* (magenta).

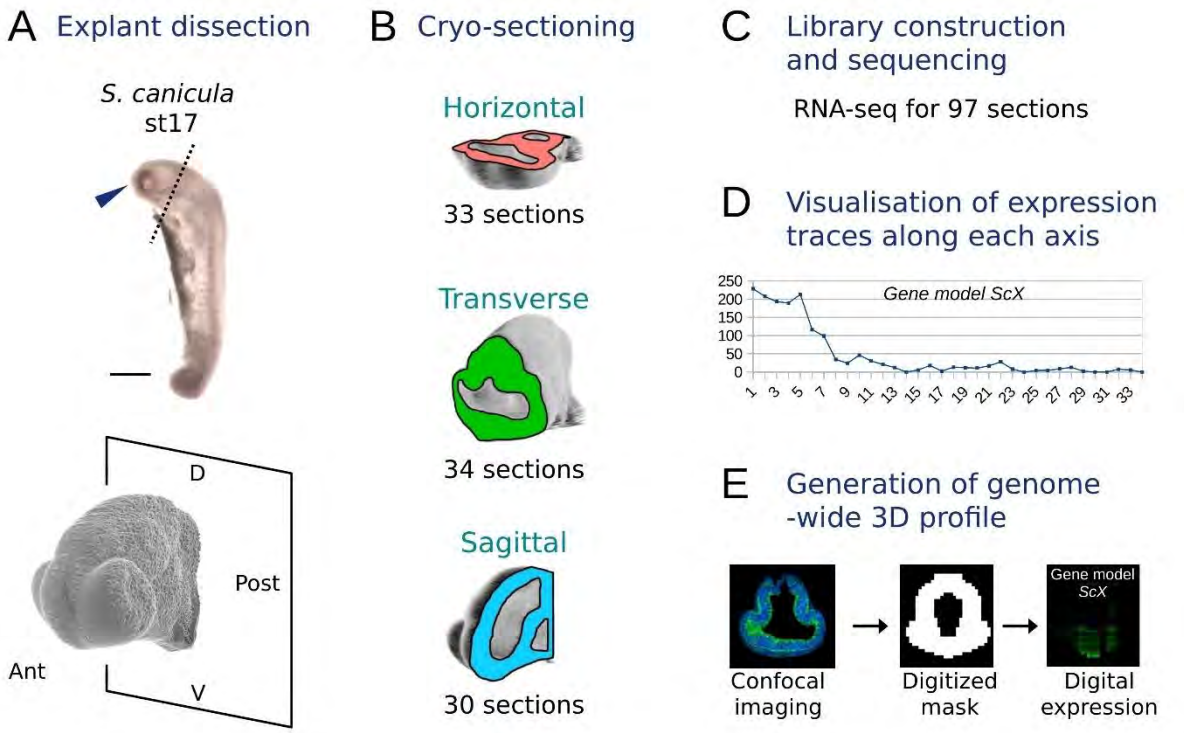

Figure 1

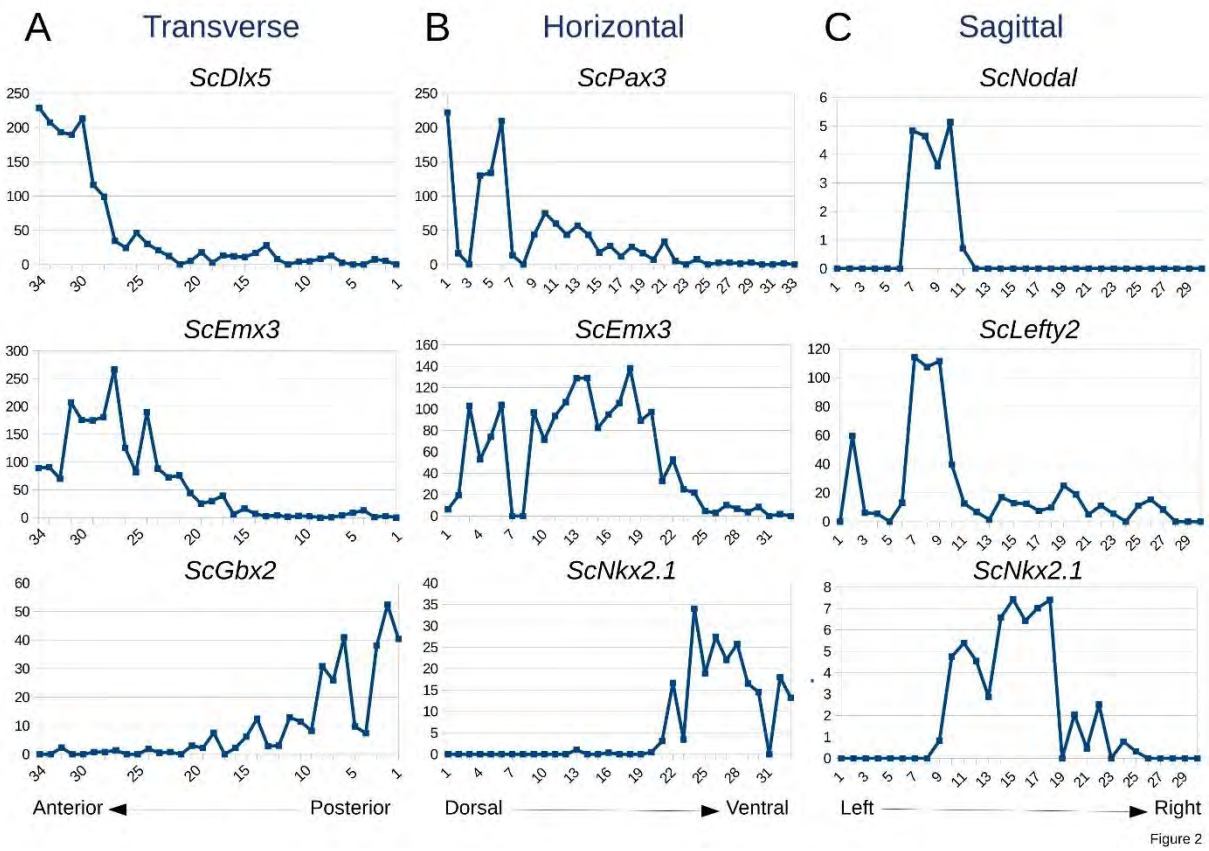

Figure 2

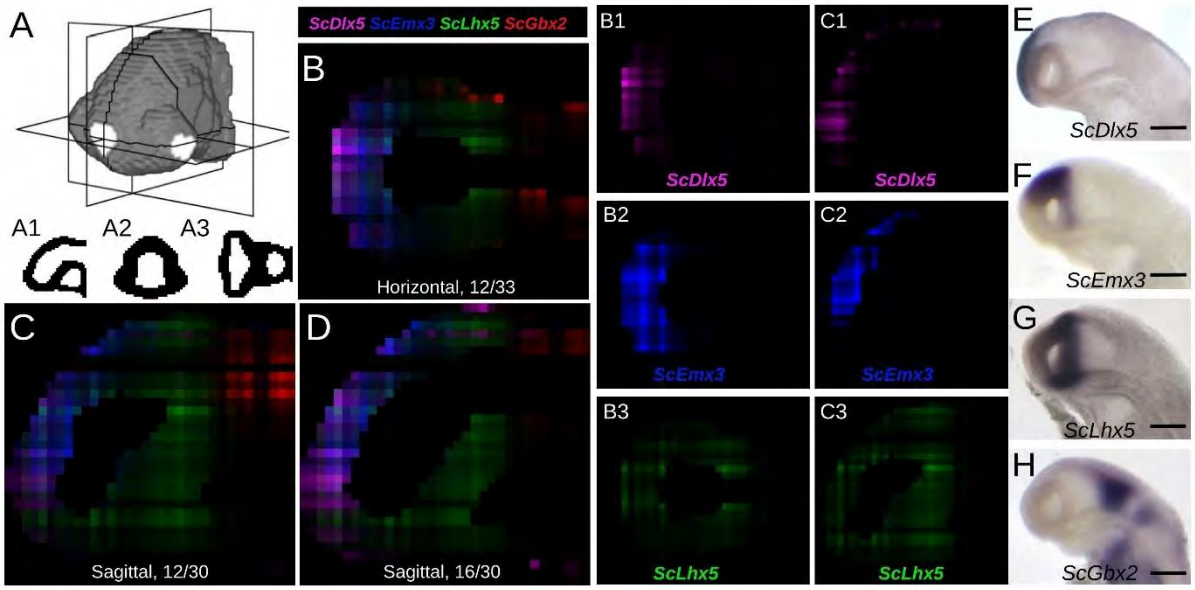

Figure 3

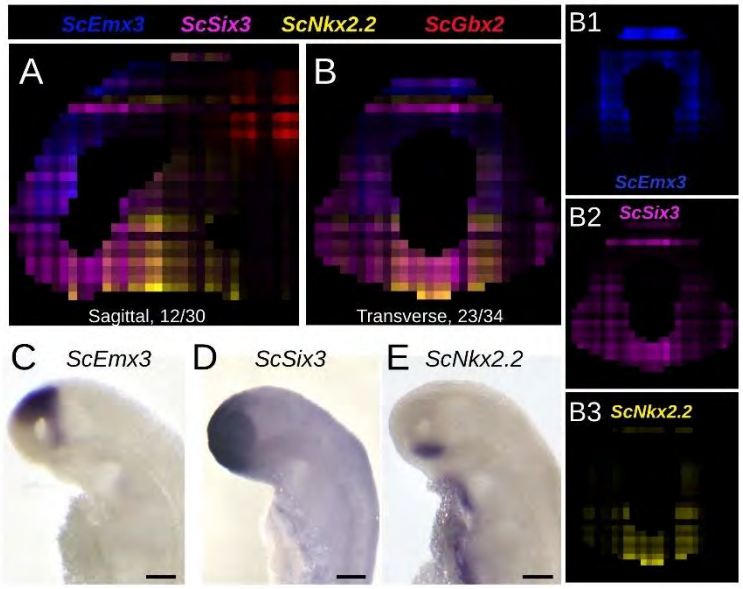

Figure 4

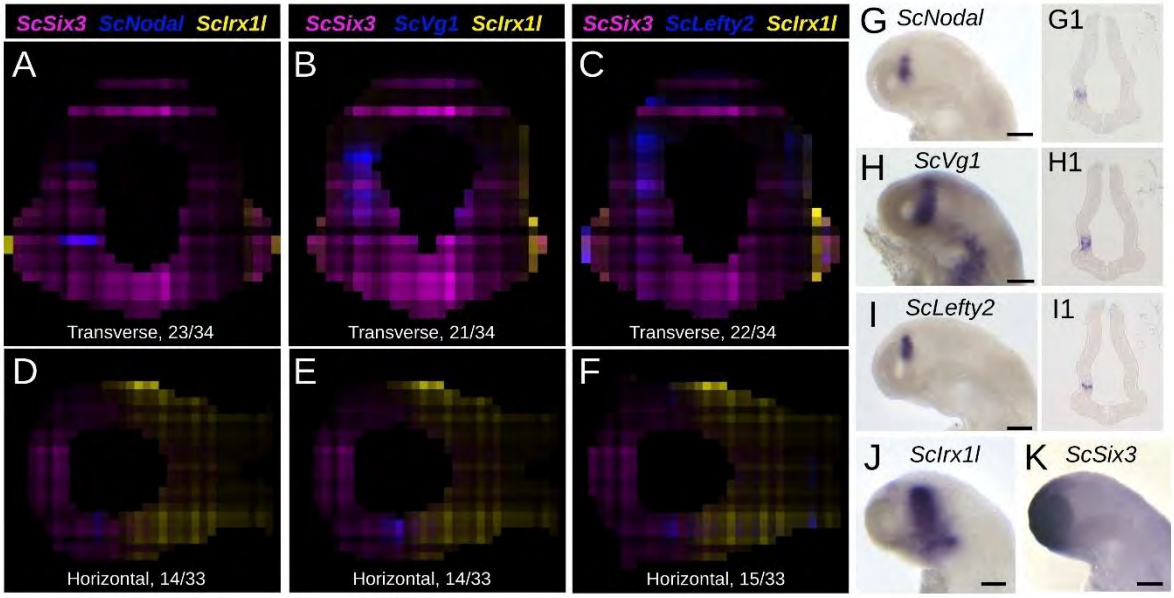

Figure 5

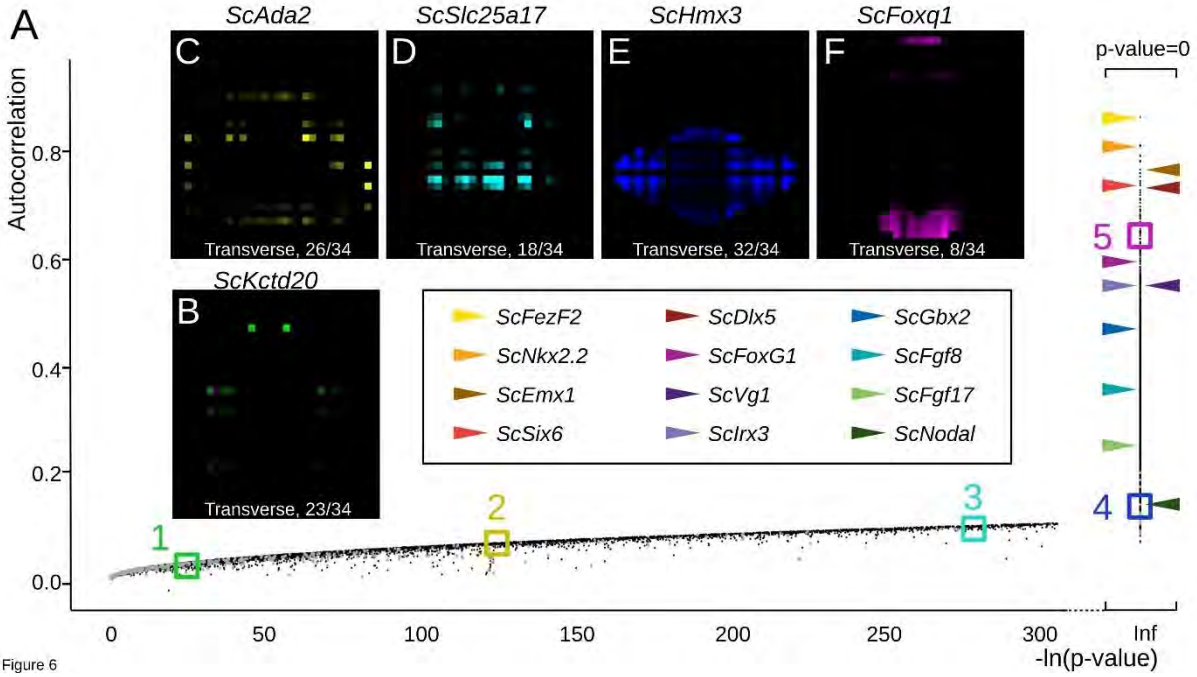

Figure 6

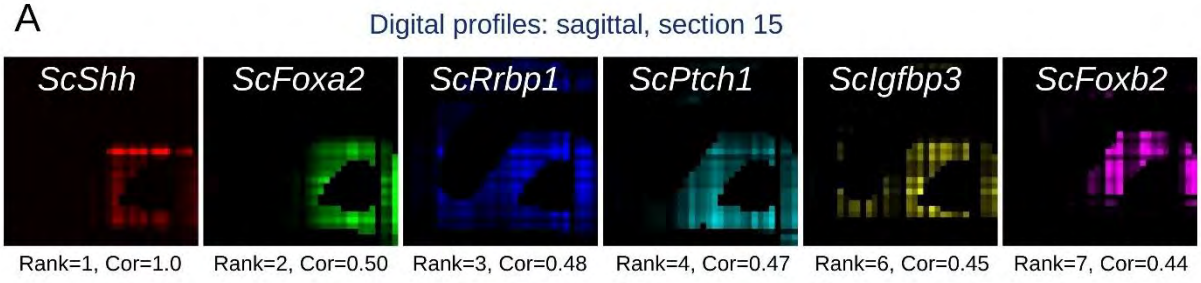

Figure 7

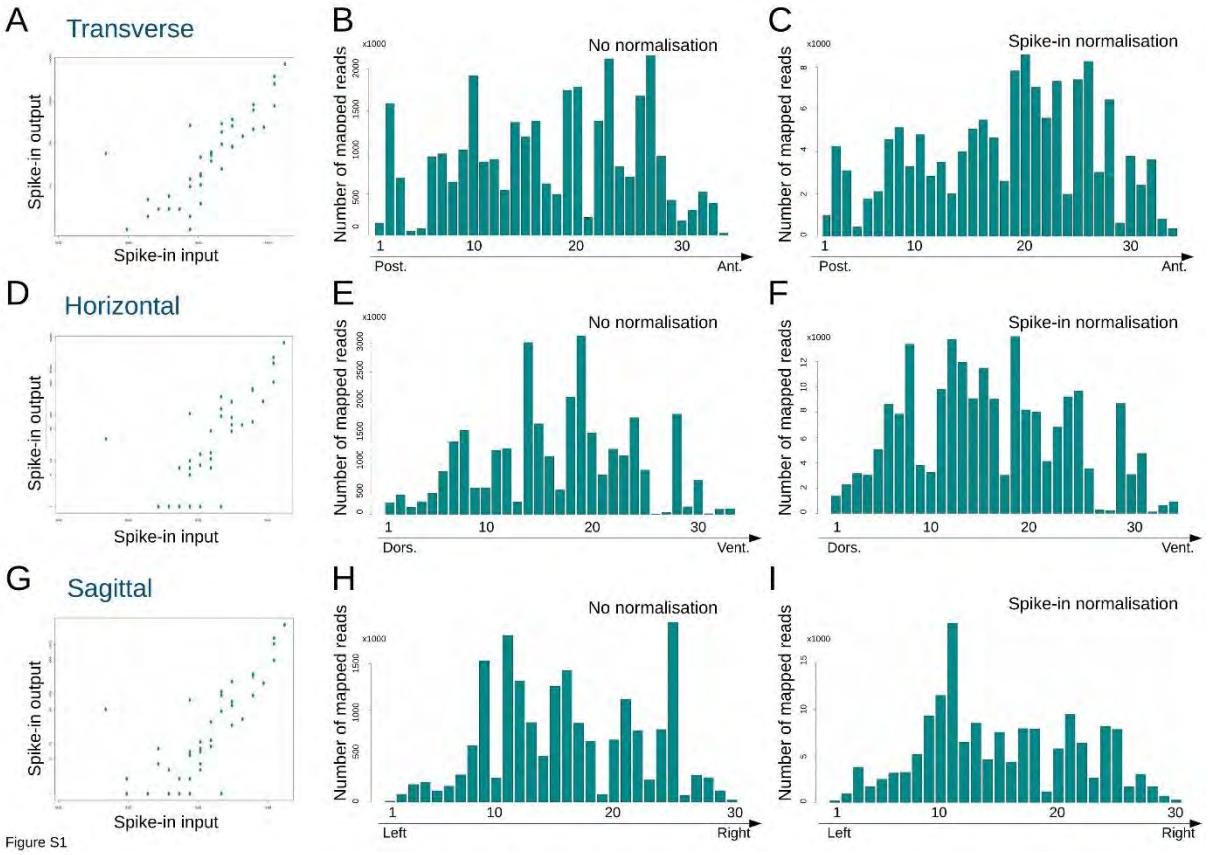

Figure S1

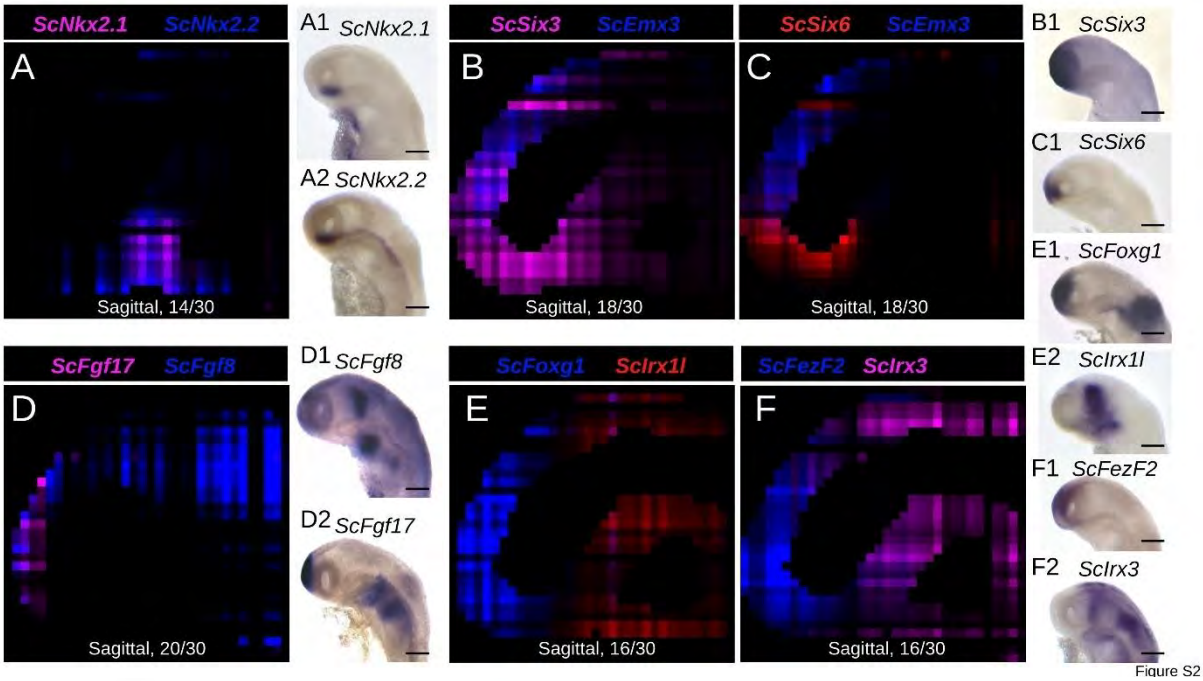

Figure S2

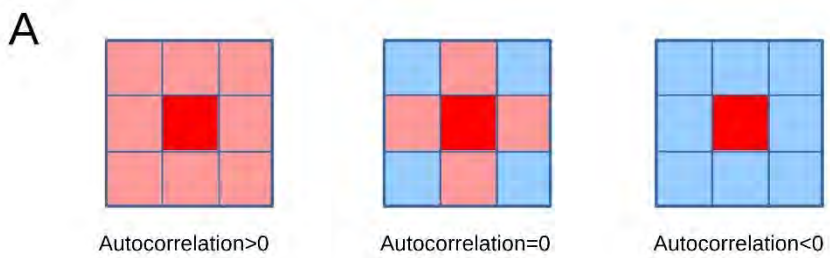

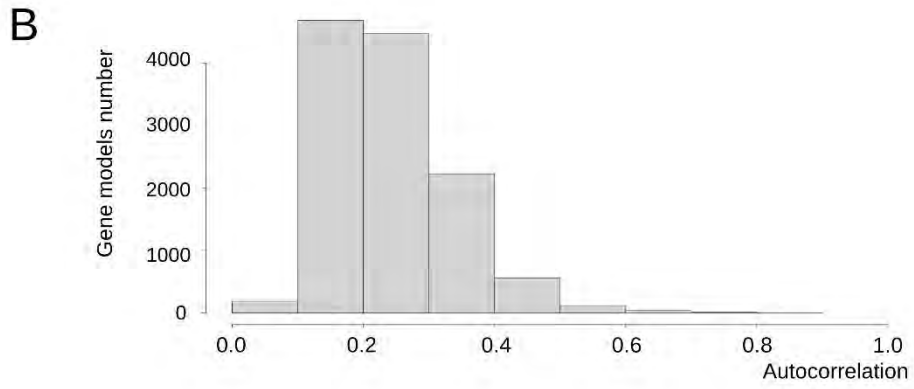

Figure S3

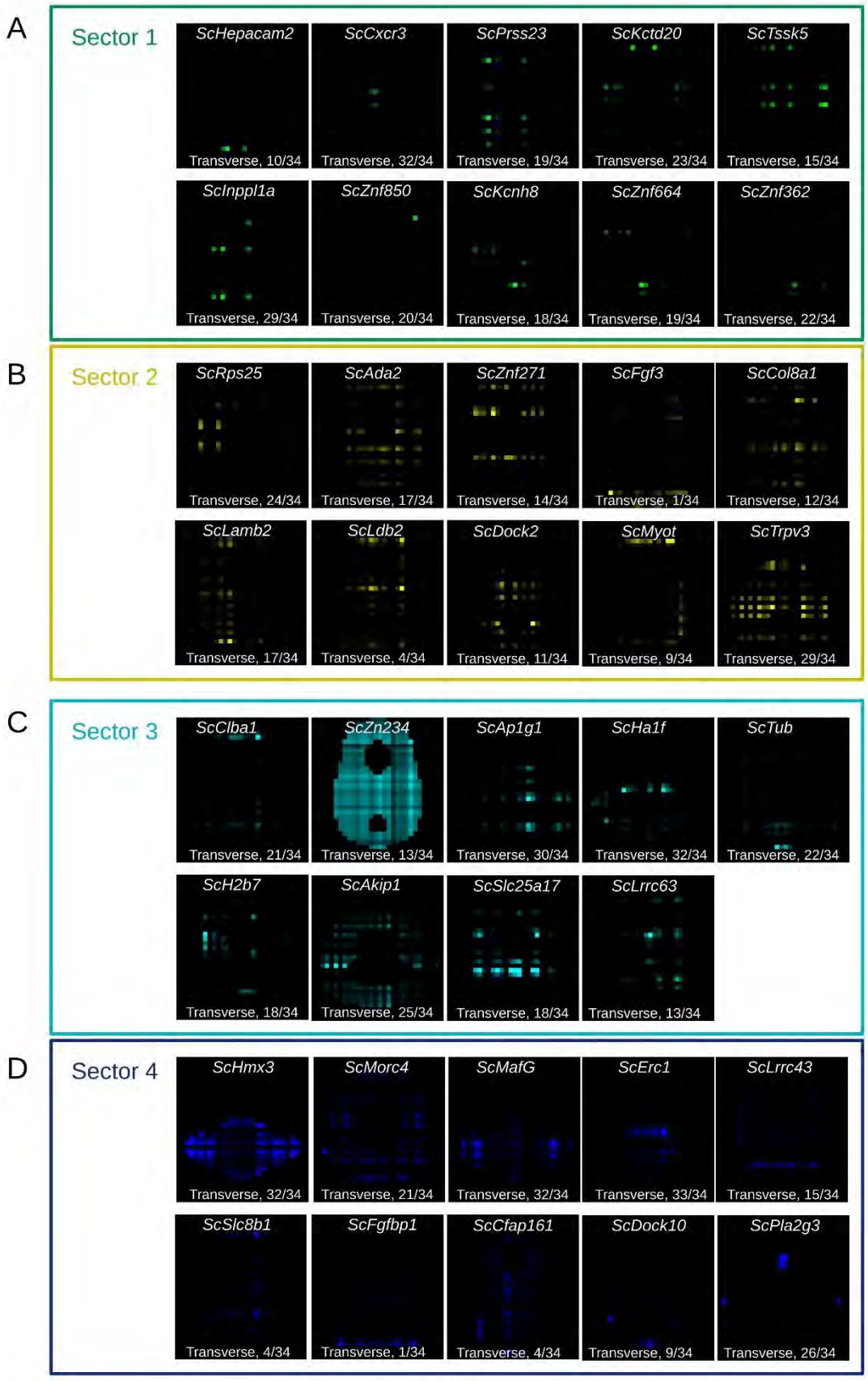
A
Sector 1
ScHepacam2
Transverse, 10/34
ScCxcr3
Transverse, 32/34
ScPrss23
Transverse, 19/34
ScKctd20
Transverse, 23/34
ScTssk5
Transverse, 15/34
ScInppl1a
Transverse, 29/34
ScZnf850
Transverse, 20/34
ScKcnh8
Transverse, 18/34
ScZnf664
Transverse, 19/34
ScZnf362
Transverse, 22/34
B
Sector 2
ScRps25
Transverse, 24/34
ScAda2
Transverse, 17/34
ScZnf271
Transverse, 14/34
ScFgf3
Transverse, 1/34
ScCol8a1
Transverse, 12/34
ScLamb2
Transverse, 17/34
ScLdb2
Transverse, 4/34
ScDock2
Transverse, 11/34
ScMyot
Transverse, 9/34
ScTrpv3
Transverse, 29/34
C
Sector 3
ScClba1
Transverse, 21/34
ScZn234
Transverse, 13/34
ScAp1g1
Transverse, 30/34
ScHa1f
Transverse, 32/34
ScTub
Transverse, 22/34
ScH2b7
Transverse, 18/34
ScAkip1
Transverse, 25/34
ScSlc25a17
Transverse, 18/34
ScLrrc63
Transverse, 13/34
D
Sector 4
ScHmx3
Transverse, 32/34
ScMorc4
Transverse, 21/34
ScMafG
Transverse, 32/34
ScErc1
Transverse, 33/34
ScLrrc43
Transverse, 15/34
ScSlc8b1
Transverse, 4/34
ScFgfbp1
Transverse, 1/34
ScCfap161
Transverse, 4/34
ScDock10
Transverse, 9/34
ScPla2g3
Transverse, 26/34

Figure S4

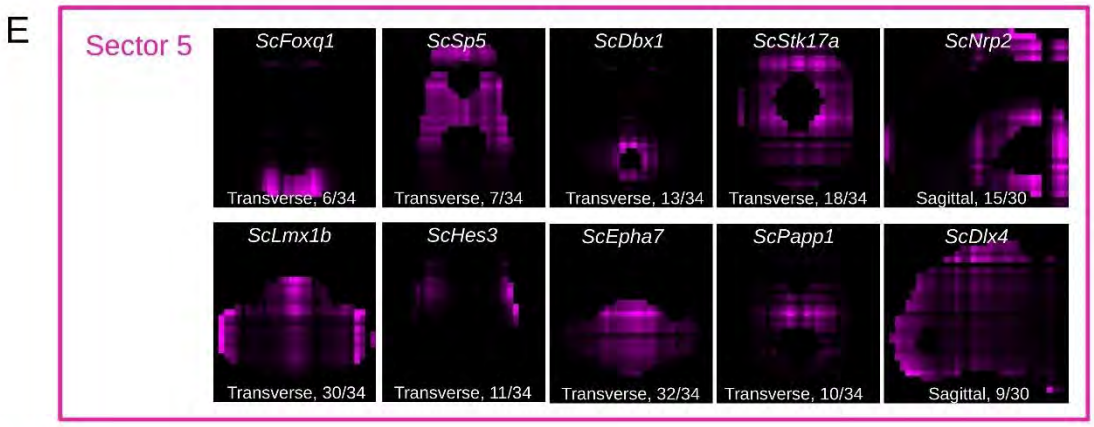
E
Sector 5
ScFoxq1
Transverse, 6/34
ScSp5
Transverse, 7/34
ScDbx1
Transverse, 13/34
ScStk17a
Transverse, 18/34
ScNrp2
Sagittal, 15/30
ScLmx1b
Transverse, 30/34
ScHes3
Transverse, 11/34
ScEpha7
Transverse, 32/34
ScPapp1
Transverse, 10/34
ScDlx4
Sagittal, 9/30

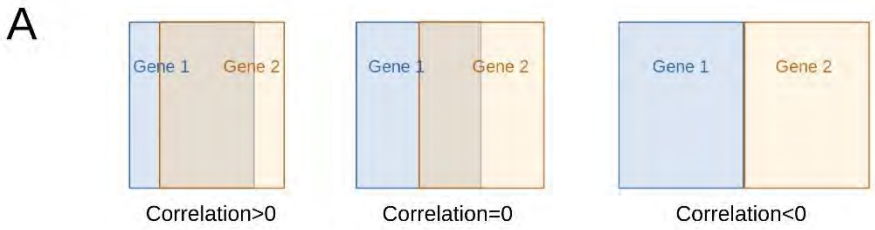
A
Gene 1
Gene 2
Correlation>0
Gene 1
Gene 2
Correlation=0
Gene 1
Gene 2
Correlation<0

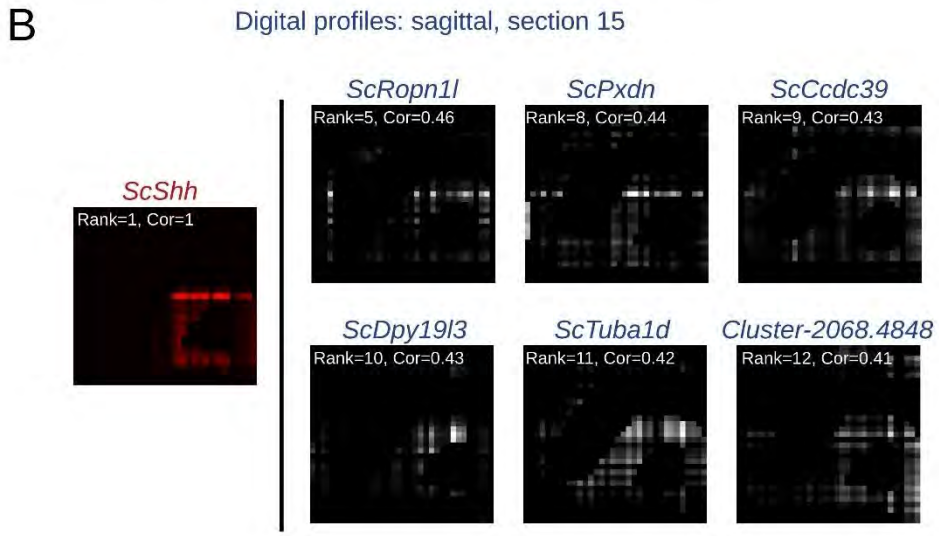
B
Digital profiles: sagittal, section 15
ScShh
Rank=1, Cor=1
ScRopn1l
Rank=5, Cor=0.46
ScPxdn
Rank=8, Cor=0.44
ScCcdc39
Rank=9, Cor=0.43
ScDpy19l3
Rank=10, Cor=0.43
ScTuba1d
Rank=11, Cor=0.42
Cluster-2068.4848
Rank=12, Cor=0.41

Figure S5

DISCUSSION GENERALE

1. Résumé des résultats

Les travaux de l'équipe précédant le début de ce travail avaient permis de démontrer une divergence mécanistique importante entre roussette et poisson-zèbre pour la formation des asymétries habénulaires. Ce travail permet de préciser les divergences et les conservations entre ces deux espèces. Il permet en particulier :

- de fournir une description détaillée des asymétries très marquées chez la roussette, par une approche non biaisée. Ces données permettent pour la première fois de proposer des hypothèses quant à leur état ancestral et leur mode de diversification chez les gnathostomes

- de mettre en évidence une logique de régulation conservée dans la formation de ces asymétries, avec une régulation temporelle de la neurogenèse, une répression à gauche transitoire de la voie Wnt et un rôle de cette voie dans l'élaboration des choix de différenciation neuronale. Des variations dans le temps et dans l'espace de cette régulation pourraient rendre compte des variations des asymétries observées chez les gnathostomes

Ces données valident a posteriori l'intérêt du modèle roussette. C'est en utilisant cette espèce comme référence que ces résultats ont pu être obtenus. Ce travail ouvre des perspectives nouvelles, visant notammentà tester les hypothèses émises.

2. Perspectives :

Les perspectives ouvertes par ce travail concernent deux aspects distincts, l'un mécanistique et l'autre évolutif, abordés successivement ci-après.

2.1 Formation des asymétries chez la roussette

Obtention d'une cartographie de résolution cellulaire et caractérisation des trajectoires cellulaires dans les habénulas de roussette

Les études par scRNA-seq effectuées chez la souris et le poisson-zèbre fournissent une image complexe, difficile à réconcilier entre les deux espèces, des types cellulaires dans les habénulas. Une caractérisation par Tomo-seq (en cours dans l'équipe) et par scRNA-seq (en cours, pour le diencéphale en collaboration avec le groupe de H. Kaessman, Heidelberg) des habénulas de roussette permettrait de disposer d'une troisième référence. Par ailleurs la question des trajectoires cellulaires pourrait être abordée par scRNA-seq au cours du développement embryonnaire. En l'absence d'approches expérimentales facilement adpatables pour préciser les lignages cellulaires conduisant à l'organisation observée, cette approche permettrait notamment de caractériser l'identité moléculaire des progéniteurs des différents sous-domaines. Les caractérisations in situ déjà disponibles pour les progéniteurs, ainsi que des comparaisons transcriptomiques effectuées entre les habénulas droite et gauche au cours de la neurogenèse, d'ores et déjà disponibles dans le laboratoire, devraient être importantes pour l'analyse de telles données.

Mécanismes impliqués

Nos résultats mettent en évidence un rôle de la voie Wnt dans un choix de différenciation neuronale. Toutefois nos traitements ont été effectués dans une fenêtre temporelle restreinte. Compte tenu du caractère dynamique de l'activité de la voie, il sera intéressant d'évaluer son implication dans la formation des autres asymétries détectées au cours de ce travail (contrôle de l'identité des progéniteurs dont nous avons pu montrer qu'elle est asymétrique, ainsi du maintien de leurs pools, contrôle de la prolifération cellulaire, de la neurogenèse et de sa chronologie, régulation d'autres choix de destins cellulaires, formation du neuropile plus important à droite qu'à gauche). Ces données devraient permettre de reposer la question des interactions entre la voie Wnt et Nodal et de ré-évaluer la possibilité de fonctions de Nodal, non compensées par une répression gauche de la voie Wnt, dans la formation des asymétries. Plus généralement, la question posée est celle des mécanismes contrôlés par Nodal dans la formation des asymétries. L'analyse du profil ARN en 3D du cerveau embryonnaire pendant la fenêtre d'activité de Nodal pourrait permettre de préciser les cibles précoces de la voie.

Au-delà de ces deux voies, un criblage pharmacologique d'autres voies de signalisation candidates pourrait être mis en oeuvre au cours de la neurogenèse. En dépit de sa simplicité apparente, cette approche est complexe puisque les chronologies de traitements et doses de drogues utilisées nécessitent des ajustements qui peuvent être lourds. Une approche par ATAC-Seq serait pertinente pour mettre en évidence, de façon globale, les différences de régulations d'expressions géniques entre les habénulas gauche et droite de roussette, ainsi que leur dynamique au cours du développement. De fait, compte tenu de la taille de l'organe, il est possible de disséquer les habénulas droite et gauche à des stades assez précoces de la neurogenèse (stade 27)

2.2 Evolution des asymétries chez les vertébrés

Diversification chez les gnathostomes

Au même titre que chez la roussette, la réalisation d'approches transcriptomiques non biaisées serait importante pour caractériser de façon détaillée et exhaustive les asymétries moléculaires et l'organisation en sous-domaines chez quelques espèces bien choisies. Les approches de type Tomo-seq ou scRNA-seq sont bien adaptées à ce type de questions et la disponibilité de génomes de bonne continuité chez un nombre croissant de vertébrés les rend accessibles. Afin de tester et préciser les relations entre sous-domaines habénulaires et nos hypothèses de pertes des asymétries, le poisson-roseau ou le lépisostée tacheté serait intéressants, de même que, chez les sarcoptérygiens, un dipneuste.

Origine chez les vertébrés

La lamproie est le second modèle que l'équipe utilise dans l'étude des asymétries habénulaires (Lagadec et al., 2015). De par sa position phylogénétique, cette espèce est essentielle pour reconstruire les états ancestraux chez les vertébrés. Comme chez la roussette, elle présente par ailleurs des asymétries habénulaires très marquées et cela dès les stades pro-larvaires

(mais avec une latéralité en taille opposée à celle observée chez la roussette) et la voie Nodal joue un rôle essentiel dans la formation des asymétries habénulaires. Il est donc intéressant d'étudier l'organisation en sous-domaine moléculaire et les mécanismes de formation des asymétries habénulaires chez cette espèce, de la même manière que cela a été fait chez la roussette dans ce travail. Des sous-domaines habénulaires ont déjà été identifiés sur des critères morphologiques et de connectivité (Schmidt & Pasterkamp, 2017; Stephenson-Jones et al., 2012), mais la réalisation de tomographie ARN ou de séquençage ARN sur cellule unique des habénulas droites contre gauche, nous permettrait d'identifier avec une résolution très supérieure et des signatures moléculaires l'organisation ancestrale des habénulas chez les vertébrés. En ce qui concerne les aspects mécanistiques, une étude des patrons de prolifération-différenciation telle que décrite dans le chapitre 1 de cette thèse, est également aisée à réaliser chez la lamproie. Elle permettrait de caractériser de possibles asymétries neurogénétiques et d'évaluer leur conservation. De plus, des approches par perte de fonction par traitements pharmacologiques, ou en utilisant le système d'édition CRISPR-Cas9 chez des individus F0 sont réalisables chez cette espèce. Elles permettraient de caractériser des mécanismes moléculaires impliquésdans la formation des asymétries chez la lamproie. La recherche des cibles de Nodal par tomographie ARN pendant la fenêtre d'activité de la voie est une autre perspective d'intérêt en vue de comparaison avec la roussette. (Lagadec et al., 2015). Plusieurs de ces approches sont en cours dans le laboratoire

BIBLIOGRAPHIE

Adrio, F., Anadón, R., & Rodríguez-Moldes, I. (2000). Distribution of choline acetyltransferase (ChAT) immunoreactivity in the central nervous system of a chondrostean, the Siberian sturgeon (Acipenser baeri). *Journal of Comparative Neurology*, *426*(4), 602–621. https://doi.org/10.1002/1096-9861(20001030)426:4<602::AID-CNE8>3.0.CO;2-7

Agetsuma, M., Aizawa, H., Aoki, T., Nakayama, R., Takahoko, M., Goto, M., … Okamoto, H. (2010). The habenula is crucial for experience-dependent modification of fear responses in zebrafish. *Nature Neuroscience*, *13*(11), 1354–1356. https://doi.org/10.1038/nn.2654

Ahumada-Galleguillos, P., Lemus, C. G., Díaz, E., Osorio-Reich, M., Härtel, S., & Concha, M. L. (2016). Directional asymmetry in the volume of the human habenula. *Brain Structure and Function*, 1–6. https://doi.org/10.1007/s00429-016-1231-z

Aizawa, H., Bianco, I. H., Hamaoka, T., Miyashita, T., Uemura, O., Concha, M. L., … Okamoto, H. (2005). Laterotopic representation of left-right information onto the dorso-ventral axis of a zebrafish midbrain target nucleus. *Current Biology*, *15*(3), 238–243. https://doi.org/10.1016/j.cub.2005.01.014

Aizawa, H., Goto, M., Sato, T., & Okamoto, H. (2007). Temporally Regulated Asymmetric Neurogenesis Causes Left-Right Difference in the Zebrafish Habenular Structures. *Developmental Cell*, *12*(1), 87–98. https://doi.org/10.1016/j.devcel.2006.10.004

Aizawa, H., Kobayashi, M., Tanaka, S., Fukai, T., & Okamoto, H. (2012). Molecular characterization of the subnuclei in rat habenula. *The Journal of Comparative Neurology*, *520*(18), 4051–4066. https://doi.org/10.1002/cne.23167

Aizawa, H., & Zhu, M. (2019). Toward an understanding of the habenula's various roles in human depression. *Psychiatry and Clinical Neurosciences*, *73*(10), 607–612. https://doi.org/10.1111/pcn.12892

Amo, R., Aizawa, H., Takahoko, M., Kobayashi, M., Takahashi, R., Aoki, T., & Okamoto, H. (2010). Identification of the zebrafish ventral habenula as a homolog of the mammalian lateral habenula. *The Journal of Neuroscience : The Official Journal of the Society for Neuroscience*, *30*(4), 1566–1574. https://doi.org/10.1523/JNEUROSCI.3690-09.2010

Amo, R., Fredes, F., Kinoshita, M., Aoki, R., Aizawa, H., Agetsuma, M., … Okamoto, H. (2014). The habenulo-raphe serotonergic circuit encodes an aversive expectation value essential for adaptive active avoidance of danger. *Neuron*, *84*(5), 1034–1048. https://doi.org/10.1016/j.neuron.2014.10.035

Andalman, A. S., Burns, V. M., Lovett-Barron, M., Broxton, M., Poole, B., Yang, S. J., … Deisseroth, K. (2019). Neuronal Dynamics Regulating Brain and Behavioral State Transitions. *Cell*, *177*(4), 970-985.e20. https://doi.org/10.1016/j.cell.2019.02.037

Baker, P. M., Jhou, T., Li, B., Matsumoto, M., Mizumori, S. J. Y., Stephenson-Jones, M., & Vicentic, A. (2016). The Lateral Habenula Circuitry: Reward Processing and Cognitive Control. *The Journal of Neuroscience*, *36*(45), 11482–11488. https://doi.org/10.1523/JNEUROSCI.2350-16.2016

Ballard, W. W., Mellinger, J., & Lechenault, H. (1993). A series of stages for development of *Scyliorhinus canicula* the lesser spotted dogfish (Chondrichthyes: Scyliorhinidae). *Journal of Experimental Zoology*, *267*(1), 1–43. https://doi.org/10.1002/jez.1402670309

Barth, K. A., & Wilson, S. W. (1995). Expression of zebrafish nk2.2 is influenced by sonic hedgehog/vertebrate hedgehog-1 and demarcates a zone of neuronal differentiation in the

embryonic forebrain. *Development (Cambridge, England)*, *121*(6), 1755–1768. Retrieved from http://www.ncbi.nlm.nih.gov/pubmed/7600991

Beretta, C. A., Dross, N., Bankhead, P., & Carl, M. (2013). The ventral habenulae of zebrafish develop in prosomere 2 dependent on Tcf7l2 function. *Neural Development*, *8*(1), 11–14. https://doi.org/10.1186/1749-8104-8-19

Beretta, C. A., Dross, N., Guiterrez-Triana, J. A., Ryu, S., & Carl, M. (2012). Habenula Circuit Development: Past, Present, and Future. *Frontiers in Neuroscience*, *6*(APR), 1–10. https://doi.org/10.3389/fnins.2012.00051

Braford, M. R. J., Northcutt, R. G., Davis, R. E., Demski, L. S., Kassel, J., Overmier, J. B., & Hollis, K. L. (1983). Fish neurobiology. The University of Michigan Press, Ann Arbor.

Braitenberg, V., & Kemali, M. (1970). Exceptions to bilateral symmetry in the epithalamus of lower vertebrates. *Journal of Comparative Neurology*, *138*(2), 137–146. https://doi.org/10.1002/cne.901380203

Burkhard, S. B., & Bakkers, J. (2018). Spatially resolved RNA-sequencing of the embryonic heart identifies a role for Wnt/β-catenin signaling in autonomic control of heart rate. *ELife*, *7*, 1–19. https://doi.org/10.7554/eLife.31515

Caprioli, A., Goitsuka, R., Pouget, C., Dunon, D., & Jaffredo, T. (2002). Expression of Notch genes and their ligands during gastrulation in the chicken embryo. *Mechanisms of Development*, *116*(1–2), 161–164. https://doi.org/10.1016/S0925-4773(02)00136-3

Carrera, I., Molist, P., Anadón, R., & Rodríguez-Moldes, I. (2008). Development of the serotoninergic system in the central nervous system of a shark, the lesser spotted dogfish Scyliorhinus canicula. *Journal of Comparative Neurology*, *511*(6), 804–831. https://doi.org/10.1002/cne.21857

Chen, L., Guo, Q., & Li, J. Y. H. (2009). Transcription factor Gbx2 acts cell-nonautonomously to regulate the formation of lineage-restriction boundaries ofthe thalamus. *Development*, *136*(8), 1317–1326. https://doi.org/10.1242/dev.030510

Chen, W. yu, Peng, X. lan, Deng, Q. sui, Chen, M. jia, Du, J. lin, & Zhang, B. bing. (2019). Role of Olfactorily Responsive Neurons in the Right Dorsal Habenula–Ventral Interpeduncular Nucleus Pathway in Food-Seeking Behaviors of Larval Zebrafish. *Neuroscience*, *404*, 259–267. https://doi.org/10.1016/j.neuroscience.2019.01.057

Cheng, R. K., Krishnan, S., Lin, Q., Kibat, C., & Jesuthasan, S. (2017). Characterization of a thalamic nucleus mediating habenula responses to changes in ambient illumination. *BMC Biology*, *15*(1), 1–21. https://doi.org/10.1186/s12915-017-0431-1

Chou, M.-Y., Amo, R., Kinoshita, M., Cherng, B.-W., Shimazaki, H., Agetsuma, M., … Okamoto, H. (2016). Social conflict resolution regulated by two dorsal habenular subregions in zebrafish. *Science (New York, N.Y.)*, *352*(6281), 87–90. https://doi.org/10.1126/science.aac9508

Clarkson, J., d'Anglemont de Tassigny, X., Colledge, W. H., Caraty, A., & Herbison, A. E. (2009). Distribution of Kisspeptin Neurones in the Adult Female Mouse Brain. *Journal of Neuroendocrinology*, *21*(8), 673–682. https://doi.org/10.1111/j.1365-2826.2009.01892.x

Combs, P. A., & Eisen, M. B. (2017). Genome-wide measurement of spatial expression in patterning mutants of Drosophila melanogaster. *F1000Research*, *6*, 41. https://doi.org/10.12688/f1000research.9720.1

Compagno, L. J. V. (1966). FAO species catalogue. Vol. 4. Sharks of the world. An annotated and

illustrated catalogue of shark species known to date. Part 2. Carchariniformes. *FAO SPECIES CATALOGUE*, *65*(3), 351–360.

Concha, M. L., Burdine, R. D., Russell, C., Schier, A. F., & Wilson, S. W. (2000a). A Nodal signaling pathway regulates the laterality of neuroanatomical asymmetries in the zebrafish forebrain. *Neuron*, *28*(2), 399–409. https://doi.org/10.1016/S0896-6273(00)00120-3

Concha, M. L., Burdine, R. D., Russell, C., Schier, A. F., & Wilson, S. W. (2000b). A Nodal Signaling Pathway Regulates the Laterality of Neuroanatomical Asymmetries in the Zebrafish Forebrain. *Neuron*, *28*(2), 399–409. https://doi.org/10.1016/S0896-6273(00)00120-3

Concha, M. L., Russell, C., Regan, J. C., Tawk, M., Sidi, S., Gilmour, D. T., … Wilson, S. W. (2003). Local tissue interactions across the dorsal midline of the forebrain establish CNS laterality. *Neuron*, *39*(3), 423–438. https://doi.org/10.1016/S0896-6273(03)00437-9

Concha, M. L., Signore, I. A., & Colombo, A. (2009). Mechanisms of directional asymmetry in the zebrafish epithalamus. *Seminars in Cell and Developmental Biology*, *20*(4), 498–509. https://doi.org/10.1016/j.semcdb.2008.11.007

Concha, M. L., & Wilson, S. W. (2001). Asymmetry in the epithalamus of vertebrates, 63–84.

Coolen, M., Menuet, A., Chassoux, D., Compagnucci, C., Henry, S., Leveque, L., … Mazan, S. (2008). The Dogfish Scyliorhinus canicula: A Reference in Jawed Vertebrates. *Cold Spring Harbor Protocols*, *2008*(12), pdb.emo111-pdb.emo111. https://doi.org/10.1101/pdb.emo111

Coolen, Sauka-Spengler, T., Nicolle, D., Le-Mentec, C., Lallemand, Y., Da Silva, C., … Mazan, S. (2007). Evolution of axis specification mechanisms in jawed vertebrates: insights from a chondrichthyan. *PloS One*, *2*(4), e374. https://doi.org/10.1371/journal.pone.0000374

Criscitiello, M. F. (2014). What the shark immune system can and cannot provide for the expanding design landscape of immunotherapy. *Expert Opinion on Drug Discovery*, *9*(7), 725–739. https://doi.org/10.1517/17460441.2014.920818

Dean, B. J., Erdogan, B., Gamse, J. T., & Wu, S.-Y. (2014). Dbx1b defines the dorsal habenular progenitor domain in the zebrafish epithalamus. *Neural Development*, *9*(1), 20. https://doi.org/10.1186/1749-8104-9-20

Debiais-Thibaud, M., Simion, P., Ventéo, S., Muñoz, D., Marcellini, S., Mazan, S., … Malik, H. (2019). Skeletal Mineralization in Association with Type X Collagen Expression Is an Ancestral Feature for Jawed Vertebrates. *Molecular Biology and Evolution*, *36*(10), 2265–2276. https://doi.org/10.1093/molbev/msz145

deCarvalho, T. N., Subedi, A., Rock, J., Harfe, B. D., Thisse, C., Thisse, B., … Hong, E. (2014). Neurtransmitter map of the asymmetric dorsal habenular nuclei of Zebrafish. *Genesis*, *52*(6), 636–655. https://doi.org/10.1002/dvg.22785

Derobert, Y., Plouhinec, J. L., Sauka-Spengler, T., Le Mentec, C., Baratte, B., Jaillard, D., & Mazan, S. (2002). Structure and expression of three Emx genes in the dogfish Scyliorhinus canicula: Functional and evolutionary implications. *Developmental Biology*, *247*(2), 390–404. https://doi.org/10.1006/dbio.2002.0700

Diniz-Filho, J. A. F., Nabout, J. C., Telles, M. P. de C., Soares, T. N., & Rangel, T. F. L. V. B. (2009). A review of techniques for spatial modeling in geographical, conservation and landscape genetics. *Genetics and Molecular Biology*, *32*(2), 203–211. https://doi.org/10.1590/S1415-47572009000200001

Dougan, S. T. (2003). The role of the zebrafish nodal-related genes squint and cyclops in patterning of

mesendoderm. *Development*, *130*(9), 1837–1851. https://doi.org/10.1242/dev.00400

Dreosti, E., Vendrell Llopis, N., Carl, M., Yaksi, E., & Wilson, S. W. (2014a). Left-right asymmetry is required for the habenulae to respond to both visual and olfactory stimuli. *Current Biology*, *24*(4), 440–445. https://doi.org/10.1016/j.cub.2014.01.016

Dreosti, E., Vendrell Llopis, N., Carl, M., Yaksi, E., & Wilson, S. W. (2014b). Left-Right Asymmetry Is Required for the Habenulae to Respond to Both Visual and Olfactory Stimuli. *Current Biology*, *24*(4), 440–445. https://doi.org/10.1016/j.cub.2014.01.016

Duboué, E. R., Hong, E., Eldred, K. C., & Halpern, M. E. (2017). Left Habenular Activity Attenuates Fear Responses in Larval Zebrafish. *Current Biology*, *27*(14), 2154-2162.e3. https://doi.org/10.1016/j.cub.2017.06.017

Ekström, P., & Ebbesson, S. O. E. (1988). The left habenular nucleus contains a discrete serotonin-immunoreactive subnucleus in the coho salmon (Oncorhynchus kisutch). *Neuroscience Letters*, *91*(2), 121–125. https://doi.org/10.1016/0304-3940(88)90754-9

Engbretson, G. A., Reiner, A., & Brecha, N. (1981). Habenular asymmetry and the central connections of the parietal eye of the lizard. *Journal of Comparative Neurology*, *198*(1), 155–165. https://doi.org/10.1002/cne.901980113

Facchin, L., Duboué, E. R., & Halpern, M. E. (2015). Disruption of Epithalamic Left-Right Asymmetry Increases Anxiety in Zebrafish. *The Journal of Neuroscience : The Official Journal of the Society for Neuroscience*, *35*(48), 15847–15859. https://doi.org/10.1523/JNEUROSCI.2593-15.2015

Faro, A., Nicolaou, S., Lekk, I., Blader, P., & Wilson, S. W. (2019). Sox1a mediates the ability of the parapineal to impart habenular left-right asymmetry, 1–23.

Fienberg, S. E. (1970). An Iterative Procedure for Estimation in Contingency Tables. *The Annals of Mathematical Statistics*, *41*(3), 907–917. Retrieved from http://www.jstor.org/stable/2239244

Fore, S., Acuña-Hinrichsen, F., Mutlu, K. A., Bartoszek, E. M., Serneels, B., Faturos, N. G., … Yaksi, E. (2020). Functional properties of habenular neurons are determined by developmental stage and sequential neurogenesis. *Science Advances*, *6*(36). https://doi.org/10.1126/sciadv.aaz3173

Freitas, R., Zhang, G. J., Albert, J. S., Evans, D. H., & Cohn, M. J. (2006). Developmental origin of shark electrosensory organs. *Evolution and Development*, *8*(1), 74–80. https://doi.org/10.1111/j.1525-142X.2006.05076.x

Freudenmacher, L., Twickel, A., & Walkowiak, W. (2020). The habenula as an evolutionary conserved link between basal ganglia, limbic, and sensory systems—A phylogenetic comparison based on anuran amphibians. *Journal of Comparative Neurology*, *528*(5), 705–728. https://doi.org/10.1002/cne.24777

Gaillard, A. L., Tay, B. H., Sirkin, D. I. P., Lafont, A. G., De Flori, C., Vissio, P. G., … Tostivint, H. (2018). Characterization of gonadotropin-releasing hormone (GnRH) genes from cartilaginous fish: Evolutionary perspectives. *Frontiers in Neuroscience*, *12*(SEP), 1–14. https://doi.org/10.3389/fnins.2018.00607

Galeeva, A., Treuter, E., Tomarev, S., & Pelto-Huikko, M. (2007). A prospero-related homeobox gene Prox-1 is expressed during postnatal brain development as well as in the adult rodent brain. *Neuroscience*, *146*(2), 604–616. https://doi.org/10.1016/j.neuroscience.2007.02.002

Gamse, J. T. (2003). The parapineal mediates left-right asymmetry in the zebrafish diencephalon. *Development*, *130*(6), 1059–1068. https://doi.org/10.1242/dev.00270

Gamse, J. T., Kuan, Y.-S., Macurak, M., Brösamle, C., Thisse, B., Thisse, C., & Halpern, M. E. (2005a).

Directional asymmetry of the zebrafish epithalamus guides dorsoventral innervation of the midbrain target. *Development*, *132*(21), 4869–4881. https://doi.org/10.1242/dev.02046

Gamse, J. T., Kuan, Y. S., Macurak, M., Brösamle, C., Thisse, B., Thisse, C., & Halpern, M. E. (2005b). Directional asymmetry of the zebrafish epithalamus guides dorsoventral innervation of the midbrain target. *Development*, *132*(21), 4869–4880. https://doi.org/10.1242/dev.02046

Gamse, J. T., Thisse, C., Thisse, B., & Halpern, M. E. (2003). The parapineal mediates left-right asymmetry in the zebrafish diencephalon. *Development*, *130*(6), 1059–1068. https://doi.org/10.1242/dev.00270

Garric, L., Ronsin, B., Roussigné, M., Booton, S., Gamse, J. T., Dufourcq, P., & Blader, P. (2014). Pitx2c ensures habenular asymmetry by restricting parapineal cell number. *Development (Cambridge)*, *141*(7), 1572–1579. https://doi.org/10.1242/dev.100305

Godard, B. G., Coolen, M., Le Panse, S., Gombault, A., Ferreiro-Galve, S., Laguerre, L., … Mazan, S. (2014). Mechanisms of endoderm formation in a cartilaginous fish reveal ancestral and homoplastic traits in jawed vertebrates. *Biology Open*, *3*(11), 1098–1107. https://doi.org/10.1242/bio.20148037

Guglielmi, L., Bühler, A., Moro, E., Argenton, F., Poggi, L., & Carl, M. (2020). Temporal control of Wnt signaling is required for habenular neuron diversity and brain asymmetry. *Development*, *147*(6), dev182865. https://doi.org/10.1242/dev.182865

Guo, Q., & Li, J. Y. H. (2019). Defining developmental diversification of diencephalon neurons through single cell gene expression profiling. *Development (Cambridge)*, *146*(12). https://doi.org/10.1242/dev.174284

Gurusinghe, C. J., & Ehrlich, D. (1985). Sex-dependent structural asymmetry of the medial habenular nucleus of the chicken brain. *Cell and Tissue Research*, *240*(1), 149–152. https://doi.org/10.1007/BF00217568

Hagemann, A. I. H., & Scholpp, S. (2012). The Tale of the Three Brothers – Shh, Wnt, and Fgf during Development of the Thalamus. *Frontiers in Neuroscience*, *6*(MAY), 1–9. https://doi.org/10.3389/fnins.2012.00076

Halluin, C., Madelaine, R., Naye, F., Peers, B., Roussigné, M., & Blader, P. (2016). Habenular neurogenesis in zebrafish is regulated by a Hedgehog, Pax6 proneural gene cascade. *PLoS ONE*, *11*(7), 1–19. https://doi.org/10.1371/journal.pone.0158210

Halpern, M. E., Liang, J. O., & Gamse, J. T. (2003). Leaning to the left: Laterality in the zebrafish forebrain. *Trends in Neurosciences*, *26*(6), 308–313. https://doi.org/10.1016/S0166-2236(03)00129-2

Hara, Y., Yamaguchi, K., Onimaru, K., Kadota, M., Koyanagi, M., Keeley, S. D., … Kuraku, S. (2018). Shark genomes provide insights into elasmobranch evolution and the origin of vertebrates. *Nature Ecology & Evolution*, *2*(11), 1761–1771. https://doi.org/10.1038/s41559-018-0673-5

Hashikawa, Y., Hashikawa, K., Rossi, M. A., Basiri, M. L., Liu, Y., Johnston, N. L., … Stuber, G. D. (2020a). Transcriptional and Spatial Resolution of Cell Types in the Mammalian Habenula. *Neuron*, *106*(5), 743-758.e5. https://doi.org/10.1016/j.neuron.2020.03.011

Hashikawa, Y., Hashikawa, K., Rossi, M. A., Basiri, M. L., Liu, Y., Johnston, N. L., … Stuber, G. D. (2020b). Transcriptional and Spatial Resolution of Cell Types in the Mammalian Habenula. *Neuron*, *106*(5), 743-758.e5. https://doi.org/10.1016/j.neuron.2020.03.011

Herkenham, M., & Nauta, W. (1979). Efferent Connections of the Habenular Nuclei in the Rat. In *J.*

Comp. Neurol. (Vol. 187, pp. 300–328). https://doi.org/10.1007/978-1-4684-7920-1_17

Herkenham, M., & Nauta, W. J. H. (1977). Afferent connections of the habenular nuclei in the rat. A horseradish peroxidase study, with a note on the fiber-of-passage problem. *Journal of Comparative Neurology*, *173*(1), 123–145. https://doi.org/10.1002/cne.901730107

Hidenori Aizawa, I. H. B., Hamaoka, T., Miyashita, T., Uemura, O., Concha, M. L., Russell, C., … Okamoto, and H. (2005). Laterotopic Representation of Left-Right Information onto the Dorso-Ventral Axis of a Zebrafish Midbrain Target Nucleus. *Current Biology*, *15*(2), 238–243. https://doi.org/10.1016/j

Holler, K., & Junker, J. P. (2019). RNA Tomography for Spatially Resolved Transcriptomics (Tomo-Seq). In *Methods in Molecular Biology* (Vol. 1920, pp. 129–141). https://doi.org/10.1007/978-1-4939-9009-2_9

Hu, H., Cui, Y., & Yang, Y. (2020). Circuits and functions of the lateral habenula in health and in disease. *Nature Reviews Neuroscience*, *21*(5), 277–295. https://doi.org/10.1038/s41583-020-0292-4

Hüsken, U., Stickney, H. L., Gestri, G., Bianco, I. H., Faro, A., Young, R. M., … Carl, M. (2014). Tcf7l2 Is Required for Left-Right Asymmetric Differentiation of Habenular Neurons. *Current Biology*, *24*(19), 2217–2227. https://doi.org/10.1016/j.cub.2014.08.006

Ichijo, H., Nakamura, T., Kawaguchi, M., & Takeuchi, Y. (2017). An Evolutionary Hypothesis of Binary Opposition in Functional Incompatibility about Habenular Asymmetry in Vertebrates. *Frontiers in Neuroscience*, *10*(January), 1–11. https://doi.org/10.3389/fnins.2016.00595

Ingham, P. W., & Mcmahon, A. P. (2001). Hedgehog signaling in animal development: paradigms and principles. https://doi.org/10.1101/gad.938601

Jhou, T., Fields, H., Baxter, M., & Saper, C. (2009). The rostromedial tegmental nucleus (RMTg), a major GABAergic afferent to midbrain dopamine neurons, selectively encodes aversive stimuli and promotes behavioral inhibition. *Neuron*, *61*(5), 786–800. https://doi.org/10.1016/j.neuron.2009.02.001.The

Junker, J. P., Noël, E. S., Guryev, V., Peterson, K. A., Shah, G., Huisken, J., … Van Oudenaarden, A. (2014). Genome-wide RNA Tomography in the Zebrafish Embryo. *Cell*, *159*(3), 662–675. https://doi.org/10.1016/j.cell.2014.09.038

Kan, L., Jalali, A., Zhao, L. R., Zhou, X., McGuire, T., Kazanis, I., … Kessler, J. A. (2007). Dual function of Sox1 in telencephalic progenitor cells. *Developmental Biology*, *310*(1), 85–98. https://doi.org/10.1016/j.ydbio.2007.07.026

Kim, U. (2009). Topographic commissural and descending projections of the habenula in the rat. *Journal of Comparative Neurology*, *513*(2), 173–187. https://doi.org/10.1002/cne.21951

Kitahashi, T., Ogawa, S., & Parhar, I. S. (2009). Cloning and expression of kiss2 in the zebrafish and medaka. *Endocrinology*, *150*(2), 821–831. https://doi.org/10.1210/en.2008-0940

Kuan, Y. S., Roberson, S., Akitake, C. M., Fortuno, L., Gamse, J., Moens, C., & Halpern, M. E. (2015). Distinct requirements for Wntless in habenular development. *Developmental Biology*, *406*(2), 117–128. https://doi.org/10.1016/j.ydbio.2015.06.006

Lagadec, R., Laguerre, L., Menuet, A., Amara, A., Rocancourt, C., Péricard, P., … Boutet, A. (2015). The ancestral role of nodal signalling in breaking L/R symmetry in the vertebrate forebrain. *Nature Communications*, *6*, 6686. https://doi.org/10.1038/ncomms7686

Lagadec, R., Lanoizelet, M., Sánchez-Farías, N., Hérard, F., Menuet, A., Mayeur, H., … Mazan, S.

(2018). Neurogenetic asymmetries in the catshark developing habenulae: mechanistic and evolutionary implications. *Scientific Reports*, *8*(1), 4616. https://doi.org/10.1038/s41598-018-22851-3

Lavado, A., & Oliver, G. (2007). Prox1 expression patterns in the developing and adult murine brain. *Developmental Dynamics*, *236*(2), 518–524. https://doi.org/10.1002/dvdy.21024

Lecourtier, L., & Kelly, P. H. (2007). A conductor hidden in the orchestra? Role of the habenular complex in monoamine transmission and cognition. *Neuroscience & Biobehavioral Reviews*, *31*(5), 658–672. https://doi.org/10.1016/j.neubiorev.2007.01.004

Lecourtier, L., Neijt, H. C., & Kelly, P. H. (2004). Habenula lesions cause impaired cognitive performance in rats: Implications for schizophrenia. *European Journal of Neuroscience*, *19*(9), 2551–2560. https://doi.org/10.1111/j.0953-816X.2004.03356.x

Lee, J. H., Daugharthy, E. R., Scheiman, J., Kalhor, R., Yang, J. L., Ferrante, T. C., … Church, G. M. (2014). Highly Multiplexed Subcellular RNA Sequencing in Situ. *Science*, *343*(6177), 1360–1363. https://doi.org/10.1126/science.1250212

Lee, M., Yoon, J., Song, H., Lee, B., Lam, D. T., Yoon, J., … Jeong, Y. (2017). Tcf7l2 plays crucial roles in forebrain development through regulation of thalamic and habenular neuron identity and connectivity. *Developmental Biology*, *424*(1), 62–76. https://doi.org/10.1016/j.ydbio.2017.02.010

Li, K., Zhang, J., & Li, J. Y. H. (2012). Gbx2 Plays an Essential but Transient Role in the Formation of Thalamic Nuclei. *PLoS ONE*, *7*(10), 1–11. https://doi.org/10.1371/journal.pone.0047111

Liang, J. O., Etheridge, a, Hantsoo, L., Rubinstein, a L., Nowak, S. J., Izpisúa Belmonte, J. C., & Halpern, M. E. (2000). Asymmetric nodal signaling in the zebrafish diencephalon positions the pineal organ. *Development (Cambridge, England)*, *127*(23), 5101–5112.

Lima, L. B., Bueno, D., Leite, F., Souza, S., Gonçalves, L., Furigo, I. C., … Metzger, M. (2017). Afferent and efferent connections of the interpeduncular nucleus with special reference to circuits involving the habenula and raphe nuclei. *Journal of Comparative Neurology*, *525*(10), 2411–2442. https://doi.org/10.1002/cne.24217

Lipiec, M. A., Bem, J., Kozinski, K., Chakraborty, C., Urban-Ciećko, J., Zajkowski, T., … Wisniewska, M. B. (2020). TCF7L2 regulates postmitotic differentiation programmes and excitability patterns in the thalamus. *Development (Cambridge)*, *147*(16). https://doi.org/10.1242/dev.190181

Mallika, C., Guo, Q., & Li, J. Y. H. (2015). Gbx2 is essential for maintaining thalamic neuron identity and repressing habenular characters in the developing thalamus. *Developmental Biology*, *407*(1), 26–39. https://doi.org/10.1016/j.ydbio.2015.08.010

Mallika, C., Guo, Q., Weber, S., Scholpp, S., & Li, J. Y. H. (2014). Pax6 regulates the formation of the habenular nuclei by controlling the temporospatial expression of Shh in the diencephalon in vertebrates. *BMC Biology*, *12*. https://doi.org/10.1186/1741-7007-12-13

Mallika, C., & Li, J. Y. H. (2012). Patterning and compartment formation in the diencephalon. *Frontiers in Neuroscience*, *6*(MAY), 1–10. https://doi.org/10.3389/fnins.2012.00066

Marra, N. J., Stanhope, M. J., Jue, N. K., Wang, M., Sun, Q., Pavinski Bitar, P., … Shivji, M. S. (2019). White shark genome reveals ancient elasmobranch adaptations associated with wound healing and the maintenance of genome stability. *Proceedings of the National Academy of Sciences*, *116*(10), 4446–4455. https://doi.org/10.1073/pnas.1819778116

Mathis, V., Barbelivien, A., Majchrzak, M., Mathis, C., Cassel, J., & Lecourtier, L. (2017). The Lateral

Habenula as a Relay of Cortical Information to Process Working Memory. *Cerebral Cortex*, *27*(December), 5485–5495. https://doi.org/10.1093/cercor/bhw316

Matsumoto, M., & Hikosaka, O. (2007). Lateral habenula as a source of negative reward signals in dopamine neurons. *Nature*, *447*(7148), 1111–1115. https://doi.org/10.1038/nature05860

Meberg, P. J., & Routtenberg, A. (1991). Selective expression of protein F1/(GAP-43) mRNA in pyramidal but not granule cells of the hippocampus. *Neuroscience*, *45*(3), 721–733. https://doi.org/10.1016/0306-4522(91)90284-U

Mészáros, J., Gajewska, S., & Tarchalska-Kryńska, B. (1985). Habenulo-interpeduncular lesions: the effects on pain sensitivity, morphine analgesia and open-field behavior in rats. *Polish Journal of Pharmacology and Pharmacy*, *37*(4), 469–477.

Metz, M., Gassmann, M., Fakler, B., Schaeren-Wiemers, N., & Bettler, B. (2011). Distribution of the auxiliary GABAB receptor subunits KCTD8, 12, 12b, and 16 in the mouse brain. *Journal of Comparative Neurology*, *519*(8), 1435–1454. https://doi.org/10.1002/cne.22610

Miyasaka, N., Morimoto, K., Tsubokawa, T., Higashijima, S. I., Okamoto, H., & Yoshihara, Y. (2009). From the olfactory bulb to higher brain Centers: Genetic visualization of secondary olfactory pathways in zebrafish. *Journal of Neuroscience*, *29*(15), 4756–4767. https://doi.org/10.1523/JNEUROSCI.0118-09.2009

Murphy, C. A., DiCamillo, A. M., Haun, F., & Murray, M. (1996). Lesion of the habenular efferent pathway produces anxiety and locomotor hyperactivity in rats: a comparison of the effects of neonatal and adult lesions. *Behavioural Brain Research*, *81*(1–2), 43–52. https://doi.org/10.1016/S0166-4328(96)00041-1

Murray, M., Murphy, C. A., Ross, L. L., & Haun, F. (1994). The role of the habenula-interpeduncular pathway in modulating levels of circulating adrenal hormones. *Restorative Neurology and Neuroscience*, *6*(4), 301–307. https://doi.org/10.3233/RNN-1994-6406

Nagalski, A., Puelles, L., Dabrowski, M., Wegierski, T., Kuznicki, J., & Wisniewska, M. B. (2016a). Molecular anatomy of the thalamic complex and the underlying transcription factors. *Brain Structure and Function*, *221*(5), 2493–2510. https://doi.org/10.1007/s00429-015-1052-5

Nagalski, A., Puelles, L., Dabrowski, M., Wegierski, T., Kuznicki, J., & Wisniewska, M. B. (2016b). Molecular anatomy of the thalamic complex and the underlying transcription factors. *Brain Structure and Function*, *221*, 2493–2510. https://doi.org/10.1007/s00429-015-1052-5

Nagao, M., Kamo, H., Akiguchi, I., & Kimura, J. (1993). Induction of c-Fos-like protein in the lateral habenular nucleus by persistent noxious peripheral stimulation. *Neuroscience Letters*, *151*(1), 37–40. https://doi.org/10.1016/0304-3940(93)90039-N

Nieuwenhuys, R. (1998a). Brachiopterygian Fishes. In *The Central Nervous System of Vertebrates* (pp. 655–699). Berlin, Heidelberg: Springer Berlin Heidelberg. https://doi.org/10.1007/978-3-642-18262-4_13

Nieuwenhuys, R. (1998b). The Coelacanth Latimeria chalumnae. In *The Central Nervous System of Vertebrates* (pp. 1007–1043). Berlin, Heidelberg: Springer Berlin Heidelberg. https://doi.org/10.1007/978-3-642-18262-4_17

O'dowd, B. F., Lee, D. K., Huang, W., Nguyen, T., Cheng, R., Liu, Y., … George, S. R. (2000). *TRH-R2 Exhibits Similar Binding and Acute Signaling but Distinct Regulation and Anatomic Distribution Compared with TRH-R1*. *Molecular Endocrinology* (Vol. 14). Retrieved from https://academic.oup.com/mend/article/14/1/183/2747846

O'Neill, P., McCole, R. B., & Baker, C. V. H. (2007). A molecular analysis of neurogenic placode and cranial sensory ganglion development in the shark, Scyliorhinus canicula. *Developmental Biology*, *304*(1), 156–181. https://doi.org/10.1016/j.ydbio.2006.12.029

Okamoto, H., & Aizawa, H. (2013). Fear and anxiety regulation by conserved affective circuits. *Neuron*, *78*(3), 411–413. https://doi.org/10.1016/j.neuron.2013.04.031

Osorio, J., Mazan, S., & Rétaux, S. (2005). Organisation of the lamprey (Lampetra fluviatilis) embryonic brain: Insights from LIM-homeodomain, Pax and hedgehog genes. *Developmental Biology*, *288*(1), 100–112. https://doi.org/10.1016/j.ydbio.2005.08.042

Palumbo, F., Serneels, B., Pelgrims, R., & Yaksi, E. (2020). The Zebrafish Dorsolateral Habenula Is Required for Updating Learned Behaviors. *Cell Reports*, *32*(8), 108054. https://doi.org/10.1016/j.celrep.2020.108054

Pandey, S., Shekhar, K., Regev, A., & Schier, A. F. (2018). Comprehensive Identification and Spatial Mapping of Habenular Neuronal Types Using Single-Cell RNA-Seq. *Current Biology*, *28*(7), 1052-1065.e7. https://doi.org/10.1016/j.cub.2018.02.040

Park-Holohan, S., Linari, M., Reconditi, M., Fusi, L., Brunello, E., Irving, M., … Piazzesi, G. (2012). Mechanics of myosin function in white muscle fibres of the dogfish, Scyliorhinus canicula. *Journal of Physiology*, *590*(8), 1973–1988. https://doi.org/10.1113/jphysiol.2011.217133

Plouhinec, J. L., Leconte, L., Sauka-Spengler, T., Bovolenta, P., Mazan, S., & Saule, S. (2005). Comparative analysis of gnathostome Otx gene expression patterns in the developing eye: Implications for the functional evolution of the multigene family. *Developmental Biology*, *278*(2), 560–575. https://doi.org/10.1016/j.ydbio.2004.11.019

Proulx, C. D., Hikosaka, O., & Malinow, R. (2014). Reward processing by the lateral habenula in normal and depressive behaviors. *Nature Neuroscience*, *17*(9), 1146–1152. https://doi.org/10.1038/nn.3779

Puelles, L., Harrison, M., Paxinos, G., & Watson, C. (2013). A developmental ontology for the mammalian brain based on the prosomeric model. *Trends in Neurosciences*, *36*(10), 570–578. https://doi.org/10.1016/j.tins.2013.06.004

Puelles, L., & Martinez-de-la-Torre, M. (1987). Autoradiographic and Golgi study on the early development of n. isthmi principalis and adjacent grisea in the chick embryo: a tridimensional viewpoint. *Anatomy and Embryology*, *176*(1), 19–34. https://doi.org/10.1007/BF00309748

Puelles, L., & Rubenstein, J. L. R. (2003). Forebrain gene expression domains and the evolving prosomeric model. *Trends in Neurosciences*, *26*(9), 469–476. https://doi.org/10.1016/S0166-2236(03)00234-0

Regan, J. C., Concha, M. L., Roussigne, M., Russell, C., & Wilson, S. W. (2009). An Fgf8-Dependent Bistable Cell Migratory Event Establishes CNS Asymmetry. *Neuron*, *61*(1), 27–34. https://doi.org/10.1016/j.neuron.2008.11.030

Roberson, S., & Halpern, M. E. (2017). Convergence of signaling pathways underlying habenular formation and axonal outgrowth in zebrafish. *Development (Cambridge)*, *144*(14), 2652–2662. https://doi.org/10.1242/dev.147751

Roberson, S., & Halpern, M. E. (2018). Development and connectivity of the habenular nuclei. *Seminars in Cell and Developmental Biology*, *78*, 107–115. https://doi.org/10.1016/j.semcdb.2017.10.007

Rodríguez-Moldes, I. (2009). A developmental approach to forebrain organization in elasmobranchs:

New perspectives on the regionalization of the telencephalon. *Brain, Behavior and Evolution*, *74*(1), 20–29. https://doi.org/10.1159/000229010

Rodríguez-Moldes, I., Ferreiro-Galve, S., Carrera, I., Sueiro, C., Candal, E., Mazan, S., & Anadón, R. (2008). Development of the cerebellar body in sharks: Spatiotemporal relations of Pax6 expression, cell proliferation and differentiation. *Neuroscience Letters*, *432*(2), 105–110. https://doi.org/10.1016/j.neulet.2007.11.059

Rodriguez-Moldes, I., Timmermans, J. P., Adriaensen, D., De Groodt-Lasseel, M. H. A., Scheuermann, D. W., & Anadon, R. (1990). Asymmetric distribution of calbindin-D28K in the ganglia habenulae of an elasmobranch fish. *Anatomy and Embryology*, *181*(4), 389–391. https://doi.org/10.1007/BF00186911

Roman, E., Weininger, J., Lim, B., Roman, M., Barry, D., Tierney, P., … Roddy, D. (2020). Untangling the dorsal diencephalic conduction system: a review of structure and function of the stria medullaris, habenula and fasciculus retroflexus. *Brain Structure and Function*, (0123456789). https://doi.org/10.1007/s00429-020-02069-8

Roussigne, M., Bianco, I. H., Wilson, S. W., & Blader, P. (2009). Nodal signalling imposes left-right asymmetry upon neurogenesis in the habenular nuclei. *Development*, *136*(9), 1549–1557. https://doi.org/10.1242/dev.034793

Roussigné, M., Blader, P., & Wilson, S. W. (2012). Breaking symmetry: The zebrafish as a model for understanding left-right asymmetry in the developing brain. *Developmental Neurobiology*, *72*(3), 269–281. https://doi.org/10.1002/dneu.20885

Roussigné, M., Wei, L., Tsingos, E., Kuchling, F., Alkobtawi, M., Tsalavouta, M., … Wilson, S. W. (2018). Left/right asymmetric collective migration of parapineal cells is mediated by focal FGF signaling activity in leading cells. *Proceedings of the National Academy of Sciences of the United States of America*, *115*(42), E9812–E9821. https://doi.org/10.1073/pnas.1812016115

Ruiz i Altaba, A. (1998). Combinatorial Gli gene function in floor plate and neuronal inductions by Sonic hedgehog. *Development (Cambridge, England)*, *125*(12), 2203–2212. Retrieved from http://www.ncbi.nlm.nih.gov/pubmed/9584120

Salas, R., Sturm, R., Boulter, J., & De Biasi, M. (2009). Nicotinic receptors in the habenulo-interpeduncular system are necessary for nicotine withdrawal in mice. *Journal of Neuroscience*, *29*(10), 3014–3018. https://doi.org/10.1523/JNEUROSCI.4934-08.2009

Santos-Durán, G. N., Menuet, A., Lagadec, R., Mayeur, H., Ferreiro-Galve, S., Mazan, S., … Candal, E. (2015). Prosomeric organization of the hypothalamus in an elasmobranch, the catshark Scyliorhinus canicula. *Frontiers in Neuroanatomy*, *09*(April), 1–17. https://doi.org/10.3389/fnana.2015.00037

Schmidt, E. R. E., & Pasterkamp, R. J. (2017). The molecular mechanisms controlling morphogenesis and wiring of the habenula. *Pharmacology Biochemistry and Behavior*, *162*, 29–37. https://doi.org/10.1016/j.pbb.2017.08.008

Servili, A., Le Page, Y., Leprince, J., Caraty, A., Escobar, S., Parhar, I. S., … Kah, O. (2011). Organization of two independent kisspeptin systems derived from evolutionary-ancient kiss genes in the brain of zebrafish. *Endocrinology*, *152*(4), 1527–1540. https://doi.org/10.1210/en.2010-0948

Signore, I. A., Guerrero, N., Loosli, F., Colombo, A., Villalón, A., Wittbrodt, J., & Concha, M. L. (2009). Zebrafish and medaka: Model organisms for a comparative developmental approach of brain asymmetry. *Philosophical Transactions of the Royal Society B: Biological Sciences*, *364*(1519), 991–1003. https://doi.org/10.1098/rstb.2008.0260

Stamatakis, A. M., Van Swieten, M., Basiri, M. L., Blair, G. A., Kantak, P., & Stuber, G. D. (2016). Lateral Hypothalamic Area Glutamatergic Neurons and Their Projections to the Lateral Habenula Regulate Feeding and Reward. *Journal of Neuroscience*, *36*(2), 302–311. https://doi.org/10.1523/JNEUROSCI.1202-15.2016

Stamatakis, Alice M, & Stuber, G. D. (2012). Activation of lateral habenula inputs to the ventral midbrain promotes behavioral avoidance. *Nature Neuroscience*, *15*(8), 1105–1107. https://doi.org/10.1038/nn.3145

Stephenson-Jones, M., Floros, O., Robertson, B., & Grillner, S. (2012). Evolutionary conservation of the habenular nuclei and their circuitry controlling the dopamine and 5-hydroxytryptophan (5-HT) systems. *Proceedings of the National Academy of Sciences of the United States of America*, *109*(3), E164-73. https://doi.org/10.1073/pnas.1119348109

Sun, S., Zhu, J., & Zhou, X. (2020). Statistical analysis of spatial expression patterns for spatially resolved transcriptomic studies. *Nature Methods*, *17*(2), 193–200. https://doi.org/10.1038/s41592-019-0701-7

Sutherland, R. J. (1982). The dorsal diencephalic conduction system: A review of the anatomy and functions of the habenular complex. *Neuroscience and Biobehavioral Reviews*, *6*(1), 1–13. https://doi.org/10.1016/0149-7634(82)90003-3

Thébault, M. T., Izem, L., Leroy, J. P., Gobin, E., Charrier, G., & Raffin, J. P. (2005). AMP-deaminase in elasmobranch fish: A comparative histochemical and enzymatic study. *Comparative Biochemistry and Physiology - B Biochemistry and Molecular Biology*, *141*(4), 472–479. https://doi.org/10.1016/j.cbpc.2005.05.009

Tomizawa, K., Katayama, H., & Nakayasu, H. (2001). A novel monoclonal antibody recognizes a previously unknown subdivision of the habenulo-interpeduncular system in zebrafish. *Brain Research*, *901*(1–2), 117–127. https://doi.org/10.1016/S0006-8993(01)02313-7

van den Brink, S. C., Alemany, A., van Batenburg, V., Moris, N., Blotenburg, M., Vivié, J., … van Oudenaarden, A. (2020). Single-cell and spatial transcriptomics reveal somitogenesis in gastruloids. *Nature*, *582*(7812), 405–409. https://doi.org/10.1038/s41586-020-2024-3

Venkatesh, B., Kirkness, E. F., Loh, Y. H., Halpern, A. L., Lee, A. P., Johnson, J., … Brenner, S. (2007). Survey sequencing and comparative analysis of the elephant shark (Callorhinchus milii) genome. *PLoS Biology*, *5*(4), 932–944. https://doi.org/10.1371/journal.pbio.0050101

Venkatesh, B., Lee, A. P., Ravi, V., Maurya, A. K., Lian, M. M., Swann, J. B., … Warren, W. C. (2014). Elephant shark genome provides unique insights into gnathostome evolution. *Nature*, *505*(7482), 174–179. https://doi.org/10.1038/nature12826

Villar-Cheda, B., Pérez-Costas, E., Meléndez-Ferro, M., Manoel Abalo, X., Rodríguez-Muoz, R., Anadón, R., & Celina Rodicio, M. (2002). Proliferating cell nuclear antigen (PCNA) immunoreactivity and development of the pineal complex and habenula of the sea lamprey. *Brain Research Bulletin*, *57*(3–4), 285–287. https://doi.org/10.1016/S0361-9230(01)00702-X

Vue, T. Y., Aaker, J., Taniguchi, A., Kazemzadeh, C., Skidmore, J. M., Martin, D. M., … Nakagawa, Y. (2007). Characterization of progenitor domains in the developing mouse thalamus. *The Journal of Comparative Neurology*, *505*(1), 73–91. https://doi.org/10.1002/cne.21467

Wagner, F., French, L., & Veh, R. W. (2016). Transcriptomic-anatomic analysis of the mouse habenula uncovers a high molecular heterogeneity among neurons in the lateral complex, while gene expression in the medial complex largely obeys subnuclear boundaries. *Brain Structure and Function*, *221*(1), 39–58. https://doi.org/10.1007/s00429-014-0891-9

Wagner, F., Stroh, T., & Veh, R. W. (2014). Correlating habenular subnuclei in rat and mouse by using topographic, morphological, and cytochemical criteria. *Journal of Comparative Neurology*, *522*(11), 2650–2662. https://doi.org/10.1002/cne.23554

Wallace, M. L., Huang, K. W., Hochbaum, D., Hyun, M., Radeljic, G., & Sabatini, B. L. (2020). Anatomical and single-cell transcriptional profiling of the murine habenular complex. *ELife*, *9*, 1–22. https://doi.org/10.7554/eLife.51271

Wang, Q., Arighi, C. N., King, B. L., Polson, S. W., Vincent, J., Chen, C., … Wu, C. H. (2012). Community annotation and bioinformatics workforce development in concert--Little Skate Genome Annotation Workshops and Jamborees. *Database*, *2012*, bar064–bar064. https://doi.org/10.1093/database/bar064

Waylen, L. N., Nim, H. T., Martelotto, L. G., & Ramialison, M. (2020). From whole-mount to single-cell spatial assessment of gene expression in 3D. *Communications Biology*, *3*(1), 602. https://doi.org/10.1038/s42003-020-01341-1

Wei, L., Blader, P., & Roussigné, M. (2019). Notch signaling restricts FGF pathway activation in parapineal cells to promote their collective migration. *ELife*, 1–23. https://doi.org/10.1101/570820

Wu, C. C., Kruse, F., Vasudevarao, M. D., Junker, J. P., Zebrowski, D. C., Fischer, K., … Bakkers, J. (2016). Spatially Resolved Genome-wide Transcriptional Profiling Identifies BMP Signaling as Essential Regulator of Zebrafish Cardiomyocyte Regeneration. *Developmental Cell*, *36*(1), 36–49. https://doi.org/10.1016/j.devcel.2015.12.010

Wu, S. Y., de Borsetti, N. H., Bain, E. J., Bulow, C. R., & Gamse, J. T. (2014). Mediator subunit 12 coordinates intrinsic and extrinsic control of epithalamic development. *Developmental Biology*, *385*(1), 13–22. https://doi.org/10.1016/j.ydbio.2013.10.023

Yamaguchi, T., Danjo, T., Pastan, I., Hikida, T., & Nakanishi, S. (2013). Distinct roles of segregated transmission of the septo-habenular pathway in anxiety and fear. *Neuron*, *78*(3), 537–544. https://doi.org/10.1016/j.neuron.2013.02.035

Yang, L. M., Hu, B., Xia, Y. H., Zhang, B. L., & Zhao, H. (2008). Lateral habenula lesions improve the behavioral response in depressed rats via increasing the serotonin level in dorsal raphe nucleus. *Behavioural Brain Research*, *188*(1), 84–90. https://doi.org/10.1016/j.bbr.2007.10.022

Yeo, S. Y., Little, M. H., Yamada, T., Miyashita, T., Halloran, M. C., Kuwada, J. Y., … Okamoto, H. (2001). Overexpression of a slit homologue impairs convergent extension of the mesoderm and causes cyclopia in embryonic zebrafish. *Developmental Biology*, *230*(1), 1–17. https://doi.org/10.1006/dbio.2000.0105

Yvernogeau, L., Klaus, A., Maas, J., Morin-Poulard, I., Weijts, B., Schulte-Merker, S., … Robin, C. (2020). Multispecies RNA tomography reveals regulators of hematopoietic stem cell birth in the embryonic aorta. *Blood*, *136*(7), 831–844. https://doi.org/10.1182/blood.2019004446

Zagami, M. T., Ferraro, G., Montalbano, M. E., Sardo, P., & La Grutta, V. (1995). Lateral habenula and hippocampal units: electrophysiological and iontophoretic study. *Brain Research Bulletin*, *36*(6), 539–543. https://doi.org/10.1016/0361-9230(94)00239-W

Zhang, Bai bing, Yao, Y. yuan, Zhang, H. fei, Kawakami, K., & Du, J. lin. (2017). Left Habenula Mediates Light-Preference Behavior in Zebrafish via an Asymmetrical Visual Pathway. *Neuron*, *93*(4), 914-928.e4. https://doi.org/10.1016/j.neuron.2017.01.011

Zhang, Beilin, Gao, Y., Li, Y., Yang, J., & Zhao, H. (2016). Sleep Deprivation Influences Circadian Gene Expression in the Lateral Habenula. *Behavioural Neurology*, (7919534).

https://doi.org/10.1155/2016/7919534

Zhang, G.-W., Shen, L., Zhong, W., Xiong, Y., Zhang, L. I., & Tao, H. W. (2018). Transforming Sensory Cues into Aversive Emotion via Septal-Habenular Pathway. *Neuron*, *99*(5), 1016-1028.e5. https://doi.org/10.1016/j.neuron.2018.07.023

ANNEXES

Brain Structure and Function (2019) 224:2325–2341
https://doi.org/10.1007/s00429-019-01906-9

ORIGINAL ARTICLE

Mitral cell development in the olfactory bulb of sharks: evidences of a conserved pattern of glutamatergic neurogenesis

A. Docampo-Seara[1] · M. Lanoizelet[2] · R. Lagadec[2] · S. Mazan[2] · E. Candal[1] · M. A. Rodríguez[1]

Received: 28 December 2018 / Accepted: 7 June 2019 / Published online: 15 June 2019

Abstract
In mammals, the development of the olfactory bulb (OB) relies in part on the expression of transcription factors involved in the specifications/differentiation of glutamatergic cells. In a previous study from our group, a high molecular similarity was reported between mammals and cartilaginous fishes regarding the neurogenic mechanisms underlying the development of glutamatergic cells in the telencephalon. However, information about the transcriptional program operating in the development of the glutamatergic system (mainly represented by mitral cells) in the OB is lacking in the catshark *Scyliorhinus canicula*, a cartilaginous fish. Using immunohistochemistry and in situ hybridization techniques, we have found that, previously to the appearance of the olfactory primordium (OP), proliferating cells expressing Pax6 with molecular hallmarks of progenitor radial glia were located in the ventrolateral pallial ventricular zone. Later in development, when the OP is recognizable, a stream of Pax6-positive cells were observed between the ventricular zone and the OP, where transcription factors involved in mitral cell development in mammals (*ScTbr2*, *ScNeuroD*, Tbr1) are expressed. Later in development, these transcription factors became expressed in a layered-like structure where *ScVglut1*, a marker of mitral cells, is also present. Our data suggest that the transcriptional program related with the specification/differentiation of glutamatergic cells in the telencephalon has been conserved throughout the evolution of vertebrates. These results, in combination with previous studies concerning GABAergic neurogenesis in sharks, have evidenced that the OB of mammals and sharks shares similarities in the timing and molecular programs of development.

Keywords Olfactory bulb · Catshark · Mitral cells · Development · Glutamatergic lineage · Pax6

Introduction

The sense of smell is essential for a variety of behaviors in vertebrates like mating, feeding, fear and aggression. The organization of the olfactory system is well conserved in vertebrates not only in terms of function, but also in connectivity and also concerning the developmental origin of different structures within the peripheral and central olfactory system. Numerous investigations in mammals indicate that the olfactory system constitutes an excellent model to study various developmental aspects of the nervous system such as neurogenesis, neuronal migration, and axon guidance (Blanchart et al. 2011; Díaz-Guerra et al. 2013; Lim and Alvarez-Buylla 2016).

In rodents, the main olfactory system is related with the olfactory chemoreception of odorants and comprises a primary olfactory pathway consisting of the nasal olfactory epithelium (OE) and the main olfactory bulb (MOB), and a secondary olfactory pathway that includes all cortical regions directly innervated by MOB projection neurons (known together as the olfactory cortex); the olfactory cortex in turn releases signals to higher cortical areas involved in conscious perception and to limbic areas that control basic drives and emotions (reviewed in Boehm 2006; Treloar et al. 2010).

E. Candal and M. A. Rodríguez have equally contributed to this work.

✉ M. A. Rodríguez
miguelangel.rodriguez.diaz@usc.es

[1] Departamento de Bioloxía Funcional, Centro de Investigación en Bioloxía (CIBUS), Universidade de Santiago de Compostela, 15782 Santiago de Compostela, Spain

[2] CNRS, Sorbonne Universités, UPMC Univ Paris 06, UMR7232, Observatoire Océanologique, Banyuls sur Mer, France

Besides, olfactory chemoreception of pheromones depends on an accessory olfactory system called vomeronasal system (VNS) that comprises the neuroepithelium of the vomeronasal organ (VNO or Jacobson's organ) and the accessory olfactory bulb (AOB); signals from the AOB are relayed to regions of the amygdala and hypothalamus implicated in behavioral and physiological effects of pheromones (for review see Boehm 2006; Huilgol and Tole 2016).

In rodents, projecting axons of the olfactory receptor neurons located in the OE reach the telencephalic vesicle and induce the growth of the olfactory bulb primordium (OP). The MOB becomes evident macroscopically around the day 12 of embryonic development (E12; Gong and Shipley 1995). During the morphogenesis of the mouse MOB, projection neurons (mitral cells) are born from pallial progenitor cells and, then, interneurons (granule and periglomerular cells) that arise from the subpallium migrate tangentially toward their destination within the MOB (Blanchart et al. 2006; Vergaño-Vera et al. 2006; Imamura and Greer 2013; Huilgol and Tole 2016). The cellular organization of the MOB and AOB is similar. Projection neurons of the MOB and anterior AOB arise from the same region; however, differences in the domains of origin and migration routes of projection neurons are present between the anterior and posterior regions of the AOB. Interneurons of the MOB and AOB are born in the same region (for review see: Huilgol et al. 2013; Huilgol and Tole 2016).

Despite most studies about the olfactory system are focused on mammals, other animal models are necessary nowadays to understand different embryological aspects occurring during development of the olfactory system. Cartilaginous fishes represent one of the three living lineages of vertebrates (cyclostomes, cartilaginous fishes and bony vertebrates). Cartilaginous fishes diverged from bony vertebrates about 450 million years ago. Embryological studies in cartilaginous fishes reveal a conserved pattern of gene expression in diverse developmental process across gnathostome vertebrates (Gillis and Shubin 2009), and also morphogenetic processes and regionalization patterns are strikingly similar to mammals (Rodríguez-Moldes et al. 2017). More recently, the whole-genome analysis of three elasmobranch species has shown the presence of genes related with homeostasis, reproduction, and mechanisms for the generation of neuronal cell diversity homologous to that found in mammals (Hara et al. 2018). These studies indicate that cartilaginous fishes represent a key model for better knowledge of evolution of gnathostome brain development.

Moreover, cartilaginous fishes possess a well-developed sense of smell that is important for survival, localizing preys, avoiding predators, and chemosensory communication (for review see: Yopak et al. 2015). Numerous investigations have been referred to the adult olfactory system in elasmobranchs fishes. Several studies have been referred to the cell organization of the OE of the catshark, where sensory ciliated neurons, which in tetrapod vertebrates project to the MOB, are lacking; however, in the OE, microvillous olfactory receptor neurons and crypt sensory neurons are clearly recognizable (Theisen et al. 1986; Ferrando et al. 2006a, b, 2009, 2010, 2012; Zaccone et al. 2011). In addition, genomic studies show that the predominant olfactory receptor type in the catshark and the elephant shark is the vomeronasal type2 receptor (V2R) (Sharma et al. 2019). These evidences together with ultrastructural and immunohistochemical data indicate that in the catshark the olfaction could mainly rely on a VNS (Ferrando and Gallus 2013). Interestingly, anatomical and molecular data show a primordial accessory olfactory system in the sea lamprey (Chang et al. 2013) and an accessory olfactory system was also identified in the African lungfish (González et al. 2010) and zebrafish (Biechl et al. 2017).

Though the OBs are laminated structures, in sharks, they do not present the six cell layers described in mammals. The cytoarchitectonic organization of the OB in the catshark has been investigated by classic staining techniques and summarized by Smeets et al. (1983). Three main layers can be observed in this species: the olfactory nerve layer, the glomerular layer and the granular layer. Two main types of cells have been described in the OB: interneurons and projection neurons. The ultrastructure of the OB (Dryer and Graziadei 1996) and the arrangement of the primary and secondary olfactory projections have been described in different elasmobranchs species (Dryer and Graziadei 1993, 1994; Yáñez et al. 2011). Besides, in juveniles and/or adults of *S. canicula,* the OB have been characterized using antibodies against enzymes like tyrosine hydroxylase (TH) (Carrera et al. 2012), glutamate acid decarboxylase (GAD) (Sueiro 2003), neuronal nitric oxide synthase (nNOS) (Ferrando et al. 2012) and choline acetyltransferase (ChAT) (Anadón et al. 2000); other neuroactive substances such as glycine (Anadón et al. 2013), serotonin (Carrera et al. 2008a) and diverse neuropeptides (Rodríguez-Moldes et al. 1993; Molist et al. 1995; Teijido et al. 2002) have also been detected in the OB of the catshark.

In contrast, studies about development of the olfactory system are scarce and mainly focused on the peripheral olfactory system (Ferrando et al. 2012; Ferreiro-Galve et al. 2012; Quintana-Urzainqui et al. 2014). Using tract-tracing and immunohistochemical techniques, the development of the peripheral olfactory system of the catshark *Scyliorhinus canicula* has been described, and numerous Pax6-expressing cells have been observed in the OE, and along the developing olfactory nerve (Ferreiro-Galve et al. 2012; Quintana-Urzainqui et al. 2014). In addition, numerous Pax6-positive cells have been also reported in the ventricular zone of the ventrolateral pallium of embryos before the appearance of the OP (Ferreiro-Galve et al. 2012). However, the phenotype

of these cells is unknown and their relationship with OB development has not been addressed so far. On the other hand, information about the origin, specification and differentiation of the OB cell types in the catshark is scarce and restricted to dopaminergic cells. These cells originate in a subpallial ventricular domain in late embryos and reach the OB following a route named lateral stream. The presence of TH-ir cells in this stream, as well as in the OB of stage 32 embryos, indicate that these cells may be the source of the granular and periglomerular cells of the mature OB (Ferreiro-Galve et al. 2012; Carrera et al. 2012; Quintana-Urzainqui et al. 2015). However, information about the development of OB glutamatergic cells (mitral cells) is lacking in sharks.

The transcriptional program involved in the specification and differentiation of mitral cells is well known in mammals and, curiously, is the same that operates on the specification/differentiation of pallial glutamatergic neurons before the mature organization of the OB is achieved (for review see: Bulfone et al. 1998; Englund et al. 2005; Díaz-Guerra et al. 2013; Imamura and Greer 2013; Kahoud et al. 2014; Roybon et al. 2015; Mihalas and Hevner 2017). Different experimental approaches carried out in mammals have shown that the transcription factor-paired homeobox 6 (Pax6), together with Sox2 (a transcription factor expressed in stem cells), is involved in neural stem cell self-renewal, neurogenesis and differentiation of specific neural cell types (Dellovade et al. 1998; Nomura and Osumi 2004; Kohwi et al. 2005; Sansom et al. 2009; Gómez-López et al. 2011; Curto et al. 2014). Pax6-expressing cells have been reported in the ventricular zone of the embryonic pallium as well as in the developing OB in mammals (Stoykova and Gruss 1994; Puelles et al. 2000), amphibians (Franco et al. 2001) and elasmobranch fishes, even though in the catshark, Pax6 is expressed throughout the VZ of the pallium, as in other vertebrates, the gradient described in mammals (lateral high, medial low and anterior high, and posterior low) is not evident in sharks (Ferreiro-Galve et al. 2012; Quintana-Urzainqui et al. 2012; Rodríguez-Moldes et al. 2017). In the MOB of rodents, projection neurons (mitral and tufted cells) derive from Pax6-positive radial glia progenitors located in the ventricular zone of the dorsal pallium (Winpenny et al. 2011; Imamura et al. 2011; Imamura and Greer 2013). Besides, Pax6 regulates the expression of two T-box genes (Tbr1 and Tbr2, the latter also known as Eomes) (Bulfone et al. 1995; Méndez-Gómez et al. 2011; Mizuguchi et al. 2012; Imamura and Greer 2013), which are also expressed along mitral cell development in the OB in rodents (Bulfone et al. 1999; Faedo et al. 2002; Winpenny et al. 2011; Mizuguchi et al. 2012; Roybon et al. 2015), birds (Bulfone et al. 1999), amphibians (Moreno et al. 2003; Brox et al. 2004) and zebrafish (Mione et al. 2001; Mueller and Wulliman 2016). In addition, the basic helix–loop–helix transcription factor NeuroD is also implicated in the terminal differentiation of mitral cells (Boutin et al. 2010; Osorio et al. 2010; Roybon et al. 2015). At the end of the embryonic period in mammals, mitral cells begin to express the glutamate vesicular transporter 1 (Vglut1; Ohmomo et al. 2011), which is also a marker of mitral cells in other groups of vertebrates such as reptiles (Sarkar and Atoji 2018). Mutant mice, where expression of Pax6, Tbr1 and Tbr2 is altered, show a disrupted OB morphogenesis indicating that this transcriptional cascade plays a key role in the correct morphogenesis of the OB (Bulfone et al. 1998; Nomura and Osumi 2004; Kahoud et al. 2014). Curiously, in mammals Tbr1 is also implicated in the specification of the anterior AOB; however, the specification of the posterior AOB is under the control of different genes (for review see: Huilgol and Tole 2016).

With the purpose of shedding light into the development of the central olfactory system in an evo–devo context, we have characterized Pax6 immunoreactive cells present in the ventricular zone of the ventrolateral pallium embryos of catshark with different progenitor markers such as Sox2 (stem cells), GFAP and BLBP (radial glia cells) and PCNA (proliferating cells). Then, we have studied the expression pattern of Pax6, once the OP emerges, and we have analyzed the expression pattern of transcription factors (such as Tbr2, NeuroD and Tbr1) and the vesicular transporter of glutamate 1 (vGlut1) related to differentiation of glutamatergic cells in the developing OB using immunocytochemistry and in situ hybridization techniques. In addition, we have carried out a BrdU pulse-chase study to determine the developmental period where these cells are generated. Finally, we have discussed our results in an evo–devo context and also at the light of the possibility of the existence of an AOB in the catshark.

Materials and methods

Experimental animals

In the present study, we have analyzed 15 embryos of *S. canicula* from stages 30 (S30) to 32 (S32) of development. Embryos were provided by the Marine Biological Model Supply Service of the CNRS UPMC Roscoff Biological Station (France) and the Oceanographic Observatory of Banyuls sur Mer (France). Embryos were staged by their external features according to Ballard et al. (1993). Sharks were raised in seawater tanks under standard conditions of temperature (15–16 °C), pH (7.5–8.5) and salinity (35 g/L) and suitable measures were taken to minimize animal pain and discomfort. All procedures were made according to the guidelines established by the European Communities Council Directive of 22 September 2010 (2010/63/UE) and by Spanish Royal Decree 53/2013 for animal experimentation

and were approved by the Ethics Committee of the University of Santiago de Compostela.

Tissue processing

Embryos were deeply anesthetized with 0.5% tricaine methane sulfonate (MS-222; Sigma, St. Louis, MO, USA) in seawater and separated from the yolk before fixation in 4% paraformaldehyde (PFA) in elasmobranch's phosphate buffer [EPB: 0.1 M phosphate buffer (PB) containing 1.75% of urea, pH 7.4] for 48–72 h depending on the stage of development. Subsequently, they were rinsed in PB saline (PBS), cryoprotected with 30% sucrose in PBS, embedded in OCT compound (Tissue Tek, Torrance, CA), and frozen with liquid nitrogen-cooled isopentane. Parallel series of sections (16–18-µm thick) were obtained in transverse planes on a cryostat and mounted on Superfrost Plus (Menzel-Glasser, Madison, WI, USA) slides.

BrdU pulse-chase experiments

BrdU pulse-chase labeling was performed by incubating three catshark embryos at S28, S29 and S30 in 10 mg/ml of BrdU in oxygenated artificial sea water, after opening the egg shell, for 2 h 30 min; embryos were then moved to untreated sea water until they achieve S31, when they were killed by overdose of MS-222 and fixed by immersion in PFA 4% for 48 h. For detection of BrdU, sections were incubated in 2 N HCl for 30 min at 50 °C to denature DNA strands. HCl reaction was stopped by addition of 0.1 M sodium tetraborate and sections were then rinsed in TBS for 10 min before antibody incubation. Sections were incubated with anti-BrdU antibody at room temperature (RT) overnight and processed for immunofluorescence as described below.

In situ hybridization

We applied in situ hybridization (ISH) for *S. canicula Tbr2/Eomes, NeuroD1, vGlut1 and Sox2 (ScSox2, ScTbr2, ScNeuroD1, ScvGlut1)* genes. These probes were selected from a collection of *S. canicula* embryonic cDNA library (mixed stages S9–S22), submitted to high-throughput EST sequencing (coordinated by Dr. Sylvie Mazan). Sense and antisense digoxigenin-UTP-labeled *ScTbr2, ScNeuroD1, ScvGlut1 and ScSox2* were synthesized directly by transcription in vitro. ISH was performed on cryostat sections of S30, S31 and S32 embryos following standard protocols (Coolen et al. 2009). Briefly, sections were permeabilized with proteinase K, hybridized with sense or antisense probes overnight at 65 °C and incubated with the alkaline phosphatase-coupled anti-digoxigenin antibody (1:2000, Roche Applied Science, Manheim, Germany) overnight at 4 °C. The color reaction was performed in the presence of BM-Purple (Roche). Color reaction was stopped by rinsing in PFA 4% for 45 min. Finally, sections were dehydrated and coverslipped. Control sense probes did not produce any detectable signal.

Immunohistochemistry

Sections were pre-treated with 0.01 M citrate buffer pH 6.0 for 30 min at 90 °C for heat-induced epitope retrieval and allowed to cool for 20 min at RT. Sections were rinsed in 0.05 M Tris-buffered saline (TBS) pH 7.4 for 5 min and treated with 10% H_2O_2 in TBS for 30 min at RT to block endogenous peroxidase activity. Sections were rinsed in 0.05 M TBS pH 7.4 for 5 min and incubated approximately for 15 h at RT with primary antibodies (see Table 1). Sections were rinsed three times in 0.05 M TBS pH 7.4 for 10 min each, and incubated in the appropriate HRP-coupled secondary antibody (see Table 1) for 1 h at RT. All dilutions were made with TBS containing 15% normal goat serum (Millipore, Billerica, MA, USA) 0.2% Triton X-100 (Sigma) and 2% bovine serum albumin (BSA, Sigma). All incubations were carried out in a humid chamber. Then, sections were rinsed three times in 0.05 M TBS pH 7.4 for 10 min each. The immunoreaction was developed with 0.25 mg/ml diaminobenzidine (DAB) tetrahydrochloride (Sigma) in TBS pH 7.4 and 0.00075% H_2O_2, or with SIGMAFAST™ 3.3-DAB tablets as indicated by the manufacturers. In Pax6 samples, 2.5 mg/ml nickel ammonium sulfate was added. Finally, the sections were dehydrated, and coverslipped.

Double in situ hybridization–immunohistochemistry

We applied double in situ hybridization–immunohistochemistry for *ScTbr2* and *ScNeuroD* probes and the Tbr1 antibody. After colorimetric detection of probes, sections were rinsed three times in 1 M PBS for 10 min each, rinsed in PFA 4% for 45 min and immunohistochemistry was performed as described above.

Double immunofluorescence

For heat-induced epitope retrieval, sections were pre-treated with 0.01 M citrate buffer (pH 6.0) for 30 min at 90 °C and allowed to cool for 20 min at RT. Sections were rinsed in 0.05 M TBS (pH 7.4) for 5 min and incubated approximately for 15 h at RT with primary antibodies (see Table 1). Sections were rinsed three times in 0.05 M TBS pH 7.4 for 10 min each, and incubated in the appropriate combination of fluorescent dye-labeled secondary antibodies (see Table 1) for 1 h at RT. All dilutions were made with TBS containing 15% normal donkey serum (Millipore, Billerica, MA, USA) 0.2% Triton X-100 (Sigma) and 2% bovine serum albumin (BSA, Sigma). All incubations were carried out

Table 1 Primary and secondary antibodies used

Primary antibody	Source	Working dilution	Secondary antibody	Source	Working dilution
Pax6	Policlonal rabbit anti-Pax6 Covance (Cat. No. PRB-278P)	1:300	Goat anti-rabbit HRP coupled	Dako, Glostrup, Denmark	1:200
PCNA	Monoclonal mouse anti-PCNA Sigma (Cat. No. P8825)	1:500	488-cojugated donkey anti-mouse	Alexa Fluor Molecular Probes, Eugene, OR	1:200
GFAP	Polyclonal rabbit anti-GFAP Dako (Cat. No. Z033429)	1:500	546-conjugated donkey anti-rabbit	Alexa fluor Molecular Probes, Eugene, OR	1:200
BLBP	Polyclonal rabbit anti-BLBP Millipore (Cat. No. ABN14)	1:300	FITC-conjugated goat anti-rat	ThermoFisher Cat. No. 31621	1:100
Tbr1	Policlonal rabbit anti-Tbr1 Chemicon (Cat. No. AB9616) Millipore (Cat. No. AB10554)	1:200			
TH	Monoclonal mouse anti-TH Millipore (Cat. No. MAB318)	1:500			
BrdU	Policlonal Rat anti-Brdu Abcam (Cat. No. ab6326)	1:100			

in a humid chamber. Sections were rinsed three times in 0.05 M TBS pH 7.4 for 10 min each and in distilled water for 30 min. Sections were then allowed to dry for 30 min at 37 °C, and mounted in MOWIOL 4-88 Reagent (Calbiochem, MerkKGaA, Darmstadt, Germany). Information about the primary and secondary antibodies is included in Table 1.

Control and specificity of antibodies

The PCNA antibody has been previously used to label progenitor cells in the brain and olfactory system of *S. canicula* (i.e. Quintana-Urzainqui et al. 2014, 2015). In addition, the specificity of the antibody against Pax6 has been tested by pre-absorption test in *S. canicula* (Ferreiro-Galve et al. 2012). The Tbr1 antibody has been previously used as a marker of pallial glutamatergic neurons in the developing brain of *S. canicula* (Docampo-Seara et al. 2018a). Antibodies against glial markers GFAP and BLBP and the enzyme TH (marker of dopaminergic cells) have been previously tested by western blot (Carrera et al. 2012; Docampo-Seara et al. 2018b).

Imaging

Fluorescent sections were photographed with the Leica TCS-SP2 scanning microscope with a combination of blue and green excitation lasers. Confocal images were acquired separately for each laser channel with steps of 2 µm along the z-axis, and collapsed images were obtained with the LITE software (Leica). Light field images were obtained with an Olympus BX51 microscope equipped with an Olympus DP71 color digital camera. Images were adjusted for contrast, brightness and intensity using Corel Draw X7.

Results

In the catshark, the OP emerges as a well-defined protrusion in ventrolateral portions of the telencephalic hemispheres in the transition from S30 to S31 of development (Ferreiro-Galve et al. 2012). While no cell layering can be appreciated at this stage, incipient glomeruli began to appear, called protoglomeruli, in the distal portion of the OP. At S32, protoglomeruli are more evident and the OB becomes conspicuous and organized in three basic layers, which are, from outside to inside, the olfactory nerve layer, the glomerular layer (protoglomeruli) and the granular layer. Mitral cells, which in the mammalian brain and in other vertebrates constitute a proper layer, do not form a defined layer in the catshark, but rather they are diffusely distributed between the glomerular and granular layers. From S32 onwards, the OB grows and the glomerular layer and granular layer form well-defined layers. For further information about the OB development in the catshark, see Quintana-Urzainqui et al. (2014, 2015).

Expression of Pax6 and progenitor cell markers in the ventrolateral pallium at stage 30

At S30 of development, before the appearance of the OP, the telencephalon is constituted by a large ventricle surrounded by the telencephalic walls. These walls are constituted by a proliferating ventricular zone and an intermediate zone comprised of neuroblasts (Docampo-Seara et al. 2018a). Pallium and subpallium are recognizable because of their differential expression of Pax6 and GAD, respectively (Carrera et al. 2008b; Quintana-Urzainqui et al. 2015; Rodríguez-Moldes et al. 2017), but their main pallial and subpallial subdivisions are not yet established (Fig. 1a). As mitral cell progenitors could be present in the pallial proliferating ventricular zone before the appearance of the OP in a way similar to what happens with mitral cell progenitors in the OB of mammals (Imamura et al. 2011), we have studied the expression pattern of Pax6 (pallial/mitral progenitor marker), *ScSox2* (stem cell marker), BLBP–PCNA and GFAP–PCNA (radial glial progenitor cell markers) in the ventricular zone of the ventrolateral portions of the pallium (the presumptive area where the OP is going to emerge) of a S30 embryo (square in Fig. 1a).

Pax6 expression in the pallium was restricted to the pallial ventricular zone in the telencephalon of a S30 embryo, including ventrolateral portions (Fig. 1b). *ScSox2* expression was also present in the pallial ventricular zone, where its expression coincides with that of Pax6 (compare Fig. 1b and c). In the same region where numerous Sox2- and Pax6-positive cells were present, numerous BLBP- and GFAP-positive cells were observed; immunoreactivity for both radial glia markers was present in the periphery of the cell bodies and in their basal and apical processes. Double immunofluorescence BLBP/PCNA and GFAP/PCNA showed that all

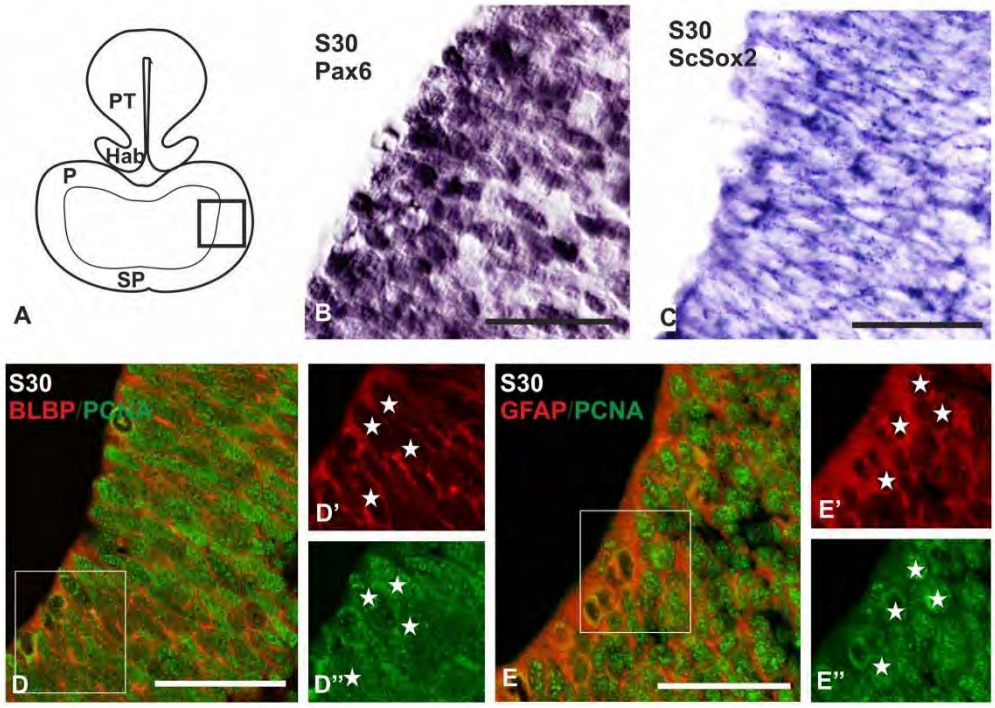

Fig. 1 Transverse sections showing the expression pattern of progenitor markers in the ventricular zone of the telencephalic walls of S30 of development. **a** Scheme showing the main divisions of the developing brain of a S30 of development. The square represents the portion of the pallium studied at this stage of development. **b** Photomicrograph at high magnification showing the expression pattern of Pax6 in the ventricular lateral portions of the pallium. Note two different intensities of immunolabeling. **c** Photomicrograph at high magnification showing the expression pattern of *ScSox2*. **d**, **d''** Double immunofluorescence BLBP/PCNA in the lateral portions of the pallium showing double-labeled cells (stars). **e**, **e''** Double immunofluorescence GFAP/PCNA in the lateral portions of the pallium showing double-labeled cells (stars). Scale bars: 25 µm. *P* pallium, *Hab* habenula, *PT* pretectum, *SP* subpallium

BLBP- and GFAP-expressing cells also expressed PCNA (Fig. 1d, and stars in Fig. 1d', d''; Fig. 1e, and stars in Fig. 1e', e'').

Expression pattern of transcription factors (Pax6, *ScTbr2*, Tbr1 and *ScNeuroD*) in S31/S32 embryos

We have studied the main transcription factors involved in mitral cell development (Pax6, Tbr2, NeuroD and Tbr1) at S31 of development (after the OP emerges) and at S32 (when the basic cytoarchitectonic pattern of the OB begins to appear). At S31, numerous Pax6 immunoreactive cells can be observed in the ventricular zone of dorsal and ventrolateral pallial regions (Fig. 2a). Interestingly, a stream of Pax6-positive cells can be appreciated coursing from the ventricular zone of the ventrolateral pallium to the OP (Fig. 2a'). Curiously, cells that seem to invade the OP show a weaker Pax6 immunoreactivity. Besides, we have also analyzed the expression pattern of *ScTbr2*, *ScNeuroD*, and Tbr1. Intense *ScTbr2* and *ScNeuroD* labeling was detected in a cell band adjacent to the most distal region of the OP, where the first protoglomeruli appear, close to the ON entry (Fig. 2b, c), while a faint labeling was observed in proximal regions of the OP. Note that the band of intense labeled cells of both *ScTbr2* and *ScNeuroD* fits with the Pax6-negative territory of the OP (compare Fig. 2a with Fig. 2b and c). In contrast, Tbr1 immunohistochemistry revealed numerous immunoreactive cells in all

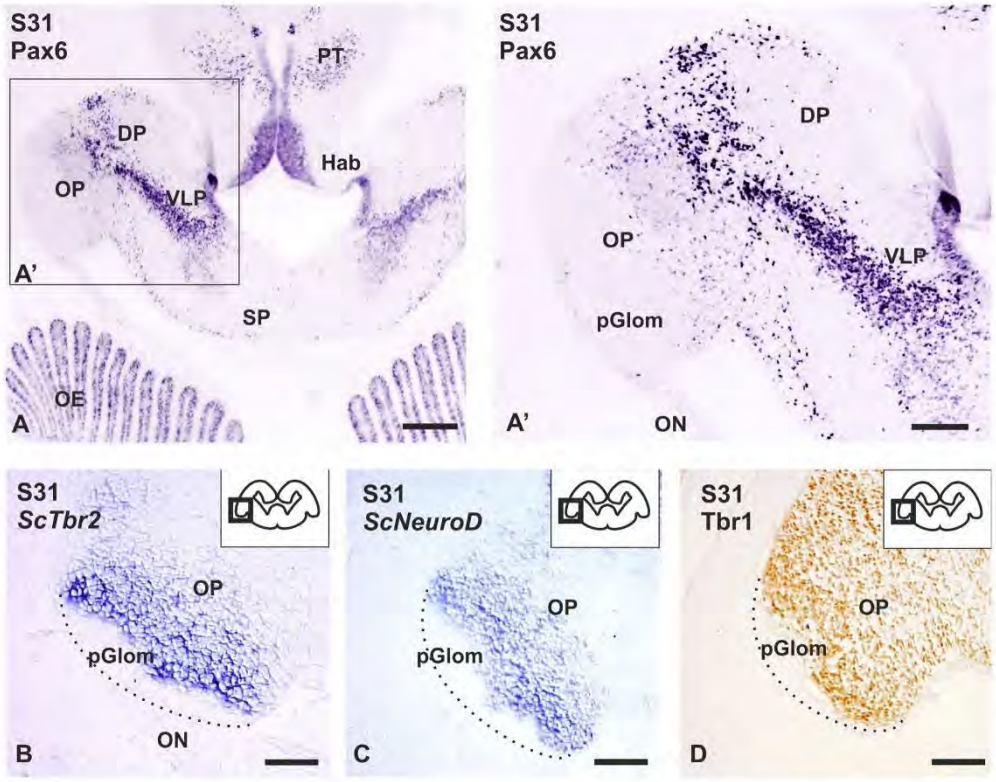

Fig. 2 Transverse sections showing the expression pattern of Pax6 and the neurogenic markers *ScTbr2, ScNeuroD* and Tbr1 in the OP of S31 of development. **a** Photomicrograph at low magnification of the telencephalon showing the expression pattern of Pax6 in a S31 of development. **a'** Detail of the expression pattern of Pax6 showing a stream of Pax6-positive cells coursing from the ventricular zone to the OP. Note that Pax6-positive cells in the OP show low levels of Pax6. In S31, *ScTbr2* (**b**) and *ScNeuroD* (**c**) are expressed as a specific cell band close to the prospective glomerular layer, meanwhile Tbr1 is expressed in all regions of the OP (**d**). Dotted lines show the limit of the OP. Scale bars: 200 µm (**a**), 100 (**a'**–**d**). *DP* dorsal pallium, *Hab* habenula, *OE* olfactory epithelium, *ON* olfactory nerve, *OP* olfactory primordium, *PT* pretectum, *SP* subpallium, *VLP* ventrolateral pallium

regions of the OP, except in the region of protoglomeruli (Fig. 2d).

At S32, the expression pattern of the three transcription factors was restricted to a dense layer of cells in the region adjacent to the protoglomeruli (Fig. 3a–c). As in S31, Tbr1-positive cells were also located in proximal regions of the prospective OB (Fig. 3c). Since the expression pattern of *ScTbr2* and *ScNeuroD* was highly coincident but the territory of Tbr1 expression seems to be wider, we performed double in situ hybridization–immunohistochemistry for *ScTbr2* and Tbr1 and for *ScNeuroD* and Tbr1 at S32 (Fig. 3d, e'). We found that most of the *ScTbr2*-expressing cells were

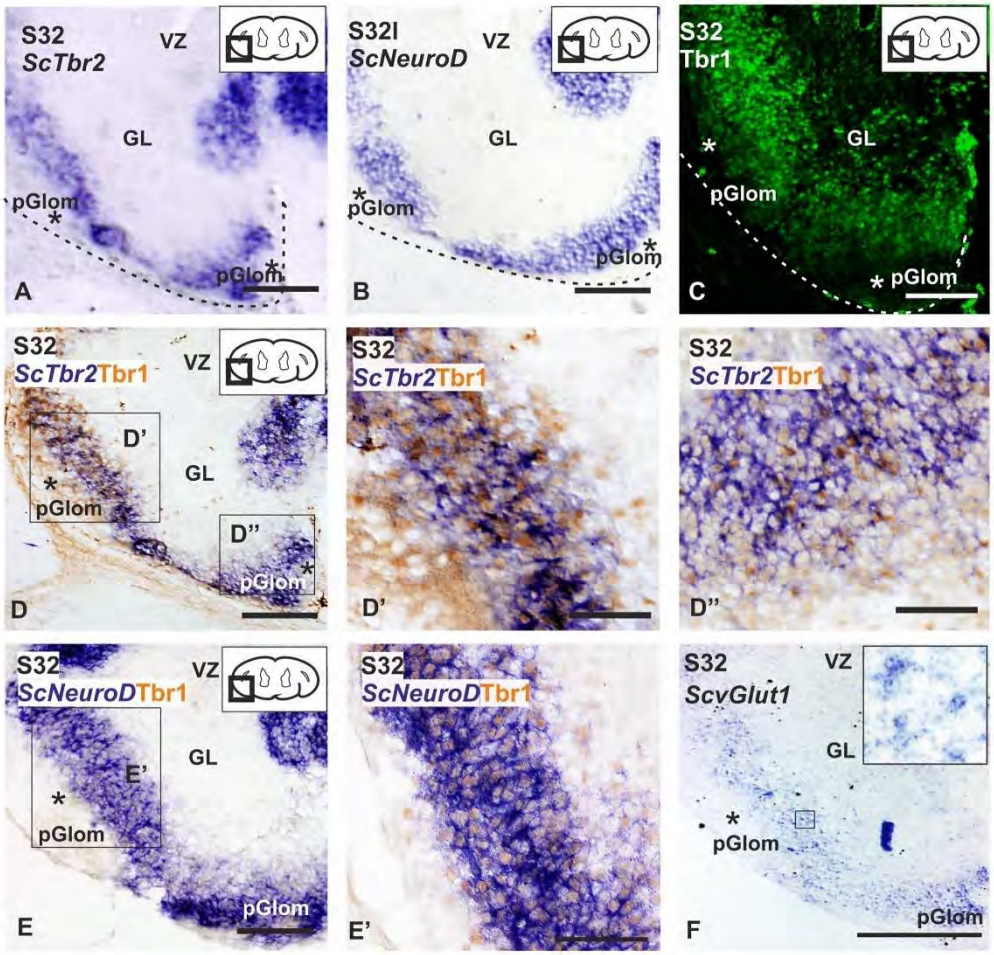

Fig. 3 Transverse sections showing the expression pattern of the neurogenic markers *ScTbr2*, *ScNeuroD*, Tbr1 and *ScvGlut1* in the OP of S32 of development. In S32 embryos *ScTbr2* (**a**), *ScNeuroD* (**b**) and Tbr1 (**c**) show a similar expression pattern. Note that Tbr1 seems to label a wider territory compared with *ScTbr2* and *ScNeuroD*. Dotted lines shows the limit of the OB. Asterisks show protoglomeruli. Double ISH–IHC between *ScTbr2* and Tbr1 (**d**) in the lateral (**d'**) and ventral (**d''**) portions of the distal OB, showing double-labeled cells. Note that in the lateral portion Tbr1 immunoreactivity is more abundant (**d'**), in contrast to the ventral portion, where *ScTbr2* is more abundant (**d''**). **e**, **e'** Double ISH–IHC between *ScNeuroD* and Tbr1 showing an almost total colocalization of both neurogenic markers. **f** Photomicrograph showing the expression pattern of *ScvGlut*1, coincident with the expression of *ScTbr2, ScNeuroD* and Tbr1. Scale bars: 100 µm (**a**, **b**, **c**, **d**, **e**, **f**), 50 µm (**d'**, **d''**, **e'**). *GL* granular layer, *OP* olfactory primordium, *pGlom* protoglomeruli, *VZ* ventricular zone

also positive for Tbr1 (Figs. 3d, d'). However, some cells expressed only *ScTbr2* or Tbr1. Curiously, most cells that only expressed Tbr1 were located in lateral regions of the distal OB (Fig. 3d'), in contrast to the ventral region, where most of the cells were positive for Sc*Tbr2* only (Fig. 3d''). Concerning *ScNeuroD* and Tbr1 cell populations, we have observed a high coexpression of both factors in the same cells (Fig. 3e, e') and no differences between the lateral and ventral regions of the OB were appreciated.

In mammals and other vertebrate groups, these transcription factors are part of a transcriptional code related with the differentiation of pallial glutamatergic neurons (reviewed by Hevner et al. 2006). However, there is no direct evidence about the involvement of these factors in the glutamatergic system in sharks. We have analyzed the expression of the glutamatergic marker *ScvGlut1* (vesicular glutamatergic transporter) in S32 embryos by in situ hybridization. We found numerous *ScvGlut1*-positive cells adjacent to the protoglomerular region (Fig. 3f), in the region occupied by *ScTbr2*/Tbr1/*ScNeuroD*-expressing cells. In addition, we have performed double immunofluorescence in early S32 embryos for Tbr1 and the enzyme tyrosine hydroxylase (TH), which is involved in dopamine synthesis and labels interneurons in the OB of sharks (Quintana-Urzainqui et al. 2015); Tbr1-expressing cells were observed at this developmental stage; however, TH immunoreactivity was still not observed in the OB (data not shown).

Expression pattern of BrdU in mitral cells presumptive territory at S31 after pulses at different developmental stages

As we have determined that cells in the ventrolateral VZ of the pallium typically express mitral cell progenitor markers before the emergence of the OP, we have decided to determine at which point of development, mitral cells are generated. For that, BrdU pulse experiments were performed in catshark embryos at S28, S29 and S30 and embryos were allowed to develop up to S31. When pulses were performed at S28, most BrdU-positive cells at S31 were concentrated in the portion of the OP that corresponds to the territory labeled by *ScTbr2* (Fig. 4a, dotted lines correspond to *ScTbr2* territory, see Fig. 2c). On the other hand, when pulses were performed at S29, most BrdU-positive cells at S31 were

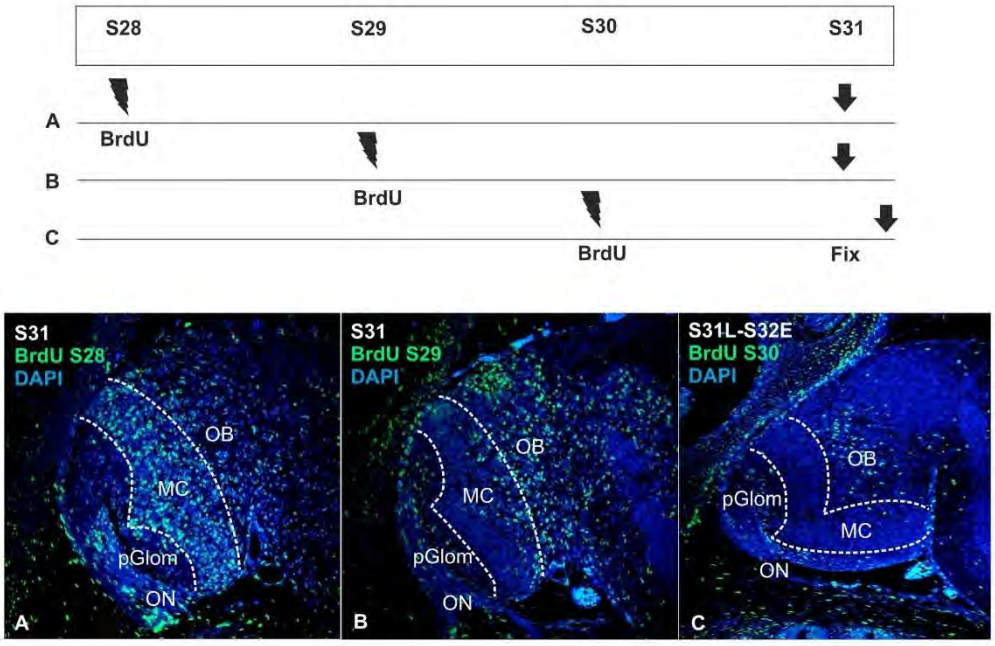

Fig. 4 Scheme and transverse sections showing BrdU immunoreactive cells (green), counterstained with DAPI (blue), in the OB of a S31 embryo after BrdU pulses at S28 (**a**), S29 (**b**) and S30 (**c**). Note that most BrdU-positive cells in mitral cell territory belong to pulses in S28 (**a**), in contrast to S30 (**c**), where almost none positive cells can be detected. Dotted lines represent *ScTbr2*- and *ScNeuroD*-positive territories, where mitral cells are located. *MC* mitral cell territory, *OB* olfactory bulb, *ON* olfactory nerve, *pGlom* protoglomeruli

concentrated in the prospective granular layer, with a small proportion of positive cells in the olfactory region that would correspond to mitral cells location (Fig. 4b). Finally, when pulses were carried out at S30, barely no BrdU-positive cells were found in the presumptive location of mitral cells at S31; in contrast, the vast majority of cells were located at the granular portion of the OP (Fig. 4c).

Discussion

In the present work, we have studied the phenotype of Pax6-expressing cells observed in the VZ of the lateroventral pallium of catshark embryos in terms of expression of proliferation and radial glial markers. In addition, we have analyzed the expression of several transcription factors implicated in the differentiation of glutamatergic lineage in the primordial OB of embryos (Pax6, *ScTbr2, ScNeuroD*, Tbr1). Our results suggest that mitral cells originate from Pax6-expressing radial glial cells in the VZ of the ventrolateral portion of the pallium that express the same transcription factors described for mitral cell progenitors in mammals (see "Discussion" below).

Pax6-positive cells present in the embryonic telencephalic ventricular zone are proliferating stem cells with molecular hallmarks of radial glia

Several investigations in mammals have shown that Pax6 is involved in the development of the olfactory placode, the OB and the olfactory cortex (Stoykova and Gruss 1994; Nomura et al. 2007). In amphibians, the expression pattern of Pax6 in the developing OB suggests that this transcription factor also plays a key role in olfactory system development (Franco et al. 2001; Moreno et al. 2008; Joven et al. 2013). In the embryonic OP of mammals, this transcription factor is highly expressed in the ventricular zone (Puelles et al. 2000; Vergaño-Vera et al. 2006). Using molecular markers of radial glia, it was shown that Pax6 is localized in progenitor radial glial cells during mammalian pallial neurogenesis, including the ventricular zone of the embryonic OB (Götz et al. 1998; Imamura and Greer 2013). In addition, mouse neural stem cell lines display many hallmarks of radial glia, like bipolar morphology, including BLBP and Pax6 expression (Conti et al. 2005; Pollard et al. 2006). The level of Pax6 is directly related with neural stem cell self-renewal, proliferation and differentiation (Sansom et al. 2009; Gómez-López et al. 2011).

Previous studies in catshark embryos show that Pax6 is expressed in the developing OE, and immature neurons positive for Pax6 are present along olfactory axons, as it happens in other vertebrates (see Ferreiro-Galve et al. 2012; Quintana-Urzainqui et al. 2014 and references therein). In addition, previous to the emergence of the OP (S30), numerous Pax6 cells were observed in the ventricular zone of the ventrolateral pallium (present results; Ferreiro-Galve et al. 2012). As the molecular phenotype of these cells was not addressed, we have compared the expression pattern of Pax6 with the expression pattern of stem cell marker (*ScSox2*) and glial markers (GFAP and BLBP) in the embryonic S30 of catshark.

In S30 embryos, numerous Pax6-expressing cells are present in the ventrolateral ventricular zone of the pallium, and differences in the intensity of the Pax6 labeling between positive cells close to the ventricle and cells located far from the ventricle are observed, which are in agreement with the previous studies in the catshark (Ferreiro-Galve et al. 2012). *ScSox2*-expressing cells are observed at the same location of Pax6-positive cells. Besides, these cells also show immunoreactivity to radial glia markers (GFAP and BLBP) and proliferative activity (PCNA immunoreactivity). Studies with neural stem cell lines indicate that Sox2 is a marker of stem cells and maintain neural stem cells in a proliferative and undifferentiated state. These studies also show that a complete ablation of Sox2 expression produces a loss of proliferative capacity; in addition, low levels of Pax6 are necessary to sustain proliferation and bipolar morphology of neural stem cells, while inactivation of Pax6 reduce the proliferative capacity of stem cells (Sakurai and Osumi 2008; Sansom et al. 2009; Gómez-López et al. 2011).

Our results show that Pax6-expressing cells located in the ventricular zone of the ventrolateral pallium express *ScSox2*, show proliferative capacity (PCNA) and molecular hallmarks of radial glia (GFAP and BLBP expression), as the mammalian neural stem cells present in the pallial ventricular zone.

Neurogenic markers related with the differentiation of glutamatergic cell lineage are expressed in the developing OB of catshark

In the developing neocortex of mammals, the transcription factor Pax6 is expressed sequentially together with other transcription factors (Tbr2 and Tbr1) in progenitor cells and postmitotic neurons of glutamatergic cell lineage (Englund et al. 2005; Hevner et al. 2006). Interestingly, the transcriptional program that operates in the differentiation of glutamatergic phenotype in the developing neocortex is also necessary for correct morphogenesis of the OB and generation of mitral cells (Bulfone et al. 1998; Imamura and Greer 2013; Kahoud et al. 2014; Roybon et al. 2015).

In rodents, mitral cells are the first cellular subtype of the OB to be born; these cells are generated around the embryonic day E12 from progenitor cells located in the ventricular zone of the OB (Hinds 1968). Progenitor cells of mitral cells express Pax6 (Winpenny et al. 2011; Imamura and Greer

2013), and in Pax6 mutant mice mitral cells are misallocated (for review see: Nomura et al. 2007). Tracking experiments in mammals with BrdU labeling show that mitral cells are generated from Pax6-positive radial glial cells and post-mitotic mitral cell precursors also express both Tbr1 and Tbr2 during embryogenesis (Bulfone et al. 1999; Faedo et al. 2002; Imamura and Greer 2013).

Expression of both transcription factors is essential for the generation of mitral cells and its expression occurs in the same developmental period in which Pax6 expression is down-regulated (Imamura and Greer 2013). In Tbr2 mutant mice, the amount of mitral cells is reduced and their organization and projections disturbed, which is similar to what happens in Tbr1 mutant mice (Bulfone et al. 1998, 1999; Imamura and Greer 2013; Kahoud et al. 2014). Moreover, the bHLH transcription factor NeuroD is expressed in the mature glomerular layer, and overexpression of NeuroD leads to the appearance of mature neurons, but knockdown of NeuroD inhibits neuronal differentiation (Boutin et al. 2010). In amphibians, expression of Pax6, Tbr1 and Tbr2 is detected in the developing OB of embryos or larvae (Brox et al. 2004; Moreno et al. 2003, 2008) and Tbr1 expression is also present in the OB of zebrafish 48 hpf (Mione et al. 2001).

In the present work, we have detected *ScTbr2* and *ScNeuroD* expression and Tbr1 immunoreactivity in the primordial OB of S31 of development. Besides, a stream of Pax6-expressing cells can be seen coursing from the VZ of the pallium to the OP of S31 (present results; Ferreiro-Galve et al. 2012). Interestingly, the expression of Pax6 decreased in *ScTbr2*- and *ScNeuroD*-positive territories. In S32 embryos, the expression of *ScTbr2*, *ScNeuroD* and Tbr1 becomes restricted to territories adjacent to protoglomeruli; TH immunoreactive granular and periglomerular cells are also observed in the OB in late S32 embryos (Carrera et al. 2012; Quintana-Urzainqui et al. 2015). We did not find TH immunoreactivity in early S32 embryos indicating that at this developmental period, TH does not colocalize with Tbr1, which is in agreement with previous results in the catshark (Carrera et al. 2012; Quintana-Urzainqui et al. 2015). The expression pattern of neurogenic markers that we found at S32 embryos (present results), seems to be adjacent to the TH-positive cell populations described previously in the catshark, which suggest us that the territories expressing *ScTbr2*, Tbr1 and *ScNeuroD* may correspond to the prospective glomerular layer, where mitral cells are intermingled.

In addition, we have shown that both *ScTbr2* and *ScNeuroD* colocalize with Tbr1, but, as in rodents, it seems that some cells express Tbr1 or Tbr2 only (Imamura and Greer 2013). In the mammalian developing OB, studies of expression of Tbr2 and Tbr1 show that mitral cells express these factors in an overlapping pattern (Imamura and Greer 2013), which is in agreement with our results. On the other hand, in mammals, NeuroD expression pattern also overlapped Tbr2 expression, but not Tbr1 expression, indicating the existence of subsets of mitral cells (Roybon et al. 2015). Besides, recent studies show that maturation of mitral cells depends on their position in the developing OB (Nguyen and Imamura 2019). Some studies in elasmobranchs based on Golgi staining have evidenced the existence of two kind of mitral cells in the OB of the sharks studied (*Sphyrna tiburo, Dasyatis sabina* and *Rhizoprionodon terranovae)*: mitral cells with dense and tight arborized dendrites and mitral cells with a loose dendrite arborization (Dryer and Graziadei 1993). As far as we know, the existence of more than one type of mitral cells has not been described in *S. canicula* and in the present work, we were not able to define different subsets of mitral cells with the same markers used in mammals. Whether our results are in line with different degrees of maturation deserves further investigations.

In the catshark, the expression pattern of the different neurogenic markers overlapped with that of *ScvGlut1* (present results). In later embryos of rodents, Vglut1 was detected in the mitral cell layer (Ohmomo et al. 2011) and a strong expression of this transporter was also observed in mitral cells of adult reptiles (Sarkar and Atoji 2018).

All these findings together suggest us that Pax6-positive cells (with molecular hallmarks of radial glial cells; see above) that are present in the pallial ventrolateral ventricular zone generate new-born neuroblasts (Pax6 positive) forming a stream of Pax6-positive cells from the ventrolateral pallium to the OP. When these Pax6-expressing cells reach the OP, it seems that they experiment a downregulation of Pax6 expression and begin to upregulate transcription factors related with the specification/differentiation of glutamatergic cells (*ScTbr2, ScNeuroD*, Tbr1); later in development, when these molecular markers are still expressed, cells begin to express a marker of glutamatergic mitral cells (*ScvGlut1*) indicating that a maturity stage has been achieved (for a summary see Fig. 5).

In addition, mitral cells in the developing OB of catshark express the same transcription factors related with the differentiation of pallial glutamatergic cell lineage (Docampo-Seara et al. 2018a), suggesting that the transcriptional program which rules glutamatergic neurogenesis in different telencephalic areas has been conserved throughout the vertebrate evolution.

The OB of mammals and sharks shares similarities in their developmental timing and molecular programs

Mitral cells are the first cell type to be born in the mammalian OB. These cells originate from progenitor cells located in the pallial/olfactory ventricular zone before the olfactory axons induce the emergence of the OP (E12) (Gong and

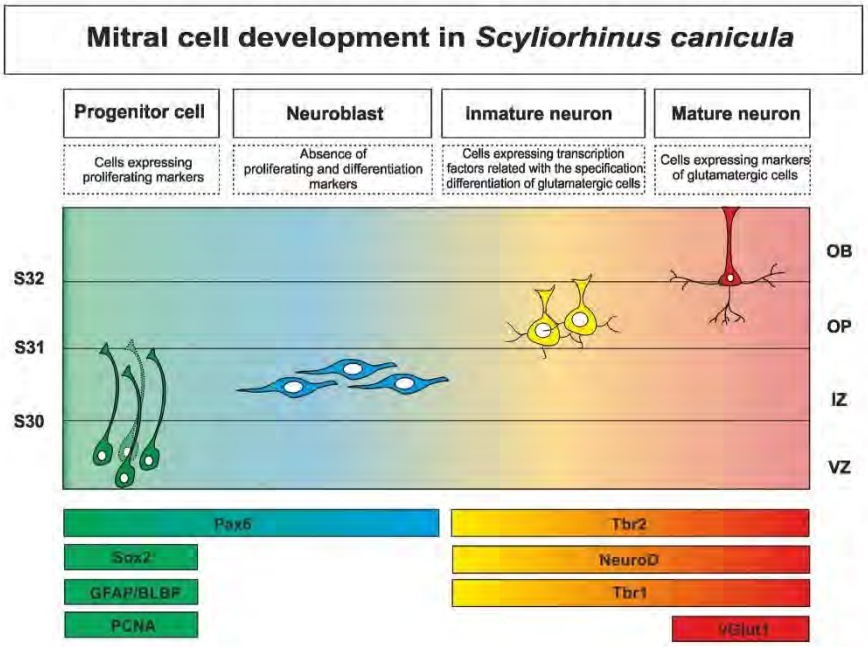

Fig. 5 Scheme summarizing the expression pattern of glutamatergic neurogenic markers implicated in mitral cell development. Cell types and their molecular hallmarks are indicated on the top of the figure. Molecular markers used in the present study are indicated below. embryonic stages of development are represented as horizontal lines and indicated in the left, and anatomical regions are indicated in the right

Shipley 1995) and reach the OB following a radial migration process. Their neurogenic timing comprises from E10 to E13, with a neurogenic peak around E11 (Blanchart et al. 2006).

In the catshark, our results indicate that mitral cells are produced in the pallial VZ before the emergence of the OP. In the present work, we have performed BrdU pulse-chase experiments in catshark embryos before the emergence of the OB (pulse in 3 catshark embryos at S28, S29 and S30 and chase at S31, when the OP and markers of mitral cells are present). We found that most mitral cells are generated by progenitor cells that have divided at S28. However, some of them are also generated at S29. In S30pulse-S31chase BrdU-positive cells in the mitral cell territory are practically inexistent. This suggests that mitral cells are generated between S28 and S29. However, we cannot discard the possibility that some mitral cells could be generated at S30 (or later) and arrive to the OB later than at S31 of development.

When mitral cells are generated, in contrast to mammals, they seem to migrate tangentially up to S31; later, at S32, a diffuse band of glutamatergic cells is present in the primordium OB, which reminds their mature disposition in the adult OB.

On the other hand, in mice, interneurons are generated after the first waves of mitral cells arrive to the OB. Around E13.5, the subpallial lateral ganglionic eminence (LGE), begins to express the distal-less homeobox gene 2 (Dlx2) and, most part of OB interneurons is produced at this embryonic time (Wichterle et al. 2001; Vergaño-Vera et al. 2006; Kohwi et al. 2007). Interneuron production is persistent through the entire life of mammals, but during development, an important neurogenic peak can be detected between E15.5 and 17.5 (Batista-Brito et al. 2008; Lledo et al. 2008). During embryonic development, interneurons follow a tangential migration to the OB and, once they achieve the OB, they migrate radially and integrate in the OB circuitry. First interneurons from LGE arrived at the OB around E14.5 (Yoshihara et al. 2005).

As in mammals, in the telencephalon of late embryos of catshark, a subventricular lateral stream of cells positive for *ScDlx2* directed towards the olfactory bulb have been observed at S31 (Quintana-Urzainqui et al. 2015). These

cells originate in the subpallial lateral ganglionic eminence homologue in sharks (LGE-h; Quintana-Urzainqui et al. 2012) from S29 on (Quintana-Urzainqui et al. 2015). After this stream reaches the OB, numerous TH-ir cells are found in the OB from late S32 embryos onwards, which indicate that these cells are the source of the granular and periglomerular cells of the mature OB (Ferreiro-Galve et al. 2012; Carrera et al. 2012; Quintana-Urzainqui et al. 2015). For an integrated view of development in the catshark of both mitral cells and interneurons, see Fig. 6.

Equivalences between different embryonic stages of rodents and sharks have been made according to different developmental key events and three periods have been established (see Table 1 in Rodríguez-Moldes et al. 2017). Stages of development comprised between E10 and 14.5 of mice and S27–31 of catshark are comparable (second period; around 30 days in the catshark), while E14.5–20 of mice corresponds to S32–34 of catshark (third period; up to 100 days in the catshark). According to this, mitral cells are born and arrive to the OP of mice and sharks in the same developmental period. In addition, neurogenesis of dopaminergic neurons (granule and periglomerular cells) in sharks and mice seem to be comparable too. However, in the catshark, we cannot discard the possibility that generation of mitral cells and interneurons could be overlapped in development due to the long protracted embryogenesis of the catshark. An integrative view of both processes shows that the OB of mammals and sharks share similarities not only in their developing molecular programs, but also in the time of generation of projection neurons and interneurons.

The presence of an accessory component in the OB of the catshark: an unsolved question

Most amphibians, reptiles and mammals possess a dual olfactory system with two separate neural pathways: the main olfactory system and the olfactory accessory system. The accessory olfactory system (or vomeronasal system; VNS) consists in a vomeronasal olfactory epithelium (VNO or Jacobson´s organ), an AOB, and the axons of the projecting neurons that reach different regions of the amygdala; from these region projections to hypothalamic regions are

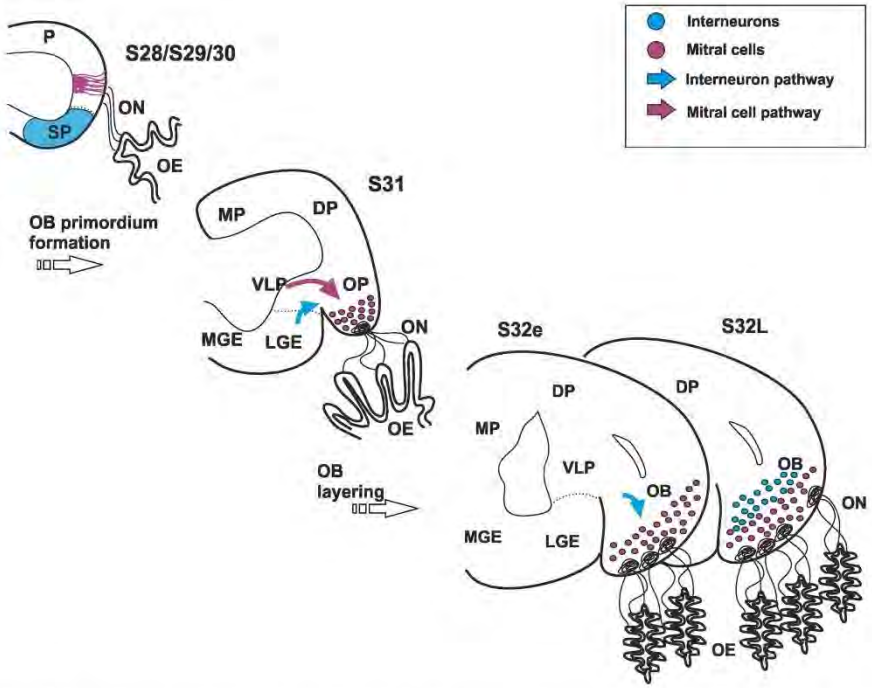

Fig. 6 Scheme summarizing an integrated view of development of both mitral cells (present results) and interneurons in the OB of catshark (data from Quintana-Urzainqui et al. (2015) and Rodríguez-Moldes et al. (2017)

observed (for review see: González et al. 2010; Maximino et al. 2013).

Although in fish a unique olfactory epithelium is present and an AOB anatomically distinct of the MOB is not recognizable, an accessory olfactory system comparable to the VNS of tetrapods has been described in the lungfish using antibodies against transcription factors and neuronal markers characteristic of distinct portions of the VNS (González et al. 2010). In the catshark, ciliated sensory neurons, the typical cell morphology of the main OE, are lacking, and the main receptor neurons of the olfactory mucosa of *Scyliorhinus canicula* are the microvillous receptor neurons and crypt neurons, whose projections show a segregated distribution in the OB (Theisen et al. 1986; Ferrando et al. 2009). Genomic studies indicate that VNS-specific genes are present in teleost fish (for review see: Grus and Zhang 2009), cartilaginous fish (Sharma et al. 2019) and sea lamprey (Grus and Zhang 2009). In the catshark, V2R, a component of the vomeronasal signaling pathway, are the predominant chemosensory receptor family, and a small number of genes for chemosensory receptors of the main olfactory system are also present (Sharma et al. 2019).

In rodents, projection neurons of the MOB and anterior AOB originate from the same pallial ventricular zone. However, projection neurons of the posterior AOB arise from caudal areas located at the diencephalic–telencephalic boundary (Huilgol et al. 2013; Huilgol and Tole 2016). In the present work, we found a migratory stream from the pallial neuroepithelium toward the OB, but we do not have observed any evidence of a migratory stream from the diencephalic–telencephalic boundary towards the OB. Numerous studies in rodents indicate that Pax6 is required for OB mitral cell specification and differentiation in the MOB and anterior AOB (Huilgol and Tole 2016). In addition, Tbr1 is also involved in the specification of the projection neurons of the anterior AOB but not in the mitral cells of the posterior AOB (Huilgol and Tole 2016). However, in amphibians Tbr1 is also implicated in the migration of posterior AOB cells (Huilgol et al. 2013).

An important component of the vomeronasal system in rodents is the secondary bulbar projections. In rodents, mitral cells of the AOB project to the medial amygdala and from this region to the hypothalamus (Halpern and Martínez-Marcos 2003). In the lungfish, a region homologue to the medial amygdala of tetrapods expresses the transcription factor orthopedia (Otp) and Islet1 (ISL1), and different neuronal markers such as nitric oxide synthase (nNOS) and substance P (SP), which is in agreement with results obtained in amphibians (for review see: Maximino et al. 2013; González et al. 2010). In a previous study in the catshark, it was suggested that in S32 embryos, a lateral subpallial region with Pax6-, Dlx2- and GAD-expressing cells represent an amygdala-like structure, and this region in the adult brain shows numerous SP-immunoreactive fibers (Rodríguez-Moldes et al. 1993; Quintana-Urzainqui et al. 2012). In addition, after DiI application to the OB of juvenile of *Scyliorhinus canicula*, retrogradely labeled cells and fibers were observed in the dorsolateral part of the basal superficial area (a LGE-h derivative in the catshark, Quintana-Urzainqui et al. 2012) and in the lateral hypothalamus (Yáñez et al. 2011). However, further investigations are necessary to elucidate whether the lateral subpallial region in the telencephalon of catshark could be homologue to some amygdaloid territories of tetrapods.

Our results indicate that transcription factors (Pax6 and Tbr1) related with the specification of the MOB and anterior AOB of mammals are present in the catshark. Although we have observed regional differences in the combined expression of Tbr1 and Tbr2 in the OB of catshark, this observation does not allow us to reach any conclusion about the existence of an accessory component in the OB of the catshark. On the other hand, genomic and other cytological data (for review see: Ferrando and Gallus 2013: Sharma et al. 2019) indicate that the vomeronasal-type receptors component are the predominant in the olfactory epithelium, whereas main olfactory receptors are minority; moreover, ciliated olfactory neurons were not found in the olfactory epithelium of catshark, which suggest that the olfactory mucosa of catshark may be similar to the vomeronasal epithelia of tetrapods. Further, studies of the expression/pattern of transcription factors and neuronal markers related with the specification/differentiation of different components of the vomeronasal system in the central nervous system are key to elucidate the existence of the brain areas/connections implicated in the processing of vomeronasal-type information in the catshark.

Conclusions

In the present work, we have carried out a detailed analysis of the transcription factors (Pax6, Tbr2, NeuroD and Tbr1) involved in the glutamatergic neurogenesis during OB development in the catshark. Proliferative Pax6-positive cells with stem cell and radial glial features are present before the emergence of the OB in the pallial ventricular zone of catshark. Cell tracking analysis using BrdU confirms that progenitors with these characteristics give rise to cells that migrate to the OP and locate in the presumptive territory where glutamatergic/mitral cells should be located. We found that mitral cells in the catshark seem to express the same battery of transcription factors found in mammals, which seem to indicate that the transcription program of glutamatergic cells specification/differentiation has been conserved throughout vertebrates evolution. However, the same factors that in mammals clearly differentiate subsets of

mitral cells (Tbr2-Tbr1, Tbr2-NeuroD) do not differentiate them in the catshark.

In addition, comparisons between our data and previous studies have evidenced that the origin and expression pattern of transcription factors related with the specification/differentiation of glutamatergic are common to mammals, evidencing a high conserved pattern of neurogenesis.

Acknowledgements We would like to thank Dr. Ferreiro-Galve for kindly providing anti-Pax6 immunohistochemically stained samples (S31).

Funding This work was supported by the Spanish Ministerio de Economía y Competitividad-FEDER (BFU2014-5863-1P and BFU2017-8986-1P) and CNRS Université Pierre et Marie Curie Grant No. ANR-16-CE13-0013-02.

Compliance with ethical standards

Conflict of interest The authors declare no conflict of interest.

Ethical approval All procedures conformed to the guidelines established by the European Communities Council Directive of 22 September 2010 (2010/63/UE) and by Spanish Royal Decree 53/2013 for animal experimentation, and were approved by the Ethics Committee of the University of Santiago de Compostela.

References

Anadón R, Molist P, Rodríguez-Moldes I, López JM, Quintela I, Cerviño MC, Barja P, González A (2000) Distribution of choline acetyltransferase immunoreactivity in the brain of an elasmobranch, the lesser spotted dogfish *(Scyliorhinus canicula)*. J Comp Neurol 420:139–170

Anadón R, Rodríguez-Moldes I, Adrio F (2013) Glycine-immunoreactive neurons in the brain of a shark (*Scyliorhinus canicula* L.). J Comp Neurol 521:3057–3082

Ballard WW, Mellinger J, Lechenault H (1993) A series of normal stages for development of *Scyliorhinus canicula*, the lesser spoted dogfish (Chondrichthyes: Scyliorhinidae). J Exp Zoo 267:318–336

Batista-Brito R, Close J, Machold R, Fishell G (2008) The distinct temporal origins of olfactory bulb interneuron subtypes. J Neurosci 28:3966–3975

Biechl D, Tietje K, Ryu S, Grothe B, Gerlach G, Wullimann MF (2017) Identification of accessory olfactory system and medial amygdala in the zebrafish. Sci Rep 7:44295

Blanchart A, De Carlos JA, López-Mascaraque L (2006) Time frame of mitral cell development in the mice OB. J Comp Neurol 496:529–543

Blanchart A, Martín-López E, De Carlos JA, López-Mascaraque L (2011) Peripheral contributions to OB cell populations (migrations towards the OB). Glia 59:278–292

Boehm U (2006) The vomeronasal system in mice: from the nose to the hypothalamus- and back! Semin Cell Dev Biol 7:471–479

Boutin C, Hardt O, de Chevigny A, Coré N, Goebbels S, Seidenfaden R, Bosio A, Cremer H (2010) NeuroD1 induces terminal neuronal differentiation in olfactory neurogenesis. Proc Natl Acad Sci USA 107:1201–1206

Brox A, Puelles L, Ferreiro B, Medina L (2004) Expression of the genes Emx1, Tbr1, and Eomes (Tbr2) in the telencephalon of *Xenopus laevis* confirms the existence of a ventral pallial division in all tetrapods. J Comp Neurol 474:562–577

Bulfone A, Smiga SM, Shimamura K, Peterson A, Puelles L, Rubenstein JL (1995) T-brain-1: a homolog of Brachyury whose expression defines molecularly distinct domains within the cerebral cortex. Neuron 15:63–78

Bulfone A, Wang F, Hevner R, Anderson S, Cutforth T, Chen S, Meneses J, Pedersen R, Axel R, Rubenstein JL (1998) An olfactory sensory map develops in the absence of normal projection neurons or GABAergic interneurons. Neuron 21:1273–1282

Bulfone A, Martinez S, Marigo V, Campanella M, Basile A, Quaderi N, Gattuso C, Rubenstein JL, Ballabio A (1999) Expression pattern of the Tbr2 (Eomesodermin) gene during mouse and chick brain development. Mech Dev 84:133–138

Carrera I, Molist P, Anadón R, Rodríguez-Moldes I (2008a) Development of the serotoninergic system in the central nervous system of a shark, the lesser spotted dogfish *Scyliorhinus canicula*. J Comp Neurol 511:804–831

Carrera I, Ferreiro-Galve S, Sueiro C, Anadón R, Rodríguez-Moldes I (2008b) Tangentially migrating GABAergic cells of subpallial origin invade massively the pallium in developing sharks. Brain Res Bull 75:405–409

Carrera I, Anadón R, Rodríguez-Moldes I (2012) Development of tyrosine hydroxylase-immunoreactive cell populations and fiber pathways in the brain of the dogfish *Scyliorhinus canicula*: new perspectives on the evolution of the vertebrate catecholaminergic system. J Comp Neurol 520:3574–3603

Chang S, Chung-Davidson YW, Libants SV, Nanlohy KG, Kiupel M, Brown CT, Li W (2013) The sea lamprey has a primordial accessory olfactory system. BMC Evol Biol 13:172

Conti L, Pollard SM, Gorba T, Reitano E, Toselli M, Biella G, Sun Y, Sanzone S, Ying QL, Cattaneo E, Smith A (2005) Niche-independent symmetrical self-renewal of a mammalian tissue stem cell. PLoS Biol 3:e283

Coolen M, Sauka-Spengler T, Nicolle D, Le-Mentec C, Lallemand Y, Da Silva C, Plouhinec JL, Robert B, Wincker P, Shi DL, Mazan S (2009) Evolution of axis specification mechanisms in jawed vertebrates: insights from a chondrichthyan. PLoS One 2:e374

Curto GG, Nieto-Estévez V, Hurtado-Chong A, Valero J, Gómez C, Alonso JR, Weruaga E, Vicario-Abejón C (2014) Pax6 is essential for the maintenance and multi-lineage differentiation of neural stem cells, and for neuronal incorporation into the adult OB. Stem Cells Dev 23:2813–2830

Dellovade TL, Pfaff DW, Schwanzel-Fukuda M (1998) OB development is altered in small-eye (Sey) mice. J Comp Neurol 402:402–418

Díaz-Guerra E, Pignatelli J, Nieto-Estévez V, Vicario-Abejón C (2013) Transcriptional regulation of OB neurogenesis. Anat Record 296:1364–1382

Docampo-Seara A, Lagadec R, Mazan S, Rodríguez MA, Quintana-Urzainqui I, Candal E (2018a) Study of pallial neurogenesis in shark embryos and the evolutionary origin of the subventricular zone. Brain Struct Funct 223:3593–3612

Docampo-Seara A, Santos-Duran GN, Candal E, Rodríguez MA (2018b) Expression of radial glial markers (GFAP, BLBP and GS) during telencephalic development in the catshark (*Scyliorhinus canicula*). Brain Struct Funct. https://doi.org/10.1007/s00429-018-1758-2

Dryer L, Graziadei PPC (1993) A pilot study on morphological compartmentalization and heterogeneity in the elasmobranch OB. Anat Embryol 188:41–51

Dryer L, Graziadei PPC (1994) Projections of the olfactory bulb in an elasmobranch fish, *Sphyrna tiburo*: segregation of inputs in the telencephalon. Anat Embryol (Berl) 190:563–572

Dryer L, Graziadei PPC (1996) Synaptology of the olfactory bulb of an elasmobranch fish, *Sphyrna tiburo*. Anat Embryol (Berl) 193:101–114

Englund C, Flink A, Lau C, Pham D, Daza RA, Bulfone A, Kowalczyk T, Hevner RF (2005) Pax6, Tbr2, and Tbr1 are expressed sequentially by radial glia, intermediate progenitor cells, and postmitotic neurons in developing neocortex. J Neurosci 25:247–251

Faedo A, Ficara F, Ghiani M, Aiuti A, Rubenstein JL, Bulfone A (2002) Developmental expression of the T-box transcription factor T-bet/Tbx21 during mouse embryogenesis. Mech Dev 116:157–160

Ferrando S, Gallus L (2013) Is the olfactory system of cartilaginous fishes a vomeronasal system? Front Neuroanat 17(7):37

Ferrando S, Bottaro M, Gallus L, Girosi L, Vacchi M, Tagliafierro G (2006a) First detection of olfactory marker protein (OMP) immunoreactivity in the olfactory epithelium of a cartilaginous fish. Neurosci Lett 413:173–176

Ferrando S, Bottaro M, Gallus L, Girosi L, Vacchi M, Tagliafierro G (2006b) Observations of crypt neuron-like cells in the olfactory epithelium of a cartilaginous fish. Neurosci Lett 403:280–282

Ferrando S, Gambardella C, Ravera S, Bottero S, Ferrando T, Gallus L, Manno V, Salati AP, Ramoino P, Tagliafierro G (2009) Immunolocalization of G-protein alpha subunits in the olfactory system of the cartilaginous fish *Scyliorhinus canicula*. Anat Rec (Hoboken) 292:1771–1779

Ferrando S, Gallus L, Gambardella C, Ghigliotti L, Ravera S, Vallarino M, Vacchi M, Tagliafierro G (2010) Cell proliferation and apoptosis in the olfactory epithelium of the shark *Scyliorhinus canicula*. J Chem Neuroanat 40:293–300

Ferrando S, Gallus L, Gambardella C, Amaroli A, Cutolo A, Masini MA, Vallarino M, Vacchi M (2012) Neuronal nitric oxide synthase (nNOS) immunoreactivity in the olfactory system of a cartilaginous fish. J Chem Neuroanat 43:133–140

Ferreiro-Galve S, Candal E, Rodríguez-Moldes I (2012) Dynamic expression of Pax6 in the shark olfactory system: evidence for the presence of Pax6 cells along the olfactory nerve pathway. J Exp Zool B Mol Dev Evol 318:79–90

Franco MD, Pape MP, Swiergiel JJ, Burd GD (2001) Differential and overlapping expression patterns of X-dll3 and Pax-6 genes suggest distinct roles in olfactory system development of the African clawed frog *Xenopus laevis*. J Exp Biol 204(Pt 12):2049–2061

Gillis JA, Shubin NH (2009) The evolution of gnathostome development: insight from chondrichthyan embryology. Genesis 47:825–841

Gómez-López S, Wiskow O, Favaro R, Nicolis SK, Price DJ, Pollard SM, Smith A (2011) Sox2 and Pax6 maintain the proliferative and developmental potential of gliogenic neural stem cells in vitro. Glia 59:1588–1599

Gong Q, Shipley MT (1995) Evidence that pioneer olfactory axons regulate telencephalon cell cycle kinetics to induce the formation of the OB. Neuron 14:91–101

González A, Morona R, López JM, Moreno N, Northcutt RG (2010) Lungfishes, like tetrapods, possess a vomeronasal system. Front Neuroanat 1:4

Götz M, Stoykova A, Gruss P (1998) Pax6 controls radial glia differentiation in the cerebral cortex. Neuron 21:1031–1044

Grus WE, Zhang J (2009) Origin of the genetic components of the vomeronasal system in the common ancestor of all extant vertebrates. Mol Biol Evol 26:407–419

Halpern M, Martínez-Marcos A (2003) Structure and function of the vomeronasal system: an update. Prog Neurobiol 70:245–318

Hara Y, Yamaguchi K, Onimaru K, Kadota M, Koyanagi M, Keeley SD, Tatsumi K, Tanaka K, Motone F, Kageyama Y, Nozu R, Adachi N, Nishimura O, Nakagawa R, Tanegashima C, Kiyatake I, Matsumoto R, Murakumo K, Nishida K, Terakita A, Kuratani S, Sato K, Hyodo S, Kuraku S (2018) Shark genomes provide insights into elasmobranch evolution and the origin of vertebrates. Nat Ecol Evol 2:1761–1771

Hevner RF, Hodge RD, Daza RA, Englund C (2006) Transcription factors in glutamatergic neurogenesis: conserved programs in neocortex, cerebellum, and adult hippocampus. Neurosci Res 55:223–233

Hinds JW (1968) Autoradiographic study of histogenesis in the mouse OB. I. Time of origin of neurons and neuroglia. J Comp Neurol 134:287–304

Huilgol D, Tole S (2016) Cell migration in the developing rodent olfactory system. Cell Mol Life Sci 73:2467–2490

Huilgol D, Udin S, Shimogori T, Saha B, Roy A, Aizawa S, Hevner RF, Meyer G, Ohshima T, Pleasure SJ, Zhao Y, Tole S (2013) Dual origins of the mammalian accessory olfactory bulb revealed by an evolutionarily conserved migratory stream. Nat Neurosci 16:157–160

Imamura F, Greer CA (2013) Pax6 regulates Tbr1 and Tbr2 expressions in olfactory bulb mitral cells. Mol Cell Neuro 54:58–70

Imamura F, Ayoub AE, Rakic P, Greer CA (2011) Timing of neurogenesis is a determinant of olfactory circuitry. Nat Neurosci 14:331–337

Joven A, Morona R, González A, Moreno N (2013) Spatiotemporal patterns of Pax3, Pax6, and Pax7 expression in the developing brain of a urodele amphibian, *Pleurodeles waltl*. J Comp Neurol 521:3913–3953

Kahoud RJ, Elsen GE, Hevner RF, Hodge RD (2014) Conditional ablation of Tbr2 results in abnormal development of the OBs and subventricular zone-rostral migratory stream. Dev Dyn 243:440–450

Kohwi M, Osumi N, Rubenstein JL, Alvarez-Buylla A (2005) Pax6 is required for making specific subpopulations of granule and periglomerular neurons in the OB. J Neurosci 25:6997–7003

Kohwi M, Petryniak MA, Long JE, Ekker M, Obata K, Yanagawa Y, Rubenstein JL, Alvarez-Buylla A (2007) A subpopulation of olfactory bulb GABAergic interneurons is derived from Emx1- and Dlx5/6-expressing progenitors. J Neurosci 27:6878–6891

Lim DA, Alvarez-Buylla A (2016) The adult ventricular-subventricular Zone (V-SVZ) and olfactory bulb (OB) neurogenesis. Cold Spring Harb Perspect Biol 8:a018820

Lledo PM, Merkle FT, Alvarez-Buylla A (2008) Origin and function of olfactory bulb interneuron diversity. Trends Neurosci 31:392–400

Maximino C, Lima MG, Oliveira KR, Batista Ede J, Herculano AM (2013) Limbic associative" and "autonomic" amygdala in teleosts: a review of the evidence. J Chem Neuroanat 48–49:1–13

Méndez-Gómez HR, Vergaño-Vera E, Abad JL, Bulfone A, Moratalla R, de Pablo F, Vicario-Abejón C (2011) The T-box brain 1 (Tbr1) transcription factor inhibits astrocyte formation in the OB and regulates neural stem cell fate. Mol Cell Neurosci 46:108–121

Mihalas AB, Hevner RF (2017) Control of neuronal development by T-box genes in the brain. Curr Top Dev Biol 122:279–312

Mione M, Shanmugalingam S, Kimelman D, Griffin K (2001) Overlapping expression of zebrafish T-brain-1 and eomesodermin during forebrain development. Mech Dev 100:93–97

Mizuguchi R, Naritsuka H, Mori K, Mao CA, Klein WH, Yoshihara Y (2012) Tbr2 deficiency in mitral and tufted cells disrupts excitatory-inhibitory balance of neural circuitry in the mouse OB. J Neurosci 32:8831–8844

Molist P, Rodriguez-Moldes I, Batten TF, Anadon R (1995) Distribution of calcitonin gene-related peptide-like immunoreactivity in

the brain of the small-spotted dogfish, *Scyliorhinus canicula* L. J Comp Neurol 352:335–350
Moreno N, Bachy I, Rétaux S, González A (2003) Pallial origin of mitral cells in the olfactory bulbs of Xenopus. NeuroReport 14:2355–2358
Moreno N, Morona R, López JM, Dominguez L, Muñoz M, González A (2008) Anuran olfactory bulb organization: embryology, neurochemistry and hodology. Brain Res Bull 75:241–245
Mueller T, Wulliman MF (2016) Atlas of early zebrafish brain development. Elsevier ISBN: 978012417269
Nguyen UP, Imamura F (2019) Regional differences in mitral cell development in the mouse olfactory bulb. J Comp Neurol. https://doi.org/10.1002/cne.24683
Nomura T, Osumi N (2004) Misrouting of mitral cell progenitors in the Pax6/small eye rat telencephalon. Development 131:787–796
Nomura T, Haba H, Osumi N (2007) Role of a transcription factor Pax6 in the developing vertebrate olfactory system. Dev Growth Differ 49:683–690
Ohmomo H, Ehara A, Yoshida S, Shutoh F, Ueda S, Hisano S (2011) Temporally distinct expression of vesicular glutamate transporters 1 and 2 during embryonic development of the rat olfactory system. Neurosci Res 70:376–382
Osorio J, Mueller T, Retaux S, Vernier P, Wullimann MF (2010) Phylotypic expression of the bHLH genes Neurogenin2, Neurod, and Mash1 in the mouse embryonic forebrain. J Comp Neurol 518:851–871
Pollard SM, Conti L, Sun Y, Goffredo D, Smith A (2006) Adherent neural stem (NS) cells from fetal and adult forebrain. Cereb Cortex 16(Suppl 1):i112–i120
Puelles L, Kuwana E, Puelles E, Bulfone A, Shimamura K, Keleher J, Smiga S, Rubenstein JL (2000) Pallial and subpallial derivatives in the embryonic chick and mouse telencephalon, traced by the expression of the genes Dlx-2, Emx-1, Nkx-2.1, Pax-6, and Tbr-1. J Comp Neurol 424:409–438
Quintana-Urzainqui I, Sueiro C, Carrera I, Ferreiro-Galve S, Santos-Durán G, Pose-Méndez S, Mazan S, Candal E, Rodríguez-Moldes I (2012) Contributions of developmental studies in the dogfish *Scyliorhinus canicula* to the brain anatomy of elasmobranchs: insights on the basal ganglia. Brain Behav Evol 80:127–141
Quintana-Urzainqui I, Rodríguez-Moldes I, Candal E (2014) Developmental, tract-tracing and immunohistochemical study of the peripheral olfactory system in a basal vertebrate: insights on Pax6 neurons migrating along the olfactory nerve. Brain Struct Funct 219:85–104
Quintana-Urzainqui I, Rodríguez-Moldes I, Mazan S, Candal E (2015) Tangential migratory pathways of subpallial origin in the embryonic telencephalon of sharks: evolutionary implications. Brain Struct Funct. https://doi.org/10.1007/s00429-014-0834-5
Rodríguez-Moldes I, Manso MJ, Becerra M, Molist P, Anadón R (1993) Distribution of substance P-like ir in the brain of the elasmobranch *Scyliorhinus canicula*. J Comp Neurol 335:228–244
Rodríguez-Moldes I, Santos-Durán GN, Pose-Méndez S, Quintana-Urzainqui I, Candal E (2017) The Brains of Cartilaginous Fishes. In: Kaas J (ed) Evolution of nervous systems, vol 1, 2nd edn. Elsevier, Oxford, pp 77–97. ISBN 978-0-12-804042-3
Roybon L, Mastracci TL, Li J, Stott SR, Leiter AB, Sussel L, Brundin P, Li JY (2015) The origin, development and molecular diversity of rodent OB glutamatergic neurons distinguished by expression of transcription factor NeuroD1. PLoS One. https://doi.org/10.1371/journal.pone.0128035
Sakurai K, Osumi N (2008) The neurogenesis-controlling factor, Pax6, inhibits proliferation and promotes maturation in murine astrocytes. J Neurosci 28:4604–4612
Sansom SN, Griffiths DS, Faedo A, Kleinjan DJ, Ruan Y, Smith J, van Heyningen V, Rubenstein JL, Livesey FJ (2009) The level of the transcription factor Pax6 is essential for controlling the balance between neural stem cell self-renewal and neurogenesis. PLoS Genet. https://doi.org/10.1371/journal.pgen.1000511
Sarkar S, Atoji Y (2018) Distribution of vesicular glutamate transporters in the brain of the turtle (*Pseudemys scripta elegans*). J Comp Neurol 526:1690–1702
Sharma K, Syed AS, Ferrando S, Mazan S, Korsching SI (2019) The chemosensory receptor repertoire of a true shark is dominated by a single olfactory receptor family. Genome Biol Evol 11:398–400
Smeets WJ, Nieuwenhuys R, Roberts BL (1983) The central nervous system of cartilaginous fishes: structure and functional correlations. Springer, Berlin
Stoykova A, Gruss P (1994) Roles of Pax-genes in developing and adult brain as suggested by expression patterns. J Neurosci 14(3 Pt 2):1395–1412
Sueiro C (2003) Estudio immunohistoquímico de los sistemas gabaérgicos del sistema nervioso central de peces elasmobranquios y su relación con sistemas catecolaminérgicos y peptidérgicos. Doctoral Thesis, Universidade de Santiago de Compostela, Spain
Teijido O, Manso MJ, Anadón R (2002) Distribution of thyrotropin-releasing hormone immunoreactivity in the brain of the dogfish *Scyliorhinus canicula*. J Comp Neurol 54:65–81
Theisen B, Zeiske E, Breuker H (1986) Functional morphology of the olfactory organs in the spiny dogfih (*Squalus acanthias* L.) and the small-spotted catshark (*Scyliorhinus canicula* L.). Acta Zool 67:73–86
Treloar HB, Miller AM, Ray A, Greer CA (2010) Development of the olfactory system. In: Menini A (ed) The neurobiology of olfaction. CRC Press/Taylor & Francis, Boca Raton (FL)
Vergaño-Vera E, Yusta-Boyo MJ, de Castro F, Bernad A, de Pablo F, Vicario-Abejón C (2006) Generation of GABAergic and dopaminergic interneurons from endogenous embryonic olfactory bulb precursor cells. Development 133:4367–4379
Wichterle H, Turnbull DH, Nery S, Fishell G, Alvarez-Buylla A (2001) In utero fate mapping reveals distinct migratory pathways and fates of neurons born in the mammalian basal forebrain. Development 128:3759–3771
Winpenny E, Lebel-Potter M, Fernandez ME, Brill MS, Götz M, Guillemot F, Raineteau O (2011) Sequential generation of OB glutamatergic neurons by Neurog2-expressing precursor cells. Neural Dev 6:12
Yáñez J, Folgueira M, Köhler E, Martínez C, Anadón R (2011) Connections of the terminal nerve and the olfactory system in two galeomorph sharks: an experimental study using a carbocyanine dye. J Comp Neurol 519:3202–3217
Yopak KE, Lisney TJ, Collin SP (2015) Not all sharks are "swimming noses": variation in OB size in cartilaginous fishes. Brain Struct Funct 220:1127–1143
Yoshihara S, Omichi K, Yanazawa M, Kitamura K, Yoshihara Y (2005) Arx homeobox gene is essential for development of mouse olfactory system. Development 132:751–762
Zaccone D, Lo Cascio P, Lauriano R, Pergolizzi S, Sfacteria A, Marino F (2011) Occurrence of neuropeptides and tyrosine hydroxylase in the olfactory epithelium of the lesser-spotted catshark (*Scyliorhinus canicula* Linnaeus, 1758). Acta Histochem 113:717–722